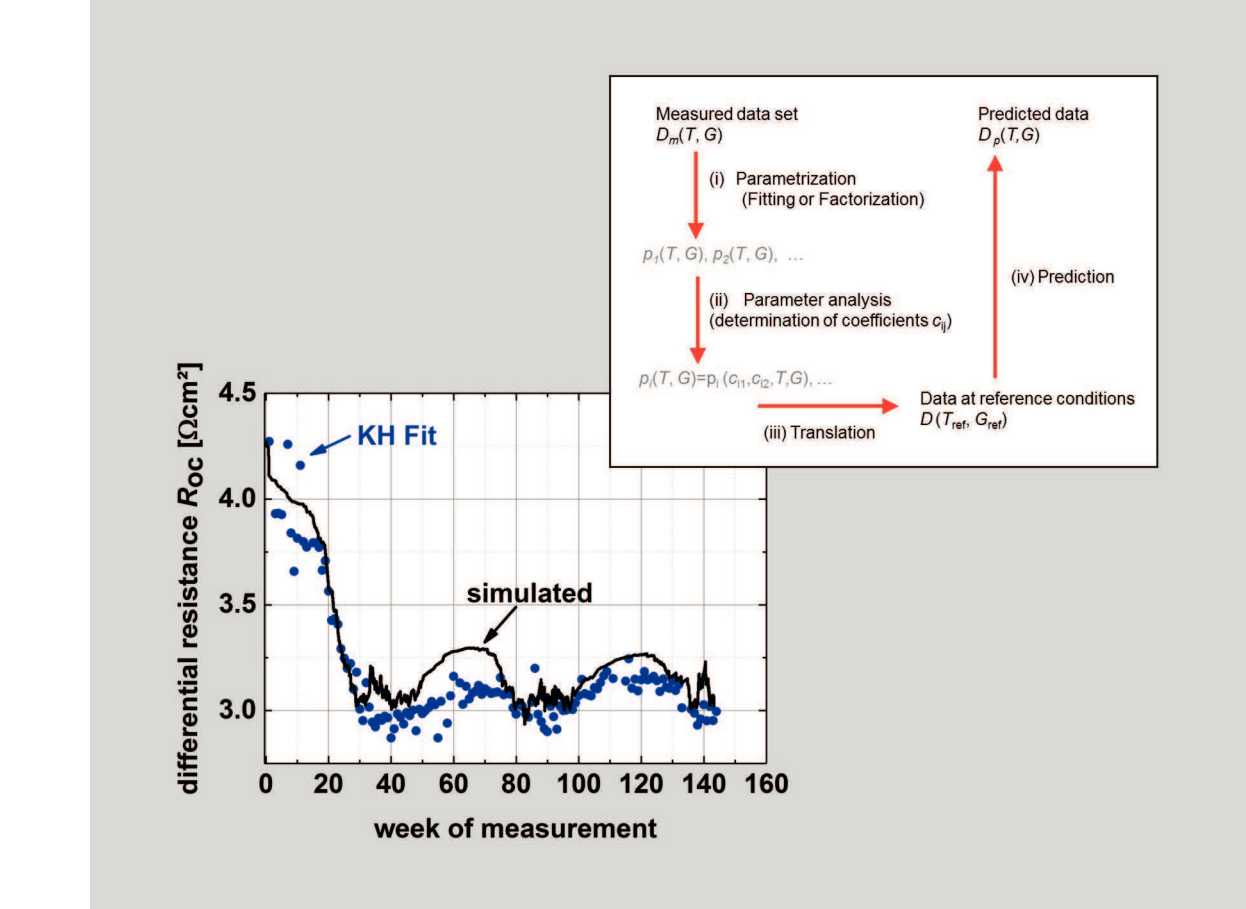
Energie & Umwelt Energy & Environment

Analysis & modeling of metastable photovoltaics



431

Analysis & modeling of metastable photovoltaic technologies: towards dynamic photovoltaic performance models

Marzella Amata Görig

Marzella Amata Görig

Energie & Umwelt / Energy & Environment Band / Volume 431 ISBN 978-3-95806-342-6

Energie & Umwelt / Energy & Environment Band / Volume 431 ISBN 978-3-95806-342-6







Schriften des Forschungszentrums Jülich Reihe Energie & Umwelt/Energy & Environment

Band / Volume 431

Forschungszentrum Jülich GmbH Institut für Energie- und Klimaforschung IEK-5 Photovoltaik

# Analysis & modeling of metastable photovoltaic technologies: towards dynamic photovoltaic performance models

Marzella Amata Görig

Bibliografische Information der Deutschen Nationalbibliothek. Die Deutsche Nationalbibliothek verzeichnet diese Publikation in der Deutschen Nationalbibliografie; detaillierte Bibliografische Daten sind im Internet über http://dnb.d-nb.de abrufbar.

Herausgeber Forschungszentrum Jülich GmbH

und Vertrieb: Zentralbibliothek, Verlag

52425 Jülich

Tel.: +49 2461 61-5368 Fax: +49 2461 61-6103 zb-publikation@fz-juelich.de www.fz-juelich.de/zb

Umschlaggestaltung: Grafische Medien, Forschungszentrum Jülich GmbH

Grafische Medien, Forschungszentrum Jülich GmbH Druck:

Copyright: Forschungszentrum Jülich 2018

Schriften des Forschungszentrums Jülich Reihe Energie & Umwelt / Energy & Environment, Band / Volume 431

D 82 (Diss., RWTH Aachen University, 2018)

ISSN 1866-1793 ISBN978-3-95806-342-6

Vollständig frei verfügbar über das Publikationsportal des Forschungszentrums Jülich (JuSER) unter www.fz-juelich.de/zb/openaccess.



This is an Open Access publication distributed under the terms of the Creative Commons Attribution License 4.0, which permits unrestricted use, distribution, and reproduction in any medium, provided the original work is properly cited.

# Contents

Α	bstra	ct		5	
Zι	usam	menfas	ssung	7	
1 Introduction				g	
2	Fun	damen	itals	15	
	2.1	Basic	physics of solar cells	15	
		2.1.1	Electronic states	16	
		2.1.2	Working principle of solar cells	20	
	2.2	Photo	voltaic performance models	23	
		2.2.1	Device simulators for thin film photovoltaics	24	
		2.2.2	Equivalent circuit models	27	
		2.2.3	Empirical models	34	
		2.2.4	General structure of PV performance models	39	
	2.3	Mode	ling of degradation and metastable effects	41	
3	Out	door d	ata and analysis method	43	
	3.1	Outdo	oor data set	43	
	3.2	3.2 Karmalkar-Haneefa model			
	3.3	Loss I	Factor Model	53	
4	Out	door d	ata analysis with the Karmalkar-Haneefa model	59	
	4.1	Paran	neterization	60	
		4.1.1	Results of the linear fits for CdTe $ \ldots  \ldots  \ldots  \ldots  \ldots  \ldots$	61	
		4.1.2	Comparison of the KH and linear fits for CdTe	64	
		4.1.3	Comparison of the KH and linear fits for all technologies	71	

### Contents

	4.2	Maximum power point fitting
		4.2.1 Analysis of the entire $JV$ curve fitting
		4.2.2 $$ Comparison of the KH fit with the one-diode model 81
		4.2.3 Analysis of the fit at the MPP
	4.3	Parameter analysis
		4.3.1 Parameter analysis for the KH model
		4.3.2 Parameter analysis for the LFM
		4.3.3 $$ Comparison of the KH model and LFM 95
	4.4	Yield prediction
		4.4.1 Methods
		4.4.2 Analysis and results $\dots \dots \dots$
	4.5	Conclusion
5	Don	radation Analysis and Modeling of CdTe Outdoor Data 109
3	5.1	Introduction degradation and annealing effects
	5.2	Coefficient analysis
	0.2	5.2.1 Open circuit voltage
		5.2.2 Differential conductance at short circuit condition
		5.2.3 Differential resistance at open circuit condition
		5.2.4 Analysis of the fill factor
		5.2.5 Ideality factor
	5.3	Analysis and modeling of different modules
		5.3.1 Analysis of different CdTe modules in Tempe 125
		5.3.2 Analysis of CdTe in different climate zones
		5.3.3 Results for the maximum power density and fill factor 131
		5.3.4 An empirical dynamic performance model
	5.4	Conclusion
_		
6		ew model for degradation and annealing of <i>a</i> -Si:H solar cells 143
	6.1	Annealing and degradation effects
	6.2	Light soaking experiment
		6.2.1 Execution of the experiment
	0.0	6.2.2 Experimental results
	6.3	Simulation model

				Contents
	6.4	6.3.1 6.3.2 6.3.3 6.3.4 Conclu	Opto-electronic device simulator	157 161 164
7	Con	clusion	1	173
Re	References 178			
Αį	peno	dices		191
Α	A Appendix for Chapter 3			193
В	Appendix for Chapter 4			197
С	Appendix for Chapter 5 205			205
	C.1 General results			
	C.2		neter and coefficient changes for all 12 CdTe modules	
		C.2.1	Open circuit voltage	
		C.2.2	Differential conductance at short circuit condition	
		C.2.3	Differential resistance at open circuit condition	223
		C.2.4	Fill Factor	
		C.2.5	Maximum Power Density	
		C.2.6	Tables with summarized analysis results	230
D	List	of Abl	breviations and Symbols	235
Ε	List	of pub	plications	241
F	Curriculum Vitae 243			243
Ad	Acknowledgments 245			

# **Abstract**

Climate change is one of the biggest problems in this century. To reduce the emissions that lead to the climate change, it is expected that renewable energy systems will become very important for our energy supply in the future. Among these renewable energies, photovoltaics (PV) belongs to one of the fastest growing technologies. The key drivers to justify an increasing share of photovoltaics in the energy market are the reduction in cost, the increase of efficiency and the increase in their reliability.

Thin film technologies have a share of the PV market of approximately only 7%. However, thin film technologies have many advantages that show their potential for the future. Their main advantages are their low costs and their promising application for new markets, as for example for climate zones with a high amount of diffuse irradiance or their possibility to use them as building-integrated modules and deposit them on flexible substrate.

A big challenge for thin film technologies is the energy yield prediction as thin film solar cells exhibit metastabilities. To solve this problem, dynamic performance models are necessary. In this thesis, the performance of thin film solar cells and modules are investigated and modeled under outdoor and laboratory conditions, whereas two approaches of dynamic performance models are implemented to improve the performance prediction of thin film modules. At the beginning of this work, a four-step procedure is defined to compare different performance models with each other. The current-density voltage (JV) curves of the outdoor modules are described with the empirical Karmalkar-Haneefa (KH) performance model. The KH model uses only four physical parameters, namely the open circuit voltage  $(V_{oc})$ , the differential resistance at the open circuit point  $(R_{oc})$ , the short-circuit current density  $(J_{sc})$ , and the differential conductance at the short-circuit point  $(G_{sc})$ , to

#### Abstract

describe the JV curve. The parameterization and the fitting quality of the whole JV curve and especially of the maximum power density are investigated. Good fits are found for single thin film technologies as CdTe, CIGS, and a-Si:H. Tandem modules as a-Si:H/ $\mu$ c-Si:H show not very good fits and for crystalline technologies the KH model cannot be recommended. Afterwards, the parameter analysis and the performance prediction of the KH model are compared to the commonly used Loss Factor Model (LFM). It is found that the KH model is suitable for outdoor description and analysis of thin film modules.

The KH model is used to analyze the metastable and long-term degradation behavior of CdTe modules. It was found that the initial and degradation phase of the module performance are influenced by  $V_{\rm oc}$  and  $G_{\rm sc}$ , and especially by  $R_{\rm oc}$ . The behavior of all these parameters is investigated for more than two years considering four different climate regions. In addition, an empirical dynamic model describing the behavior of  $R_{\rm oc}$  in the four climate zones is implemented. It was found that the consolidation phase of  $R_{\rm oc}$  and  $G_{\rm sc}$  as well as the seasonal behavior of  $R_{\rm oc}$  are evoked by the effect of voltage-dependent photo-current.

In the last part of this thesis, finally the approach for a physical dynamic performance model is investigated. The investigation is done for a-Si:H solar cells as already a good knowledge exists about their metastable behavior. In a first step, a huge long-term light-soaking experiment has been done which considers different cell thicknesses, different light intensities and the dynamic response after changing of the light intensity. The performance is described with a combination of a device simulator and rate equation describing the evolution of defects directly. The performance of the investigated cells can be described in a suitable range with this model. However, due to the lack of physical knowledge of the exact defect evolution, a further improvement of the rate equations requires further investigation. For this, the developed dynamic performance model provides a very good template.

# Zusammenfassung

Der Klimawandel ist eine der größten Herausforderungen dieses Jahrhunderts. Aufgrund der erforderlichen Reduktion der Emissionen, die den Klimawandel hervorrufen, gewinnen erneuerbare Energien zunehmend an Bedeutung. Dabei gehört Photovoltaik (PV) zu den erneuerbaren Energien, die sehr schnell wachsen. Die Herausforderungen, die das Wachstum von Photovoltaik am Energiemarkt auch in Zukunft rechtfertigen, sind die Kostenreduzierung, eine steigende Effizienz und eine steigende Zuverlässigkeit dieser Technologie.

Dünnschichtsolarzellen haben aktuell einen Anteil am Photovoltaikmarkt von nur 7%. Sie besitzen jedoch viele Vorteile, die ihr Potential für die Zukunft aufzeigen. Ihre größten Vorteile sind ihre geringen Kosten und ihre vielversprechenden Anwendungen für neue Märkte, sei es in Klimaregionen wie Indien mit sehr hohem Anteil an diffusem Licht oder ihre Möglichkeit als gebäudeintegrierte Module genutzt zu werden sowie auf flexiblen Substraten deponiert zu werden.

Eine große Herausforderung für Dünnschichtmodule ist die Energievorhersage, da Dünnschichtsolarzellen metastabile Effekte aufweisen. Um dieses Problem zu lösen sind dynamische Performancemodelle erforderlich. In dieser Arbeit wird die Performance von Dünnschichtsolarzellen und -modulen unter Außen- und Laborbedingungen untersucht und simuliert. Dabei werden zwei Ansätze für dynamische Performancemodelle implementiert um die Energievorhersage von Dünnschichtmodulen zu verbessern.

Zu Beginn wird in einem ersten Schritt eine vier-Schritt Prozedur definiert, mit der verschiedene Performancemodelle miteinander verglichen werden können. Für die Außenmodule wurden die Stromdichte-Spannungskurven (JV) mithilfe des Karmalkar-Haneefa (KH) Modells beschrieben. Das KH Modell benötigt nur vier physikalische Parameter zur Beschreibung der JV Kurve. Bei den Parametern han-

#### Zusammenfassung

delt es sich um die Leerlaufspannung ( $V_{\rm oc}$ ), den differentiellen Widerstand am Leerlaufpunkt ( $R_{\rm oc}$ ), die Kurzschlussstromdichte ( $J_{\rm sc}$ ) und die differentielle Leitfähigkeit am Kurzschlusspunkt ( $G_{\rm sc}$ ). Die Parametrisierung, der qualitative Fit der gesamten JV Kennlinie und besonders der Fit an der maximalen Leistungsdichte wurden untersucht. Dabei wurden gute Fits für einfache Dünnschichttechnologien wie CdTe, CIGS und a-Si:H erzielt. Bei Tandemmodulen wie a-Si:H/ $\mu$ c-Si:H sind die Fits qualitativ schwächer und für kristalline Technologien kann der KH Fit nicht empfohlen werden. Nach dieser Analyse wurde die Parameteranalyse und die Performancevorhersage mit dem KH Modell und denen des bekannten Loss Factor Modells (LFM) miteinander verglichen. Dabei wurde festgestellt, dass das KH Modell für die Beschreibung von Dünnschichtmodulen unter Außenbedingungen geeignet ist.

Das KH Modell wurde zur Analyse der metastabilen Effekte und des Langzeit-Degradationsverhalten von CdTe verwendet. Es wird gezeigt, dass die Anfangs- und Degradationsphase der Modulleistung von  $V_{\rm oc}$ ,  $G_{\rm sc}$  und stark von  $R_{\rm oc}$  beeinflusst werden. Das Verhalten dieser Parameter wurde für mehr als zwei Jahre in vier verschiedenen Klimazonen untersucht. Zudem wurde ein empirisches dynamisches Modell für das Verhalten von  $R_{\rm oc}$  für vier Klimazonen aufgestellt und festgestellt, dass die Konsolidierungsphase von  $R_{\rm oc}$  und  $G_{\rm sc}$  sowie die saisonalen Schwankungen von  $R_{\rm oc}$  durch den Effekt der spannungsabhängigen Stromdichte hervorgerufen werden.

Im letzten Teil dieser Arbeit wird schließlich der Ansatz eines physikalischen dynamischen Performancemodells untersucht. Die Untersuchungen werden dabei für a-Si:H Solarzellen gemacht, da für diese Technologie bereits viel über ihr metastabiles Verhalten bekannt ist. In einem ersten Schritt wurde zunächst ein aufwändiger Lichtalterungsversuch durchgeführt, welcher den Effekt von verschiedenen Zelldicken, verschiedenen Lichtintensitäten und das dynamischen Verhalten nach einem Lichtintensitätenwechsel berücksichtigt. Die Zellperformance wird mit einem Modell bestehend aus einem Devicesimulator und einer Ratengleichung simuliert, die direkt die Defektevolution beschreibt. Die Performance der untersuchten Solarzellen konnte mithilfe des Modells gut simuliert werden. Aufgrund fehlenden physikalischen Wissens der genauen Defektevolution sind für weitere Verbesserungen der Ratengleichung jedoch weitere Untersuchungen notwendig. Dafür stellt das entwickelte dynamische Performancemodel eine gute Grundlage dar.

# 1. Introduction

There's one issue that will define the contours of this century more dramatically than any other, and that is the urgent and growing threat of a changing climate

— Barack Obama, 44th U.S. President

Climate change is one of the biggest problems in this century. Barack Obama illustrated that clearly by the above quote at the 2014 UN Climate Change Summit. In the following year, the 21st United Nations Climate Change Conference, COP 21, was held in Paris. During this conference, at the 21st December 2015, finally the agreement to limit the global average temperature rise to less than 2°C [1] was reached. This agreement is considered as a "major step" for climate negotiations [1]. To achieve that goal the worldwide greenhouse gas (GHG) emissions have to be reduced significantly. The majority GHG emission arises primarily from energy production in China, the United States, and the European Union [1], where approximately 80% of the primary energy supply derives from fossil fuels as coal, oil, and natural gas [2]. In addition, the worldwide energy demand is expected to increase by 48% from 2012 to 2040 [3]. Thereby, the electrical power sector belongs to the most dynamic areas of growth among all energy markets [3]. 2012 the world net electricity demand was  $21.6 \times 10^{12}$  kWh [3]. It is assumed that this demand will increase by 69% to  $36.5 \times 10^{12}$  kWh in 2040 [3]. To stop climate change and also meet the increase in energy demand, a transformation of the worldwide energy supply to sustainable energy systems is essential.

In 2014 the world total primary energy consumption was  $5.74 \times 10^{20} \,\mathrm{J}$  [3]. The annual amount of energy which is delivered to earth in form of solar irradiation is with  $5.4 \times 10^{24} \,\mathrm{J}$  [4] more than enough to satisfy our annual energy demand. Renewable energies such as photovoltaics, wind energy and hydro power represent

#### Introduction

the most direct way to convert this solar energy into electrical power.

Photovoltaics (PV) belongs to one of the most promising energy sources to fulfill the requirements for a sustainable energy market, especially for the electricity market. The photovoltaic market has experienced significant growth. From 2000 to 2014 the worldwide photovoltaic capacity has increased by a factor of 100, reaching a cumulative capacity of 178 GW[5]. However, this is not sufficient to effectively reduce GHG emissions. To facilitate a more rapid uptake of PV as a power source, the PV industry focuses on three main work programs [6]:

- 1. Cost reduction of PV cells and modules
- 2. Development of high-efficiency cells and modules
- 3. Increase in the reliability of PV technologies

The available photovoltaic technologies can be divided into two main classes: crystalline and thin film. Crystalline Silicon solar cells have always dominated the market [7], with thin film technologies making up the rest. The thin film market consists of three dominant technologies: hydrogenated amorphous silicon (a-Si:H), Cadmium Telluride (CdTe), and Copper Indium Gallium Diselenide (CIGS). In the early 1980s, a-Si:H was the first thin film technology that entered the commercial PV market [8] and dominated the thin film market until 2006. Since then CdTe has been dominant in the thin film technology market which made in 2014 approximately 7% of the worldwide PV market[7]. However, thin film technologies have a number of benefits compared to crystalline Silicon technologies. Thin film technologies are potentially cheaper as less material is used. Indeed, modules of a-Si:H, CdTe, and CIGS haven been cheaper per Watt peak than cyrstalline Silicon modules, even though the difference has become smaller in recent years [9]. Thin film technologies have a better performance under high irradiance environments with diffuse light and high temperature, which make them better suitable for regions like India [9]. India is a large potential market for thin film technologies as it is expected that half of the projected worldwide energy demand from 2012 to 2040 will be due to non-OECD Asia countries, which includes India [3]. Another important benefit of thin film technologies is that they can be used for a much wider application range than crystalline technologies as they can be deposit on flexible substrate. That makes them suitable for building integrated PV application. It can be expected that the

market of building integrated PV application will increase in the future [9]. Finally, thin film materials have become important for new cell design such as Silicon Hetero Junction (SHJ) solar cells (see for example [10]).

Despite these significant benefits, the market share of thin film solar cells is decreasing [9]. The main factor limiting the uptake and widespread use of thin film solar cells is the reliability. Reliability is essential for a power generation source. The motivation for the work of this thesis is to increase the reliability of thin film solar technologies. Increasing reliability means an increase in the system lifetime, system availability and predictability as well as a decrease in degradation and the operation and maintenance (O&M) costs [11]. The reliability has a major influence on the PV plant performance, and is thus an important factor for the financial investors and therefore for the uptake of thin film technology. Kurz et al. [11] showed that the cost of electricity to the consumer is inversely proportional to the energy produced by the module, i.e. by doubling the generation per year, the electricity cost is reduced by the half. Module degradation reduces the energy generation of the module, and therefore increase the electricity cost. A 1% degradation per year leads to an increase of electricity cost of 13% compared to the case with no degradation [11]. The exact number of the electricity cost depends, of course, on the considered technology and the environmental conditions.

To increase the reliability, a better prediction of the energy generation of thin film technologies is required, where the prediction of power must include degradation. The most common approach for long-term prediction is to include degradation rates (see for example [12]). Degradation rates, however, can vary between modules and do not consider metastable effects. Metastable effects refer to shorter terms than degradation. They lead to changes in the performance due to changes in environmental conditions and are reversible. The origination and annealing of metastable effects depend on the technology and they are important for thin film technologies [11]. For example, CdTe and CIGS show in general an increase in their performance under light-soaking and forward bias and a performance decrease under dark-conditions and high temperature ([13, 14]), whereas the performance of a-Si:H solar cells decrease upon exposure to light and increase by annealing at high temperature [15].

#### Introduction

In industry, PV modules are normally rated under standard test (ST) conditions to classify them. ST conditions are defined as an irradiance of 1000 W/m<sup>2</sup> with an air mass of 1.5 and a cell or module temperature of 25°C [16]. However, these conditions occur rarely in the real environment [16]. Under outdoor exposure, the PV modules experience variations in solar radiation, temperature, humidity, wind, and operating voltage. These all lead to generation of metastabilities during the outdoor exposure [16]. The metastable effects can lead to seasonal variation of the performance (see for example [17]). For more accurate energy yield prediction, it is therefore important to study the behavior of PV modules under outdoor conditions. As thin films have a more complex physics than crystalline Silicon modules due to their metastable effects, they have been investigated less than crystalline Silicon solar cells. The reliability of thin film performance models increases if metastable effects are included. Therefore, the influence of metastable effects need to be understood at all levels, from single device solar cells, up to outdoor exposed PV modules. Then a physically based, dynamic performance model can be developed to improve the reliability of thin film technologies and therefore improve their future capacity to use their potential.

Currently, there is no suitable performance model that includes the influence of metastable effects. This thesis aims to change this.

In this thesis, two different approaches for the investigation of metastable effects and developing of dynamic performance models are used. These are (i) an empirical approach for the description of outdoor thin film modules and (ii) a physical approach for the description of thin film solar cells measured at defined laboratory conditions. However, beside metastable effects also general degradation effects need to be considered, when describing the performance of solar cells especially at outdoor conditions. Also this aspect is considered in this thesis. The focus of the investigation lies in this thesis on a-Si:H and CdTe, two important thin film technologies. Other thin film technologies as CIGS and tandem modules, as a-Si:H/ $\mu$ c-Si:H, are taken also into account in this thesis. In the following, the structure of the thesis will be introduced in more detail.

In the literature, already many performance models exist. Therefore, in Chapter 2 first an overview about existing performance models will be given. In Sec-

tion 2.1 the basic physics of solar cells is introduced. Based on this, in Section 2.2 an overview about performance models will be given, whereas in Section 2.2.1 device simulators for thin film solar cells are introduced. In the following subsections, the models get more and more simple. At the end of Section 2.2.3, performance models that only model the maximum power density are shown. These models can be considered as the most simple performance models. Afterwards, a four step procedure is introduced in Section 2.2.4 that allows to compare different performance models with each other. Finally, in Section 2.3, the problematic of metastable effects for performance modeling is introduced.

In Chapter 3, the outdoor data that are analyzed in this thesis are introduced. For analyzing the data, an empirical performance model is chosen: the Karmalkar-Haneefa (KH) model. It is explained in detail in Section 3.2. The KH model is a simple, empirical performance model. However, to investigate how suitable it is for thin film outdoor modules, the Loss-Factor-Model (LFM) is chosen as a reference model. This is also an empirical performance model and is introduced in Section 3.3.

In Chapter 4, the KH model is analyzed with the four step procedure to identify if this model is suitable for the performance analysis of thin film modules. The results of the model investigation are compared to the LFM. Section 4.1 starts with the parameterization step. In Section 4.2, the fitting of the whole current density-voltage (JV) curve is analyzed and compared to the one-diode model. The main focus lies here on the maximum power point fitting. Section 4.3 continues then with the parameter analysis of the KH model and LFM and finally, in Section 4.4 the energy yield prediction with the KH model and the LFM are done and compared to each other.

After the analysis of the KH model, Chapter 5 deals then with the analysis of the outdoor data with the KH model. A detailed degradation analysis and investigation of metastable effects of CdTe for more than two years based on the results obtained with the KH model is made in Section 5.2. Afterwards, the behavior of the open circuit voltage  $(V_{oc})$ , the differential resistance at the open circuit point  $(R_{oc})$ , the differential conductance at the short-circuit point  $(G_{sc})$ , the fill factor (FF), and finally, the maximum power density  $(P_{mpp})$  are investigated also for different CdTe modules for four different climate regions. Based on the analyzing of the outdoor

#### Introduction

data of CdTe, an empirical model describing the behavior of  $R_{\rm oc}$  in the four climate zones are implemented.

After the empirical approach for the investigation and modeling of metastable effects, Chapter 6 deals with a physical approach for the analysis and modeling of metastable effects towards a dynamic performance model. Here, a-Si:H cells are investigated at the laboratory under defined conditions. Therefore, first a degradation experiment with different cell thicknesses under different light intensities are done. Also light changes are made to investigate the dynamical response of the cells. The experiment and its results are explained in Section 6.2. Then a new degradation model that describes the defect changes is developed and combined with a device simulator. The results and its limitations are investigated in Section 6.3.

Finally, in Chapter 7 the conclusions drawn in the individual chapters are summarized.

This work was carried out in the framework of the project "PV-Klima", project number 0325517C, funded by the Bundesministerium für Wirtschaft und Energie (BMWi).

In this chapter an introduction of performance modeling for solar cells and modules will be given. Therefore, first important physical models for the performance of solar cells will be explained in Section 2.1. Second, an overview about the main performance models will be given in Section 2.2, starting with device simulators in Section 2.2.1. In the afterwards following subsections the performance models will get more and more simplified, going on with equivalent circuit models in Section 2.2.2, and finally giving an overview about empirical performance models in Section 2.2.3. To compare the different models with each other, a four step procedure for this comparison will be introduced in Section 2.2.4. Finally, in Section 2.3, metastable effects of a-Si:H, CIGS, and CdTe and modeling approaches for those effects will be introduced.

Before starting with the physics and the performance models, it has to be mentioned that in this thesis, the term "parameters" in combination with performance models will be used to describe measurable physical values as for example  $J_{\rm sc}$  or  $V_{\rm oc}$ . The term "coefficients" is used for values that describe the dependence of parameters on environmental conditions, for example temperature coefficients. The environmental conditions are classified as "variables".

# 2.1. Basic physics of solar cells

Photovoltaics is the conversion of sunlight into electricity. Photovoltaic cells themselves are semiconductors with selective contacts. The electronic states of the semiconductor define the basic characteristic of the photovoltaic cell and also the interaction between light and semiconductor. For the full understanding of the device physics an understanding of the electronic structure of the semiconductor is therefore

essential.

In this section, first the basic electronic structure of semiconductors will be introduced. Afterwards, the main working principle of solar cells is explained.

#### 2.1.1. Electronic states

In Figure 2.1, the schematic band diagram of an intrinsic semiconductor is shown, with the band gap  $E_g$ , the Fermi-level  $E_f$ , and the conduction and valence band  $E_c$  and  $E_v$ , respectively. At the temperature  $T=0\,\mathrm{K}$ , there are no electrons in the conduction band and the valence band is fully filled by electrons. The band gap  $E_g$  is calculated by

(2.1)

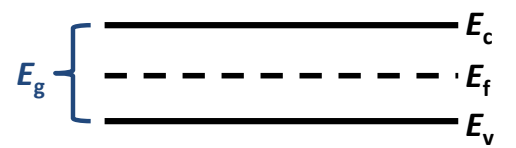


Figure 2.1. - Schematic band diagram of an intrinsic semiconductor

Describing the electronic states of crystalline Silicon, only the extended states in the valence and conduction bands have to be considered. However, amorphous devices as a-Si:H solar cells exhibit besides the extended states also two types of localized states, namely the tail states and the mid-gap states. In Figure 2.2 a schematic band diagram of a-Si:H with all three states is shown.

Describing the electronic structure of amorphous devices as a-Si:H, all three states have to be considered. Therefore, all three electronic states will be discussed in the following. It will be started with the extended states. Afterwards, the two localized states are explained.

Figure 2.2. - Schematic band diagram of a-Si:H in the Gaussian-distributedamphoteric mode. DOS indicates the density of states.

#### Extended states

The extended electronic states in semiconductors are in the conduction and valence band. From the Maxwell-Boltzmann approximation (see [18]), the carrier concentration in equilibrium for the extended states can be written as

$$n = N_c \exp\left(\frac{E_{fn} - E_c}{kT}\right) \tag{2.2}$$

$$n = N_c \exp\left(\frac{E_{fn} - E_c}{kT}\right)$$

$$p = N_v \exp\left(\frac{E_v - E_{fp}}{kT}\right),$$
(2.2)

where n and p are the charge carrier concentrations for electrons and holes, respectively, and  $N_c$  and  $N_v$  are the effective density of states in the conduction and valence band edge, respectively. The quasi-Fermi levels for electrons and holes are described with  $E_{fn}$  and  $E_{fp}$ , respectively, and k is the Boltzmann constant.

If the n- and p- concentrations are smaller than the effective density of states  $(N_c \text{ or } N_v)$  and the Fermi levels are more than several kT below the effective density of states, the Maxwell-Boltzmann statistic is a suitable model to describe the carrier

concentration for the extended states[18]

#### Tail states

The random nature of amorphous semiconductors leads to a blurring of the energy levels of the conduction and valence band edge. These are the so called "tail states". The tail states are trapping centers and can be described with one continuous distribution. They are single electron states, so they can be occupied by one or zero electrons. They behave like acceptor states at the conduction band edge and like donor states at the valence band edge. So an occupied acceptor-like state is negatively charged, and neutral if it is empty. A donor-like state is neutral if it is occupied and positively charged if it is empty. The density of states (DOS) formed by the band tails decreases exponentially from the bands towards the bandgap. The band tail slopes are characteristic for a given amorphous material and are an indicator of material quality [19]. The experimentally measured slope is called Urbach energy and is governed by the wider tail which is typically the valence-band tail [19]. The DOS of the localized band-tail states are described by  $N_{cbt}$  for the conduction and by  $N_{vbt}$  for the valance band-tail distribution with [20]

$$N_{cbt} = N_{c0} \exp\left(\frac{E - E_c}{E_{c0}}\right) \tag{2.4}$$

$$N_{vbt} = N_{v0} \exp\left(\frac{E_v - E}{E_{v0}}\right),\tag{2.5}$$

where  $E_{c0}$  and  $E_{v0}$  are the characteristic band-tail slope energies. The charge occupation and the recombination in these states are calculated with the Schockley-Read-Hall (SRH) theory [21]. Tail states exist also for CdTe [22] and CIGS [23] solar cells.

#### Dangling bond states

Crystalline Silicon has a diamond cubic structure, where each Silicon atom forms four bonds to other Silicon atoms. Hence, each bond consists of two atoms. Amorphous hydrogenated Silicon solar cells suffer under the lack of long range order which

leads to the situation where the bonding requirements are not fulfilled for all atoms. These states are called "dangling bond". The atomic hydrogen present in the material can passivate these bonds. This passivation greatly reduces the dangling bond concentration from  $10^{25} \,\mathrm{m}^{-3} - 10^{26} \,\mathrm{m}^{-3}$  to  $10^{21} \,\mathrm{m}^{-3} - 10^{22} \,\mathrm{m}^{-3}$  [20]. However, there are still enough dangling bonds left that have a high impact on the cell performance and need to be considered in the device simulation. A Silicon atom having danglingbonds with one electron has a neutral state which has an electronic state indicated as  $D^0$ . If the electron of one dangling-bond is missing, the net charge of the Silicon atom is positive and the electronic state is denoted as  $D^+$ . And with a second electron in the dangling bond, the atom is negatively charged and the state is indicated as  $D^-$ . The dangling bond is an amphoteric state that can have two energy levels: the  $E^{+/0}$  level related to the transition between the positively and neutrally charged states of the dangling bond, and the  $E^{0/-}$  level related to the transition between the neutrally and negatively charged states of the dangling bond. The states are close to mid gap and serve as recombination centers. The energy difference between those two states is the correlation energy U.

For the distribution of the dangling-bond states the Gaussian-distributed-amphoteric-defect model and the defect-pool model are the most used model. The Gaussian-distributed-amphoteric-defect model describes the two energy states with Gaussian distribution separated with the energy U [19]. In Figure 2.2, a schematic band diagram for the Gaussian-distributed-amphoteric mode is shown. The defect-pool model calculates the absolute position and the DOS in dependence of the Fermi-level  $E_F$  [19]. More information about these two models can be obtained from the work of Pieters in [20]. The recombination and trapping processes over the amphoteric states are described with the theory of Sah and Shockley [24].

It should be noted, that in recent years alternative models have been developed that pose that the DB states are actually voids (see for example [25]). However, for the device simulation the origin of these states is of no consequence as only their distribution and properties are used.

#### 2.1.2. Working principle of solar cells

In the previous subsection, the basic electronic structure for solar cells has been considered. Based on this, this subsection deals now finally with the working principle of solar cells.

The most fundamental working principle of a photovoltaic solar cell is the photoelectric effect. Thereby, electron—hole pairs are created via the absorption of sunlight. To excite an electron into the conduction band, the energy of the absorbed photon needs to be at least as large as the band gap of the semiconductor. However, to generate usable current, the electron and hole need to be collected at the selective contacts of the solar cells. The transport is therefore an essential process for solar cells. In Figure 2.3, the two processes electron-hole pair generation and transport are visualized. However, not every generated electron-hole pair is collected by the contacts as the charge carrier transport is limited. Electron-hole pairs that are not collected recombine before they reach the contacts. As in this thesis, degradation processes are in main focus, the recombination process will be explained in more detail in the following. However, first the transport equation for semiconductors will be explained as they are fundamental for semiconductor device simulation.

**Figure 2.3.** – Schematic band diagram for a solar cell. The two processes electronhole pair generation and transport are visualized with a red and two green arrows, respectively.

#### Semiconductor equations for charge carrier transport

The Poisson equation in connection with the continuity equations for electrons and holes are the basic equations, describing the physics of semiconductor devices and by this also photovoltaic cells [4]. Considering the transport equations in one dimension (z), they can be written as

2.1 Basic physics of solar cells

$$\frac{\partial^2 \varphi}{\partial z^2} = -\frac{\partial E}{\partial z} = -\frac{\rho}{\epsilon_r \epsilon_0},\tag{2.6}$$

where  $\varphi$  is the vacuum level related electrostatic potential induced by the space charge density  $\rho$ , which is normalized to the relative and the dielectric constant of vacuum ( $\epsilon_r$ ,  $\epsilon_0$ , respectively). The electrical field is E. The continuity equations are

$$\frac{\partial n}{t} = \frac{1}{q} \frac{\partial J_n}{\partial z} + G_n - R_n \tag{2.7}$$

and

$$\frac{\partial p}{t} = -\frac{1}{q} \frac{\partial J_p}{\partial z} + G_p - R_p, \tag{2.8}$$

where q is the elementary charge, G is the the generation rate through photon absorption, R the recombination rate, t the time, and  $J_n$  and  $J_p$  the electron and hole current densities, respectively, that are described by

$$J_n = \mu_n n \frac{\partial E_{fn}}{\partial z} \tag{2.9}$$

$$J_p = \mu_p p \frac{\partial \widetilde{E}_{fp}}{\partial z},\tag{2.10}$$

where  $\mu_n$  and  $\mu_p$  are the band drift mobilities for electrons and holes, respectively. The total current density can then be described as:

$$J = J_n + J_p. (2.11)$$

#### Recombination

As explained in Section 2.1.1, the tail states and dangling bond states in amorphous devices act as charge trapping and recombination centers and influence the electrical properties of the material significantly. Basically, the recombination process that can happen in semiconductor devices can be divided in two parts: the radiative and

non-radiative recombination.

The radiative recombination is the opposite process of the generation of an electron/hole pair by the absorption of a photon. During the recombination, the excited electron loses its energy. This energy generates either a photon or phonons. If the recombination process releases a photon, this is called radiative or band-to-band recombination as the electron from the conduction band directly combines with a hole in the valence band.

Semiconductors can be classified by the band gap, which is either direct or indirect. In semiconductors with a direct band gap as for example Cadmium Telluride (CdTe), Copper Indium Gallium Diselenide (CIGS), and a-Si:H, the recombination needs only one particle. In contrast, the recombination of an electron/hole pair in an indirect semiconductor as for example crystalline Silicon releases a phonon additional to the photon. Therefore, the right momentum of the phonon is needed for this. As two particles are needed for this recombination in an indirect semiconductor, radiative recombination is here less probable than in semiconductors with a direct band gap.

Shockley-Read Hall recombination belongs to the most important non-radiative recombination process of solar cells. This recombination happens when a trap state occupied by an electron captures a hole or vice versa.

The recombination via the SRH mechanism can be described as [26, 27]

$$R_{\text{SRH}} = \frac{pn - n_i^2}{\tau_p (n + n_1) + \tau_n (p + p_1)},$$
 (2.12)

where  $n_i$  is the intrinsic carrier concentration under equilibrium,  $\tau_n$  the lifetime for electrons when the recombination centers are completely empty and  $\tau_p$  the lifetime for holes when all recombination centers are occupied by electrons, and  $n_1$  and  $p_1$  are the equilibrium electron and hole concentrations when the Fermi level coincides with the position of the recombination centers [27]. The SRH model is a suitable model for recombination via states in the forbidden band gap [28] and is valid for most parts of crystalline Si solar cells [29].

## 2.2. Photovoltaic performance models

In the previous section, the basic physics of solar cells has been explained. The physics of the solar cell determines the characteristic current density-voltage (JV) curve of each solar cell which describes the performance of the solar cell. In this section, different performance models for solar cells and modules will be introduced.

In Figure 2.4, a typical illuminated JV curve with the main points the short circuit current density  $(J_{\rm sc})$ , the open circuit voltage  $(V_{\rm oc})$ , and the maximum power point (MPP) are shown. The illuminated JV curve of a solar cell can be considered in a first approximation as the superposition of the JV curve of the solar cell in the dark with the light generated current density  $J_L$ . In physical correct term, the JV curve is shifted by illumination down into the fourth quadrant, where power can be extracted. However, in the PV outdoor performance community it has been common to plot the illuminated JV curve in the first quadrant. This will be done also in this work when showing outdoor data. In contrast, for results from single cells in the lab the JV curve is shown in the fourth quadrant.

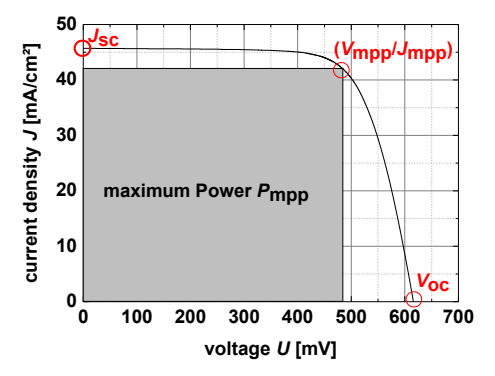


Figure 2.4. – Typical JV curve with main points.

In the literature, many performance models exist describing the whole or parts of the JV curve. Performance models are essential to extract information from the JV curve and analyze the behavior of solar cells. The available performance models in the literature can be divided in three groups, namely device simulators, equivalent circuit models, and empirical models. In this thesis, all three types of performance

models will be used. Therefore, an overview about the three model types will be given in the following, starting with device simulators.

#### 2.2.1. Device simulators for thin film photovoltaics

At the beginning of the performance modeling, a challenge for the physical simulation of solar cells was the numerical solution of the Poisson equation (see Equation 2.6) and the continuity equations (see Equation 2.8) with the right boundaries conditions. 1964 Gummel introduced an iterative procedure to solve these differential equations [30]. He did it for a one-dimensional transistor model. The carrier concentration was calculated with the Maxwell-Boltzmann statistic and the recombination with the SRH theory. Since then, device simulators have been improved significantly and also special device simulators for photovoltaics have been developed. Regarding the considered photovoltaic technology, the requirements for the device simulator differ.

The simulation of thin film photovoltaics has led to special device simulators for this technology. As in this thesis, the device simulation will be used for thin film solar cells, in the following the main thin film device simulators will be introduced.

Compared to single crystalline Silicon solar cells, thin film solar cells consist of much more layers, especially if tandem solar cells are considered. The used materials for thin film solar cells come along with more complex physics and therefore is one of the main reasons why numerical modeling of thin films is not so well developed as for crystalline Si solar cells [31]. According to Burgelman et al. [31], a device simulator for thin film solar cells has to fulfill the following criteria: simulation of multiple semiconductor layers (minimum of six layers), correct handling of graded materials (bandgap  $E_g$ , electron affinity  $\chi$ , effective density of states  $N_c$  and  $N_v$ , optical absorption, etc.) along the depth axis of the device, consideration of discontinuities in the energy bands  $E_c$  and  $E_v$  at the interface between the layers and the effect of deep energetic states, both in the bulk of the semiconductor layers and at the interfaces. Of course, most of the points are also valid for crystalline Si solar cells. However, the requirements for crystalline Si devices tend to be more relaxed.

One of the main points that distinguish crystalline Si solar cells from thin

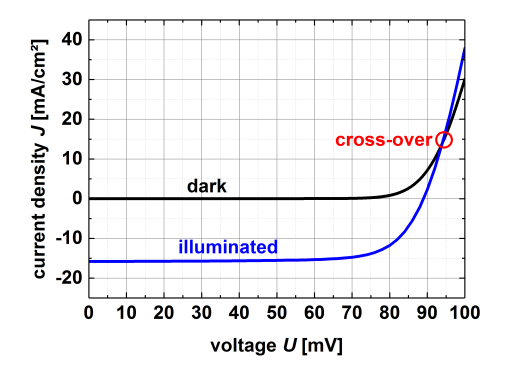


Figure 2.5. – Typical illuminated and dark JV curve for an a-Si:H solar cell. The data are derived from ASA for a 300-nm thick solar cell.

films like a-Si:H, CdTe, and CIGS solar cells is that for those solar cells the "superposition principle" (with voltage-independent photocurrent) is invalid [32]. At high forward bias, the illuminated curves lie above the dark curve, and the curves intersect in one point. This is also called "cross-over". In Figure 2.5, the dark and illuminated JV curve for a 300-nm thick a-Si:H solar cell are shown. The data are derived from the device simulator ASA (Advanced Semiconductor Analysis). Note, that the JV curve is shown in the fourth quadrant. The failure of superposition is due to bias-dependent photocurrent. Various authors have investigated this effect and explained it in different ways (see for example [33, 34, 35]). However, this effect cannot be neglected for JV analysis. This already indicates that the basic model for SRH recombination, as described in Section 2.1.2, is not enough for thin film modeling. The special needs for those cells led to development of new device simulators. The main three device simulators for thin film solar cells are AMPS (Analysis of Microelectronic and Photonic Structures), SCAPS (Solar cell CAPacitance Simulator), and ASA. They are all one-dimensional device simulators. All three models will be introduced briefly in the following.

AMPS was developed by Fonash *et al.* at the Pennsylvania State University and released in 1997 [36]. It is especially well adapted to simulate amorphous and polycrystalline solar cells with large densities of point defects in the energy gap and therefore, is often used for *a*-Si:H and CuInSe2-based solar cells [36].

SCAPS was published in 1996 by A. Niemegeers and M. Burgelman from the University of Gent [37]. It was mainly developed for polycrystalline CdTe and CIGS/CIS solar cells [37] for which it is still used. SCAPS allow to define up to seven layers and in each layer up to three deep levels. The level can be classified as donor, acceptor, or neutral level and can be energetically distributed in the forbidden zone (single level, uniform band, Gauß, or exponential tail) [38]. It also includes recombination at the interface states and their occupation via an extension of the SRH formalism [38].

ASA has been developed since 1987 at the Delft University of Technology and today is a commonly used advanced computer program for simulating solar cells based on amorphous and crystalline semiconductors [39, 21]. In 2007 the version ASA5 was published by B. Pieters et al in [39]. The ASA5 version will be also used in this thesis. ASA is a very flexible model and compared to the other two device simulators, it offers a large number of layers and meshing nodes [31]. For each layer, most of the parameters can be spatial distributed. For example, for the effective density of states, doping densities, and mobilities a constant, graded linear, or exponential distribution can be defined or the parameter distribution can be read directly from a file [31]. In addition, as it has mainly developed for a-Si:H solar cells, it also contains special recombination and density of states models. For the distribution of the dangling-bond states, the amphoteric-defect model and the defect-pool model are the most used model, as explained in Section 2.1.1. Both models are provided in ASA [21]. The modeling of dangling-bond states distribution will be important for Chapter 6.

With ASA, spatial resolved device simulations for the depth of the solar cells can be made. As a device simulator, it considers the main physical effects with respective models. For development of new cell concepts and deep physical understanding of the solar cells, device simulators as ASA are necessary. If a parameter set is defined for the considered solar cell, the cell performance can be modeled for a large temperature and irradiance range. However, for each considered cell a huge amount of parameters have to been known that are not always available. One possibility to solve this problem is to substitute the device simulator with an equivalent circuit model. This model will be introduced in the next section.

#### 2.2.2. Equivalent circuit models

Equivalent circuit models are important models for the performance modeling of solar cells and modules. In this subsection, an introduction about equivalent circuit models will be given as well as different parameterization techniques will be discussed.

In 1949 Shockley published his theoretical investigation about pn junction devices [40]. From this theory, diodes can be describes with the Shockley diode equation as

$$J = J_0 \left[ \exp\left(\frac{qV}{n_{\rm id}kT}\right) - 1 \right],\tag{2.13}$$

with  $J_0$  the diode's ideal reverse-bias saturation current density and  $n_{\rm id}$  the ideality factor, also known as the quality factor. For a pn-junction diode with recombination in the neutral zone(s) as the dominant recombination mechanism,  $n_{\rm id}$  would be unity (ideal diode behavior). In 1955 Prince described a solar cell with an ideal pn junction and a constant current source parallel to it [41]. The pn junction is represented by a diode and also today the common description of a solar cell. The diode describes the dark JV curve and the total recombination current density in the device. Additional components for this description of a solar cell are a parallel and a series resistance. The parallel resistance can originate from shunts, which partly short circuit the contacts of the diode. The series resistance hampers the charge carrier transport, for example at the the contacts. All components together lead to the well-known "five parameter model". The schema of this equivalent circuit model is shown in Figure 2.6 and the respective equation is [42]

$$J = J_L - J_0 \left[ \exp\left(\frac{V + J \times R_s}{a}\right) - 1 \right] - \frac{V + J \times R_s}{R_{sh}}$$
 (2.14)

with

$$a = \frac{N_s n_{\rm id} kT}{q},\tag{2.15}$$

where the light current density is  $J_L$ , the series and parallel resistances are  $R_s$  and  $R_{sh}$ , respectively, and  $N_s$  is the number of cells in series. With  $N_s$ , the model is also applicable to modules. If only one solar cell is considered,  $N_s$  is one. It has to

be mentioned that Equation 2.14 is valid for a fixed temperature. In opposite to device simulators, here only five parameters, namely  $J_L$ ,  $J_0$ ,  $R_s$ ,  $R_{sh}$ , and  $n_{id}$  have to be considered. The ideality factor  $n_{id}$  is normally between one and two [43]. All five parameters can be considered as functions of cell temperature and absorbed irradiance [43]. The JV curve is obtained directly from Equation 2.14. However, indepth physical information gets lost. Compared to the device simulator, the spatial resolved information is no longer possible with the equivalent circuit model. The equivalent circuit model is a simplified physical model that can be used for individual solar cells, modules, or an array consisting of several modules [43].

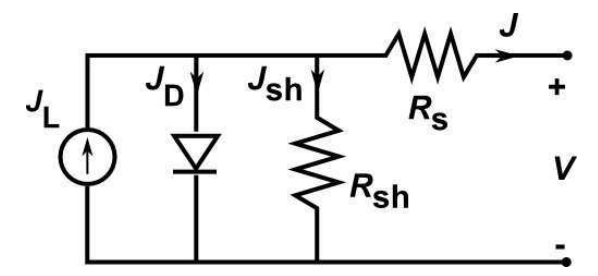


**Figure 2.6.** – Equivalent circuit model of a PV device. This model represents the five parameter model.

A more precise model than the one-diode model is the two-diode model which is for example explained in [44]. Here, two parallel diodes instead of one are used to model the device. For solar cells where the electric field is not over the whole solar cell thickness, one diode with  $n_{\rm id} \approx 1$  models the recombination that takes place in the quasi-neutral region(s) and a second diode with  $n_{\rm id} \approx 2$  represents the non-radiative recombination that takes mostly place in the depletion region. Under low light conditions, the recombination in the depletion region becomes more important [45]. Hence, the two-diode model provides a better description for solar cells over a wide range of irradiance levels. The additional diode extends the parameter amount according to Equation 2.13 to in total seven parameters. Of course, also models exist with even more diodes as for example the three-diodes model published by Nishioka [46]. However, those models are not the common models for PV module performance. Most studies have found out that for crystalline Si solar cells the one-diode model is sufficient for PV modelling [47]. The one- and two-diodes were originally thought to describe the behavior of mono- and poly-crystalline Si solar

cells. However, they are today also used for thin film solar cells [48].

The introduced equivalent circuit models are build on the superposition of a dark diode and a photocurrent source. Wagemann et al. [49] have shown that this is valid for crystalline Si solar cells. However, as explained in the subsection before, thin film solar cells show a different behavior. Therefore, in the literature adapted equivalent circuit models for those cells exist. One example is the model of Merten et al. [34]. They modified the one-diode model by extending it with a new term that takes the recombination losses in the intrinsic layer of a-Si:H solar cells into account [34]. Hegedus et al. [50] suggested for thin film solar cells the one-diode model extended with a general term for parasitic losses, that also accounts for voltage-depended photocurrent.

The equivalent circuit model shown in Figure 2.6 can be considered as the basic of equivalent circuit models for solar cells. It will be used also in this thesis as well for crystalline Si but also for thin film solar cells. The mathematical description of this model is Equation 2.14, which is an implicit equation describing the relationship between current and voltage. However, five parameters have to been determined for this model. Extending the model with more diodes, as for example the two-diode models, the amount of parameters that need to be calculated increases. The parameter determination is a challenging part of these models due to the solving of non-linear equations. For the two-diode model even two exponential terms have to be solved. In the literature, only a few solutions to calculate the seven-parameter equivalent circuit exist. In addition, these solutions are mostly related to the single cell and not to the entire module [51]. As the equivalent circuit model in this thesis will be used to describe outdoor module data, it has been decided to take the one-diode model. The parameterization of the one-diode model will be discussed in more detail in the following.

#### Parameterization of the one-diode model

Despite the long history and the importance of the one-diode model in the performance modeling of photovoltaic, no standard method has been adopted by the broad community. However, without a standard method for estimating the five model parameters, different estimation techniques can lead to different model parameter

values even when the parameter values are obtained from the same measurement set. Hence, uncertainties regarding model parameters contributes to uncertainties of PV system performance prediction [52]. Therefore, Hansen defines three criteria that a successful parameter estimation method should fulfill, namely [53]:

- 1. Robustness the parameters can be obtained for a wide range of module technologies and in the presence of reasonable measurement errors.
- 2. Reliability the same parameter values should be obtained repeatedly when the model is applied to the same data by different analysts.
- 3. Accessibility a full documentation and easy implementation of the method should be available and it should be possible that the method can be used by anyone with adequate general background in PV modeling and in numerical analysis techniques.

The parameterization procedure can be defined in two parts. First, the set of equations that describe the parameters have to be defined. Afterwards, the equations have to be solved. The parameterization methods themselves can then be divided in two groups. The first group deals with methods that use only values typically found on a manufacturer's data sheet, i.e.  $J_{\rm sc}, V_{\rm oc}$  etc., and the second group deals with methods that use, in some manner, the full range of measured voltage and current data of the JV curve [52].

Methods that only use manufacturer's data are very commonly used [52]. A well-known representative of this group is the method from de Soto et al. [42]. Other models using values from manufacturer's data sheet are described in [43, 54, 55]. De Soto et al. [42] obtain the five parameters by solving five independent equations. The data sheet information they need for their method are the  $J_{\rm sc}$ ,  $V_{\rm oc}$ , the current density  $(J_{\rm mpp})$  and voltage  $(V_{\rm mpp})$  at the maximum power point, as well as the temperature coefficient of the open circuit voltage and the temperature coefficient of the short circuit current density. The four parameters  $J_{\rm sc}$ ,  $V_{\rm oc}$ ,  $J_{\rm mpp}$ , and  $V_{\rm mpp}$  are normally all measured at standard test condition (STC). From the  $J_{\rm sc}$ ,  $V_{\rm oc}$ , and MPP values three J-V pairs are obtained that are substituted in Equation 2.14. A fourth equation is obtained by setting  $\delta P/\delta V=0$  (where P=JV) at the MPP. Finally, the fifth equations is derived by translating the Equation 2.14 at the  $V_{\rm oc}$  to another cell temperature different from STC. However, this group of model is

not suitable to consider outdoor JV data that exhibit metastable and degradation effects as the values of the parameters at STC can change over time. Therefore, in this thesis the second group for the parameterization method is used.

Methods from the second group for the parameterization have different approaches. Some methods work with approximations of Equation 2.14 over parts of its domain. One of the very first parameterization methods are from Kennerud [56] and Charles [57]. They derived two of their five equations from describing Equation 2.14 at the slope of the  $J_{\rm sc}$  and  $V_{\rm oc}$  point. The slopes were determined from experimental JV curves with certain errors [57]. Afterwards, the equations were solved numerically. Phang et al. [58] took these equations, made certain approximations and derived by this explicit equations for the five parameters. Hence, no numerical solution but an analytical solution could be applied to the equation system. An often used approximation by Phang et al., used also by others, is given by [58]

$$R_{sh} \approx -\frac{dV}{dJ}\bigg|_{J=Jsc}. (2.16)$$

Also the method of Kim et al. works with approximations for the parameters  $J_L$ ,  $J_0$ , and  $n_{\rm id}$  [59]. However, the  $R_s$  and  $R_{sh}$  values are obtained with a least square method, fitting to the whole JV curve. Other models fit all parameters. For example, Dallago et al. [60] define an incremental conductance derived from Equation 2.14. With this conductance and  $R_s$ , they define fitting ranges for the five parameters. With an optimization model, they change  $R_s$  and by this also the other parameters, whereas they search for a maximal coefficient of determination  $(R^2)$  value between the experimental and the modeled JV curve. Also in this thesis, the parameters for the one-diode model will be fitted.

Those models that fit at least one parameter have three parts to classify them. The first part is the parameter of the objective function. That can be the current density of the JV curve, which is mostly used, as for example in Dallago  $et\ al.\ [60]$ , or for example the maximum power point as in [61]. The second part is the error metric. This can be for example the coefficient of determination [60] or the mean square error [62]. Finally, the third part is the numerical technique with which the iteration is done to minimize the error. Here, firstly, conventional nonlinear

#### Fundamentals

fitting algorithms, such as the least-squares method (LSM) and variations of it, have been put forward to solve this problem [63]. Later, also optimization techniques as the Levenberg Marquardt method were used [64]. With the advancement in computing, the use of artificial intelligence techniques has increased greatly [65]. Artificial intelligence techniques include Fuzzy control, evolutionary algorithms and Neural Networks [65]. The most widely used evolutionary algorithm in PV models is the genetic algorithm [65] and is for example used by Moldovan et al. [66]. Its advantage is that no assumption is made about the values of the parameters [66]. Moldovan et al. used this method to extract parameters from organic solar cells, where many of the assumptions other models made to define initial values are not valid [66]. The genetic algorithm belongs to the global optimization methods. All named techniques that are used to minimize the error of the measured and experimental values are optimization methods. Optimization methods are defined as "an approach to solving design problems with N variables" [67]. Optimizer solutions as for example the conventional nonlinear fitting algorithms search for a local optimal solutions, whereas global optimizer techniques as for example the genetic algorithm find the global optimal solution that meets all of the constrained conditions for the objective function [67]. Optimization techniques need in general a specific computer capacity and are not very simple to implement and use compared to the conventional nonlinear fitting algorithm. Of course, global optimizers require a certain expertise as they control the trade off between reliability and speed.

#### Lambert W-function

To overcome the difficulties with the parameterization of the implicit Equation 2.14, exact analytical methods based on the Lambert W-function have been pushed forward, which will be discussed in the following as it is also used in this thesis. In the mathematics, the Lambert W-function is a set of functions, or more exactly the branches of the inverse function with the definition  $x = W(x) \exp(W(x))$  [63]. The Lambert W-function derives from the year 1758, when Lambert solved the trinomial equation  $x = q + x^m$  by giving a series development for x in powers of q [68]. 1779 Euler discussed it further and transformed Lambert's equation into a more symmetrical form [68]. Banwell [69] used the Lambert W-function to analyze a biploar

transistor circuit. Four years later, in 2004, Jain and Kapoor [70] were the first ones to use the Lambert W-function to analyze solar cells. Also in this thesis, the Lambert W-function is used when analyzing the one-diode model.

To derive the Lambert W form for the one-diode model, one can start with a transcendental function [53]

$$p^{ax+b} = cx + d, (2.17)$$

make the substitution [53]

$$-t = ax + \frac{ad}{c} \tag{2.18}$$

and obtain [53]

$$tp^t = -\frac{a}{c}p^{b-\frac{ad}{c}} \,. \tag{2.19}$$

The definition of Lambert's W leads to

$$t = \frac{W\left(-\frac{a}{c}p^{b-\frac{ad}{c}}\ln p\right)}{\ln p}.$$
 (2.20)

With this a solution of Equation 2.17 in terms of Lambert's W is obtained as [53]

$$x = -\frac{1}{a \ln p} W\left(-\frac{a \ln p}{c} p^{b - \frac{ad}{c}}\right) - \frac{d}{c}. \tag{2.21}$$

Applying this to Equation 2.14 leads to [53]

$$J = \frac{R_{sh}}{R_{sh} + R_s} (J_L + J_0) - \frac{V}{R_{sh} + R_s} - \frac{n_{id}V_{th}}{R_s}W\left(\frac{R_sJ_0}{n_{id}V_{th}}\frac{R_{sh}}{R_{sh} + R_s}\exp\left(\frac{R_{sh}}{R_{sh} + R_s}\frac{R_s(J_L + J_0) + V}{n_{id}V_{th}}\right)\right).$$
(2.22)

The parameterization procedure for models based on the Lambert's W method stays the same as explained before: definition of an objective function, an error metric, and the numerical solver. Depending on the numerical solution also appropriate

#### **Fundamentals**

initial conditions have to be determined. In this thesis, the parameter of the objective function is the current density. The error metric is the root-mean-square error and as a numerical solver the Nelder-Mead simplex algorithm [71] is used.

Performance modeling based on equivalent circuits is a simplification of the device modeling as explained in this section. Therefore, these models are limited to certain ranges. For example, if the one-diode model is fitted to high irradiance, it is not very suitable for low light conditions as different recombination effects cannot all be considered in the ideality factor  $n_{\rm id}$ . The parameterization of this model is based on approximations and numerical optimization of the respective equation for the considered equivalent circuit model as the equation cannot be described with elementary functions. This makes it difficult to use the one-diode model for large amount of data and therefore, empirical models have become important for performance modeling. Empirical models are only based on the description of the measured JV curves. For measurement of outdoor data these models can be adapted to different technologies and are used to analyze a huge amount of data. The empirical models will be introduced in the following.

# 2.2.3. Empirical models

Empirical performance models can be divided in two classes: the first one deals only with modeling of the performance, i.e. they consider only the  $P_{\rm mpp}$  of the measured JV curve. The second class deals with the parameterization of the JV curve, i.e. it considers the whole or several parts of JV curve. Both types of models will be discussed in this subsection, starting with the performance models that parameterize the JV curve. Afterward, also models that only deal with the performance of the JV curve will be considered.

Empirical models that parameterize the JV curve can be sub-divided in two groups. The first group only deals with parts of the JV curve. These performance models consider certain measurement points of the JV curve, for example the  $J_{\rm sc}$  and  $V_{\rm oc}$ . The  $P_{\rm mpp}$  is then calculated by these parameters. The second group are fitting models. These performance models fit empirical equations to the whole JV curve and can so describe each point of it. The  $P_{\rm mpp}$  can then be calculated by

setting  $\delta P/\delta V = 0$  (where P = JV).

A very common empirical model is the Sandia Array Performance Model (SAPM), presented by King  $et\ al.$  [72]. It belongs to the group that considers parts of the JV curve. The SAPM is also implemented in the often used PVLIB Toolbox [73]. In the following, the SAPM will be explained as a representative of empirical performance models to show the general modeling process of empirical models.

The SAPM considers six parameters at the JV curve. These are the  $J_{\rm sc}$ ,  $V_{\rm oc}$ , and the current density and voltage at the maximum power density  $J_{\rm mpp}$  and  $V_{\rm mpp}$ , respectively. The two other points are defined as  $J_x$  and  $J_{xx}$ . The parameter  $J_x$  is the current density at the voltage equal to one-half of the open-circuit voltage and  $J_{xx}$  the current density at a voltage midway between  $V_{\rm mpp}$  and  $V_{\rm oc}$  [72]. The maximum power can be calculated with  $J_{\rm mpp}$  and  $V_{\rm mpp}$ . However, in some cases, for example in battery charging application, other voltages than  $V_{\rm mpp}$  are necessary [72]. With the six parameters, measured at five different points, the shape of the JV curve can be estimated.

For each of the six parameters, the SAPM offers one equation to translate the parameter to other temperature and irradiance conditions. The main parts of translation equations, as in the SAPM, are always the consideration that the  $J_{\rm sc}$  and the irradiance show a linear correlation and the  $V_{\rm oc}$  and the irradiance show a logarithmic correlation. These relations can be derived from the five-parameter equation of the one-diode equation (see Equation 2.14). These simplified equations, of course, cannot compete with the device simulators. In the empirical models, just the main relations between the physical parameters are considered. Other effects are ignored and of course lead to limitations of the model application. However, empirical performance models allow fast performance analyses of the main parameters. A difficult part of these models are the calculations of the coefficients of the translation equation, for example the temperature coefficients.

Exemplary, the translation equation for  $J_{\text{mpp}}$  in the SAPM is [72]

$$J_{\text{mpp}} = J_{mppo} \{ C_0 E_e + C_1 E_e^2 \} \times \{ 1 + \alpha_{\text{Jmpp}} (T_c - T_o) \},$$
 (2.23)

#### **Fundamentals**

where  $J_{mppo}$  is the current density at MPP at reference condition,  $T_c$  the cell temperature inside the module,  $T_o$  the reference cell temperature,  $E_e$  the effective irradiance, and  $\alpha_{\rm Jmpp}$  the temperature coefficient. The values  $C_0$  and  $C_1$  are empirical constants. According to the definition at the beginning of this chapter,  $C_0$ ,  $C_1$ , and  $\alpha_{\rm Jmpp}$  are the coefficients,  $J_{\rm mp}$  and  $J_{mppo}$  are the parameters and  $E_e$ ,  $T_c$ , and  $T_o$  are the variables.

The temperature coefficients can be taken from the manufacture's data sheet or can be measured [72]. The determination of the temperature coefficient is important for many empirical performance models (e.g. [74]) and will be also important for the work of this thesis. The measurements of the temperature coefficient are described in [75]. The measurements can be done indoor or outdoor. Nevertheless, the "measured" temperature coefficient can deviate from the "real" temperature coefficients due to spatially non-uniform temperature distributions during the measurement [72]. According to the IEC 6081, the measurements to determine temperature coefficients under natural sunlight should fulfill the following requirements [76]:

- 1. "the total irradiance is at least as high as the upper limit of the range of interest
- 2. the irradiance variation caused by short-term oscillations (clouds, haze, or smoke) is less than  $\pm 2\%$  of the total irradiance as measured by the reference device
- 3. the wind speed is less than  $2 \,\mathrm{m \, s^{-1}}$ ".

The environmental conditions that are considered for the performance model are very important in general for empirical performance models. As already shown in Equation 2.23, the SAPM model uses the effective solar irradiance and the cell temperature. The effective solar irradiance describes the fraction of the solar irradiance to which the cells inside the module actually respond [72]. For  $J_{\rm sc}$ , even the influence of variation in the solar spectrum and the optical losses due to solar angle-of-incidence is considered with empirical functions in the SAPM [72]. For the cell temperature, the equations of the SAPM are based on assumptions for thermal heat conduction through the module materials. Depending on the module material, different coefficients are provided by King et al. [72]. The SAPM takes several influences into account for a precise performance modeling and prediction. However, it is also possible to simplify the model by using only the in-plane irradiance

and back-of-module temperature as well as to calculate all coefficients directly from the measurement points. These simplifications still lead to a suitable performance model [77]. For the choice of a suitable performance model, it is important to consider which information about the environmental conditions are provided by the considered data set.

In opposite to the SAPM, more simple performance models with less parameters and coefficients exist. One example is the Loss Factor Model by Sutterlüti et al. [74] that uses five parameters derived from the JV curve and the irradiance and temperature. To describe the shape of the JV curve, this model takes the slopes at the short-circuit and open-circuit point as well as the fill factor into account. The environmental conditions can be described with the measured in-plane irradiance on the module and the back-of-module temperature. The model is described in detail in Section 3.3.

Similar to the one-diode model, many performance models haven been developed primarily for crystalline Si technologies. In this thesis, the performance modeling of thin film technologies is investigated. Stein *et al.* compared the one-diode model with the SAPM and LFM for thin film and crystalline Si modules [78]. They found that the one-diode model appears to exhibit a strong sensitivity to temperature for the thin film modules, whereas the parameterization was done according to De Soto [42]. The lowest bias errors for all technologies was achieved with the LFM. This is also the reason, why the LFM is taken in this thesis as a reference performance model.

The other mentioned group of the empirical models are the fitting models. They describe mathematically the shape of the JV curve. The fitting equation normally does not have any physical meaning. A very simple one is the Karmalkar-Haneefa (KH) model [79]. This model will be explained in detail in Section 3.2. Its advantages are that it uses a simple expression to describe the JV curve and only needs four parameters. Other fitting models are published by Das [80] and Miceli et al. [48]. However, due to the empirical description of the JV curve, these models are limited to certain applications as for example for modules measured under forward bias but not under reverse bias. In this thesis, the KH Model and its suitability for thin film performance modeling will be investigated in detail in Chapter 4.

#### **Fundamentals**

Finally, the last group of performance models are those that only model the maximum power output. The three most common models in this category are:

- 1. the Matrix Method developed mainly by LEEE-TISO [81]
- 2. the MotherPV method (Meteorogical, Optical and Thermal Histories for the Energy Rating of PhotoVoltaics) developed by INES/CEA [82]
- 3. the SSC model (Site-Specific Condition) developed at CREST [83]

These models can again be divided in two groups according to Friesen *et al.* [84]. Models as the Matrix method use one equation to describe the power. Models as the MotherPV and the SSC model separates the temperature influence from the module efficiency [84].

**Table 2.1.** – Environmental input data required by each model for performance modeling. Adapted from [85]

Environmental Inputs	Matrix	MotherPV	SSC
Ambient Temperature	X		
Device Temperature		X	Χ
Irradiance in plane	X	X	X
Irradiance horizontal			X
Spectral Information			Χ

Another division of model types can be made my considering which environmental input data they use. This information is shown in Table 2.1. The advantages of the models that concentrate only on the maximum power are of course that they are very simple and can be implemented very fast because they neglect many physical information. The aim of empirical models like the MotherPV method is to describe the energy production of modules at specific conditions with a simple and fast method [86]. Empirical models that only concentrate on the performance are the most simple performance models. In contrast to them, the device simulators are the most complex performance models that have also the most physical information. All other introduced performance models are in between those.

Considering the application of the single PV performance models, it can be stated that if the energy yield prediction of complete power plants is the aim of the performance modeling, empirical models are the suitable choice. However, for the failure analysis of PV modules empirical models that parameterize the JV curve and

equivalent circuit models need to be taken. For the physical understanding of single solar cells, especially regarding metastable defects, device performance modeling is necessary. Despite their differences, all performance models have certain aspects in common. These aspects allow to compare these performance models with each other. These aspects will be explained in the next subsection.

## 2.2.4. General structure of PV performance models

In the subsections before, different PV performance models have been introduced. Considering the type of PV performance model, the models differ in their suitable applications. However, despite their differences, all performance models describe at the end a performance of a PV device and their main interest is to describe it as precise as possible. Until the performance prediction can be done, all performance models have to go through four steps, that determine how precise these models are. In this subsection, the four steps will be introduced.

In Figure 2.7, the general scheme of how PV performance models use this four step process is shown. In the first step, the parameters for the performance model have to be determined. This can be either done by fitting, for example for the one-diode model with optimization techniques (see Section 2.2.2), or by determining directly from the measured JV curve as it can be done for the SAPM. In this step, a first error can be stated. Of course, due to numerical problems with the fitting method or due to measurement errors in the directly parameter extraction, these errors influence the further application of the performance model.

After the parameters are obtained, the dependence on environmental conditions is determined, i.e. the coefficients of the performance model are calculated. For example, for the  $J_{\rm mpp}$  of the SAPM this means that Equation 2.23 is fitted to the measured  $J_{\rm mpp}$  values so that the temperature coefficient as well as the coefficients  $C_0$  and  $C_1$  can be calculated. The application of these translation equations is normally limited to a certain temperature and irradiance range as they are empirically motivated. But of course, also environmental conditions as the wind speed can lead to false temperature coefficients (see Section 2.2.3).

In a third step, the parameters and/or JV curves are translated to reference

Figure 2.7. – General scheme how photovoltaic performance models use a four step process to analyse measured outdoor data  $D_{\rm m}$  via (i) parametrization and (ii) parameter analysis to find the coefficients for the parameters' dependence on the variables temperature T and irradiance G. Then the data can be (iii) translated to reference conditions and finally expected output data  $D_{\rm p}$  are calculated from the respective variables T and G.

conditions. These reference conditions allow for example to compare modules at different locations with each other. Of course, the determined reference condition depends on the error of the parameter and coefficient extraction as well as on the translation equation.

Finally, if the reference conditions are known, the parameters of the performance models can be calculated for a given irradiance and temperature together with the translation equations. This way, energy yield prediction can be done. For given values, the prediction can be compared to real values and the final error for the performance model can be determined. The prediction error is the most important quality factor for performance modeling. Of course, it is also influenced by how accurate temperature and irradiance values are.

Comparing different performance models with each other, the considered performance models can be compared with each other for each of these four steps and the respective errors can be calculated. This will be done in Chapter 4, where the KH model and LFM are compared with each other. However, the errors are not independent of each other. Errors in the parameterization steps of course influence the error of the following three steps.

# 2.3. Modeling of degradation and metastable effects

In Section 2.2 different performance models have been introduced for describing the characteristic JV curve of PV solar cells. However, due to degradation and metastable behavior the characteristic of the solar cell can change over time and therefore lead to a change in the JV curve. In the following, the metastable effects of a-Si:H, CIGS, and CdTe will be introduced briefly and afterwards modeling approaches for degradation and metastable effects will be introduced.

For a-Si:H modules, the Staebler-Wronski-effect [87] describes the metastable changes upon exposure to light and application of a certain bias and temperature. The effect is reversible by annealing at high temperature [15]. Although, the effect is known very well, the detailed physics behind it is still unclear. Also for  $\mu$ c-Si:H the effect plays an important role regarding its amorphous content. With reduced amorphous phase, the cells become more stable [88]. Therefore, it is also important for tandem cells as a-Si:H/ $\mu$ c-Si:H. The degradation and annealing effects of a-Si:H cells are described in more detail in Chapter 6.

CIGS and CdTe solar cells show a different behavior under light-soaking. For CIGS, Rau *et al.* show that temperature treatment leads to a decrease of the dark conductivity, whereas light-soaking can reestablish the previous state [14]. Also the open circuit voltage improves under light-soaking and forward bias. However, Sasala and Sites [13] have shown that the total voltage change diminishes as the temperature increased above room temperature.

CdTe shows in parts a similar behavior. The  $V_{\rm oc}$  increases with light-soaking and forward bias and decreases under dark-conditions [13]. This may happens due to a depopulation of trap states in the absorber junction [13]. The degradation and

#### **Fundamentals**

annealing effects of CdTe cells are described in more detail in Chapter 5.

In addition to the metastable behavior, also long-term degradation occurs [89]. Ishii *et al.* found out that it can take about two years until thin film modules are stable [89].

Due to metastabilities and degradation, the performance of thin film solar cell depends on the environmental conditions the cell was exposed to before. To consider metastable and degradation effects of a solar cell into the performance modeling, a time-dependent performance modeling is necessary. One of the first time-dependent performance models has been done by Klaver et al. [90]. They combined a device simulator with a rate equation for the defect evolution to describe the light-induced degradation of a-Si:H solar cells. However, they consider only cells under stable environmental conditions. Describing the dynamic behavior of thin film modules, acquires a lot of knowledge about the physics of these solar cells. Until now, no suitable dynamic performance model of thin film modules for outdoor application has been developed. One of the few promising dynamic performance models has been developed by Zhu et al. [91] for a-Si:H solar cells. They considered changing temperature treatment for a-Si:H cells and developed a dynamic performance model that combines the maximum power modeling with a rate equation describing the defect evolution.

Considering the reliability of thin film modules, the demand of dynamic performance models is increasing which comes along with the analysis of the degradation and metastable effects. In general, it can be summarized that a dynamic performance model consists of a (stationary) performance model as introduced in Section 2.2 and a rate equation that considers the time-dependent change of the solar cell characteristic as described in Section 2.1. In this thesis, thin film solar cells and modules will be analyzed under dynamic environmental conditions and based on this analysis, two different dynamic performance models will be developed.

# 3. Outdoor data and analysis method

In this chapter, the outdoor data set that is later analyzed is explained. The data set is provided by TÜV Rheinland. After the introduction of the data set, two empirical performance models, namely the Karmalkar-Haneefa and the Loss Factor Model, are introduced. The Karmalkar-Haneefa model is explained in Section 3.2 and the Loss Factor Model in Section 3.3.

# 3.1. Outdoor data set

The main part of the investigated data set covers three different technologies measured in four different locations. The three different technologies are CdTe, CIGS, and a-Si:H/ $\mu$ c-Si:H. The locations are Cologne in Germany, Ancona in Italy, Chennai in India, and Tempe in Arizona, USA. Furthermore, data of two additional technologies were collected in Cologne, namely a-Si:H and poly-crystalline Silicion (poly-Si). For CdTe three and for CIGS four modules per test site were investigated. For all other technologies, one module per test site was investigated. A detailed overview of the investigated outdoor module set is shown in Table 3.1. To distinguish between the three CdTe modules, they are classified as "CdTe1", "CdTe2", and "CdTe3", respectively. The label for the four CIGS modules follows analog, i.e. "CIGS1", "CIGS2", "CIGS3", "CIGS4".

Each test site was equipped with identical samples and a measuring system developed by TÜV Rheinland [92]. All PV modules were brand-new samples manufactured in 2013 [92]. Furthermore, they are full-size as they can be bought on the market [93]. Regarding the installation, the modules are mounted facing south. In

Table 3.1. – Investigated modules

PV modules	locations	Quantity per location
$a$ -Si:H/ $\mu$ c-Si:H	4	1
$a ext{-Si:H}$	1 (Cologne)	1
$\operatorname{CdTe}$	4	3
CIGS	4	4
poly-Si	1 (Cologne)	1

addition, the modules are shaded neither by trees or building parts, nor by other solar modules [93]. They are open rack mounted without thermal insulation and in a distance of 10 cm to each other. The tilting angle is 35° in Cologne and in Ancona. In Tempe the tilting angle is 33.5° and in Chennai it is 15°. Each module is equipped with a seperate electronic DC load which allows synchronous performing of the JV-curve measurement every ten minutes with measurement duration below 1 s [94]. The 4-wire contacting for independent current and voltage measurement starts directly at the connector of the PV modules. Every 30 s the  $P_{\rm mpp}$  is measured.

For measurement of the back-of-module temperature, each module is equipped with two Pt100 sensors on the back. The irradiance in the plane of the array is measured by a ventilated pyranometer. The measurement of the temperature and irradiance were taken synchronous to the JV curve measurement [94]. More details on the various test sites can be found in Appendix A.

Each module, except for the a-Si:H one, is measured for more than two years. The time frames for the different locations are:

Ancona: 1st November 2013 to 31st July 2016

**Tempe**: 13th December 2013 to 31st July 2016 **Chennai**: 1st February 2014 to 31st July 2016

Cologne: 12th March 2014 to 30th June 2016

The data for the a-Si:H module in Cologne are from a different measurement set up. The data are also provided by TÜV Rheinland and measured at the same locations as the other modules. However, the module was measured in the time frame: 31st May 2015 to 15th June 2016. In addition, also the time intervals for the measurement are different than described before. Here, the JV curves were

measured only every 30 minutes. The irradiance is measured before and after the JV curve measurement. This measurement allows to take irradiance fluctuation during the JV curve measurement into account and filter the JV curve data. In this thesis, only data of the a-Si:H module in Cologne were used where the irradiance change before and after the JV curve measurement is < 5%. In other literature even lower values of 2% are used as a criteria (see [78]). However, for the other modules of the investigated data set no irradiance filter can be used. This leads, of course, to a higher noise in the measurements than with the filter criteria of 2%. For the JV curve data, the noise in the measurement at low irradiance ( $< 200 \, \mathrm{W/m^2}$ ) is very high. Therefore, in the following chapters only data measured under at least  $250 \, \mathrm{W/m^2}$  are taken into account.

**Table 3.2.** – Test site specifications. Data are taken from [95, 96]

	Cologne	Ancona	Chennai	Tempe
	Germany	$\mathbf{Italy}$	India	${f Arizona}$
Latitude	50.922813	43.474195	33.42404	12.984217
Longitude	6.991705	13.074653	-111.910036	79.987987
Altitude [m]	65	125	355	35
Tilt Angle	35°	$35^{\circ}$	$33.5^{\circ}$	15°
Azimuth (true	180°	180°	180°	180°
$\operatorname{north-based})$				

In Table 3.2, the test site specifications are listed in more detail for all four test sites. Also the latitude and longitude of the test sites are given here. With this coordinates, the exact location of the test sites can be obtained.

In Figure 3.1, the locations of the four test sites are shown on the Köppen-Geiger climate type map of the world published by Peel et al. [97]. Each color indicates one climate zone here. It can be derived that with the four test sites four of 30 possible climate zones are covered. Considering only the five main climate classes of the Köppen-Geiger system, which are classified as A-E in [97], it is found that three climate classes are covered with the test site, namely one tropical (Chennai), one arid (Tempe) and two temperate (Ancona and Cologne). This shows that with the available data set a wide range of climate conditions can be covered. In more detail, the test sites in Chennai, Tempe, Cologne, and Ancona are in the climate zones Tropical-Savannah, Arid-Desert-Hot, Temperate-without dry seasons-warm

### Outdoor data and analysis method

summer, and Temperate-dry summer-hot summer, respectively. In [97] these climate zones are claimed as Aw, Bwh, Cfb, and Csa, respectively. The first letter always indicates the main climate class. The climate zones of the test sites mean in detail that in Chennai very hot temperatures over the whole year with some very dry and very wet months occur. In Tempe warm temperatures with low precipitation is typical. Ancona is in a region with more moderate temperatures than Chennai and Tempe but still hot and dry summers occur here. And finally, the region of Cologne can be described with moderate temperatures, warm summer and moderate precipitation. The detailed definition of the respective climate zones can be found in [97].

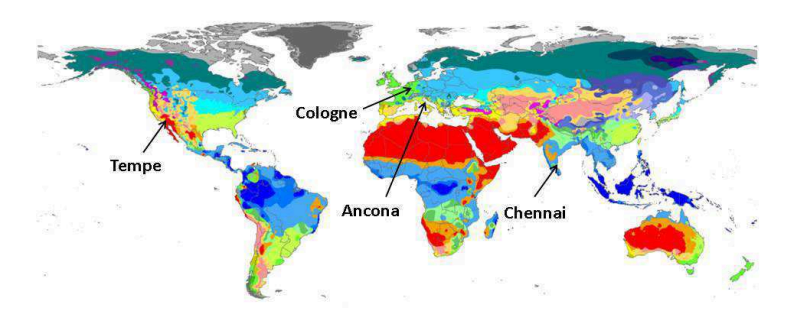


Figure 3.1. – Outdoor test sites in Ancona, Cologne, Chennai, and Tempe on the Köppen-Geiger climate type map of the world published by Peel et al. [97]. Each color indicates one climate zone. The exact legend for the climate zones can be found in [97].

In Table 3.3, the average measured environmental conditions at the test sites are shown. They are in good agreement with the Köppen-Geiger classification. As mentioned before, the low irradiance data are not considered in the data analysis. By this, around 5%-19% of the data are neglected. The most extreme conditions are the high irradiance and low precipitation in Tempe, the high temperature and high precipitation in Chennai and the low irradiance and temperature in Cologne.

Another environmental condition is soiling. This effect has been investigated for this data set by Herrmann *et al.* [98]. Whereas soling for Cologne and Ancona is negligible, it has a higher impact in Chennai and Tempe. Herrmann *et al.* show

that in the first year of operation soiling leads to power losses of -3.7% in Tempe and -2.3% in Chennai. Chennai shows lower losses due to more rainfall. In the first year of operation Herrmann *et al.* observed also that the surface of standard glass is efficiently cleaned by rainfall and therefore, losses due to soiling can regenerate up to 99% compared to a module that is cleaned on a regular basis [98]. However, for long-term exposure, permanent soiling has a high impact on the power, in particular if moss is formed on the glass from organic dust settlement[98]. During the outdoor-exposure of the modules, the modules were not cleaned. Therefore, soiling effects have to be considered especially for modules in Tempe and India.

Table 3.3. – Environmental conditions of the test sites. Data are taken from [95]

Location	Annual in-plane solar irradiation [kWh /m²]	$egin{aligned}  extbf{Low} \  ext{irradiance} \  ext{contribution} \ (< 200   ext{W/m}^2) \end{aligned}$	$ \begin{array}{c} \textbf{Average} \\ \textbf{ambient} \\ \textbf{temperature} \\ \textbf{(>}15\mathrm{W/m^2)} \end{array} $	$egin{array}{l} { m Average} & { m annual} & { m amount of} & { m precipitation} & { m [mm]} & { m } \end{array}$
Cologne	1195	19%	$15.2^{\circ}\mathrm{C}$	774
Ancona	1556	12%	$18.1^{\circ}\mathrm{C}$	757
Chennai	1861	9%	$30.3^{\circ}\mathrm{C}$	1197
Tempe	2360	5%	$27.4^{\circ}\mathrm{C}$	219

For the data analysis, beside the low irradiance data also data with unphysical  $J_{\rm sc}$ ,  $V_{\rm oc}$ , differential resistance at the open circuit point  $(R_{\rm oc})$ , and the differential conductance at the short-circuit point  $(G_{\rm sc})$  are neglected in the following data analysis. These parameters were determined with the KH method. The exact procedure for the parameterization step is explained in Chapter 4. In Figure 3.2, as an example, the weekly measured back-of-module temperature and in-plane solar irradiance measured for the CdTe1 module, excluding low irradiance and unphysical JV curve parameters, are shown for Cologne and Tempe. At the top of the plots, the months and year of every 40th week is shown. The red line in the plots always indicates the respective maximal measured value for the week, the blue line the minimal weekly measured value and the black line the average weekly measured value. The plots for Ancona and Chennai can be found in Appendix A. It can be seen that the seasonal variation of the irradiance is in Cologne higher than in Tempe. In addition, due to filtering out low irradiance data (min values are in Figure 3.2

### Outdoor data and analysis method

not lower than  $250 \,\mathrm{W/m^2}$ ), the average irradiance is shifted stronger for Cologne than for Tempe due to different share of low irradiance (see Table 3.3). However, it is still observed that the average irradiance in Tempe is higher than in Cologne.

For the temperature, it can be seen that in Tempe higher values are obtained than in Cologne. At both test sites, the seasonal variations of the temperatures are clearly visible.

In summary, it can be stated that the temperature and irradiance data show the typical behavior for the respective climate zones. This means that the used filter process does not change the data strongly and is therefore suitable for the data analysis.

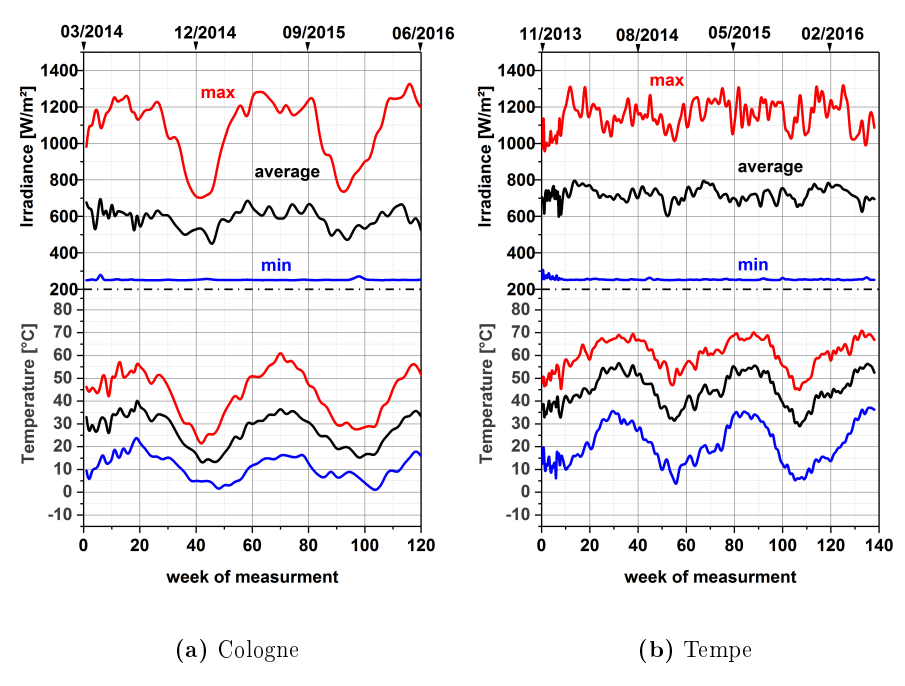


Figure 3.2. – Weekly back-of-module temperature and in-plane solar irradiance measured for the CdTe1 module in a) Cologne and b) Tempe

For the analysis of the measured current-voltage (JV) curves per module, the data were transformed to JV curves per cells, i.e. the voltage was transformed

to voltage per cell and the current to current per cm<sup>2</sup> single cell area. With this transformation, the JV data are independent from the module design and allow to estimate whether the  $V_{\rm oc}$  and  $J_{\rm sc}$  are comparable for the respective technology. In the next two sections, the analysis method for these data will be introduced.

# 3.2. Karmalkar-Haneefa model

In this thesis, the Karmalkar-Haneefa model will be investigated in detail to find out how suitable it is for the analysis of thin film solar cells. The available data for the analysis have been introduced in the previous section. In this section, now the Karmalkar-Haneefa model will be explained.

In 2008, Karmalkar and Haneefa introduced the power law function according to [79]

$$j = 1 - (1 - \gamma)v - \gamma v^m$$
, with  $j = J/J_{sc}$ ,  $v = V/V_{oc}$ . (3.1)

Transforming the equation, one obtains

$$J(V) = J_{\rm sc} \left[ (1 - \gamma) \frac{V}{V_{\rm oc}} + \gamma \left( \frac{V}{V_{\rm oc}} \right)^m - 1 \right] \quad . \tag{3.2}$$

This equation belongs to the models that transform the JV characteristic implicit representation into an explicit form [99]. With their model, Karmalkar and Haneefa wanted to derive a simple explicit JV model, which yields closed-form solutions of the maximum power point and the fill factor and in addition, allows prediction of these parameters from a few measurements [79]. For the Karmalkar-Haneefa (KH) model, only four parameters are needed, namely  $J_{\rm sc}$ ,  $V_{\rm oc}$ ,  $\gamma$ , and m. The values  $J_{\rm sc}$  and  $V_{\rm oc}$  can be derived directly from the measurement. The values  $\gamma$  and m can be calculated from two additional measurement points as [100]

$$\gamma \approx (j \mid_{v=0.6} -0.4) / 0.6 \tag{3.3}$$

$$m = \log \left[ (0.4 - (1 - \gamma) v |_{i=0.6}) \gamma^{-1} \right] \log v |_{i=0.6} . \tag{3.4}$$

#### Outdoor data and analysis method

Equation 3.3 is valid for  $0.6^m \ll 0.6$  [100]. The points j=0.6 and v=0.6 are taken as those measurement points are not close to either the short- or open-circuit point as small measured values are prone to large percentage errors [79]. In addition, the derivation of  $\gamma$  is based on neglecting the term  $\gamma v^m$  in Equation 3.1, which is only valid if the taken point is not on the sharply turning curve corner [79]. However, in this thesis  $\gamma$  and m will be determined by fitting Equation 3.2 to the whole measured JV curve.

The maximum power point is derived by first calculating the normalized peak power voltage  $v_{\rm mpp} = V_{\rm mpp}/V_{\rm oc}$  and then calculating  $j_{\rm mpp} = J_{\rm mpp}/J_{\rm sc}$  with Equation 3.1. The value  $v_{\rm mpp}$  itself is obtained by setting  $d\left(jv\right)/dv\mid_{v=vpp}=0$ . According to Karmalkar and Haneefa [79], the solution can be empirically adjusted as

$$v_{\text{MPP}} \approx (m+1)^{-1/m} - 0.05 (1-\gamma)$$
 (3.5)

and finally, the fill factor FF is given by [79]

$$FF = v_{\text{MPP}} \times j_{\text{MPP}} = v_{\text{MPP}} \left[ 1 - (1 - \gamma) v_{\text{MPP}} - \gamma v_{\text{MPP}}^m \right]$$
 (3.6)

In [100], Saleem and Karmalkar and in [79], Karmalkar and Haneefa applied the model on several types of solar cells. They found out that the model is applicable on several solar cells. In Figure 3.3, for example one KH fit and the respective measured jv curve for poly-Si, CdTe, CIGS, a-Si:H/ $\mu$ c-Si:H, and a-Si:H in Cologne are shown. However, Karmalkar and Haneefa say that the model is valid for moderately convex JV curves with  $0.56 \le FF \le 0.77$  [79]. Therefore, Karmalkar and Saleem modified the model in [101] to cover a wider range of solar cells from concave (FF < 0.25) to highly convex (FF > 0.85) curve shapes [101]. However, this model introduces two additional parameters. In the following work, the simple KH model introduced in [79] will be used for the analysis of the outdoor data due to the small necessary parameter set.

In Figure 3.3, the KH Model was applied for different types of solar technologies, namely poly-Si, CdTe, CIGS, a-Si:H/ $\mu$ c-Si:H, and a-Si:H. The data are taken from the measured modules in Cologne. For comparison, the respective measured JV curves are shown here as well. It can be seen that also thin film modules can

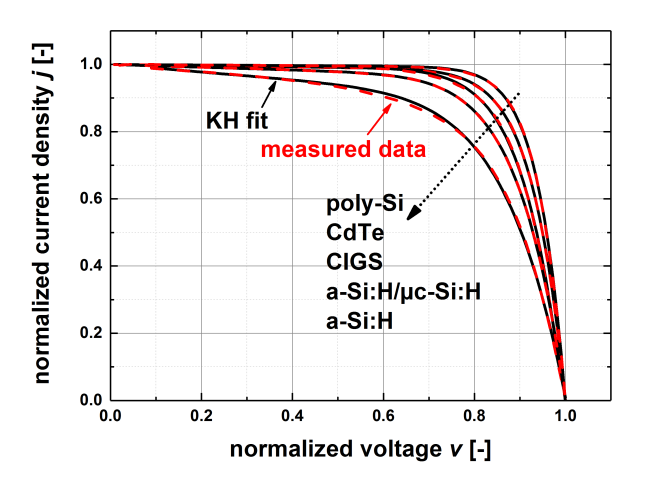


Figure 3.3. – Exemplary one KH fit per technology (black lines) and the respective measured jv curves for poly-Si, CdTe, CIGS, a-Si:H $/\mu$ c-Si:H and a-Si:H in Cologne (red dashed lines).

in general be described with the KH model. One aim of this thesis is to obtain a model with a small amount of parameters that is easy to fit to outdoor data for thin films and allow a physics-based analysis. For this, the used parameters need to be physically meaningful. In the next chapter (Chapter 4), it will be discussed if the parameters of the KH model are physically meaningful. Figure 3.3 indicates that the model is not limited to one type of technology. The further analysis of the applicability of the KH model for different solar cell technologies will also follow in the next chapter. Due to its simplicity, the KH model can be fast implemented. Also in [102] the authors achieved fast implementations of the KH model.

As can be seen in the Equations 3.1 to 3.6, m and  $\gamma$  are important parameters. Both parameters describe the shape of the JV curve [101]. In Equation 3.1, the linear term captures the slow fall in current with voltage near the  $J_{\rm sc}$  point and the power law term describes the rapid fall near the  $V_{\rm oc}$  point [100]. From Equation 3.1 one obtains that  $\gamma$  and m are are directly related to the differential resistances  $R_{\rm oc}$  and  $R_{\rm sc}$ , respectively, as [103]

Outdoor data and analysis method

$$\frac{1}{R_{\rm sc}} = \frac{dJ}{dV} \bigg|_{V=0} = \frac{J_{\rm sc}}{V_{\rm oc}} \left(1 - \gamma\right) \tag{3.7}$$

and

$$\frac{1}{R_{\rm oc}} = \frac{dJ}{dV} \bigg|_{V=V_{\rm oc}} = \frac{J_{\rm sc}}{V_{\rm oc}} \left(1 - \gamma + \gamma m\right) . \tag{3.8}$$

Inversion of equations 3.7 and 3.8 yiels [103]

$$m = \frac{V_{\text{oc}} \left( G_{\text{oc}} - G_{\text{sc}} \right)}{J_{\text{sc}} - V_{\text{oc}} G_{\text{sc}}} \tag{3.9}$$

and

$$\gamma = 1 - G_{\rm sc} \frac{V_{\rm oc}}{J_{\rm sc}} , \qquad (3.10)$$

with  $G_{\rm sc} = 1/R_{\rm sc}$  and  $G_{\rm oc} = 1/R_{\rm oc}$  the differential conductances at the short-circuit and open-circuit point, respectively.

In the following work, Equation 3.2 will be used and fitted with the lowest root mean square (rms) error to the measured JV curve according to

$$rms = \sqrt{\frac{1}{n} \sum_{i=1}^{n} \left(\frac{J_{\text{KH}}^{i} - J_{\text{raw}}^{i}}{J_{sc,\text{raw}}}\right)^{2}}$$
, (3.11)

where the subscript "KH" indicates the respective value of the KH model and the subscript "raw" the measured value. The symbol n indicates the amount of measured JV points per JV curve.

From the fit  $J_{\rm sc}$ ,  $V_{\rm oc}$ , m, and  $\gamma$  are determined. Then, with equations 3.7 and 3.8,  $G_{\rm sc}$  and  $R_{\rm oc}$  are determined, respectively. In the next section, the Loss Factor Model will be discussed which will be later used as a reference model to evaluate the KH model.

# 3.3. Loss Factor Model

In 2011, Sutterlüti et al. introduced the "Loss Factor Model" (LFM) [74]. The LFM is based on physically normalized parameters and a set of coefficients that describe how these parameters depend on irradiance and module temperature. Already in 2005, Ransome et al. showed how using normalized values for  $J_{\rm sc}$  allows a better failure analysis [104]. Ransome et al. normalized here the measured  $J_{\rm sc}$  to the  $J_{\rm sc}$ at reference condition. In this section, the LFM will be introduced, whereas the parameterization and the translation to reference conditions will be explained.

The LFM was developed to simulate PV performance, determine instabilities, find faults, and predict the energy yield for several PV technologies [105, 106]. The LFM is taken as a reference model in this thesis as it has been applied to various thin film technologies, different locations (see for example [74, 107]), and different fill factors [108]. In addition, it has been used for long term analyses (see for example [109]). Very good parameter [110] and maximum power point prediction [78] have been achieved with the LFM.

The LFM uses five parameters. In the original literature, the parameters are indicated with prefixes, for example the prefix "n" is used to classified normalized parameters [111]. For a better readability, in this thesis, the superscripts "n", "m", and "r" are used to indicate normalized, measured, and reference parameters, respectively. Information about temperature corrected parameters are given in the subscript of the respective parameter.

In the LFM, the normalized parameters are calculated from measured outdoor and reference JV parameters [111]. The reference parameters can be taken for example from indoor flash measurements at STC or from name plate values [111]. The parameters are defined as [78, 105]:

$$J_{\rm sc}^{\rm n} = \frac{J_{sc}^{\rm m}}{J_{sc}^{\rm r}}/G_i \tag{3.12}$$

$$R_{sc}^{\rm n} = \frac{J_{\rm r}^{\rm m}}{J_{\rm sc}^{\rm m}} \tag{3.13}$$

$$J_{\text{sc}}^{\text{n}} = \frac{J_{\text{sc}}^{\text{m}}}{J_{\text{sc}}^{\text{r}}} / G_{i}$$

$$R_{\text{sc}}^{\text{n}} = \frac{J_{\text{r}}^{\text{m}}}{J_{\text{sc}}^{\text{m}}}$$

$$V_{\text{oc}}^{\text{n}} = \frac{V_{\text{oc}}^{\text{m}}}{V_{\text{oc}}^{\text{r}}}$$

$$(3.12)$$

$$(3.13)$$

Outdoor data and analysis method

$$R_{\rm oc}^{\rm n} = \frac{V_{\rm r}^{\rm m}}{V_{\rm oc}^{\rm m}} \tag{3.15}$$

$$R_{\text{oc}}^{\text{n}} = \frac{V_{\text{r}}^{\text{m}}}{V_{\text{oc}}^{\text{m}}}$$

$$FF^{\text{n}} = \frac{FF^{\text{m}}}{R_{\text{oc}}^{\text{n}} \times R_{\text{sc}}^{\text{n}} \times FF^{\text{r}}}$$

$$(3.15)$$

 $G_i$  is the irradiance measured in suns. In Figure 3.4, the key points of the LFM are visualized, which are  $J_{\rm sc}^{\rm n}, R_{\rm sc}^{\rm n}, V_{\rm oc}^{\rm n}, R_{\rm oc}^{\rm n}$ , and  $FF^{\rm n}$ . Shown are a reference JV curve and a measured JV curve. The abbreviation "MMF" indicates the correction for the Miss-Match-Factor. Regarding the available data set, this could not be done in this thesis. Only an irradiance correction is done, when translating from the reference to the measured value and vice versa. This will be explained later in this section. For the  $V_{\rm oc}$ , a correction for the temperature is very important and is in Figure 3.4 indicated as "tcorr". The match of the tangents at  $V_{\rm oc}$  and  $J_{\rm sc}$  is the point  $(V_{\rm r},J_{\rm r})$ and is needed to obtain  $R_{sc}^{n}$  and  $R_{oc}^{n}$ . The maximum power point for the measured JV curve is indicated as  $P_{\mathrm{MPP}}^{\mathrm{m}}$ .

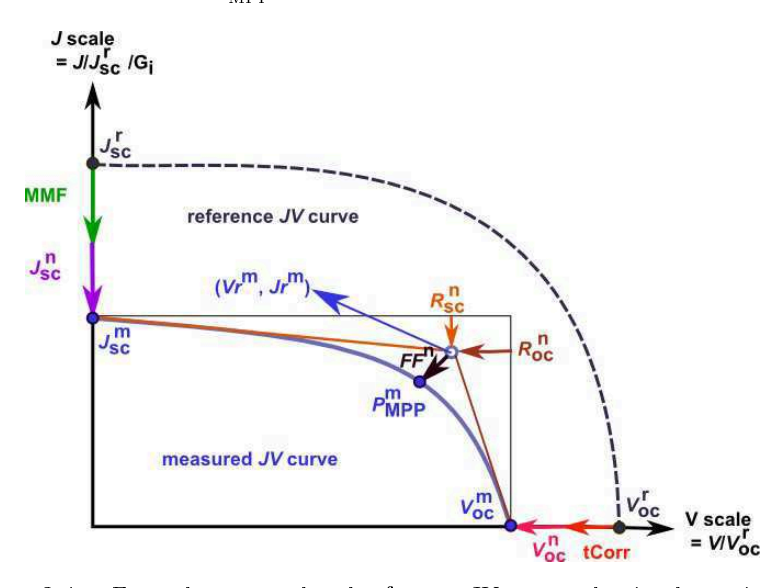


Figure 3.4. – Example measured and reference JV curves showing key points and their graphical derivation. Plot is adapted from [74, 105].

The here introduced Loss Factor Model is referred to LFM-A [74]. In a second version of the LFM, the LFM-B, the parameter  $FF^n$  has been substituted by the product of  $\left[J_{mpp}^{\rm m}/J{\bf r}^{\rm m}\times J_{sc}^{\rm r}/J_{mp}^{\rm r}\right]$  and  $\left[V_{mpp}^{\rm m}/V{\bf r}^{\rm m}\times V_{oc}^{\rm r}/V_{mpp}^{\rm r}\right]$ . Thus the model was extended to six parameters. With the aim to obtain a good performance model with few parameters, in the following only the LFM-A will be considered when referring to the LFM. From the five parameters,  $P_{\text{mpp}}^{\text{n}}$  is obtained as:

$$\begin{split} P_{\text{mpp}}^{\text{n}} &= J_{\text{sc}}^{\text{n}} R_{\text{sc}}^{\text{n}} V_{\text{oc}}^{\text{n}} R_{\text{oc}}^{\text{n}} F F^{\text{n}} \\ &= \frac{J_{\text{sc}}^{\text{m}} V_{\text{oc}}^{\text{m}} F F^{\text{m}}}{J_{\text{sc}}^{\text{r}} V_{\text{oc}}^{\text{r}} F F^{\text{r}}} \frac{1}{G_i} \\ &= \frac{P_{\text{mpp}}^{\text{m}}}{P_{\text{mpp}}^{\text{m}}} \frac{1}{G_i} \ . \end{split}$$

$$(3.17)$$

After obtaining the parameters, they are corrected for the module temperature. Normally, also a spectral mismatch correction is done for the  $J_{\rm sc}$  [105]. However, in the considered data set of Section 3.1, no data are available for this correction. In the following, therefore, only a temperature correction will be done. For the temperature coefficients calculation, the data first have to be filtered. According to Sutterlüti et al. [112], the filtered data should be at high irradiance (> 500 W/m²), within an hour of solar noon, at clear sky and high module temperature (> 25 °C) over a short time period to avoid effects due to diffuse conditions, snow, angle of incidence, degradation etc.. Afterwards, a linear regression fit of the LFM parameters is done vs. temperature. The temperature correction term is defined as [78]:

$$T_{\text{corr},i} = 1 + \alpha_i \times (T_{\text{meas}} - T_{\text{ref}}) \quad . \tag{3.18}$$

Taking STC for the reference values,  $T_{\rm ref}$  is 25 °C. The temperature correction is done for  $J_{\rm sc}$ ,  $V_{\rm oc}$ , FF, and  $P_{\rm mpp}$ [78]. However, with the relation [78]

$$\alpha_{Pmpp} = \alpha_{Jsc} + \alpha_{Voc} + \alpha_{FF} \tag{3.19}$$

and Equation 3.17, only three temperature coefficients, namely for  $J_{\rm sc}$ ,  $V_{\rm oc}$ , and FF have to be determined. The temperature coefficient itself is obtained by dividing the gradients of the linear regression fits by the intercepts [105]. For example, for

Outdoor data and analysis method

 $J_{\rm sc}$ , the temperature coefficient is calculated by:

$$\alpha_{\rm Jsc} = \frac{1}{J_{\rm sc.G.ref}^{\rm n}} \times \frac{\partial J_{\rm sc.G}^{\rm n}}{\partial T_{meas}} \quad . \tag{3.20}$$

In Figure 3.5, as an example, the linear regression fits are shown for one week measurement for the CIGS1 module measured in Italy. As only information about module temperature and irradiance are available, the data were fitted for high irradiance ( $> 800 \, \mathrm{W/m^2}$ ) and high module temperature ( $> 25 \, ^{\circ}\mathrm{C}$ ) and the time period was set to one week. Hence, not all above explained filter requirements from Sutterlüti et al. [112] could be fulfilled. This leads to higher noise data that affect the calculation of the temperature coefficient. However, as the LFM will be used to compare it with the KH model, for which the same data set than the LFM is used, the reduced filter possibilities are not problematic. Nevertheless, this aspect has to be mentioned when comparing both models.

For the reference value for the LFM, neither indoor flash measurements at STC nor name plate values were available. The used reference value calculation is described in Section 4.3.

All these mentioned problems indicate already that the LFM needs, in best case more, information than is available, which makes it more difficult to adapt it to all data sets. Nevertheless, the available data set provides enough information to use the LFM. The results of this analysis are shown in the next chapter.

From the above described temperature correction, the temperature correction for the parameters are calculated by

$$J_{\text{sc,T}}^{\text{n}} = J_{\text{sc}}^{\text{n}}/T_{\text{corr,Jsc}} \tag{3.21}$$

$$V_{\text{oc,T}}^{\text{n}} = V_{\text{oc}}^{\text{n}}/T_{\text{corr,Voc}} \tag{3.22}$$

$$FF_{\mathrm{T}}^{\mathrm{n}} = FF^{\mathrm{n}}/T_{\mathrm{corr,FF}} \quad . \tag{3.23}$$

In a next step, the three temperature corrected parameters  $(J_{\text{sc,T}}^n, V_{\text{oc,T}}^n, FF_{\text{T}}^n)$  and the two remaining parameters  $(R_{\text{oc}}^n, R_{\text{sc}}^n)$  are fitted to  $G_i$  with [78]:

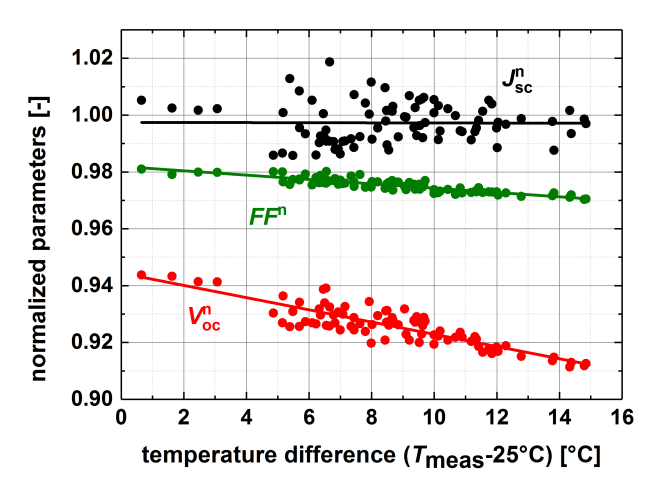


Figure 3.5. – Example linear regression fit (line) for the temperature coefficient calculation for the LFM. Data are taken from the CIGS1 module measured in Italy. The fit is done for  $J_{\rm sc}^{\rm n}$  (black dots),  $V_{\rm oc}^{\rm n}$  (red dots), and  $FF^{\rm n}$  (green dots).

$$f_n(G_i) = c_1 + c_2 \times \log G_i - c_3 \times G_i^2$$
 (3.24)

Equation 3.24 is empirical and is fitted to all data and all five parameters. In Figure 3.6, the results of the  $f_n$ -fit with Equation 3.24 are shown for all five LFM parameters. The data are taken from the CIGS1 module measured in Italy. It can be seen that Equation 3.24 fits all data very well. With the Equations 3.17, 3.18, and 3.24, the parameters and the  $P_{\rm mpp}$  can be translated to all reference conditions. These translations will be done in Section 4.3.

In the next chapter, the LFM will be taken as a reference performance model for thin film modules and the KH model will be compared to it to investigate if the KH model is as suitable as the LFM for performance analysis.

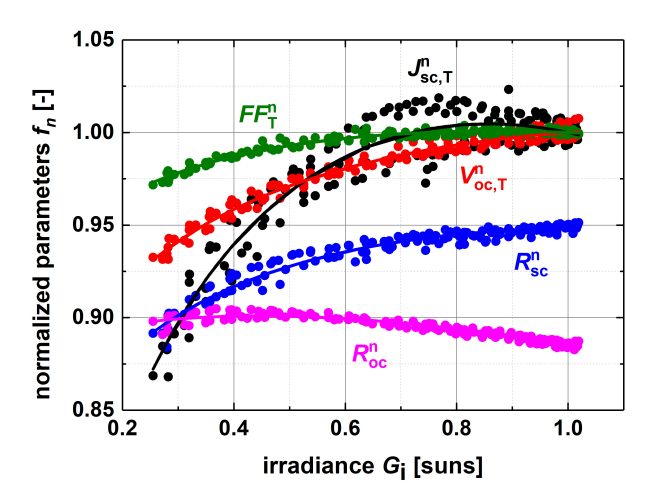


Figure 3.6. – Example  $f_n$ -fit (lines) for all five LFM parameters. Data are taken from the CIGS1 module measured in Italy. The fits are done for  $J_{\text{sc},T}^n$  (black dots),  $V_{\text{oc},T}^n$  (red dots),  $FF_{\text{T}}^n$  (green dots),  $R_{\text{oc}}^n$  (magenta dots), and  $R_{\text{sc}}^n$  (blue dots).

# 4. Outdoor data analysis with the Karmalkar-Haneefa model

In this chapter, the use of the Karmalkar-Haneefa model for performance modeling will be discussed and compared to the Loss-Factor Model. As discussed in Section 2.2.4, the four steps of performance modelling are: (i) the parametrization, (ii) the parameter analysis, (iii) the translation to a reference condition, and (iv) the energy yield prediction. Each of these steps introduces a certain error. As mentioned in the previous chapter, the LFM is an established performance model for thin-film modules. The KH model, however, is not very well-known. The KH model has two obvious advantages compared to the LFM. First, the KH model uses less parameters (only four) than the LFM (five) and secondly, no numerical determination of the slopes at short-circuit and open-circuit points are necessary, as these slopes are derived from a fit to the whole JV characteristic. This parameterization step will be investigated further in Section 4.1. Afterwards, in Section 4.2 the KH JV curve fitting, especially at the MPP will be investigated. In Section 4.3, the parameter analysis and the translation to reference condition are investigated for the KH model and compared to the LFM. Finally, in Section 4.4, the last step of the four-step procedure, the prediction, is investigated for the KH model and also compared to the LFM. It should be noted that the outdoor data that are used in this chapter were previously introduced in Section 3.1 and that for better comparison, the outdoor data are transferred to cell level.

# 4.1. Parameterization

Comparing the parameterization of the KH model (see Section 3.2) and the LFM (see Section 3.3), it should be noted that the LFM requires an additional parameterization step, whereas for the KH model the parameterization step is the fitting procedure of the KH Equation 3.2. For performance models like the LFM, a common method for the parameterization step is a linear fit around V=0 to determine  $V_{\rm sc}$  and  $V_{\rm sc}$  and the KH fits will be first investigated in detail and then compared to each other. All investigations in this section will be done with the data of the Cologne test site.

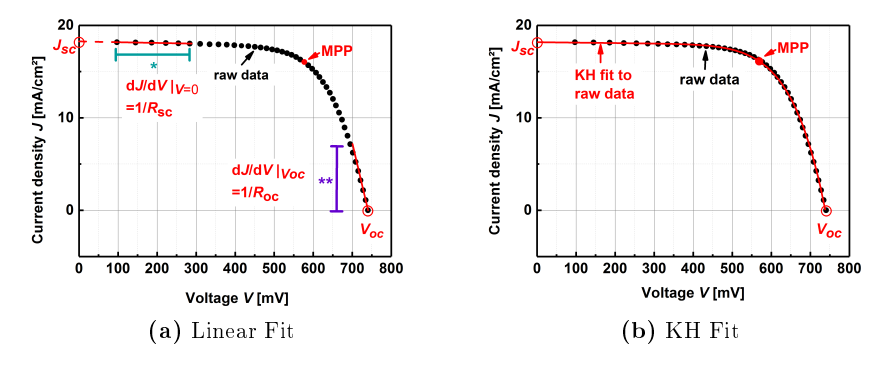


Figure 4.1. – Parameter determination with a) two linear fits and b) the KH fit

Figure 4.1 shows the two parameterization methods for the same JV curve. In Figure 4.1a, the two linear fits (red lines) are shown and in Figure 4.1b, the KH fit (red line) is shown. Using the KH fitting model, the four physical parameters  $J_{\rm sc}$ ,  $V_{\rm oc}$ ,  $R_{\rm sc}$ , and  $R_{\rm oc}$  are obtained directly from a single fit of the entire JV curve.

For the linear fitting methods, first of all the fitting ranges have to be defined. In Figure 4.1a, one fitting range is shown as example to determine  $J_{\rm sc}$  and  $R_{\rm sc}$  (green, one asterisk) as well as  $V_{\rm oc}$  and  $R_{\rm oc}$  (violet, two asterisks). The reason for the fitting range is that often significant variations in these fitted resistance values arise from measurement errors. To reduce the statistical spread in the determined resistance values, the fit is commonly applied over a defined voltage range. However, this leads

to the situation that the determined values deviate from the actual reciprocal slopes at  $V_{\rm oc}$  and  $J_{\rm sc}$ . In the next subsection, it will be investigated how sensitive the parameterization of the parameters is to the fitting procedure.

In addition, it can be observed from Figure 4.1 that the outdoor JV curve measurement starts above V=0 and ends before J=0, which is common for outdoor measurements. Figure 4.1 shows that the measured maximal voltage is not so far away from J=0, whereas the minimal measured voltage can vary several mV from V=0 (see Figure 4.1). For this reason, not only  $R_{\rm sc}$  and  $R_{\rm oc}$  are determined by fitting but also  $J_{\rm sc}$  and  $V_{\rm oc}$ . Therefore, the fits need to be extrapolated (red dashed lines) to  $J_{\rm sc}$  and  $V_{\rm oc}$ . All this needs to be considered when doing the parameterization step for the performance models. Therefore, in the next subsection, first the detailed fitting procedure for the linear fits will be explained before the results are shown.

### 4.1.1. Results of the linear fits for CdTe

In this subsection, the influence of the linear fitting is analyzed for the first CdTe module (CdTe1) measured in Cologne. To investigate the influence of the linear fitting procedure to the parameterization, first different fitting ranges have to be defined.

For the definition of the linear fitting range, the Maximum Power Point (MPP) was chosen as a reference point. Then, relating to this MPP, the range for the single linear fits was determined. For the determination of  $J_{\rm sc}$  and  $R_{\rm sc}$ , the range was chosen as  $[V_{\rm min}, x \times V_{\rm mpp}]$ , with  $V_{\rm min}$  as the minimal measured voltage,  $V_{\rm mpp}$  as the voltage at MPP, where  $x = \{1/4, 1/3, 1/2, 5/8\}$ . For  $V_{\rm oc}$  and  $R_{\rm oc}$ , the linear fitting range was chosen as  $[J_{\rm min}, y \times J_{\rm mpp}]$ , with  $J_{\rm min}$  as the current density at the maximal measured voltage,  $J_{\rm mpp}$  as the current density at MPP and y as a variable, where  $y = \{1/7, 1/4, 1/2, 5/8\}$ . The fit itself was performed with the least squares method in the defined range. As mentioned before, in Figure 4.1a, two fitting ranges are shown as example. Here,  $J_{\rm sc}$  and  $R_{\rm sc}$  were determined with a fitting range of  $[V_{\rm min}, 1/2 \times V_{\rm mpp}]$  (green, one asterisk) and for  $V_{\rm oc}$  and  $R_{\rm oc}$  a fitting range of  $[J_{\rm min}, 1/2 \times J_{\rm mpp}]$  was taken as example (violet, two asterisks). In the following, it will be shown how these four parameter are influenced with changing linear fitting

ranges.

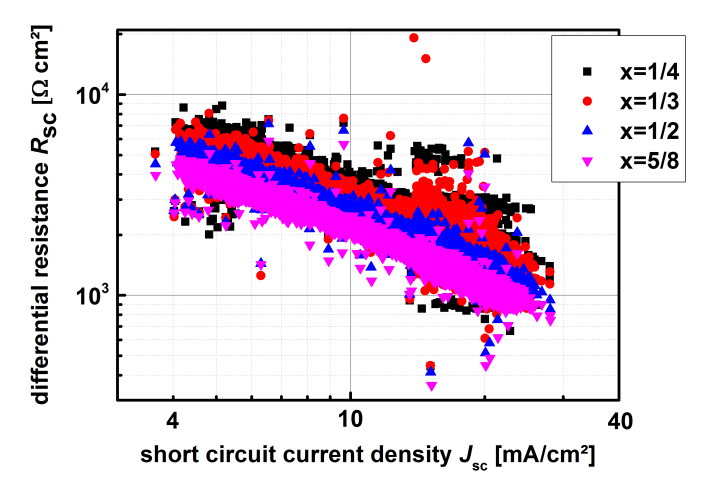


Figure 4.2. – Results for  $R_{sc}$  by using different linear fitting ranges for CdTe1. The fitting range was chosen to be  $[V_{min}, x \times V_{mpp}]$ . Here, the influence of x is shown. Each of the four plots represents one of the following x values: 1/4 (black squares), 1/3 (red dots), 1/2 (blue up-pointing triangles), 5/8 (magenta down-pointing triangles). For easier comparison of the different  $R_{\rm sc}$  values, the  $J_{\rm sc}$  value of each JV curve has been calculated with x=1/2.

Using different fitting ranges for the linear fits, it was found that the values obtained for  $R_{\rm sc}$ , and to a lesser extent for  $R_{\rm oc}$ , depend strongly on the fitting range, whereas the values for  $V_{\rm oc}$  and  $J_{\rm sc}$  have a much weaker dependence. Therefore, it will be concentrated on  $R_{\rm sc}$  in this subsection. The other three parameters will be mentioned later in comparison with the KH model.

Figure 4.2 shows the results for  $R_{\rm sc}$  calculated for the CdTe1 module in Cologne. For each JV curve,  $R_{\rm sc}$  has been calculated by varying x from 1/4 (black squares) to 5/8 (magenta down-pointing triangles). The resulting  $R_{\rm sc}$  values are shown as a function of the measured  $J_{\rm sc}$  value. Thereby, the  $J_{\rm sc}$  values have been calculated with x=1/2 for each JV curve. Two trends can be observed: First, it can be seen that the  $R_{\rm sc}$  values decrease with  $J_{\rm sc}$  and secondly, it can be observed that small fitting ranges lead to higher  $R_{\rm sc}$  values than larger fitting ranges. The different fitting

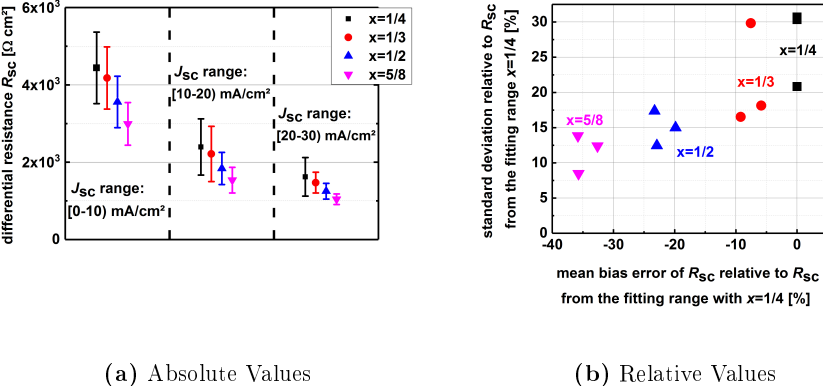


Figure 4.3. – Mean and standard deviation for  $R_{\rm sc}$  for different  $J_{\rm sc}$  ranges using different linear fitting ranges. Each of the four plots represents one of the following x values: 1/4 (black squares), 1/3 (red dots), 1/2 (blue up-pointing triangles), 5/8 (magenta down-pointing triangles). In a) the absolute values are shown. In each  $J_{\rm sc}$  range, the fitting range with x = 1/4 shows the highest average value for  $R_{\rm sc}$  and the highest standard deviation. The average  $R_{\rm sc}$  value is decreasing by decreasing the x value for the fitting range. In b) the relative bias and standard deviation values are shown. For each  $J_{\rm sc}$  range, the respective values are related to the  $R_{\rm sc}$  value obtained from the fit with x=1/4. Negative bias values indicate a mean  $R_{\rm sc}$  value that is lower than the mean value obtained from the fit with x = 1/4. The three  $J_{\rm sc}$  ranges are not labeled here.

ranges can lead to a difference in the obtained  $R_{\rm sc}$  value of a factor of two.

In a next step, the mean and standard deviations of the  $R_{\rm sc}$  values for the different fitting are investigated. The results are shown in Figure 4.3a. In Figure 4.3a, the absolute mean and standard deviation for  $R_{\rm sc}$  is calculated for three different  $J_{\rm sc}$ ranges. This is done as the  $R_{\rm sc}$  values depend on  $J_{\rm sc}$  as mentioned before. For each  $J_{\rm sc}$  range, four different linear fitting ranges are investigated. It can be seen from Figure 4.3a that as the fitting range is increased  $R_{\rm sc}$  and the standard deviation are decreased.

The absolute mean and standard deviations values can also be considered in relation to each other. This is done in Figure 4.3b. Here, the average value obtained with the smallest fitting range, i.e. x = 1/4, is set for each considered  $J_{sc}$  range as Outdoor data analysis with the Karmalkar-Haneefa model

a bias error of zero, as it can be assumed that the smallest fitting range shows in average the closet fit to the "real"  $R_{\rm sc}$  value. The standard values and average values from the other fitting ranges were set in relation to this value for each  $J_{\rm sc}$  range. Then the respective relative mean bias and standard deviations were calculated for each fitting range and for each  $J_{sc}$  range by

relative mean bias = 
$$\frac{\mu_{\text{Rsc,x,i}} - \mu_{\text{Rsc,x}=1/4,i}}{\mu_{\text{Rsc,x}=1/4,i}}$$
(4.1)

$$\begin{array}{l} {\rm relative\ mean\ bias} = \frac{\mu_{\rm Rsc,x,i} - \mu_{\rm Rsc,x=1/4,i}}{\mu_{\rm Rsc,x=1/4,i}} \\ {\rm relative\ standard\ deviation} = \frac{\sigma_{\rm Rsc,x,i}}{\mu_{\rm Rsc,x=1/4,i}} \end{array} , \qquad (4.1)$$

with  $\mu_{\text{Rsc},x,i}$  the mean value of  $R_{\text{sc}}$  calculated with a specific linear fitting range xover a specific  $J_{\rm sc}$  range i. The variable  $\sigma_{{\rm Rsc},{\rm x,i}}$  indicates the standard deviation of  $R_{\rm sc}$  obtained for a specific linear fitting range x over a specific  $J_{\rm sc}$  range i.

A negative bias value indicates a mean  $R_{\rm sc}$  value that is lower than the mean value obtained from the fit with x = 1/4 in the respective  $J_{sc}$  range. The three different  $J_{sc}$  ranges shown in Figure 4.3b are the same as in Figure 4.3a, however, they are not labeled here. Figure 4.3b visualizes the trade-off between standard deviation and mean bias error: A small fitting range leads to a high standard deviation and a small mean bias error, whereas a large fitting range leads to a small standard deviation and a high mean bias error.

For a reliable parametrization, a low standard deviation is needed. However, a low standard deviation can only be obtained with a high mean bias error, as explained. A compromise for this problem can be found in mean fitting ranges, as for example x = 1/2. Here, neither the standard deviation nor the mean bias error show values that are too high. Based on these results, the difference between the KH and the linear fitting methods will be investigated in the following.

# 4.1.2. Comparison of the KH and linear fits for CdTe

Using the KH equation for fitting JV curves, the values for  $J_{\rm sc}$  and  $V_{\rm oc}$  show only small deviations compared to the values calculated by the linear fit. Further information for this can be found in Appendix B. The largest deviation between the

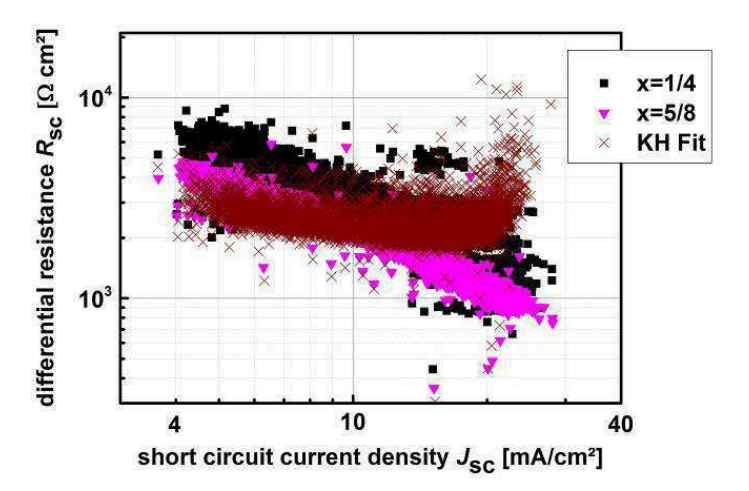


Figure 4.4. – Results for  $R_{\rm sc}$  by using the KH fit (dark red crosses) for CdTe. The results are compared to the two linear fittings with x=1/4 (black squares) and x=5/8 (magenta down-pointing triangles).

KH fit and the linear fits can be observed for the  $R_{\rm sc}$  values. In the following, the deviation between the  $R_{\rm sc}$  values from the KH and the linear fit will be investigated in more details. Afterwards, also the  $R_{\rm oc}$  value will be considered.

In Figure 4.4, the obtained  $R_{\rm sc}$  values of the KH and the linear fits are plotted as a function of  $J_{\rm sc}$ , whereas  $J_{\rm sc}$  is determined with the linear fitting with x=1/2. The results of the KH fit are compared to the  $R_{\rm sc}$  values obtained with linear fitting ranges with x=1/4 and x=5/8, i.e. a very small and a very large fitting range, respectively. It can be seen that the KH- $R_{\rm sc}$  values show only a slight dependency on  $J_{\rm sc}$ , compared to the higher dependency of the  $R_{\rm sc}$  values obtained from the linear fits. Additionally, the standard deviation for the  $R_{\rm sc}$  values from the KH fit show a high uncertainty for high  $J_{\rm sc}$  (see also Appendix B). This uncertainty can be reduced by using a weighting factor in the range  $[V_{\rm min}, x \times V_{\rm mpp}]$ . As explained in Section 3.2, the KH equation (Equation 3.2) is fitted with the lowest rms error to the measured JV curve with Equation 3.11. By using the weighting factor, the error in the range  $[V_{\rm min}, x \times V_{\rm mpp}]$  is weighted more than the error of the rest of the JV curve.

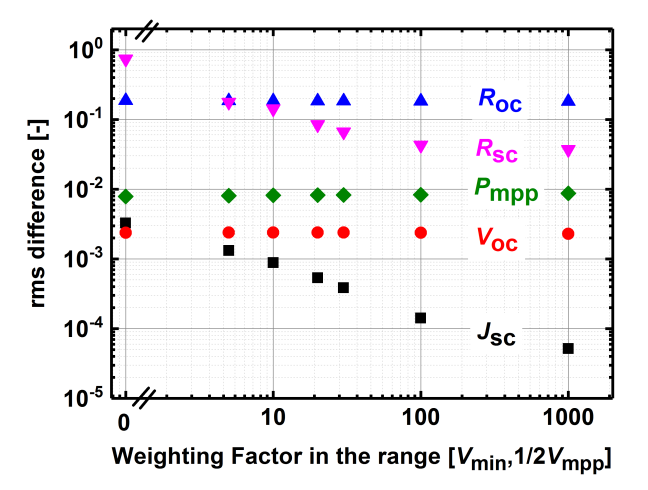


Figure 4.5. – The root mean square (rms) difference between the parameters obtained from a linear fit in the range  $[V_{\min}, 1/2 \times V_{\mathrm{mpp}}]$  and the KH fit. The KH fit was weighted differently in the range  $[V_{\min}, 1/2 \times V_{\mathrm{mpp}}]$ . By increasing the weighting factor from zero to 1000 the rms value is decreasing. The data are taken from the CdTe1 module. The KH fit is compared to the values of the linear fits with x=1/2 and y=1/7.

In Figure 4.5, the influence of a weighting factor in the range  $[V_{\min}, 1/2 \times V_{\text{mpp}}]$  is shown. The weighting factor was increased from zero to 1000. The root mean square (rms) difference is calculated with

rms difference = 
$$\sqrt{\frac{\sum_{i=1}^{n} \left(1 - \frac{pr_{\text{KH},i}}{pr_{\text{lin},i}}\right)^{2}}{n}},$$
 (4.3)

where  $pr_{\text{KH}}$  is the investigated parameter calculated by the KH fit and  $pr_{\text{lin}}$  the same parameter calculated by the linear fitting method, and n is the number of investigated JV curves.

In Figure 4.5, the rms difference for the five parameters  $R_{\rm oc}$ ,  $R_{\rm sc}$ ,  $P_{\rm mpp}$ ,  $V_{\rm oc}$ , and  $J_{\rm sc}$  are determined between the KH fit with different weighting factors and the linear fits with x=1/2 and y=1/7. It can be seen that without the weighting factor, the deviation between the linear fit and the KH fit is highest for  $R_{\rm sc}$ . The

weighing factor reduces the difference for both the  $R_{\rm sc}$  and  $J_{\rm sc}$  values obtained from the KH fit. For a weighing factor larger than five, the overall deviation for all parameters is reduced and the  $R_{\rm oc}$  value becomes the parameter with the highest deviation between the linear fit and the KH fit. Nevertheless, it can be told that for all technologies a weighting factor of 30 in the range  $[V_{\rm min}, 1/2 \times V_{\rm mpp}]$  leads to a significant reduction of the rms difference compared to the  $R_{\rm sc}$  values obtained from the linear fitting range  $[V_{\rm min}, 1/2 \times V_{\rm mpp}]$ . With this fitting range, the smallest weighting factor suffices to achieve a rms value for  $R_{\rm sc}$  that is lower than that for the  $R_{\rm oc}$  values for all single junction thin-film technologies. In the following, the KH fit will be always weighted with a factor of 30 in the range  $[V_{\rm min}, 1/2 \times V_{\rm mpp}]$ .

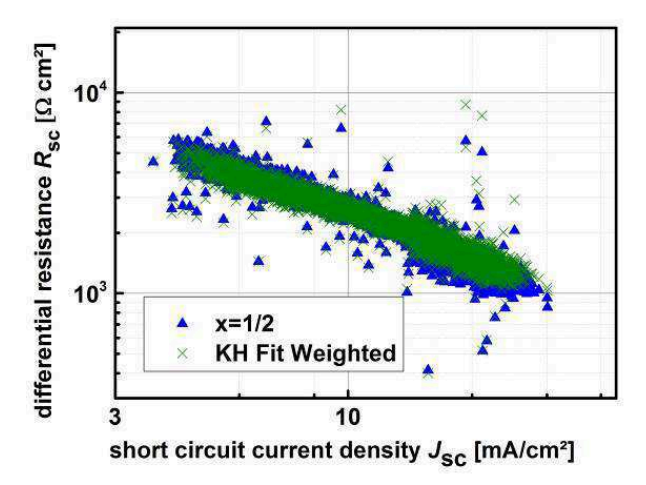


Figure 4.6. – Results for  $R_{\rm sc}$  by using a KH fit that is weighted with a factor of 30 in the range  $[V_{\rm min}, 1/2 \times V_{\rm mpp}]$  (green crosses) for CdTe. The results are compared to the results for linear fitting with x=1/2 (blue up-pointing triangles).

In Figure 4.6, the  $R_{\rm sc}$  values obtained from the KH fit with a weighting factor of 30 in the range  $[V_{\rm min}, 1/2 \times V_{\rm mpp}]$  are shown over  $J_{\rm sc}$  for the CdTe1 module and compared to  $R_{\rm sc}$  values obtained from the linear fit with x=1/2. It can be seen that now the behavior over  $J_{\rm sc}$  for the KH- $R_{\rm sc}$  values are comparable to the  $R_{\rm sc}$  values from the linear fit with x=1/2.

In a next step, the mean and standard deviation values for the  $R_{\rm sc}$  of the weighted KH fit are compared to the  $R_{\rm sc}$  values of the linear fits. This is done in Figure 4.7. In Figure 4.7a, the absolute mean and standard deviations of  $R_{\rm sc}$  for three  $J_{\rm sc}$  ranges are shown. Also for high  $J_{\rm sc}$  values, the  $R_{\rm sc}$  of the KH fit is now competitive to the linear fits and the high standard deviations are reduced significantly. For comparison, in Appendix B, the same plot as Figure 4.7a but with the not weighted KH fit results can be found.

In Figure 4.7b, the relative mean bias and standard deviation errors of  $R_{\rm sc}$  are shown for the linear fit and the weighted KH fit for each of the three  $J_{\rm sc}$  ranges. For the linear fit with x=1/2 and the weighted KH fit, the  $J_{\rm sc}$  ranges are labeled with numbers. The label numbers increase with higher  $J_{\rm sc}$  ranges. For the KH fit, it can be seen that with higher  $J_{\rm sc}$  values the mean bias error decreases while the standard deviation increases. Nevertheless, the mean bias error is smaller than 25% for all values and the standard deviation is smaller than 20%. For the analysis of  $R_{\rm sc}$ , this is a good compromise between too high mean bias errors or too high standard deviations as already discussed in the previous subsection for the linear fit. In the following, the  $R_{\rm sc}$  values from linear fits are calculated only with x=1/2.

As stated before, after using the described weighting factor for the KH fit, the highest deviation of the parameters from the KH fit compared to the linear fits can now be found in the  $R_{\rm oc}$ . That is why in the following the  $R_{\rm oc}$  will be investigated in more detail.

In Figure 4.8, the  $R_{\rm oc}$  values obtained from the KH fit and different linear fits are considered in respect to the  $J_{\rm sc}$ . It can be seen that the  $R_{\rm oc}$  values from the KH fit show the same behavior over the  $J_{\rm sc}$  as the values from the linear fits, i.e. the  $R_{\rm oc}$  values from the KH fits are physical meaningful. Therefore, no additional weighting factor is necessary.

A more detailed investigation of the  $R_{\rm oc}$  can be made by considering its mean values and standard deviations in certain  $J_{\rm sc}$  ranges. This is done in Figure 4.9. In Figure 4.9a, the absolute mean and standard deviation values of  $R_{\rm oc}$  for three different  $J_{\rm sc}$  ranges can be seen. Figure 4.9a shows that the mean value of  $R_{\rm oc}$  decreases for each  $J_{\rm sc}$  range with decreasing linear fitting range. The KH fit shows the lowest mean values. Nevertheless, most of the values from the KH fit are still in

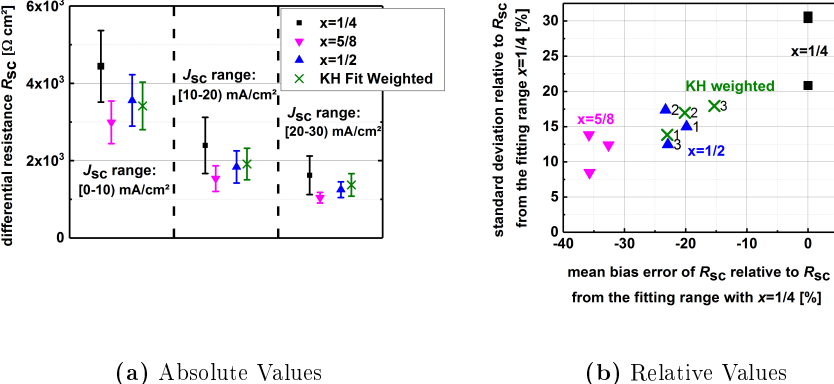


**Figure 4.7.** – Mean and standard deviation of  $R_{\rm sc}$  for different  $J_{\rm sc}$  ranges using different linear fitting ranges and the weighted KH fit. Each of the three plots represents one of the following x values: 1/4 (black squares), 1/2(blue up-pointing triangles), 5/8 (magenta down-pointing triangles). The green crosses represent the values of the KH fit, whereas the fit was weighted with a factor of 30 in the range  $[V_{\min}, 1/2 \times V_{\text{mpp}}]$ . In a) the absolute values are shown. In b) the relative bias and standard deviation values are shown. For each  $J_{\rm sc}$  range, the respective values for the mean bias error are related to the  $R_{\rm sc}$  value obtained from the fit with x = 1/4. Negative bias values indicate a mean  $R_{\rm sc}$  value that is lower than the mean value obtained from the fit with x = 1/4. The three  $J_{\rm sc}$  ranges are only labeled for the KH fit and x=1/2. The label "1" indicates the  $J_{\rm sc}$  ranges [0-10) mA  $/{\rm cm}^2$ , "2" and "3" the respective following increasing  $J_{\rm sc}$  ranges.

the range that is also obtained by the linear fits. If the linear fitting range could be decreased further to  $y \to 0$ , the difference between the linear and the KH fit would also decrease.

In Figure 4.9b, the relative mean bias and standard deviation errors are shown for the same linear fits and KH fit for each  $J_{\rm sc}$  range than in Figure 4.9a. The  $J_{\rm sc}$  ranges are not labeled. However, for each fit the highest standard deviation is obtained for low  $J_{\rm sc}$  values and the low standard deviation is obtained for high  $J_{\rm sc}$  values. All mean bias errors are related to the respective mean value from the linear fit with y = 1/7. Figure 4.9b shows that with the KH fits the lowest standard deviations can be obtained and the mean bias error is smaller than 20%, which is suitable for the performance analysis. It can be assumed, that the "real" mean bias

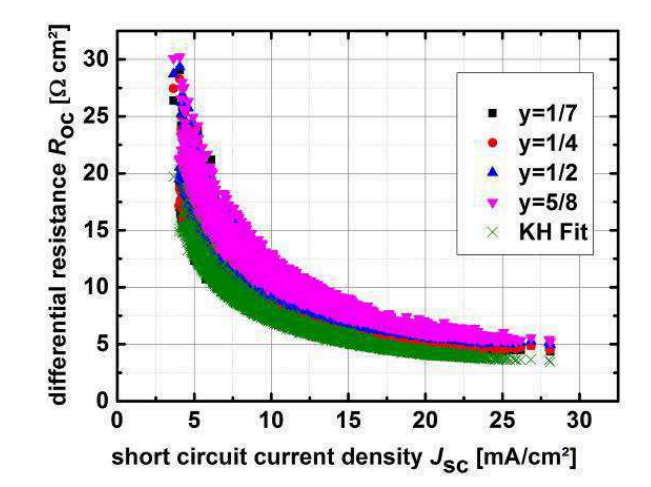


Figure 4.8. – Results for  $R_{\rm oc}$  by using different linear fitting ranges and one KH fit for CdTe. The linear fitting ranges were chosen as  $[J_{\rm min}, y \times J_{\rm mpp}]$ . Each of the four following plots represents one of the following y values: 1/7 (black squares), 1/4 (red dots), 1/2 (blue up-pointing triangles), 5/8 (magenta down-pointing triangles). The green crosses represent the values of the KH fit.

error for the KH fit is even lower if smaller linear fitting ranges at the open circuit voltages can be obtained. In summary, it can be states that low standard deviations for  $R_{\rm oc}$  are obtained with the KH fit and that the  $R_{\rm oc}$  values from the KH fit are best comparable to the values from linear fits with  $y \to 0$ . Regarding the available data set, the smallest linear fitting range can be obtained with y = 1/7.

After the detailed investigation of  $R_{\rm oc}$  and  $R_{\rm sc}$ , in Table 4.1, all four parameter values obtained from a linear fit with x=1/2 and y=1/7 are compared with those obtained from x=1/4 and y=5/8 and the values from the linear fit with x=1/2 and y=1/7 are compared to the values from the weighted KH fit. The KH fit was weighted with a factor of 30 in the range  $V=[V_{\rm min},1/2\times V_{mpp}]$ . Considering the two linear fits, it can be seen that the values from x=1/4, y=5/8 differ from the values from x=1/2, y=1/7 more than the values from the linear fit with x=1/2, y=1/7 compared to the values from the weighted KH fit. By using a weighting factor in the range  $J=[J_{\rm min},1/2\times J_{\rm mpp}]$ , the deviation for  $R_{\rm oc}$  and  $V_{\rm oc}$  between

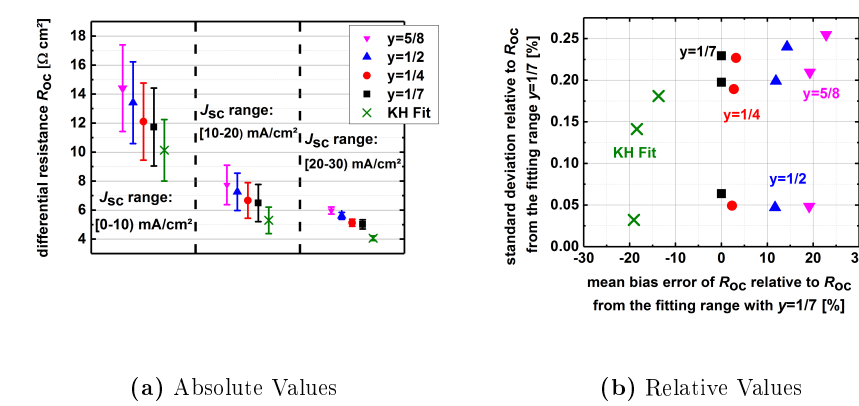


Figure 4.9. – Mean and standard deviation for  $R_{\rm oc}$  for different  $J_{\rm sc}$  ranges using different linear fitting ranges and the KH fit. Each of the four following plots represents one of the following y values: 1/7 (black squares), 1/4 (red dots), 1/2 (blue up-pointing triangles), 5/8 (magenta down-pointing triangles). The green crosses represent the values of the KH fit whereas the fit was weighted with a factor of 30 in the range  $[V_{\rm min}, 1/2 \times V_{\rm mpp}]$ . In a) the absolute values are shown. In b) the relative mean bias and standard deviation values are shown. For each  $J_{\rm sc}$  range, the respective values are related to the  $R_{\rm oc}$  value obtained from the fit with y=1/7. Negative bias values indicate a mean  $R_{\rm oc}$  value that is lower than the mean value obtained from the fit with y=1/7. The three  $J_{\rm sc}$  ranges are not labeled here.

the linear fit and the KH fit could be reduced further, of course (not shown here). However, this would then lead to an increase in the deviation for  $R_{\rm sc}$  and  $J_{\rm sc}$  in the same fit. Nevertheless, the results show that the parameters obtained from the KH fit lie in the range of those obtained from linear fits with rms values between  $3.5 \times 10^{-4}$  for  $J_{\rm sc}$  to 0.238 for  $R_{\rm oc}$  (Table 4.1).

# 4.1.3. Comparison of the KH and linear fits for all technologies

After the detailed analysis of the KH fit for the CdTe1 module measured in Cologne, finally also the other technologies of the Cologne test site are investigated. In Figure 4.10, the rms difference between the KH fit and the linear fits with x = 1/2

Table 4.1. – Comparison between the rms difference and the standard deviation (std) for different fits using the data of the CdTe1 module measured in Cologne. On the left side, the rms difference and std are calculated between two linear fits. The first fit uses x=1/2 and y=1/7. The second fit uses x=1/4 and y=5/8. On the right side, the rms difference and std are calculated between the KH fit and one linear fit. The linear fit uses x=1/2 and y=1/7, whereas the KH fit is weighted with a factor of 30 in the range  $V=[V_{\min},1/2\times V_{\min}]$ .

8 · [········/ · ······/ · ·····									
	Linear	Fit	KH Fit &	linear Fit					
Parameter	$(x = \{1/2, 1/4\}, y = \{1/7, 5/8\}$		(x = 1/2, y = 1/7)						
	rms diff.	$\operatorname{std}$	rms diff.	$\operatorname{std}$					
$R_{ m sc}$	$4.21 \times 10^{-1}$	$3.06 \times 10^{-1}$	$6.63 \times 10^{-2}$	$6.28 \times 10^{-2}$					
$J_{ m sc}$	$1.29 \times 10^{-6}$	$9.137 \times 10^{-4}$	$3.5 \times 10^{-4}$	$3.488 \times 10^{-4}$					
$R_{ m oc}$	$2.13 \times 10^{-1}$	$6.93 \times 10^{-2}$	$2.38 \times 10^{-1}$	$5.66 \times 10^{-2}$					
$V_{ m oc}$	$2.78 \times 10^{-3}$	$5.85 \times 10^{-4}$	$2.48 \times 10^{-3}$	$1.1 \times 10^{-3}$					

and y=1/7 is shown for all technologies. The data are taken from one module per technology (CdTe1, CIGS1, a-Si:H, a-Si:H/ $\mu$ c-Si:H, poly-Si) and all parameters were investigated. It can be seen that the rms difference for the  $R_{\rm oc}$  value is always highest for all single junction thin film technologies. This is related to the weighting factor. By using a weighting factor in the range  $[V_{\rm min},1/2\times V_{mpp}]$ , the deviation of  $R_{\rm sc}$  from the KH fit compared to the linear fit can be reduced significantly as mentioned before. By this, the  $R_{\rm oc}$  becomes the parameter with the highest deviation between both methods for the mentioned technologies. Nevertheless, the deviations can be justified because the behavior of all four parameters in respect to  $J_{\rm sc}$  (respectively irradiance) is the same compared to the parameters of the linear fits. In addition, the parameters of the KH fit seems to be the best method to obtain the "real"  $R_{\rm oc}$  value, i.e. to be closest to the slope  $\delta V/\delta J$  at J=0. In Figure 4.10, it can be observed that for CIGS and a-Si:H even lower deviation for the  $R_{\rm oc}$  than for CdTe can be achieved. A more detailed investigation of the  $R_{\rm oc}$  parameterization for CIGS, a-Si:H, a-Si:H/ $\mu$ c-Si:H, and poly-Si can be found in Appendix B.

Figure 4.10 shows also that the results for the rms difference between the KH and the linear fits deviate slightly for the a-Si:H/ $\mu$ c-Si:H tandem module from the single junction thin film modules. For the parameters  $R_{\rm oc}$ ,  $J_{\rm sc}$ ,  $V_{\rm oc}$ , and  $P_{\rm mpp}$ , the results obtained for the single junction thin films are similar to the results for the a-Si:H/ $\mu$ c-Si:H module. The exception is the  $R_{\rm sc}$  value. Here, the rms difference

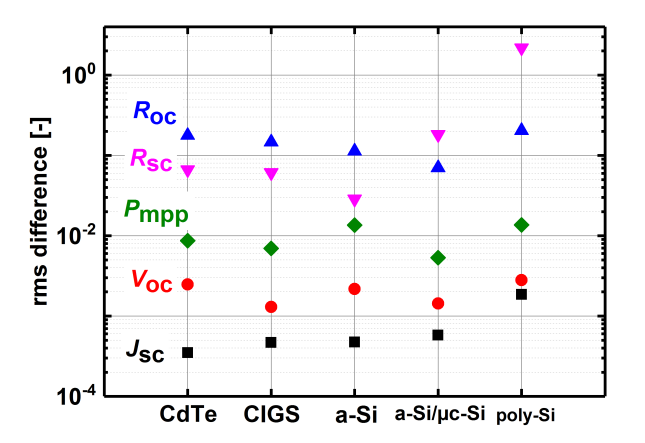


Figure 4.10. – rms difference for all technologies between the linear fits with x=1/2 and y=1/7 and the KH fit with a weighting factor of 30 in the range  $V=[V_{\min},1/2\times V_{\max}].$ 

between the KH and the linear fit is the highest compared to the other parameters. As the rms difference is below 0.2 it still can be considered as a suitable value. Also the rms difference for the two different linear fits, investigated in Table 4.1, shows this magnitude for the  $R_{\rm sc}$  fit. For poly-Si, however, the rms differences shown in Figure 4.10 do not lead to justifiable values. Here, the  $R_{\rm sc}$  difference is very high compared to the linear fit. The rms difference reaches a value above 2. Also the  $R_{\rm oc}$  value exhibits a high rms difference.

In Figure 4.11a, the absolute values for the  $R_{\rm sc}$  from the poly-Si module in Cologne are shown for the linear fit with x=1/2 and the weighted KH fit. The  $R_{\rm sc}$  is considered vs. the  $J_{\rm sc}$ . Comparing the  $R_{\rm sc}$  values from the KH and the linear fit, it can be seen that  $R_{\rm sc}$  from the KH fit show a different behavior than the  $R_{\rm sc}$  values from the linear fit, especially for high  $J_{\rm sc}$  values. This is the reason, why the rms difference for poly-Si is so high in Figure 4.10. In addition, Figure 4.11b shows the absolute  $R_{\rm oc}$  values from the KH and the linear fit (y=1/7) for the poly-Si module. It can be seen that here the  $R_{\rm oc}$  values from the KH fit are too low compared to the linear fit. This explains the high rms difference of the  $R_{\rm oc}$  for poly-Si in Figure 4.10.

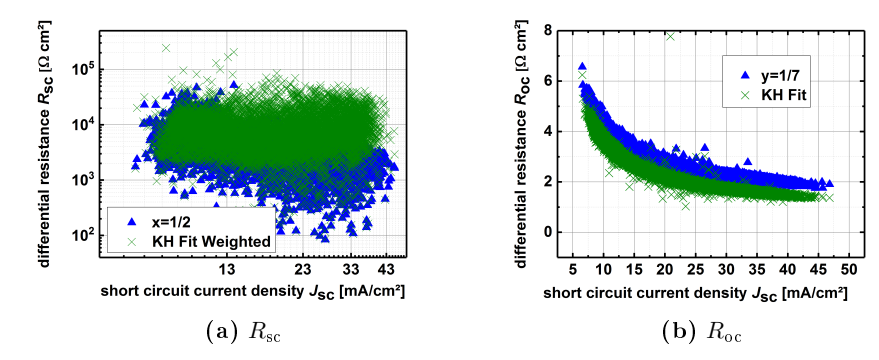


Figure 4.11. – Differential resistance determination with the KH fit (weighted with a factor of 30 in the range  $[V_{\min}, 1/2 \times V_{\text{mpp}}]$  (green crosses) and the linear fitting method (blue up-pointing triangles) with a) x = 1/2 for the  $R_{\text{sc}}$  determination and b) y = 1/7 for the  $R_{\text{oc}}$  determination

In summary, the results of the investigation of the KH parameters show that the KH fitting method with an additional weighting factor near  $J_{\rm sc}$  is a suitable method for determining the physical parameters  $R_{\rm sc}$ ,  $J_{\rm sc}$ ,  $V_{\rm oc}$ , and  $R_{\rm oc}$  from measured JV curves for thin film technologies as these parameters show only small differences compared to the linear fits. However, for crystalline Si technologies the  $R_{\rm sc}$  values are not fitted properly. For the thin film technologies, the parameterization by the KH fitting allows now a better comparison between the KH fit and other performance models like the LFM. If these models access to the same physical parameters, this enables a better comparison between the KH model as a fitting model and the LFM as a factorization model.

# 4.2. Maximum power point fitting

In Section 4.1, the parameterization for  $J_{\rm sc}$ ,  $R_{\rm sc}$ ,  $V_{\rm oc}$ , and  $R_{\rm oc}$  have been investigated. However, these are parameters describing mainly the edge of the measured JV curve. In this section, the rest of the JV curve fitting, especially the MPP, will be investigated. It should be noted that for all following KH fits in this thesis a weighting factor of 30 in the range  $[V_{\rm min}, 1/2 \times V_{\rm mpp}]$  has been used.

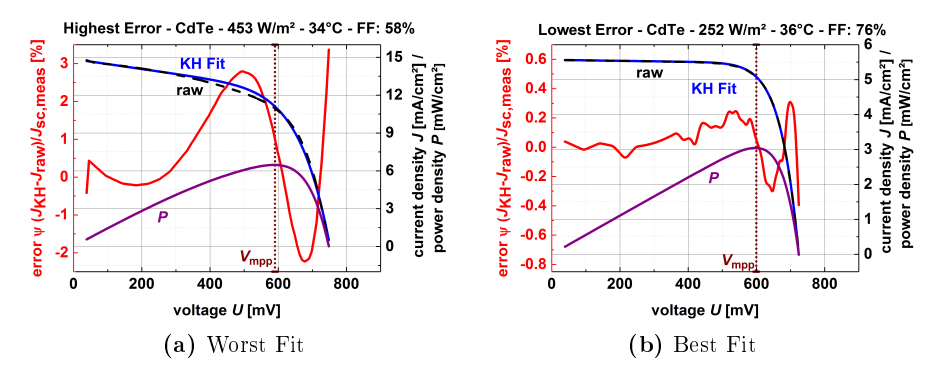


Figure 4.12. – KH fit for the JV curve of the CdTe1 module measured in Cologne. With a) the highest and b) the lowest rms error for the KH fitting method that could be achieved. Shown are the KH fit (blue line), the measured raw JV curve (black dashed line), the error  $\psi$  (red line) and the maximum power density (violet line). In addition, the vertical brown dashed line indicates the  $V_{\rm mpp}$  value.

In Figure 4.12, two JV curve fits with the KH model for the CdTe1 module in Cologne are shown. In addition, also the raw JV curves, the error  $\psi$ , and the power density (calculated from the raw data points) are shown. The error  $\psi$  of the fitted JV curve for each measure point i was calculated using

$$\psi^i = \frac{J_{\text{KH}}^i - J_{\text{raw}}^i}{J_{\text{sc.meas}}} \quad , \tag{4.4}$$

where the  $J_{\rm KH}^i$  indicates the current density at voltage i obtained from the KH fit. The symbol  $J_{\rm raw}^i$  indicates the current density at voltage i obtained from the raw JV curve, and  $J_{\rm sc,meas}$  indicates the measured  $J_{\rm sc}$  value. Here, the measured  $J_{\rm sc}$  value was calculated with a linear fit from the fitting range  $[V_{\rm min},1/2\times V_{\rm mpp}]$  as explained in Section 4.1. Figure 4.12a shows the results for the CdTe1 module measured at  $453\,{\rm W/m^2}$  and at  $34\,{\rm ^{\circ}C}$ . The fill factor was determined with the raw data and is 58%. In Figure 4.12b, the module is measured at  $252\,{\rm W/m^2}$  and at a temperature of  $36\,{\rm ^{\circ}C}$ . The fill factor of the module is 76%. It can be seen that  $\psi$  varies between 3.4% and -2.2% in Figure 4.12a, whereas in Figure 4.12b, it only varies between 0.3% and -0.4%. The KH fit in Figure 4.12a can therefore be classified as a bad fit and the fit in Figure 4.12b as good fit.

Outdoor data analysis with the Karmalkar-Haneefa model

Close to the  $J_{\rm sc}$ , both KH fits show only small deviations compared to the measured J values. This is mainly due to the weighting factor of 30 that was introduced in the section before. Small fluctuations in the  $\psi$  value, that can be seen in Figure 4.12b, are caused by noise in the measurement. Close to the open circuit, the KH fit shows increasing deviations in the J value for both fits. However, in Figure 4.12a, this effect is stronger. It has been shown in Section 4.1 that the KH fit regarding the  $V_{\rm oc}$  is very good. However, small deviations occur here, too. Deviations in the  $V_{\rm oc}$  also lead to deviations in the J value and in the slope at the open circuit. In Section 4.1, mean bias errors for the  $R_{\rm oc}$  of the KH fit have been investigated. Therefore, the  $\psi$  values close to the open circuit can be considered as a problem of the deviation in the  $R_{\rm oc}$ , i.e. the slope at the open circuit. Figure 4.12a shows the highest values in  $\psi$  compared to all investigated JV curves of the CdTe1 module in Cologne. With a maximal value for  $\psi$  of 3.4%, this maximal error in the current density is not very high.

In Figure 4.12, also the power density P is plotted (violet line) and the  $V_{\rm mpp}$  (brown dashed lined). It can be seen that around the  $P_{\rm mpp}$  two peaks for the  $\psi$  appear. In both plots, the shape around the  $P_{\rm mpp}$  is not fitted correctly and this leads then to errors in the  $P_{\rm mpp}$  determination. In the following subsections, it will be analyzed on which conditions the error of the KH fit for the whole JV curve and especially at the maximum power point depends on.

### 4.2.1. Analysis of the entire JV curve fitting

For the analysis of the entire JV curve fitting, a qualitative index for the fit is defined by the rms error. The rms error for each JV curve is defined by

rms error = 
$$\sqrt{\frac{1}{n} \sum_{i=1}^{n} \left(\frac{J_{\text{KH}}^{i} - J_{\text{raw}}^{i}}{J_{sc,\text{meas}}}\right)^{2}}$$
, (4.5)

where n is the amount of measurement points for the respective investigated JV curve. For the fit in Figure 4.12a, the highest rms error (0.15%) for all investigated JV curves of the CdTe1 module in Cologne is obtained. For the fit in Figure 4.12b, the lowest rms error (1.32e-2%) for all investigated JV curves of the CdTe1 module

in Cologne is obtained.

The shape of the JV curve is defined by the parameters  $\gamma$  and m as explained in Section 3.2. Karmalkar et~al.~[101] investigated different JV curve shapes and they derived three regions for the  $\gamma$  and m which define physical meaningful JV curve shapes. These regions can be described as

$$m \ge 0, 0 \le \gamma \le (1 - m)^{-1} \text{ for } 0 \le m < 1$$
 (4.6a)

$$-\infty \le \gamma \le \infty \text{ for } m = 1 \tag{4.6b}$$

$$-(m-1)^{-1} \le \gamma \le 1 \text{ for } m > 1$$
 (4.6c)

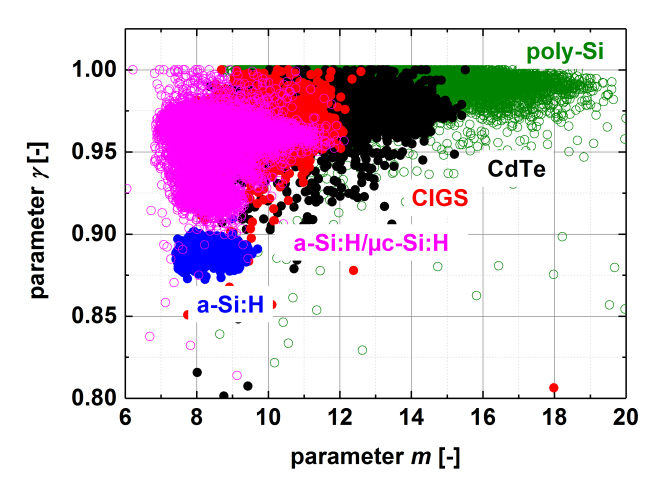


Figure 4.13. –  $\gamma$  and m values for all five solar cell technologies measured in Cologne. Each color defines one of the following technologies: a-Si:H (blue), a-Si:H/ $\mu$ c-Si:H (magenta), CIGS (red), CdTe (black), and poly-Si (green).

In Figure 4.13, the  $\gamma$  and m values are plotted for all five module technologies measured in Cologne. It can be seen that the  $\gamma$  and m values can all be described with Equation 4.6c. In addition, the  $\gamma$  value for all JV curves is bigger than zero. With this, the results are in agreement with the results of [101]. Also in [101], for

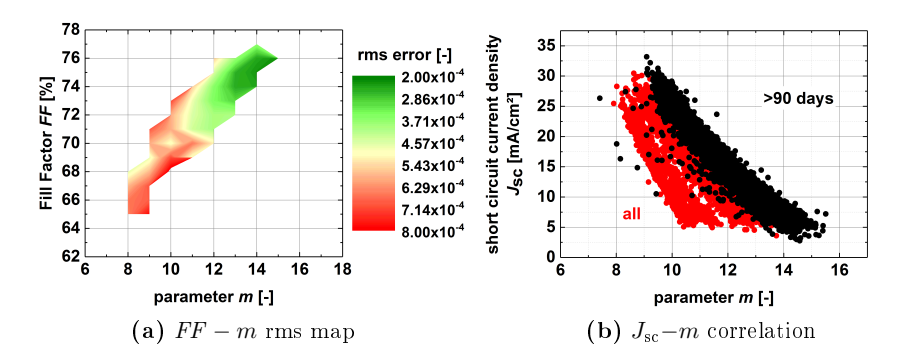


Figure 4.14. – Correlation for m with a) FF and the rms error and b)  $J_{\rm sc}$ . The data are taken from the CdTe1 module measured in Cologne.

all fitted JV curves, the  $\gamma$  and m values are in the third range (Equation 4.6c) and for all cells, except for some polymer cells,  $\gamma > 0$  was achieved. Furthermore, in Figure 4.13, also typical ranges for the different technologies can be observed. For the a-Si:H technologies, the smallest average  $\gamma$  and m values are achieved (0.889  $\pm$  0.005; 8.3  $\pm$  0.5, respectively), the highest are are achieved for poly-Si (0.99  $\pm$  0.01; 13.4  $\pm$  2.3). All other technologies lie in between those both. In ascending order for  $\gamma$ , the following values are achieved for the other technologies: a-Si:H/ $\mu$ c-Si:H (0.96  $\pm$  0.02; 8.6  $\pm$  0.8), CIGS (0.97  $\pm$  0.007; 10  $\pm$  0.9), and CdTe (0.977  $\pm$  0.008; 11.9  $\pm$  1.5). It can be seen in a general trend that high  $\gamma$  values lead to high m values as well, i.e. that cells with low  $R_{\rm oc}$  values are likely to have high  $R_{\rm sc}$  values and therefore higher fill factors. Thereby the parameter m is the factor for solar cells that influences the cells quality most (see also [101]).

In Figure 4.14a, the correlation between the m value and the FF is plotted for the CdTe1 module in Cologne. With increasing m, higher fill factors are obtained which is in agreement with [101]. Additionally, the color scale in Figure 4.14a indicates the rms error of the whole JV-curve fit. It can be seen that with higher FF and higher m, the rms error decreases.

Considering Equation 3.9 and taking into account that  $G_{oc} >> G_{sc}$ , a simplified equation for Equation 3.9 is obtained:

$$m \approx \frac{V_{\rm oc}G_{\rm oc}}{J_{\rm sc}} \quad . \tag{4.7}$$

Equation 4.7 shows that m depends mainly on  $V_{\rm oc}$ ,  $G_{\rm oc}$ , and  $J_{\rm sc}$ .

In Figure 4.14b, the correlation of m and  $J_{\rm sc}$  is plotted for CdTe. Considering all data (red dots), no clear correlation can be observed between  $J_{\rm sc}$  and m. However, if only measured JV curves after the first 90 days are considered, the correlation between  $J_{\rm sc}$  and m becomes more clear. With increasing  $J_{\rm sc}$ , m is clearly decreasing. This indicates that metastable effects that occur at the beginning of the outdoor exposure have a high impact in the first days and lead to a different correlation between  $J_{\rm sc}$  and m compared to long term JV data. By excluding the data from the first 90 days, especially the low m values are excluded and the rms values are increasing in general. Further details can be found in Appendix B. As m shows a correlation to the rms error of the KH fit and m shows an inverse proportional behavior to  $J_{\rm sc}$ , in the following, it will be investigated how  $J_{\rm sc}$  and the rms error are correlated to each other.

From all investigated parameters, the  $J_{\rm sc}$  value shows the clearest correlation to the rms error of the KH fit for all investigated single junction solar technologies. Figure 4.15 shows the results for the  $J_{\rm sc}$  and rms error correlation for all measured technologies in Cologne. The results for the CdTe1 module are shown in Figure 4.15a. For CdTe, only JV curves after the first 90 days are investigated (Figure 4.15a). It can be seen that the rms error increases with  $J_{\rm sc}$ . The same results are obtained for the poly-Si modules (see Figure 4.15b). For CIGS, the fluctuation of the rms error could be reduced as well by considering only values measured after the first 90 days. Here, Figure 4.15c shows that for  $J_{\rm sc}$  values greater than  $16\,{\rm mA/cm^2}$ , the rms error increases with  $J_{\rm sc}$ . However, the minimum rms is obtained around  $14\,{\rm mA/cm^2}$ – $16\,{\rm mA/cm^2}$ . For  $J_{\rm sc}$  values lower  $14\,{\rm mA/cm^2}$ , the rms error is decreasing with  $J_{\rm sc}$ . For a-Si:H modules, it can be observed that higher  $J_{\rm sc}$  values lead to lower rms values (see Figure 4.15d).

For the tandem module  $a\text{-Si:H}/\mu\text{c-Si:H}$ , no clear trend for the rms error depending on  $J_{\text{sc}}$  is obtained (see Figure 4.15e). A trend for the rms error can be observed if only  $\gamma$  values < 0.95 are considered. For small  $\gamma$  values, the rms error is decreasing with  $J_{\text{sc}}$ . The  $\gamma$  value has for the  $a\text{-Si:H}/\mu\text{c-Si:H}$  module a much higher

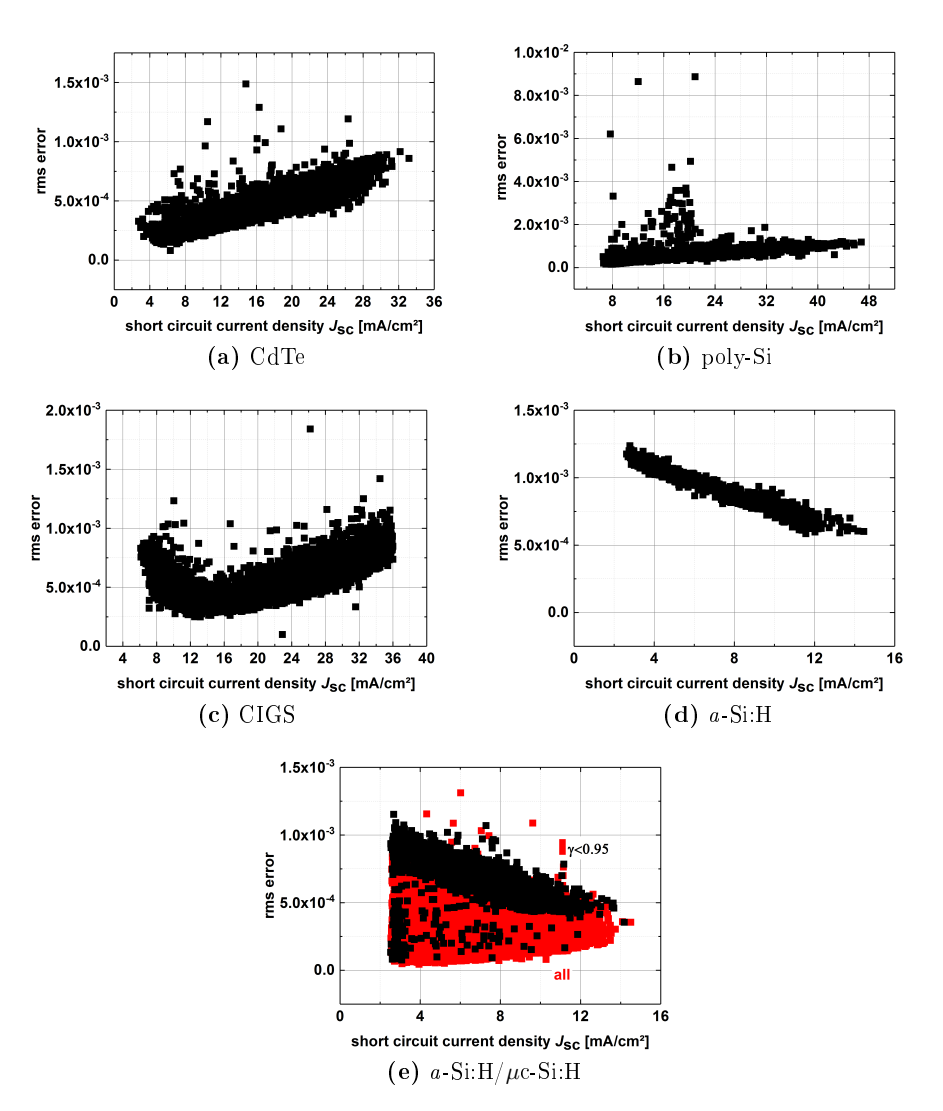


Figure 4.15. – Correlation between  $J_{\rm sc}$  and the rms error of the KH fit for the whole JV curve measured in Cologne for a) CdTe (>90 days), b) poly-Si, c) CIGS (>90 days), d) a-Si:H, and e) a-Si:H/ $\mu$ c-Si:H.

impact on the rms error than for the other technologies. It was already shown in Figure 4.13 that for the a-Si:H/ $\mu$ c-Si:H module the value distribution of  $\gamma$  is the highest for all investigated technologies.

It has been shown that the rms error of the KH fit for all single junction technologies shows a dependency on  $J_{\rm sc}$  and hence also on the irradiance. Whereas c-Si and CdTe technologies show a better fit at low irradiance, a-Si:H shows better fits at high irradiance. For CIGS a mixed trend is observed. Before the influence of this result is investigated further, the results of the KH fit for the entire JV curve are compared to the one-diode model (see Section 2.2.2).

## 4.2.2. Comparison of the KH fit with the one-diode model

In this thesis, the Lambert W form for the one-diode model has been used (see Equation 2.22). The parameters were determined with an unconstrained nonlinear optimizer and for the error metric the rms error was chosen with

rms error = 
$$\sqrt{\frac{1}{n} \sum_{i=1}^{n} \left(J_{\text{Diode}}^{i} - J_{\text{raw}}^{i}\right)^{2}}$$
, (4.8)

where  $J_{\text{Diode}}^{i}$  indicates the current density at voltage i obtained from the one-diode model fit.

As an example, the same JV curve as plotted in Figure 4.12a was fitted with the one-diode model. The  $\psi$  value shows that the fit at the MPP is not very good. In addition, compared to the KH fit, the fit with the one-diode model is not good around the  $J_{\rm sc}$  either.

For a general comparison between the one-diode model and the KH fit for all technologies measured in Cologne, the mean and standard deviation for the rms error are compared with each other in Table 4.2. It can be seen that for the poly-Si module the best results are obtained with the one-diode model and the worst with the KH model. For all other thin film technologies, the KH fit shows better results for the whole JV curve than the one-diode model. The best fit is achieved for the tandem module. The CdTe module shows also a very low rms error. As explained before, the rms error for the KH fit gets for CdTe and CIGS worse with increasing irradiance. Considering Tempe, where the highest irradiance for all locations have been measured, the average rms error for the KH fit increases for both technologies. For the CdTe1 and CIGS1 module a rms error of  $6.12 \times 10^{-2}\%$  and  $7.02 \times 10^{-2}\%$ 

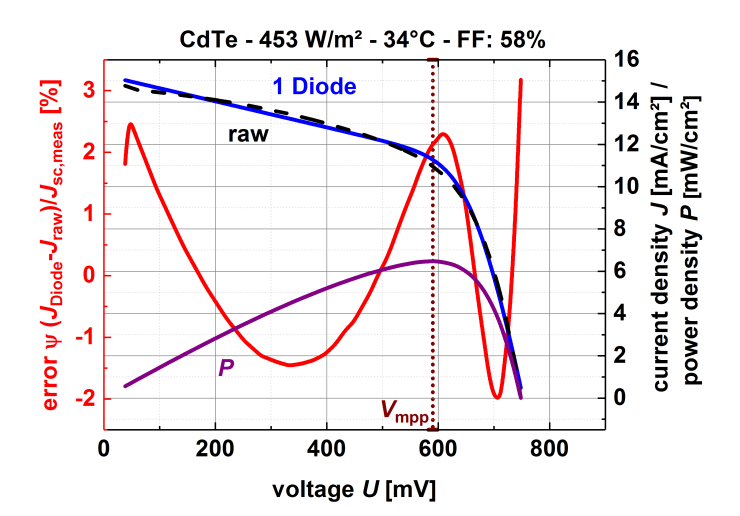


Figure 4.16. – JV curve fit with the one-diode model for the CdTe1 module measured in Cologne. It should be noted that the same JV curve shown in Figure 4.12a was taken. Shown are the one-diode fit (blue line), the measured raw JV curve (black dashed line), the error  $\psi$  (red line), and the maximum power density (violet line). In addition, the brown dashed line indicates the  $V_{\rm mpp}$  value.

is achieved, respectively, for the KH fit, whereas for the one-diode model the rms error for CdTe1 and CIGS1 is  $6.89 \times 10^{-2} \%$  and  $4.32 \times 10^{-2} \%$ , respectively.

In general, this means that the KH fit is for thin film technologies such as a-Si:H, CdTe, and a-Si:H $/\mu$ c-Si:H modules in average a better fitting model than the one-diode model, whereas for poly-Si technologies the one-diode model works better. For CIGS, the KH fit is a better fitting model for locations with low irradiance and the one-diode model is a better fit for locations with high irradiance.

As described before, the rms error of the KH fit depends on the  $J_{\rm sc}$  for the investigated technologies. For the one-diode model, the rms error of the investigated JV curve fit does not show any dependence on  $J_{\rm sc}$ , temperature or other environmental conditions. Regarding the KH model, the question arises if the dependence of the rms error on  $J_{\rm sc}$  has an influence on the KH fit at the MPP. This will be investigated in the following subsection.

**Table 4.2.** – Comparison between the rms error and the standard deviation (std) between the KH fit and the one-diode model for all five investigated technologies measured in Cologne.

	RMS erro	r for the	RMS Error for the	
technology	KH Fit		one-diode model	
	mean [%]	std [%]]	mean [%]	std [%]]
a-Si:H/μc-Si:H	$4.09 \times 10^{-2}$	$2.19 \times 10^{-2}$	$1.9 \times 10^{-1}$	$4.3 \times 10^{-2}$
a-Si:H	$5.39 \times 10^{-2}$	$1.73 \times 10^{-2}$	$8.72 \times 10^{-2}$	$2.08 \times 10^{-2}$
CdTe	$4.25 \times 10^{-2}$	$1.66 \times 10^{-2}$	$8.56 \times 10^{-2}$	$1.53 \times 10^{-2}$
CIGS	$5.24 \times 10^{-2}$	$1.55 \times 10^{-2}$	$7.09 \times 10^{-2}$	$1.83 \times 10^{-2}$
poly-Si	$5.95 \times 10^{-2}$	$2.8 \times 10^{-2}$	$3.87 \times 10^{-2}$	$5.15\times10^{-5}$

#### 4.2.3. Analysis of the fit at the MPP

For the analysis of the fit at the MPP, in Figure 4.17, the relation of the measured and the fitted maximum power density obtained from the KH model and the one-diode model are shown. As an example, the CdTe1 and the CIGS1 modules measured in Cologne are shown here. The results for all other technologies can be found in Appendix B. The raw maximum power point density  $P_{\rm mpp, fat}$  is normalized to the fitted maximum power point density  $P_{\rm mpp, fit}$ . For an ideal fit, the result of this normalization would be equal to one. It can be seen that for CdTe the accuracy of the  $P_{\rm mpp, fit}$  of the KH model depends linearly on  $P_{\rm mpp, raw}$ , i.e. with increasing  $P_{\rm mpp}$  the fit of the maximum power density gets worse. This relation is in agreement with previously obtained result that the rms error of the KH fit for the whole JV curve depends on  $J_{\rm sc}$  as the power density depends also linearly on  $J_{\rm sc}$ .

For all investigated single junction technologies, one obtains for  $P_{\rm mpp,KH}$  a linear relationship for the normalized  $P_{\rm mpp,raw}$  value. Only for the tandem module this behavior is not very clear (see Appendix B for more details). The technologies differ from each other when consider where  $P_{\rm mpp,KH}$  is closest to the raw  $P_{\rm mpp}$ . For poly-Si and CdTe, the  $P_{\rm mpp}$  fit is best for low  $P_{\rm mpp}$  (or low irradiance), whereas for a-Si:H the  $P_{\rm mpp}$  fit is best for high  $P_{\rm mpp}$  (or high irradiance). For CIGS, a medium  $P_{\rm mpp}$  is best. Similar to the one-diode model, the fitted  $P_{\rm mpp}$  for CIGS shows a strong error increase for too low  $P_{\rm mpp}$ . In general, it can be said that for the error in  $P_{\rm mpp}$ , a similar trend as for the total fit error is obtained as shown in the previous subsection.

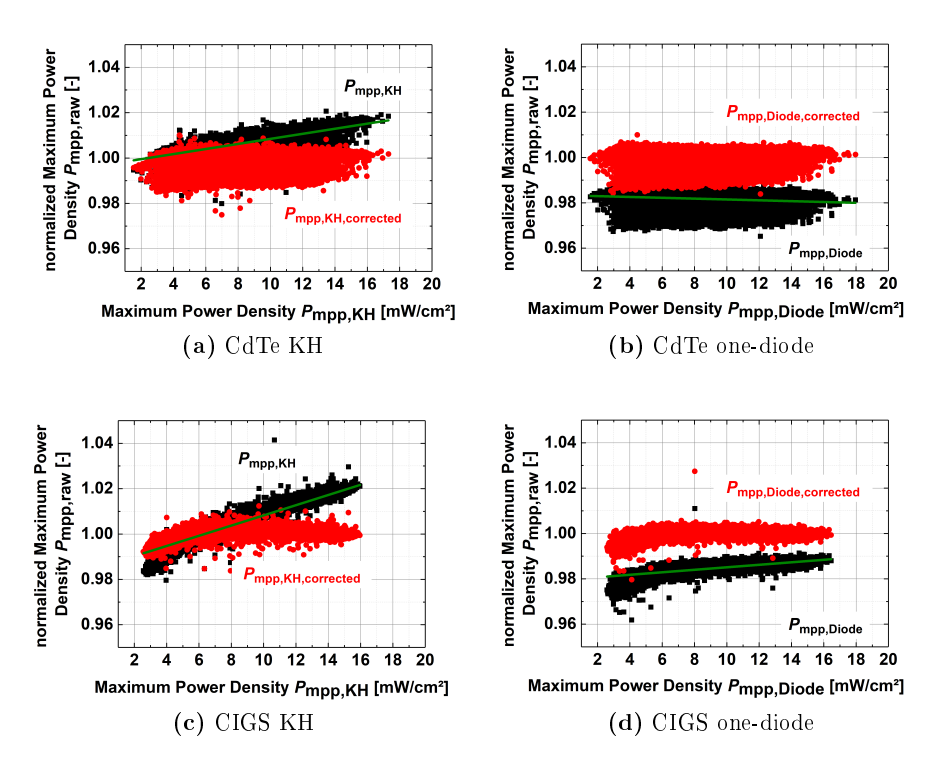


Figure 4.17. – Uncorrected (black squares) and corrected (red dots)  $P_{\rm mpp}$  fits for the CdTe and CIGS modules measured in Cologne. The plots show the  $P_{\rm mpp,raw}/P_{\rm mpp,fit}$  as a function of  $P_{\rm mpp,fit}$ . The green line indicates the linear correction polynom. a) shows the results for the CdTe1 module fitted with the KH method, b) the CdTe1 module fitted with the one-diode model, c) the CiGS1 module fitted with the KH model, and d) the CiGS1 module fitted with the one-diode model.

The one-diode model shows for the MPP fit for all technologies rather an offset error than a linear relationship like the KH model. However, to improve the MPP fit for both models, a linear correction factor was introduced as in [103]. For this, the following fit equation from Ulbrich et al. [103] was used for all technologies:

$$\frac{P_{\text{mpp,raw}}}{P_{\text{mpp,fit}}} = a + bP_{\text{mpp,fit}} \quad , \tag{4.9}$$

whereas a and b are fitting coefficients. This equation is independent of the time

during which the modules are measured and is therefore applied on all data for each technology. The fit of Equation 4.9 is also plotted in Figure 4.17.

In a next step, the resulting fitted  $P_{\text{mpp,fit}}$  can then be corrected by

$$P_{\text{mpp,corr}} = aP_{\text{mpp,fit}} + b^2 P_{\text{mpp,fit}} . (4.10)$$

This  $P_{\rm mpp}$  correction can be understood as an optional 6th and 7th parameter for the KH fit, when the weighting factor introduced in Section 4.1 is considered as the 5th parameter in addition to the normal four KH parameters. However, the correction can also be used to improve the one-diode fit.

In Figure 4.18, the comparison between the  $P_{\rm mpp}$  fit with and without correction for all five technologies fitted with the KH model as well as the one-diode model are shown. The mean fit error was determined by

mean fit error = 
$$\frac{1}{n} \sum_{i=1}^{n} \left| 1 - \frac{P_{\text{mpp,raw,i}}}{P_{\text{mpp,fit,i}}} \right| \times 100 . \tag{4.11}$$

For all thin film technologies, the mean fit error of  $P_{\rm mpp}$  for the KH model is smaller than the one for the one-diode model. The highest mean fit error with the KH fit for the thin-film technologies is obtained for a-Si:H with 1.3%. However, after the  $P_{\rm mpp}$  correction with Equation 4.10, the errors for both models are close to zero.

In this section, it could be shown that the KH fit is recommended for thin film but not for crystalline Si technologies. Based on these results, in the further analysis, the KH fit analysis is done only for the four thin film technologies. The  $P_{\rm mpp}$  correction is optional.

# 4.3. Parameter analysis

Considering the four step process, the parameter analysis follows after the parameterization step (see Section 2.2.4). In this section, the parameter analysis step of the KH model and the LFM are investigated. For both models, the  $V_{\rm oc}$ ,  $R_{\rm oc}$ ,  $J_{\rm sc}$ , and  $R_{\rm sc}$  values are determined with the KH method (see Section 4.1). This way,

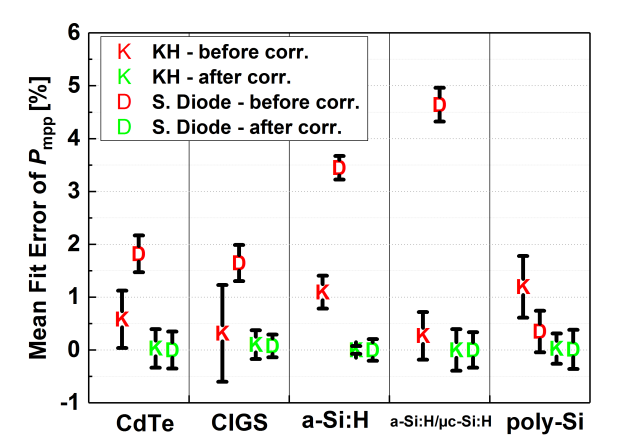


Figure 4.18. – Mean fitting error with standard deviation for the  $P_{\rm mpp}$  for all technologies.

differences in the parameter analysis with the LFM and KH model are not affected by the parametrization step.

For the parameter analysis, the dependence of irradiance and temperature on the individual parameters are investigated. In the investigated data set, the plane of array irradiance  $\phi$  and back-of-module temperature T are available.

In the following, first the parameter analysis of the KH model is investigated. Then the parameter analysis of the LFM is considered, and finally, the parameter analysis of both models are compared with each other.

## 4.3.1. Parameter analysis for the KH model

For the KH model, the dependencies on irradiance and temperature for the four KH parameters are described as [103]:

$$J_{\text{sc.meas}}(\phi_{\text{meas}}, T_{\text{meas}}) = \{\alpha_{\text{Jsc}} T_{\text{meas}} + \kappa_{\text{Jsc}}\} \phi_{\text{meas}}$$
(4.12)

$$G_{\rm sc,meas} \left( J_{\rm sc,meas}, T_{\rm meas} \right) = G_{\rm sc,0} + \alpha_{\rm Gsc} T_{\rm meas} + \kappa_{\rm Gsc} J_{\rm sc,meas}$$
 (4.13)

$$V_{\text{oc,meas}}(J_{\text{sc,meas}}, T_{\text{meas}}) = V_{\text{oc}}^0 - \{\alpha_{\text{Voc}} - \varepsilon_{\text{Voc}} \log(J_{\text{sc,meas}})\}T_{\text{meas}}$$
 (4.14)

$$R_{\text{oc,meas}}(J_{\text{sc,meas}}, T_{\text{meas}}) = R_{\text{s}} + \beta_{\text{Roc}} T_{\text{meas}} / J_{\text{sc,meas}} + \alpha_{\text{Roc}} T_{\text{meas}},$$
 (4.15)

with the temperature coefficient  $\alpha$ , where  $\alpha_{\rm Jsc}$  also describes a dependence on  $\phi$ , the irradiance coefficient  $\varepsilon$  describing the dependence on  $\log{(J_{\rm sc})}$  and T, the coefficient  $\beta$  describing the dependence on  $T/J_{\rm sc}$ , and the constants  $G_{\rm sc,0}$ ,  $V_{\rm oc}^0$ , and  $R_{\rm s}$ . The index "meas" stands for measured values.

To translate the measured  $J_{\rm sc}$  values to the reference value  $J_{\rm sc,ref}$  at the conditions  $T_{\rm ref}$  and  $\phi_{ref}$ , one takes Equation 4.12 once with the reference values and once with the measured values, calculate the difference and add it to  $J_{\rm sc,meas}$  as

$$J_{\text{sc,Tref,}\phi\text{ref}} = J_{\text{sc, meas}} + \left[J_{\text{sc, meas}}\left(\phi_{\text{ref}}, T_{\text{ref}}\right) - J_{\text{sc, meas}}\left(\phi_{\text{meas}}, T_{\text{meas}}\right)\right] \quad . \tag{4.16}$$

Then, after translation one obtains

$$J_{\text{sc,Tref},\phi_{\text{ref}}} = J_{\text{sc, meas}} + \alpha_{\text{Jsc}} \left( T_{\text{ref}} \phi_{\text{ref}} - T_{\text{meas}} \phi_{\text{meas}} \right) + \kappa_{\text{Jsc}} \left( \phi_{\text{ref}} - \phi_{\text{meas}} \right) .$$

$$(4.17)$$

For the other three parameters ( $V_{\rm oc}$ ,  $R_{\rm oc}$ ,  $G_{\rm sc}$ ), the dependence on the irradiance  $\phi_{\rm meas}$  is substituted by  $J_{\rm sc,meas}$ . This is done to reduce the uncertainty due to variations in the spectrum. The spectrum changes with location and seasons [113]. The variation of the spectrum influences the performance of the technologies depending on their spectrum response [114]. The interdependence of  $J_{\rm sc}$  and  $\phi$  allows to substitute  $\phi$  with  $J_{\rm sc}$ . By taking  $J_{\rm sc}$  instead of  $\phi$ , the problems of changing spectra are solved. This approach is similar to the effective irradiance method for the SAPM by using a predetermined array  $J_{\rm sc}$  [72].

Figure 4.19 shows exemplary results for the translation of  $J_{\rm sc}$  to STC. The data are taken from the CIGS1 module measured in Italy at the last three recorded days (29th of July 2016 to 31st of July 2016), i.e. at the end of the outdoor exposure time. Shown are the raw or measured  $J_{\rm sc}$  data (black squares), the  $J_{\rm sc}$  corrected to standard temperature (red dots), and the  $J_{\rm sc}$  data corrected to standard irradiance

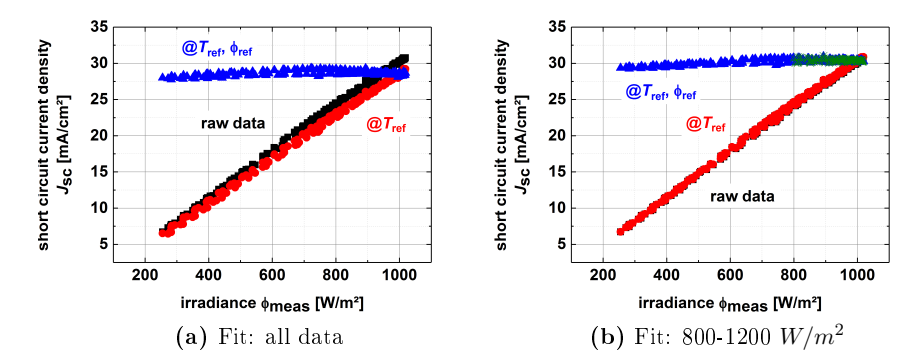


Figure 4.19. – Translation of  $J_{\rm sc}$  to STC using different fitting ranges: a) all data are used for the fit and b) only data in the range  $800\,{\rm W/m^2} \le \phi \le 1200\,{\rm W/m^2}$  (green dots) are used. Data are taken from the CIGS1 module measured in Italy during 29th of July 2016 to 31st of July 2016.

and temperature (blue triangles). In Figure 4.19, the influence of the data on the parameter fitting for the translation equations is investigated.

In Figure 4.19a, all available data are taken for the fit. First, the data are fitted to Equation 4.12 to determine  $\alpha_{\rm Jsc}$  and  $\kappa_{\rm Jsc}$ . Afterwards, the reference data are calculated using Equation 4.17 and ST conditions for  $\phi_{\rm ref}$  and  $T_{\rm ref}$ . For the translation to  $T_{\rm ref}$ , only the first part of Equation 4.17 is taken. It can be seen that the  $J_{\rm sc}$  data corrected to standard temperature differ for high irradiance strongly from the raw data which is not usual for  $J_{\rm sc}$  as  $J_{\rm sc}$  normally only shows a weak dependence on T. This observed behavior can be traced back to fitting procedure of the temperature coefficient. Low irradiance and temperature are measured normally during the morning and evening. However, during this time also spectral shift occurs. This effect leads to a shift in the linear constant  $\alpha_{\rm Jsc}$ . Due to more measurement points in the evening and morning, the T fit described as

$$J_{\rm sc} \left( \phi_{\rm meas}, T_{\rm ref} \right) = \alpha_{\rm Jsc} T_{\rm meas} \phi_{\rm meas} \tag{4.18}$$

leads to an underestimation of  $J_{\rm sc}$  ( $\phi_{\rm meas}, T_{\rm ref}$ ) at high irradiance. The  $J_{\rm ref}$  is determined as  $28.6\,{\rm mA/cm^2}$ . In addition, also the translation to  $\phi_{ref}$  shows a non-linear behavior at low irradiance. This may occurs due to defects that have a higher impact

at low irradiance than at high irradiance. However, the influence of the non-linear behavior at low irradiance for the  $J_{\rm sc}$  cannot be described by Equation 4.12. To obtain translated reference values that are not influenced by non-linear effects at low irradiance, the fit with Equation 4.12 was in Figure 4.19b only done for high irradiance (800 W/m<sup>2</sup>  $\leq \phi \leq 1200$  W/m<sup>2</sup>) and high temperature ( $T \geq 25$  °C). Such filtering is common in PV performance modeling. In addition, for many PV performance models the coefficient determination is done also at clear-sky conditions [78]. The filtering for high irradiance and temperature leads to a better fit for the STC values. Now it can be seen that the  $J_{\rm sc}$  data corrected to standard temperature do not differ much from the raw data. In addition, between 800 - 1200 W/m<sup>2</sup> the translated values to STC are flat. Still at the low irradiance, the non-linear behavior is obvious. This filtering process to determine the coefficients of the translation equations is also used in the following for the remaining three KH parameters to determine the coefficients in Equation 4.13 to 4.15.

After the coefficients of Equation 4.13 to 4.15 were obtained, the measured values of the parameters  $G_{\rm sc}$ ,  $R_{\rm oc}$ , and  $V_{\rm oc}$  were translated to ST conditions analog to Equation 4.16. Transforming the respective equations leads to:

$$G_{\text{sc.ref}} = G_{\text{sc.meas}} + \alpha_{\text{Gsc}} (T_{\text{ref}} - T_{\text{meas}}) + \kappa_{\text{Gsc}} (J_{\text{sc.ref}} - J_{\text{sc.meas}})$$
 (4.19)

$$V_{\text{oc,ref}} = V_{\text{meas}} - \{\alpha_{\text{Voc}} - \varepsilon_{\text{Voc}} \log (J_{\text{sc,meas}})\} (T_{\text{ref}} - T_{\text{meas}}) + \varepsilon_{\text{Voc}} \log \left(\frac{J_{\text{sc,ref}}}{J_{\text{sc,meas}}}\right) T_{\text{ref}}$$

$$(4.20)$$

$$R_{\text{oc,ref}} = R_{\text{oc,meas}} - \beta_{\text{Roc}} \left( T_{\text{meas}} / J_{\text{sc,meas}} - T_{\text{ref}} / J_{\text{sc,ref}} \right)$$

$$- \alpha_{\text{Roc}} \left( T_{\text{sc,meas}} - T_{\text{sc,ref}} \right)$$

$$(4.21)$$

The parameter  $J_{\text{sc,ref}}$  is obtained by fitting Equation 4.12 to the data of the first week and subsequently determining  $J_{\text{sc,meas}}$  ( $\phi_{\text{ref}}$ ,  $T_{\text{ref}}$ ) by using again Equation 4.12.

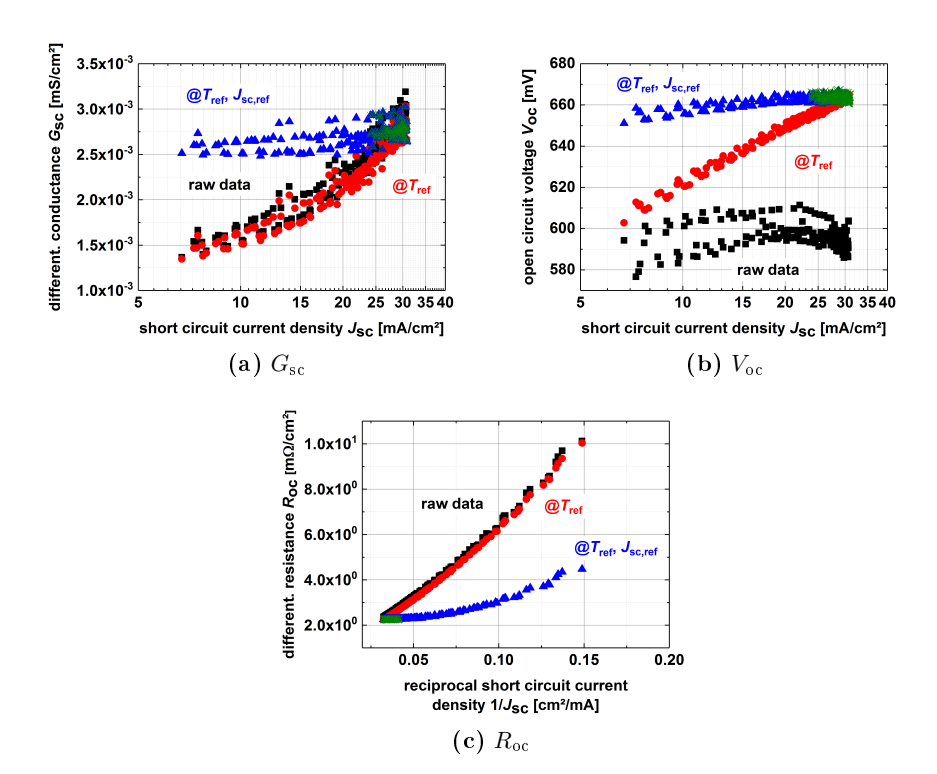


Figure 4.20. – Translation of a)  $G_{\rm sc}$  b)  $V_{\rm oc}$  and c)  $R_{\rm oc}$  to STC. The data are taken from the CIGS1 module measured in Italy during 29th of July 2016 to 31st of July 2016.

This value is then used as  $J_{\text{sc,ref}}$  for all other time intervals to determine the parameters in Equation 4.19 to 4.21.

The results of the translated  $G_{\rm sc}$ ,  $R_{\rm oc}$ , and  $V_{\rm oc}$  values are shown in Figure 4.20. The green dots indicate the fitting range. Shown are the respective raw data, the translation to standard temperature, and the translation to standard temperature and  $J_{\rm sc,ref}$ .

Equation 4.13 describes  $G_{\rm sc}$  in dependence of T and  $J_{\rm sc}$ . In an ideal solar cell,  $G_{\rm sc}$  would not depend much on  $J_{\rm sc}$ . However, in Figure 4.20a a strong correlation between  $G_{\rm sc}$  and  $J_{\rm sc}$  can be observed. The strong correlation between  $J_{\rm sc}$  and  $J_{\rm sc}$  can be explained with voltage-dependent photocurrent collection [103, 115]. This

effect is especially important for thin film technologies [116]. Here, the photocurrent  $J_{\rm ph}$  at a given voltage  $V_i$  can be described as [115]

$$J_{\rm ph}\left(V_{i}\right) = J_{\rm ph}^{\rm max} \times \eta_{\rm c}\left(V_{i}\right) \quad , \tag{4.22}$$

where  $J_{\rm ph}^{\rm max}$  is the maximum photocurrent with complete collection, which can be obtained at a sufficiently large reverse bias [115]. The photocurrent  $J_{\rm ph}$  depends linearly on  $\phi$ . The value  $\eta_{\rm c}$  ( $V_i$ ) describes the voltage dependent collection efficiency. At low forward bias,  $\eta_{\rm c}$  ( $V_i$ ) can vary from 1 to 0 [115]. However, as in Section 2.2 explained, at high voltages the JV characteristics of the illuminated cell can also crosses the dark JV curve. In this case,  $\eta_{\rm c}$  ( $V_i$ ) can also achieve negative values.

In Figure 4.20b, the results for the translated  $V_{\rm oc}$  values are shown. Equation 4.14 for the  $V_{\rm oc}$  fitting is derived from the standard diode equation of an illuminated cell with [117] (see also Section 2.2.2):

$$J = J_{\rm sc} - J_0 \left[ \exp\left(\frac{qV}{n_{\rm id}kT}\right) - 1 \right] , \qquad (4.23)$$

and substituting  $J_0$  with [118]

$$J_0 = J_{00} \exp\left(\frac{-E_a}{n_{\rm id}kT}\right) ,$$
 (4.24)

with  $E_a$  the activation energy and  $J_{00}$  the weakly temperature-dependent reference current density. For  $V_{\text{oc}}$ , this leads to the expression

$$V_{\rm oc} = E_a/q - n_{\rm id}kT/q \times \log(J_{00}) + n_{\rm id}kT/q \times \log(J_{sc}) \quad . \tag{4.25}$$

This means that  $E_a/q = V_{oc}^0$ ,  $n_{id}k/q \times \log(J_{00}) = \alpha_{Voc}$ , and  $n_{id}k/q = \varepsilon_{Voc}$ .

In Figure 4.20b, the  $V_{\rm oc}$  data are plotted as a function of  $J_{\rm sc}$ . It can be seen that the  $V_{\rm oc}$  data that are translated to STC are not all lying on a horizontal line. However, at a  $J_{\rm sc}$  value above  $23\,{\rm mA/cm^2}$ , a more or less constant  $V_{\rm oc}$  value for STC can be observed (green crosses in Figure 4.20b). For  $J_{\rm sc}$  values lower than  $23\,{\rm mA/cm^2}$ , the  $V_{\rm oc}$  increases with the short circuit current density. The deviation of the constant  $V_{\rm oc}$  value at low  $J_{\rm sc}$  values occurs due to a not pure logarithmic behavior between  $J_{\rm sc}$  and  $V_{\rm oc}$  for the full irradiance range. For low irradiance, the

Outdoor data analysis with the Karmalkar-Haneefa model

behavior ( $V_{\rm oc}$  vs.  $\log J_{\rm sc}$ ) can be described with a "double-exponential" or "double-logarithmic" behavior [103]. The double-logarithmic behavior is known for many solar cells [119] and can be described with the two diode model as explained in Section 2.2.2.

An explanation for the double-logarithmic behavior can be defects that have a higher influence at low irradiance than at high irradiance. As the data in Figure 4.20b are derived from a module that was exposed for a long time outdoor, degradation effects are a plausible explanation. However, the results from Figure 4.20b show that analyzing thin-film technologies over a long time range leads to the fact, that Equation 4.14 works well for high irradiance, but not well for low irradiance ranges.

Finally, in Figure 4.20c, the results for  $R_{\rm oc}$  are shown. The respective Equation 4.15 derives from Werner *et al.* [120]. Here, the differential resistance under forward bias is described as:

$$R_{\rm oc} = \frac{n_{\rm id}kT}{q} \frac{1}{J_{sc}} + R_{s,tot} \quad . \tag{4.26}$$

The first term describes the influence of the differential diode resistance and the second the influence of the linear resistance. Considering that the linear resistance depends also on T and set  $\frac{n_{\rm id}k}{q}=\beta_{Roc}$  leads to Equation 4.15. In Figure 4.20c, it is obvious that  $R_{\rm oc}$  depends strongly on  $1/J_{\rm sc}$ . This is due to the differential diode resistance. Similar to  $V_{\rm oc}$ , the corrected values to STC show a constant value for high irradiance (green crosses). However, for low irradiance another slope appears. This may also be explained with the "doubel-exponential" behavior as already described for  $V_{\rm oc}$ . Again, this cannot be described by the fitting equation Equation 4.21 as this equation is based on the single-diode equation.

In summary, the KH model is described with four parameters. For the translation of the parameters, two coefficients for  $J_{\rm sc}$  and respective three coefficients for the other three parameters are necessary. So in total 11 coefficients are necessary for the parameter analysis. In the following, the parameter analysis of the LFM is investigated.

#### 4.3.2. Parameter analysis for the LFM

In this thesis, the LFM-A version of the Loss Factor Model is taken, as explained in Section 3.3. Contrary to the one step T and  $\phi$  translation used for the KH model, the LFM uses a two step procedure. First, the T translation follows with Equation 3.18. This leads to Equation 3.21, 3.23, and 3.22. The translation equations to  $T_{ref}$  for the five parameters are then:

$$J_{\rm sc,Tref} = \frac{J_{sc}^{\rm m}/G_i}{T_{\rm corr,Jsc}}$$
(4.27)

$$V_{\text{oc,Tref}} = \frac{V_{\text{oc}}^{\text{m}}}{T_{\text{corr,Voc}}} \tag{4.28}$$

$$G_{\rm sc,Tref} = \frac{J_{\rm sc,Tref} \left( 1 - R_{sc}^{\rm n} \right)}{R_{oc}^{\rm n} V_{\rm oc,Tref}}$$

$$\tag{4.29}$$

$$R_{\text{oc,Tref}} = \frac{V_{\text{oc,Tref}} \left(1 - R_{oc}^{\text{n}}\right)}{R_{sc}^{\text{n}} J_{\text{sc,Tref}}}$$

$$\tag{4.30}$$

$$FF_{\text{Tref}} = \frac{FF^{\text{m}}}{T_{\text{corr} FF}} \times R_{sc}^{\text{n}} \times R_{\text{oc}}^{\text{n}} . \tag{4.31}$$

 $G_i$  is the normalized plane of array irradiance and is defined as

$$G_i = \frac{\phi_{\text{meas}}}{\phi_{\text{ref}}} \quad . \tag{4.32}$$

The temperature translation can be done without any reference value. In this work,  $\phi > 800\,\mathrm{W/m^2}$  and  $T > 25\,^\circ\mathrm{C}$  are used to determine the temperature coefficients  $\alpha_\mathrm{Jsc}$ ,  $\alpha_\mathrm{Voc}$ , and  $\alpha_\mathrm{FF}$ . Note that [112] filters data that were measured within an hour of solar noon, under clear sky conditions and under  $\phi > 500\,\mathrm{W/m^2}$  and  $T > 25\,^\circ\mathrm{C}$  to determine these temperature coefficients. For the investigated data set, it cannot be determined which data set corresponds to clear sky and solar noon conditions. However, it is expected that the conditions  $\phi > 800\,\mathrm{W/m^2}$  and  $T > 25\,^\circ\mathrm{C}$  will correspond predominantly to clear sky and solar noon conditions.

After the translation to  $T_{\rm ref}$ , the translation to  $\phi_{\rm ref}$  is done for the parameters. For this, Equation 3.24 is used. For  $J_{\rm sc}$ ,  $V_{\rm oc}$ , and FF Equation 3.24 requires the respective reference values. However, as no reference values for the single modules are

Outdoor data analysis with the Karmalkar-Haneefa model

available, the respective reference value is included in the fitting equation according to:

$$f_n(G_i) = c_1 + c_2 \times \log G_i - c_3 \times G_i^2$$

$$\Leftrightarrow J_{\text{sc,Tref}} = J_{\text{sc,ref}} \times \left(c_1 + c_2 \cdot \log G_i - c_3 \times G_i^2\right)$$

$$\Rightarrow J_{\text{sc,Tref}} = C_1 + C_2 \times \log G_i - C_3 \times G_i^2 . \tag{4.33}$$

The fitting equations for  $V_{\rm oc}$  and FF follow analog. For  $R_{\rm oc}^{\rm n}$  and  $R_{\rm sc}^{\rm n}$ , the two additional fitting equations

$$R_{\text{oc}}^{\text{n}} = c_1 + c_2 \times \log G_i - c_3 \times G_i^2 \tag{4.34}$$

$$R_{\rm sc}^{\rm n} = c_1 + c_2 \times \log G_i - c_3 \times G_i^2 \tag{4.35}$$

are used. To transform from the  $C_i$  values to the LFM  $c_i$  values, the relation

$$c_i = \frac{C_i}{C_1 - C_3} \tag{4.36}$$

is used. For the parameters  $J_{\rm sc}^{\rm n}$  and  $V_{\rm oc}^{\rm n}$ , the fitting conditions as described in [78] are set as  $c_1 \leq 1 \pm 0.1$  and  $c_{2,3} \leq 0 \pm 0.1$ . Finally, the translation equation for  $J_{\rm sc}$  to the reference conditions  $\phi_{\rm ref}$  and  $T_{\rm ref}$  is:

$$J_{\text{sc,Tref},\phi\text{ref}} = \frac{J_{\text{sc,Tref}}}{c_1 + c_2 \times \log G_i - c_3 \times G_i^2}$$

$$= \frac{J_{\text{sc}}^{\text{m}}/G_i}{T_{\text{corr,Jsc}}} \frac{1}{c_1 + c_2 \times \log G_i - c_3 \times G_i^2}$$

$$= \frac{J_{\text{sc,meas}}/G_i}{\{1 + \alpha_{Jsc} \times (T_{\text{ref}} - T_{\text{meas}})\}\{c_1 + c_2 \times \log G_i - c_3 \times G_i^2\}} . \tag{4.37}$$

The result for the two translation equations 4.27 and 4.37 for  $J_{\rm sc}$  is shown in Figure 4.21. Note that contrary to the determination of  $\alpha_{\rm Jsc}$ , for the determination of  $C_1...C_3$ , all data are used. In the following, the results of Figure 4.21 will be discussed and compared to the KH model. Afterwards, the parameter analysis of

the KH model and the LFM will be compared in more detail.

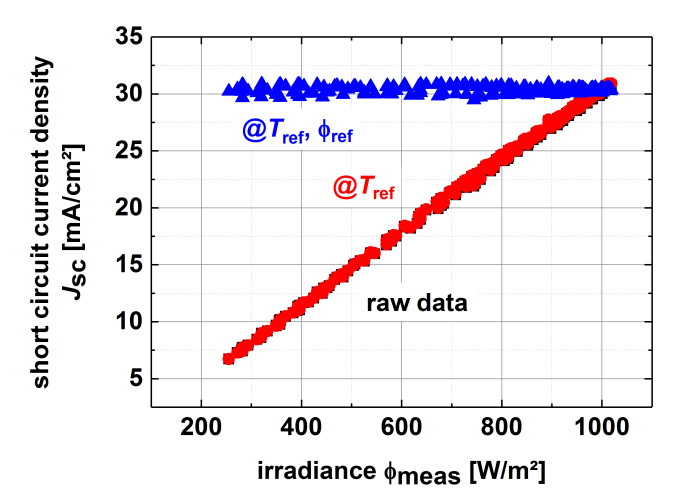


Figure 4.21. – Translation of  $J_{\rm sc}$  to STC for the LFM. Data are taken from the CIGS1 module measured in Italy during 29th of July 2016 to 31st of July 2016.

## 4.3.3. Comparison of the KH model and LFM

Comparing the result of Figure 4.21 to the one obtained with the KH model (see Figure 4.19b), it can be seen that the LFM translation to STC is better for low irradiance conditions than the KH translation. However, this it not surprising, considering the respective translation equation of the LFM, Equation 4.33 (or the general Equation 3.24). For  $J_{\rm sc}$ , the LFM translation equation does not only include a proportional interdependence between  $J_{\rm sc}$  and  $\phi$  but also a logarithmic and quadratic correlation. Hence, the changed correlation observed in Figure 4.19b can be compensated. This also reduce the "double exponential" behavior for  $V_{\rm oc}$  and  $R_{\rm oc}$ . In summary, i.e. that due to the additional  $\phi$  correlation terms compared to the translation equations of the KH model (Equations 4.12 to 4.15) better STC translation for low irradiance could be achieved for the LFM. However, there is no clear physical meaning of the additional coefficients, which does not allow to analyze

the parameters further by using their coefficients. For the KH model, however, this additional parameter analysis will be done in the next chapter.

Table 4.3. – Comparison between the calculated parameters for STC with the KH model and the LFM. The considered data are from the CIGS1 module measured in Italy. The considered time interval is 29th July 2016 - 31st July 2016.

	KH Model		LFM		
Parameter		$\phi >$		$\phi >$	$\phi >$
		$800  { m W/m^2}$		$800\mathrm{W/m^2}$	$1000\mathrm{W/m^2}$
	all data	T > 25 °C	all data	$T > 25^{\circ}\mathrm{C}$	T > 25 °C
$J_{ m sc} [{ m mA/cm^2}]$	28.6	30.4	27.3	30.4	30.4
$G_{ m sc} [{ m mS/cm^2}]$	$2.7 \times 10^{-3}$	$2.8 \times 10^{-3}$	$2.4 \times 10^{-3}$	$2.5 \times 10^{-3}$	$2.4 \times 10^{-3}$
$V_{ m oc}[{ m mV}]$	655.4	663.3	602.7	642.9	668.2
$R_{ m oc} [{ m m}\Omega/{ m cm}^2]$	2.15	2.26	2.48	2.37	2.46

Another problem is observed by changing the filter for the data that are used to calculate the coefficients of the translation equations for both models. The results are shown in Table 4.3. The same data set is here taken as before (CIGS1, Italy, 29th July - 31st July 2016). In the table, the results for the obtained STC parameters  $J_{\rm sc}$ ,  $V_{\rm oc}$ ,  $G_{\rm sc}$ , and  $R_{\rm oc}$  are shown when using different fitting ranges for the coefficient determination. First, the coefficients for Equation 4.12 to 4.15 were determined for the KH model by using all data of this week. Then the STC values were calculated by using the Equation 4.12 to 4.15 with the determined coefficients and  $T_{\rm meas}=25\,{\rm ^{\circ}C}$ and  $\phi_{\rm meas} = 1000 \, {\rm W/m^2}$ . In the next step, the coefficients were determined by fitting the equations only with data that were measured under  $\phi > 800 \, \mathrm{W/m^2}$  and T > 25 °C. Then the STC parameters were calculated again. The same was done for the LFM. The changing fitting ranges were only used to determine  $\alpha$  (Equation 3.18). For the coefficients  $c_1...c_3$  always all data were taken. It can be seen in Table 4.3 that the values of the obtained STC parameters with the KH model and the LFM are for all parameters similar except for  $V_{oc}$ . Whereas the obtained  $V_{oc,ref}$  values with the KH model vary only in between 1.2%, the values for the LFM vary with the same data ranges in between 6.3%. Comparing the LFM  $V_{\text{oc,ref}}$  with the one of the KH model that are obtained with the data  $\phi > 800 \,\mathrm{W/m^2}$  and  $T > 25 \,^{\circ}\mathrm{C}$ , there is still a difference of 3%. The values become almost same if for the LFM only data with  $\phi > 1000 \,\mathrm{W/m^2}$  an  $T > 25 \,^{\circ}\mathrm{C}$  are used. This indicates that the fitting range for the determination of the temperature coefficient is very sensitive. This problem does not appear for the KH model.

Depending on the analyzed data set, the fitting procedure of the KH model seems to be more robust than the one of the LFM. Regarding outdoor data, it is important to have a not too sensitive parameter analysis. This is one reason why in the next chapter the KH model is used for the degradation analysis as the fitting procedure for the parameter analysis fulfill the requirement of a robust analysis.

Beside the fitting ranges in dependence on  $\phi$  and T, also the time interval plays a significant role. This problem will be discussed in the following.

In Figure 4.22, the translation to STC with the KH model for  $V_{\rm oc}$  is shown using different time intervals and dates. Here, the CdTe1 module measured in Arizona was investigated. In Figure 4.22a, the results for the second week (day 8-14) are shown, using a time interval of one week to fit the translation equation. It can be seen that the STC values for high  $J_{\rm sc}$  values  $(15-25\,{\rm mA/cm^2})$  show a broad distribution. The reason for this is that during the first weeks metastable effects play an important role for CdTe (see Chapter 5 for more information). This leads to fast changing STC values and so the rate of change in module properties interacts with the STC corrections. This problem can be solved by using shorter time intervals. In Figure 4.22b, the time interval is set to two days (day 11-12). Here, the STC values for the high  $J_{\rm sc}$  values show a more homogeneous behavior. In Figure 4.22c, the results for the week 20 are shown, using a time interval of one week. It can be seen that here the results of the translation to STC show a very homogeneous behavior, contrary to the results of Figure 4.22a where also a time interval of one week is used. However, in Figure 4.22c, the modules have been exposed already for 20 weeks.

Summarizing the results of Figure 4.22, it is recommended to use small time intervals for the parameter analysis for thin film technologies during the first weeks. When the thin film modules are already exposed for some weeks, the time interval can be set to one week.

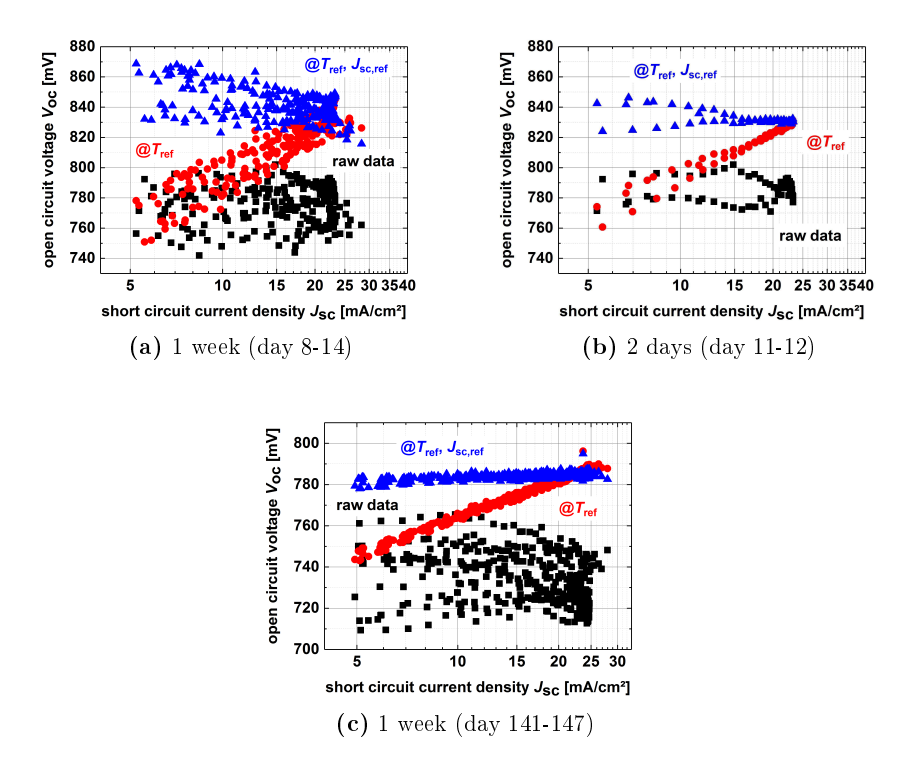


Figure 4.22. – Translation of  $V_{\rm oc}$  to STC for the KH model using different time intervals and dates. For a) a time interval of one week was used (day 8-14), for b) a time interval of two days was used (day 11-12), and for c) a time interval of one week (day 141-147) was used. The data are from the CdTe1 module measured in Arizona.

## 4.4. Yield prediction

In this section, finally the last step of the four step procedure, the prediction, (see Section 2.2.4) is investigated. In general, uncertainties in energy yield prediction arises from uncertainties in the measurement as well as in the modeling [121]. This is why two research directions have come up in the literature. One is dealing with forecasting of environmental conditions especially of irradiance (see for example [122]) and the other is dealing with performance modeling. Both are influencing each other and a good energy yield prediction can only be achieved taking both into

account.

In the scope of this thesis, the work is concentrated on the part of the performance modeling. In this section, the suitability of the KH model for energy yield prediction is investigated. As a reference, the LFM is used again, where its parameterization is done with the KH fit (see Section 4.1). Before showing and discussing the results, first the methods are introduced that are used to do and analyze the energy yield prediction of both models.

#### 4.4.1. Methods

For the energy yield prediction with the KH model, the first step is to predict the four parameters  $J_{\rm sc}$ ,  $G_{\rm sc}$ ,  $V_{\rm oc}$ , and  $R_{\rm oc}$  with the translation equations 4.12 to 4.15. Therefore, the coefficients of the translation equations are determined from a time interval  $[t_i; t_{i+1}]$  and the environmental parameters  $\phi_{meas}$  and  $T_{meas}$  are from a time  $t_{i+1} + \delta(t)$ . As mentioned before (see Section 4.3), a time interval of one week is in general suitable to determine the necessary coefficients. Therefore, the data from week i are taken to determine the coefficients for the parameter analysis as described in Section 4.3. Then the environmental conditions  $\phi_{meas}$ , respectively  $J_{\rm sc,meas}$ , and  $T_{\rm meas}$  are taken from the next week (i+1) to predict the power density for this week. In many papers, long-term energy yield prediction is done, i.e. prediction on a monthly or yearly basis (see [123], [124]). However, due to metastable and degradation effects this is not useful in this case. This is why a concentration on short-term prediction is preferred. Also short-term prediction is gaining more importance by growing photovoltaic capacity as planning of the daily power plant mix is an important factor of our energy market [122].

It has to be mentioned that contrary to the approach in Section 4.3, all data were used for the KH coefficient determination. This is due to the fact that the power density should be predictable for all temperature and irradiation conditions of the module. Therefore, it is important to consider also the influence of the low irradiance on the translation equations. After the parameters m and  $\gamma$  are determined with Equation 3.9 and 3.10, respectively, the predicted JV curve is determined with the KH equation (Equation 3.2) and from that  $P_{\rm mpp,pred}$  is calculated.

Outdoor data analysis with the Karmalkar-Haneefa model

For the LFM, the same prediction method as for the KH model was used. In a first step, the parameters are determined by using the coefficients from week i and  $\phi_{meas}$  and  $T_{meas}$  from week i+1. By transforming Equation 4.37 and the respective translation equations for the other parameters, the parameters are determined by:

$$J_{\text{sc}}^{\text{n}}\left(\phi_{\text{meas}}, T_{\text{meas}}\right) = \left\{1 + \alpha_{Jsc} \times (T_{\text{ref}} - T_{\text{meas}})\right\} \times \left\{c_{1,Jsc} + c_{2,Jsc} \times \log G_{i} - c_{3,Jsc} \times G_{i}^{2}\right\}$$
(4.38)

$$V_{\text{oc}}^{\text{n}}\left(\phi_{\text{meas}}, T_{\text{meas}}\right) = \left\{1 + \alpha_{Voc} \times \left(T_{\text{ref}} - T_{\text{meas}}\right)\right\} \times \left\{c_{1,Voc} + c_{2,Voc} \times \log G_i - c_{3,Voc} \times G_i^2\right\}$$

$$(4.39)$$

$$FF^{n}(\phi_{\text{meas}}, T_{\text{meas}}) = \{1 + \alpha_{FF} \times (T_{\text{ref}} - T_{\text{meas}})\} \times \{c_{1,FF} + c_{2,FF} \times \log G_{i} - c_{3,FF} \times G_{i}^{2}\}$$

$$(4.40)$$

$$R_{\rm sc}^{\rm n}\left(\phi_{\rm meas}, T_{\rm meas}\right) = c_{1,Rsc} + c_{2,Rsc} \times \log G_i - c_{3,Rsc} \times G_i^2$$
 (4.41)

$$R_{\text{oc}}^{\text{n}}\left(\phi_{\text{meas}}, T_{\text{meas}}\right) = c_{1,Roc} + c_{2,Roc} \times \log G_i - c_{3,Roc} \times G_i^2$$
 (4.42)

Afterwards,  $P_{\text{mpp,pred}}$  is calculated by Equation 3.17.

The value of  $P_{\rm mpp,pred}$  can then be compared for both models with the real measured power density  $P_{\rm mpp,raw}$  for the respective week. The error function is determined as

$$\psi = \frac{P_{\text{mpp,raw}} - P_{\text{mpp,pred}}}{P_{\text{mpp,raw}}} \quad . \tag{4.43}$$

For energy yield prediction, not the prediction of single JV curves are important but the prediction of average power densities [123]. Therefore, the mean and standard deviation of Equation 4.43 for one week intervals are determined. However, these statistical values are very sensitive to outliers. Comparing different models, the results should not be influenced by such outliers that may arise due to errors in measurements. Therefore, outliers were not considered. The outliers are defined by using the interquartile range (IQR) [125]. The IQR is defined as

$$IQR = Q_1 - Q_3$$
 , (4.44)

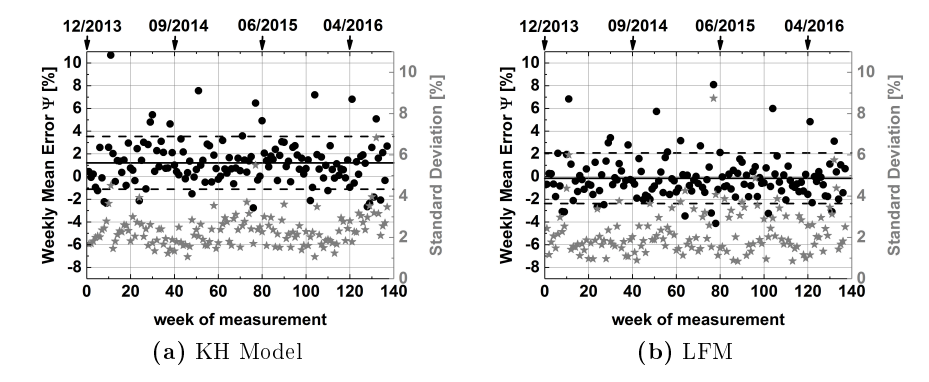


Figure 4.23. – Weekly average prediction error and standard deviation for the power density. The prediction is done a) with the KH model and b) with the LFM. Data are taken from the CdTe1 module measured in Arizona.

with Q1 as the first quantile and  $Q_3$  as the third quantile. With the IQR, the mean error  $\psi$  is determined with those values that are in the range

$$Q_1 - 1.5 \times IQR < \psi < Q_3 + 1.5 \times IQR$$
 (4.45)

Values outside this range are defined as outliers [125] and are not considered. Then, an average error and standard deviation of  $\psi$  for each week is defined. The results will be shown in the following.

## 4.4.2. Analysis and results

In Figure 4.23, the results of the mean prediction error  $\psi$  and the standard deviation for the CdTe1 module measured in Arizona are shown for both models, whereas in Figure 4.23a the results of the KH model and in Figure 4.23b the results of the LFM are shown. It can be seen that until week 40 the error for both models shows a higher fluctuation than after week 40. For the KH model also a seasonal fluctuation of the error  $\psi$  can be observed and an offset which leads in general to the situation that the KH model underestimates the  $P_{\rm mpp}$ .

The weekly results of both models are in some points very similar. The error for each week is smaller than 10%. Until week 40 the error for both models shows a

higher fluctuation than after week 40. This is most likely due to metastable effects. The seasonal fluctuation of  $\psi$  obtained by the KH model can be explained due to the fact that the KH translation equations were applied to all data. The fluctuation of  $\psi$  can be reduced by only considering high irradiance. The LFM shows less seasonal variations. This is due to the fact, that regarding the model for the T correction only data were fitted with  $\phi_{\rm meas} > 800\,{\rm W/m^2}$  and  $T_{\rm meas} > 25\,{\rm ^{\circ}C}$ . So the obtained coefficients of the translation equations are not affected by low irradiance and temperature that have a higher impact in winter than in summer.

It has to be noted that the LFM fit was only done for such weeks where at least five JV curves were measured with  $\phi_{\rm meas} > 800\,{\rm W/m^2}$ . To do a better comparison with the KH model, the prediction for the KH model was only done where this requirement is also fulfilled although the KH fit was applied to all data.

The offset of the  $\psi$  error for the KH model shows that the KH model in general underestimates the maximum power density. This fact has been already discussed in Section 4.2, where it was showed that the KH model underestimates the  $P_{\rm mpp}$  for CdTe with increasing  $P_{\rm mpp}$  values. In Arizona, in general, high irradiances are measured which lead to high  $P_{\rm mpp}$  values and therefore to a higher underestimation of the  $P_{\rm mpp}$  values by the KH model than for regions with lower irradiance.

For some weeks, high errors are obtained. One example is the prediction of week 11. For the KH model, a mean error of  $\psi=10.7\%$  is obtained for this week, whereas for the LFM  $\psi=6.8\%$  is obtained. The reason for these relative high errors is the result of the parameter analysis of week 10. Doing the parameter analysis as described in Section 4.3, a STC value for  $J_{\rm sc}$  of  $21\,{\rm mA/cm^2}$  is obtained for week 10, whereas at the beginning (week 1) and for week 11 the STC values are  $23.8\,{\rm mA/cm^2}$  and  $23.5\,{\rm mA/cm^2}$ , respectively. The lower STC value for week 10 compared to the other two weeks can be a hint of soiling problems. However, the low STC value for  $J_{\rm sc}$  has an influence of the fitting coefficients for both models and therefore leads to relative high errors for the  $P_{\rm mpp}$  prediction.

Contrary to the weeks with relative high prediction errors, also weeks with low errors are obtained. One example is the prediction of week 21 (2nd May - 8th May 2014) with the coefficients obtained from week 20 (25th April - 1st May 2014). For the LFM, here an value for  $\psi$  of -0.67% and a standard deviation of 0.9% is

obtained. Stein *et al.* [78] also investigated prediction errors for the LFM. However, they relate the prediction error to the maximum power density at STC as

$$\psi_{\rm STC} = \frac{P_{\rm mpp,pred} - P_{\rm mpp,raw}}{P_{\rm mpp,STC}} . \tag{4.46}$$

Applying Equation 4.46 to week 21, a error  $\psi_{STC}$  of 0.48% and a standard deviation of 0.6786% is obtained. In Figure 4.24 the results for the single  $P_{\rm mpp}$  prediction errors of week 21 are shown for the LFM. The red line indicates the relative mean bias error for the whole week and the dashed red lines the respective standard deviation. However, the overall mean bias error is much higher than obtained by Stein et al. in [78]. However, Stein et al. obtained the JV curves from modules that were mounted on an azimuth/elevation 2-axis tracker pointed at the sun for all measurements. In addition, they filtered out all curves that were obtained during unstable irradiance conditions (irradiance changes > 2%) [78]. This filter could not be used for the data as explained in Section 3.1. Considering the prediction errors shown in Figure 4.24, the relative small errors in this week compared to the other weeks can be explained by considering the values for the coefficients of the translation equations in week 20, where the coefficients are determined, and week 21, for which the prediction is done. In both weeks, the coefficient values are quite similar, which leads to similar reference values in these two weeks. For example, the  $P_{\rm mpp}$  in week 20 is calculated with the LFM to be  $12.9\,{\rm mW/cm^2}$  and in week 21 it is 13.1 mW/cm<sup>2</sup>. This explains why small predictions error for week 21 are achieved by using the translation coefficients of week 20.

In a next step, from the single  $\psi$  errors and standard deviations per week an average weekly error and standard deviation was estimated for the whole measurement time. In Figure 4.23, the average weekly error is shown with a horizontal solid line and the average weekly standard deviation with two dashed lines. The average weekly error for the CdTe1 module measured in Arizona for the KH model is 1.2% and the standard deviation 2.3%. For the LFM it is  $-0.15\% \pm 2.2\%$ . These values were calculated for each technology at each location. In Figure 4.25, the results for Cologne are shown. In addition to the average weekly error and standard deviation, also the range of the weekly  $\psi$  values are shown, i.e. the maximum mean weekly error and the minimum mean weekly error. The KH model and the LFM are both

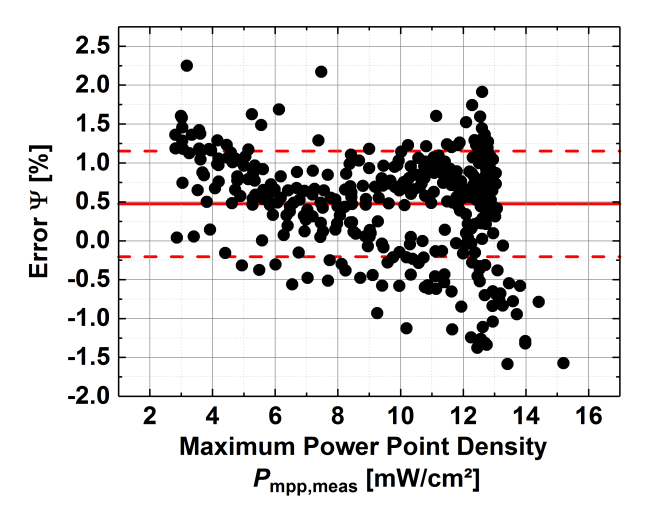


Figure 4.24. – Prediction error  $\psi_{\rm STC}$  for the LFM for week 21 (2nd May - 8th May 2014), taking the coefficients obtained from week 20 (25th April - 1st May 2014).

investigated with two versions each. For the KH model the uncorrected  $P_{\rm mpp}$  version (purple dots) and the corrected  $P_{\rm mpp}$  version (black dots) (see Section 4.2) are investigated. It can be seen that with the correction of  $P_{\rm mpp}$  with Equation 4.10 the average weekly error  $\psi$  can be improved for most of the modules. However, the improvement is very little compared to the influence of the "outlier weeks", i.e. weeks with a high prediction error. Outlier weeks happen when the environmental conditions between two weeks change dramatically so that prediction occurs with abnormal high errors. Another influence is soiling, for example due to dust or snow. For the LFM, as described before, the four parameters  $J_{\rm sc}$ ,  $R_{\rm sc}$ ,  $V_{\rm oc}$ , and  $R_{\rm oc}$  are taken from the KH fit according to Section 4.1. However, the prediction was done once with the FF obtained from the KH fit (blue marks) and once with the raw FF values (orange marks). This investigation allows to separate the influence of the error introduced by the FF from the KH fit from the error introduced by the FF from the raw measured JV points. It can be seen that for most of the modules, the prediction with the raw FF leads to better prediction values. Therefore, a full parameterization with the KH model for the LFM is not recommended.

The results for the other locations are shown in Appendix B. They are comparable with the results from Arizona. For all locations, all investigated model versions show low average prediction errors (smaller than  $\pm 2\%$ ). Only for the a-Si:H/ $\mu$ c-Si:H module measured in Arizona a high average value of 4% was obtained. This is due to high errors of the outlier week.

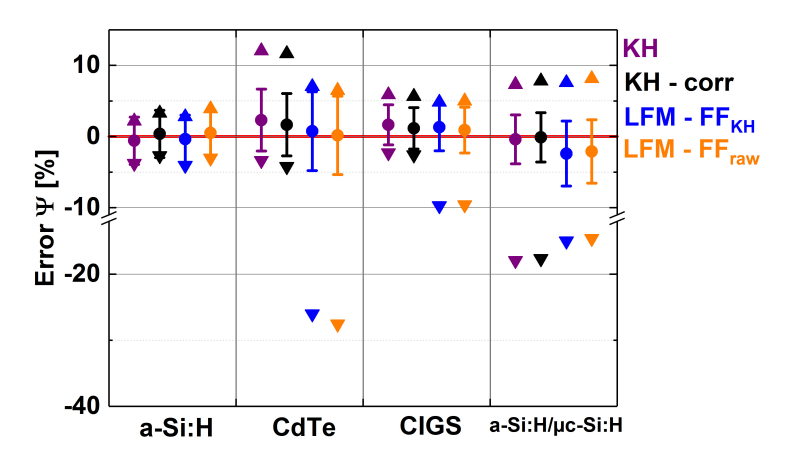


Figure 4.25. – Comparison between the prediction error for  $P_{\rm mpp}$  calculated with the KH model and the LFM. Investigated are the four modules a-Si:H, CdTe1, CIGS1 and a-Si:H/ $\mu$ c-Si:H measured in Cologne. Shown are the mean weekly error (dot), the mean weakly standard deviation, the maximum mean weekly error (upwards triangle) and the minimum mean weekly error (downwards triangle). The colors indicate the investigated model and method: KH model without  $P_{\rm mpp}$  correction (purple), KH model with  $P_{\rm mpp}$  correction (black), LFM with FF taken from the KH fit (blue), and LFM with raw FF (orange).

In Section 4.3, it has been already demonstrated that the fitting range, i.e. the temperature and irradiance range, for the determination of the temperature coefficients for the LFM is very sensitive. In this section, a relative wide fitting range for the temperature coefficient of LFM with  $\phi > 800\,\mathrm{W/m^2}$  an  $T > 25\,^\circ\mathrm{C}$  has been used. For the translation equations of the KH model and the  $\phi$  translation equation of the LFM, even all data haven been used. The results of the prediction for the two models show again that the LFM is more sensitive to the fitting range than the KH model. This means that it can be expected that the prediction results will change for the LFM strongly with another fitting range for the coefficients. The sensitivity of

the LFM leads to more extreme values for  $\psi$  than the KH fit. However, the average  $\psi$  value over all weeks is not affected so much from that as the outlier weeks normally neutralize each other. At the end, both models show comparable prediction errors and standard deviations for all investigated technologies and locations as the KH model tends to offsets errors for  $\psi$  and the LFM to high sensitivity of outlier weeks. Both disadvantages seem to have at the end the same impact on the average error  $\psi$ .

The prediction errors can be reduced by taking only suitable data for the parameter analysis into account. That means as well to neglect low irradiance and to neglect data that show fluctuations in the calculation of STC values for example due to soiling effects. However, in this section all data were used to do the maximum power density prediction so that the prediction is not limited to certain temperature and irradiance conditions and can be done for a wide range of climate zones.

The goal was to show if the KH model is as suitable as the LFM for energy yield prediction. Considering the results, it can be stated that both models have their disadvantages and advantages. In summary, both are suitable for energy yield prediction. It can stated that the two main advantages for the KH model are that it is a very robust method and only needs four parameters. An additional correction for the  $P_{\rm mpp}$  prediction can be done if higher accuracy is desired. The big advantage of the LFM is that it fits low light conditions better than the KH model.

#### 4.5. Conclusion

In the first part of this chapter, in Section 4.1, the fitting parameters of the KH model were compared with the parameters obtained from classical linear fits. For the linear fits, it was found that the range of the linear fits has a high influence on  $R_{\rm oc}$  and  $R_{\rm sc}$ , whereas  $J_{\rm sc}$  and  $V_{\rm oc}$  are only slightly affected by the fitting range. Indeed, a higher fitting range leads to increased values of  $R_{\rm oc}$  and  $G_{\rm sc}$ . However, this also decreases the statistical error of the value. A fitting range of  $[V_{\rm min}, 1/2 \times V_{\rm mpp}]$  was defined as a suitable compromise for  $R_{\rm sc}$  as here the influence of the fitting range is strongest. Comparing the KH parameters with the parameters of the linear fits, the highest discrepancy between both parameters can be found for the  $R_{\rm sc}$  vs.

 $J_{\rm sc}$  behavior. This problem can be solved by a weighting factor of 30 in the range  $[V_{\rm min}, 1/2 \times V_{\rm mpp}]$ . For the single junction thin film modules CIGS, CdTe, and a-Si:H, the using of the weighting factor leads to the effect that after the weighting the highest difference between the KH and the linear fit can be found for the  $R_{\rm oc}$ . Only for the a-Si:H/ $\mu$ c-Si:H module and the c-Si module, the  $R_{\rm sc}$  difference still remains the highest between the linear and the KH fitting parameters. In total, the analysis of the parameterization shows that with the weighting factor the KH model is a suitable method to obtain  $R_{\rm sc}$ ,  $R_{\rm oc}$ ,  $J_{\rm sc}$ , and  $V_{\rm oc}$  for thin film modules.

The consideration of the whole JV curve fit in Section 4.2 enhances the analysis that the KH fit is suitable for thin film modules, whereas the KH model cannot be recommended for poly-Si modules. It could be shown that the quality of the KH fit depends on the irradiance under which the JV was measured. The JV curves of a-Si:H solar modules are fitted well under high irradiance, whereas the JV curves of CdTe modules are fitted better under low light conditions. This correlation can also be found in the fit at the MPP. The quality of the fit at the MPP shows a linear correlation to the  $P_{\rm mpp}$  value. With increasing maximum power density, the KH fitted  $P_{\rm mpp}$  tends to underestimate the real power for CdTe. For a-Si:H, the KH fit overestimates the real  $P_{\rm mpp}$  with decreasing power density. The KH fit for CIGS modules shows a mixed behavior as well as for a-Si:H/ $\mu$ c-Si:H modules. A linear correction term for the KH fit at the MPP improves the KH fit for the  $P_{\rm mpp}$ .

For the parameter analysis of the KH fit, translation equations based on the one-diode model have been used. Those equations and the results have been compared to the LFM. It could be shown that for low irradiance, the translation equations are influenced by the doubel-exponential behavior of the thin films. The translation equations of the LFM can compensate this effect. Therefore, more coefficients are needed. However, these additional coefficients do not have a physical meaning. Furthermore, it could be shown that the translation equations of the KH fit are more stable regarding the fitting range than the translation equation of the LFM for the temperature. However, it is recommended to determine the coefficients of the KH translation equations at high irradiance ( $\phi > 800\,\mathrm{W/m^2}$ ) and temperature ( $T > 25\,\mathrm{^{\circ}C}$ ).

Comparing the yield prediction of the LFM and the KH model, it could be

Outdoor data analysis with the Karmalkar-Haneefa model

shown that regrading the available data set, both models show similar results considering the mean and the standard values for the yield prediction. In summary, it can be stated that the KH model is a suitable model for thin film model analysis.

# Degradation Analysis and Modeling of CdTe Outdoor Data

In this chapter, the outdoor data from the CdTe modules are analyzed in some detail. In addition, an empirical dynamic performance model for the  $R_{\rm oc}$  is introduced for different climate conditions. As described in Chapter 4, the KH model is suitable for performance modeling of thin film modules. Therefore, the KH model will be used in this chapter for the outdoor analysis. However, first an overview about degradation effects for CdTe solar cells will be given. In the next step, a detailed degradation analysis for a CdTe module in Arizona based on the coefficient analysis from the translation equations is made. Afterwards, the parameters  $V_{\rm oc}$ ,  $G_{\rm sc}$ , and  $R_{\rm oc}$  as well as the fill factor and the  $P_{\rm mpp}$  are investigated also for other CdTe modules and for four different climate zones. Based on the results, an empirical model for the  $R_{\rm oc}$  behavior will be implemented.

## 5.1. Introduction degradation and annealing effects

In Section 4.4, the KH model has been used for short term prediction of the module performance. This prediction is based on the assumption that the characteristic of the PV module does not change much from one week to another. However, it could be seen that this assumption is suitable for modules that have been already outside for several weeks. At the beginning of the exposure, this assumption is more prob-

lematic. The reason is that for nearly all PV technologies, especially the thin film modules, the performance changes under extended duration illumination or "light soaking" [15]. These changes include metastable effects, so that the performance of the device depends on the history of illumination, electrical bias, temperature, as well as long-term effects [15].

Many thin film solar cell technologies exhibit metastable behavior (see Section 2.3). In this chapter, it will be focused on typical metastable and degradation effects of CdTe. For CdTe, a common known metastable effect can be observed for the  $V_{\rm oc}$ . The  $V_{\rm oc}$  increases with light-soaking and forward bias and decreases under dark-conditions [13]. The reason for this effect is not yet very well understood. One explanation is that this effect may happen due to a depopulation of trap states in the absorber junction [13].

Another interesting effect arises at the back-contact metalization. The electron affinity of p-type CdTe is with 5.6 eV to 5.7 eV [126] very high and makes it therefore difficult to produce an ohmic contact. Simply applying a metal to the CdTe back side will form a Schottky barrier. This Schottky barrier acts as a reverse-biased diode [127] and leads to an increasing contact resistance and a reduced solar cell performance [128]. To lower this barrier, a common approach is to use an intermediate highly doped semiconductor, which leads to an increasing of the conductivity and creates a tunneling barrier [128]. The typical process to achieve such an efficient back contact will be explained briefly in the following.

By etching the CdTe surface, a Te rich surface is obtained which has an increased conductivity and is  $p^+$ -type [128]. Then a thin layer of Cu (60 Å) or a graphite paste mixed with Cu on the Te rich surface is applied on the surface. Annealing leads to an intermixed Cu2-xTe degenerated semiconductor layer [128]. The diffusion of Cu into the p-type CdTe leads then to a sharp decreasing of resistivity of this material due to formation of Cu-related acceptor level in the band gap of CdTe [129]. This diffusion is the reason why high efficiency CdTe solar cells are achieved with Cu containing back contacts [130]. However, Cu can also diffuse from the back contact through the cells [131]. The CdS layer acts as a Cu sink here [131]. The Cu diffusion through the cell leads to a decreasing of the back contact field and therefore leads to performance losses. This degradation effect increases with

higher temperature [15]. In addition to the back contact problem, also a decrease in doping concentration close to the CdS/CdTe junction and an increased resistance in the transparent front contact have been identified as degradation mechanism [127].

To improve the reliability of CdTe modules, it is important to consider all these kinds of degradation and metastable effects. Until now, no performance model exists that includes a suitable degradation model for outdoor PV modules. The most common approach for long-term prediction is to use degradation rates that were calculated before (see for example [12]). These general degradation rates are influenced by several factors. The degradation and metastable effects depend on the investigated technology (see Section 2.3) and on the environmental conditions and therefore also on the location. In the following, a detailed degradation analysis will be done for the CdTe1 module in Tempe. Afterwards, the measured outdoor data for CdTe will be investigated also for different locations and different CdTe modules.

## 5.2. Coefficient analysis

The KH model requires the consideration of four parameters, namely  $J_{\rm sc}$ ,  $V_{\rm oc}$ ,  $G_{\rm sc}$ , and  $R_{\rm oc}$ . However, from these parameters also the fill factor and the maximum power density can be calculated (see Section 3.2). In Section 4.3, one week was determined as a general suitable time range for determining the standard values of the parameters. In order to improve the precision of the analysis, a deviation from this general time interval is needed in some cases. This will be explained in the following.

The suitable time range to determine standard values of the parameters depends on the environmental conditions of the location and the time that the module has been already exposed outside. As explained in Section 4.3, the fit for the translation equations should be done with data that are measured at high irradiance  $(800\,\mathrm{W/m^2} \le \phi \le 1200\,\mathrm{W/m^2})$  and high temperature  $(T \ge 25\,\mathrm{^{\circ}C})$ . To achieve a suitable amount of data that fulfill that requirement, a longer time interval is recommended for the modules that are measured in Cologne than for the modules measured in the other three locations. In addition, as metastable effects have a strong impact in the first weeks, a shorter time interval should be considered for the

#### Degradation Analysis and Modeling of CdTe Outdoor Data

first weeks compared to the later weeks. Taking both aspects into consideration, the following time intervals are taken for the modules measured in the respective location:

- 1. Cologne: Time interval of 7 days for the weeks 1-20; Time interval of 14 days for all other weeks
- 2. Ancona: Time interval of 7 days for all weeks
- 3. Chennai & Tempe: Time interval of 2 days for the weeks 1-8; Time interval of 7 days for all other weeks

It should be noted that in this chapter for more convenient writing, it will be referred to these time intervals in general as "weekly". So "weekly data" does not mean that the time interval for this data is always exactly one week but rather depends on the considered time and location.

For each time interval, the standard values for the four KH parameters as well as the differential conductance  $G_{\rm sc}$  and the differential resistance  $R_{\rm oc}$  are determined. Doing so, a degradation analysis during the outdoor exposure is possible for any solar cell technology. As in this chapter, the focus lies on CdTe, the results for the time interval calculations are shown for this technology in Tempe in Figure 5.1. The results for the other two technologies (CIGS and  $a\text{-Si:H}/\mu\text{c-Si:H}$ ) are shown for Tempe in the appendix Appendix C.1. All significant technologies show degradation and metastable effects. These will be analyzed in more detail in the following for CdTe.

In Figure 5.1, the normalized STC parameters are shown for the CdTe1 module. The parameters are normalized to their initial values. For Tempe, this means that the values calculated from the first two days are set as initial conditions. At the top of the two plots, the respective month and year of every 40th week of the measurement are given. In addition, a temperature bar is given, showing the mean temperature of the considered data for each time interval. From the temperature bar, the seasonal changes of the environmental conditions can be seen. It should be noted that, as explained in Section 3.1, only those temperature data are taken where the respective measured irradiance  $\phi$  is higher than  $250\,\mathrm{W/m^2}$  and no unphysical JV curve parameters are measured.

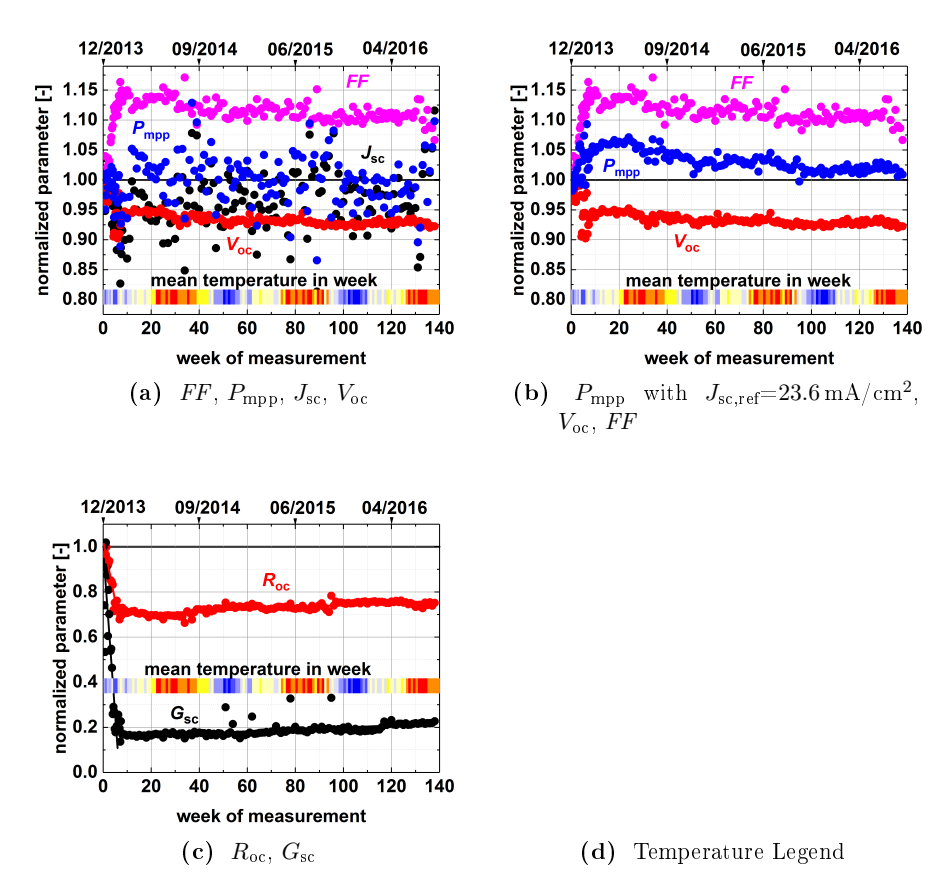


Figure 5.1. – Normalized STC parameters for CdTe1 in Tempe. The parameters are normalized to their initial values. The reference values are calculated for the respective defined time intervals for Tempe, i.e. for the weeks 1-8 a time interval of two days are considered and for all other weeks the reference values are calculated on a weekly basis. In a) the results for  $P_{\rm mpp}$ ,  $J_{\rm sc}$ ,  $V_{\rm oc}$ , and FF and in c) the results for  $R_{\rm oc}$  and  $G_{\rm sc}$  are shown. For comparison, in b) the results for  $P_{\rm mpp}$ ,  $V_{\rm oc}$ , and FF are shown, where for the calculation of the STC  $P_{\rm mpp}$  values a constant value for  $J_{\rm sc}$  with  $J_{\rm sc,ref}{=}23.6\,{\rm mA/cm^2}$  is taken for all weeks. In d) the legend for the temperature values is shown.

In Figure 5.1a, the normalized parameters FF,  $P_{\rm mpp}$ ,  $J_{\rm sc}$ , and  $V_{\rm oc}$  are shown. It can be seen that  $V_{\rm oc}$  degrades continuously over the time. However, the degradation is faster during the first weeks. In contrast, two opposite trends are observed for the

fill factor: During the first weeks the FF increases by almost 15% (relative). This consolidation period is followed by a continuous degradation. For the short circuit current density no degradation behavior is observed. However, the strong scattering of the weekly reference values for  $J_{\rm sc}$  affect the weekly reference values for  $P_{\rm mpp}$ .

In Figure 5.1b, the normalized parameters FF,  $V_{\rm oc}$ , and  $P_{\rm mpp}$  are shown, whereas the  $P_{\rm mpp}$  values are calculated with a constant  $J_{\rm sc}$  value, namely  $J_{\rm sc,ref}=23.6\,{\rm mA/cm^2}$  as the initial value, for all time intervals. Figure 5.1b indicates that the scattering of  $P_{\rm mpp}$  can be reduced with this method. It can be seen that the maximum power density first increases and then decreases similar to the FF. However, the effect of the initial increasing of  $P_{\rm mpp}$  is reduced by the influence of the deceasing  $V_{\rm oc}$ . The described trends of the  $V_{\rm oc}$ ,  $J_{\rm sc}$ , FF, and  $P_{\rm mpp}$  can be seen also for all other three locations for CdTe (see Appendix C.1).

A further insight into the degradation behavior is obtained by considering  $R_{\rm oc}$  and  $G_{\rm sc}$ . In Figure 5.1c, the normalized values for STC are shown over the measured time. It can be seen that both values are first decreasing and then slowly increasing. The behavior of  $R_{\rm oc}$  and  $G_{\rm sc}$  match well to the behavior of the fill factor. In total, the behavior of  $P_{\rm mpp}$ , FF,  $R_{\rm oc}$ , and  $G_{\rm sc}$  can be divided best in two parts, which can be called:

- 1. Consolidation
- 2. Degradation

In Figure 5.1c, the consolidation and degradation phase for  $R_{\rm oc}$  and  $G_{\rm sc}$  can be observed. The consolidation phase for the CdTe1 module in Arizona continues the first six weeks for  $R_{\rm oc}$  and  $G_{\rm sc}$ . It can be described as a linear decay as illustrated in Figure 5.1c. During this time,  $R_{\rm oc}$  decreases by about 5.3% per week and  $G_{\rm sc}$  by about 14.7% per week. After that, a slow degradation starts. This degradation can be approximated with a linear fit from week 10 to week 138. Here,  $R_{\rm oc}$  increases about  $4.7 \times 10^{-2}$ % per week and  $G_{\rm sc}$  about  $4.3 \times 10^{-2}$ % per week.

Figure 5.1 shows the results for one location, namely Tempe, and one module, namely CdTe1. To calculate the STC values of one parameter the respective KH translation equation of the parameter was used (see Section 4.3). In this section, the coefficients of these translation equations will be analyzed in detail for all four

parameters to investigate the degradation behavior of CdTe. For this, the data from Tempe are used. The coefficient analysis will be started with analysis of  $V_{oc}$ .

#### 5.2.1. Open circuit voltage

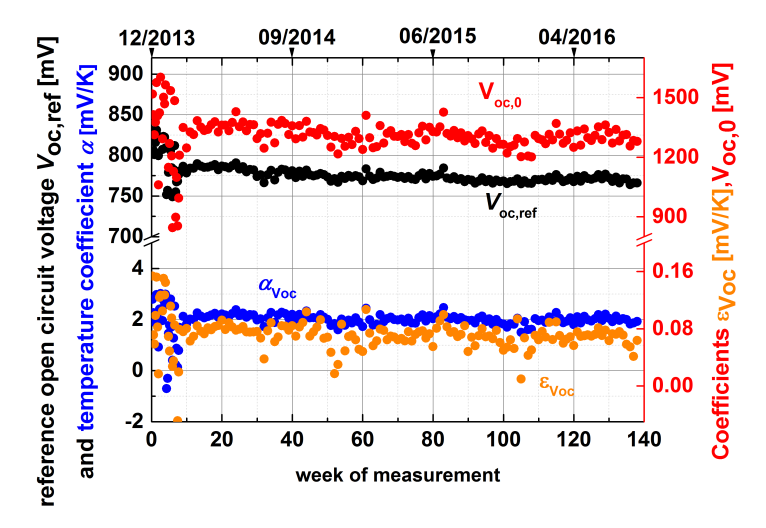


Figure 5.2. – Weekly data of  $V_{\rm oc}$  (black points) at STC and the three coefficients  $V_{\rm oc}^0$  (red points),  $\alpha_{\rm Voc}$  (blue points), and  $\varepsilon_{\rm Voc}$  (orange points). The data are taken from the CdTe1 module measured in Tempe.

For the analysis of  $V_{\rm oc}$ , the respective translation equation is as shown in Equation 4.14. The  $V_{\rm oc}$  is described with three parameters, namely  $V_{\rm oc}^0$ ,  $\alpha_{\rm Voc}$ , and  $\varepsilon_{\rm Voc}$ . In Figure 5.2, the weekly STC values of  $V_{\rm oc}$  are shown as well as the weekly determined coefficients  $V_{\rm oc}^0$ ,  $\alpha_{\rm Voc}$ , and  $\varepsilon_{\rm Voc}$ . It can be seen that all three coefficients decrease in similar ways as  $V_{\rm oc}$ . The open circuit voltage decreases about 7.04% from week 1 to week 134. It should be noted that actually data until week 138 are available. However,  $V_{\rm oc}$  as well as the three coefficients suffer between week 134 and 138 under high fluctuations. Therefore, the degradation rate for  $V_{\rm oc}$  and the three coefficients are determined between week 1 and 134 in the following. The coefficient  $V_{\rm oc}^0$  decreases from 1518 mV to 1310 mV, which, on its own, would lead to a decreasing of the  $V_{\rm oc}$  of 25%. The temperature coefficient  $\alpha_{\rm Voc}$  decreases from 2.79 mV /K to 2.03 mV /K. Together with  $T_{\rm ref}$  =298.15 K, the term  $\alpha_{\rm Voc} \times T_{\rm ref}$  would

lead to an increasing of  $V_{\rm oc}$  of 27.28%. The increasing of the temperature coefficient leads also to the fact that during outdoor exposure,  $V_{\rm oc}$  becomes less dependent on temperature. Finally, the coefficient  $\varepsilon_{\rm Voc}$  decreases from  $15.37 \times 10^{-2} \,\mathrm{mV}$  /K to  $7.12 \times 10^{-2} \,\mathrm{mV}$  /K. Together with  $T_{\rm ref} = 298.15 \,\mathrm{K}$  and  $J_{\rm sc,ref} = 23.61 \,\mathrm{mA/cm^2}$ , the term  $\varepsilon_{\rm Voc} \log (J_{\rm sc,ref}) \, T_{\rm ref}$  would lead to a  $V_{\rm oc}$  decreasing of about 9.36%. The three terms together end up with a total decreasing of  $V_{\rm oc}$  of the mentioned 7.04%.

It should be noted that the highest change of  $V_{\rm oc}$  and its three coefficients happen in the first seven weeks. Here  $V_{\rm oc}$  decreases already by 6%. The coefficient  $V_{\rm oc}^0$  decreases from 1518 mV to about 1349 mV,  $\alpha_{\rm Voc}$  from 2.79 mV /K to about 2.13 mV /K, and  $\varepsilon_{\rm Voc}$  from  $15.37 \times 10^{-2}$  mV /K to about  $8 \times 10^{-2}$  mV /K.

As  $E_a/q = V_{oc}^0$  (see Equation 4.25), the decreasing in  $V_{oc}^0$  indicates a decreasing in the activation energy of  $J_0$ . The initial value of  $qV_{oc}^0 = E_a = 1518 \,\mathrm{meV}$  is not easy to understand because  $E_a > E_g(\mathrm{CdTe}) = 1.45 \,\mathrm{eV}$  [126]. Whether or not such an activation energy is physically true or rather an artifact, the unstable initial state of the module should be subject to further investigations. After the consolidation phase (week 7),  $E_g$  is 1349 meV and so smaller than  $E_g(\mathrm{CdTe})$ . The further decrease of  $V_{oc}^0$  during the degradation phase points to an increasing influence of interface recombination with  $E_a < E_g$ . This could be a result of Cu diffusion into the space charge region of the device. Overall a higher activation energy in the present 12 CdTe modules can be seen as compared to the same analysis of Ulbrich et al. [103] who found  $E_a \approx 1130 \,\mathrm{meV}$  for a CdTe module produced more than 10 years ago. In the following, the coefficient analysis will be continued with  $G_{sc}$ .

#### 5.2.2. Differential conductance at short circuit condition

In Figure 5.3, the weekly values of the two terms of the  $G_{\rm sc}$  translation equation (see Equation 4.13) are shown for the CdTe1 module in Tempe. The values of the two terms are compared with the weekly  $G_{\rm sc,ref}$  values at STC. In Figure 5.3a,  $G_{\rm sc,ref}$  (black dots) is compared to the term  $\kappa_{\rm Gsc}J_{\rm sc,ref}$  (red dots) and in Figure 5.3b,  $G_{\rm sc,ref}$  (black dots) is compared to  $G_{\rm sc,0,Tref}$  (dark yellow dots). The term  $G_{\rm sc,0,Tref}$  is calculated by

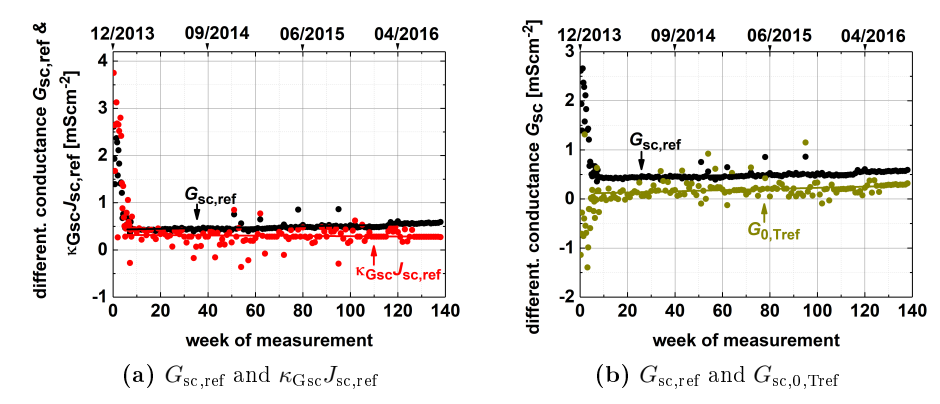


Figure 5.3. – Weekly time values for STC for the two terms of the  $G_{\rm sc}$  translation equation and for  $G_{\rm sc,ref}$ . The data are taken from the CdTe1 module in Tempe. Shown are the values for a)  $G_{\rm sc,ref}$  and  $\kappa_{\rm Gsc}J_{\rm sc,ref}$  and b)  $G_{\rm sc,ref}$  and  $G_{\rm sc,0,Tref}$ .

$$G_{\text{sc.0.Tref}} = G_{\text{sc.0}} + \alpha_{\text{Gsc}} T_{\text{ref}} , \qquad (5.1)$$

and describes the shunt conductance at reference temperature with  $J_{\rm sc}=0$ . The sum of  $\kappa_{\rm Gsc}J_{\rm sc,ref}$  and  $G_{\rm sc,0,Tref}$  is equal to  $G_{\rm sc,ref}$ .

Considering the consolidation phase of  $G_{\rm sc}$ , i.e. the first six weeks, it can be seen that  $G_{\rm sc,ref}$  is mainly influenced by the decrease of the  $\kappa_{\rm Gsc}$ -term, which is equivalent to the decreasing of  $\kappa_{\rm Gsc}$  as  $J_{\rm sc,ref}$  remains constant. At the beginning of the outdoor exposure, the  $\kappa_{\rm Gsc}$ -term is even higher than the  $G_{\rm sc,ref}$  value, which results in negative  $G_{\rm sc,0,Tref}$  values. Of course, negative  $G_{\rm sc,0,Tref}$  values are not physical. They are a result from the linear extrapolation to  $J_{\rm sc}=0$ . Nevertheless, the high values of the  $\kappa_{\rm Gsc}$ -term at the beginning indicate that  $G_{\rm sc}$  depends very strongly on  $J_{\rm sc}$ , which is an indication of voltage-dependent photocurrent. However, the influence of the  $\kappa_{\rm Gsc}$ -term on  $G_{\rm sc,ref}$  becomes less significant during the consolidation phase, which leads to a decreasing of  $G_{\rm sc,ref}$ . Hence, it can be stated that the improvement of  $G_{\rm sc}$  occurs due to a decreasing of voltage-dependent photocurrent.

Considering the degradation phase of  $G_{\rm sc,ref}$ , that set in after the consolidation phase, the degradation is mainly influenced by  $G_{\rm sc,0,Tref}$ . From week 6 to week 138  $G_{\rm sc,ref}$  increases by about  $8.99 \times 10^{-4} \, {\rm mS} \, / {\rm cm}^2$  per week. The term  $\kappa_{\rm Gsc} J_{\rm sc,ref}$ ,

#### Degradation Analysis and Modeling of CdTe Outdoor Data

however, decreases in this time about  $-2.8 \times 10^{-4} \,\mathrm{mS} \,/\mathrm{cm^2}$  and the term  $G_{\mathrm{sc,0,Tref}}$  degrades about  $1.18 \times 10^{-3} \,\mathrm{mS} \,/\mathrm{cm^2}$ . This behavior shows that the degradation, in opposite direction to the consolidation phase, is dominated by a general degradation of the shunt resistance. This may also happen due to the Cu impurity in the material. However, the coefficient analysis of  $G_{\mathrm{sc}}$  shows that the consolidation and degradation phase of  $G_{\mathrm{sc}}$  occurs due to two different mechanisms. The decreasing of  $G_{\mathrm{sc}}$  in the consolidation phase occurs due to decreasing of the voltage-dependent photocurrent, whereas the long term degradation is mainly influenced due to a general degradation of the shunt resistance. In the following, the coefficient analysis will be continued with  $R_{\mathrm{oc}}$ .

#### 5.2.3. Differential resistance at open circuit condition

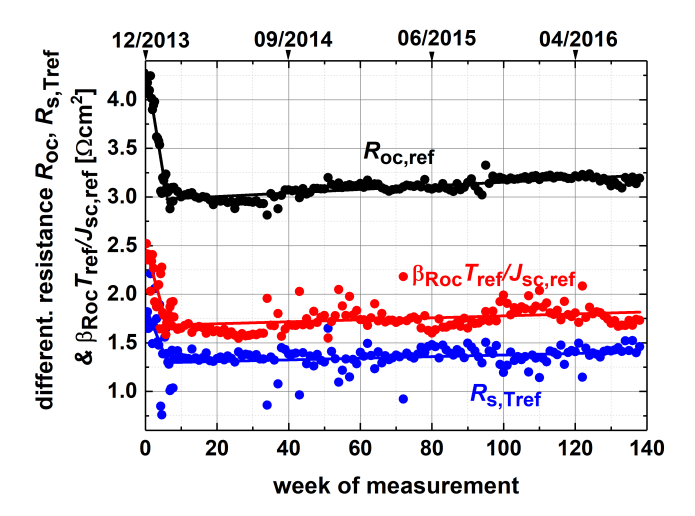


Figure 5.4. – Weekly data of  $R_{\rm oc}$  (black points) at STC and the terms  $\beta_{\rm Roc}T_{\rm ref}/J_{\rm sc,ref}$  (red points) and  $R_{\rm s, Tref}$  (blue points). The data are taken from the CdTe1 module measured in Tempe.

In Figure 5.4, the weekly STC values for  $R_{\rm oc}$  (black points) as well as the two terms  $\beta_{\rm Roc}T_{\rm ref}/J_{\rm sc,ref}$  (red points) and  $R_{\rm s,\ Tref}$  (blue points) are shown. The term  $R_{\rm s,\ Tref}$  is given by

$$R_{\rm s. Tref} = R_{\rm s} + \alpha_{\rm Roc} T_{\rm ref}.$$
 (5.2)

According to the translation equation of  $R_{\rm oc}$  (see Equation 4.15),  $R_{\rm oc, ref}$  is equal to the sum of  $\beta_{\rm Roc}T_{\rm ref}/J_{\rm sc,ref}$  and  $R_{\rm s, Tref}$ . Both terms have an impact on the decreasing of  $R_{\rm oc}$  in the consolidation phase and on its increasing in the degradation phase. However, the shares of  $\beta_{\rm Roc}T_{\rm ref}/J_{\rm sc,ref}$  and  $R_{\rm s, Tref}$  on  $R_{\rm oc, ref}$  change during the time. In the first six weeks  $R_{\rm oc, ref}$  decreases by about  $0.22\,\Omega$  cm<sup>2</sup> per week. The  $\beta$ -term deceases in this time by about  $0.13\,\Omega$  cm<sup>2</sup> per week and therefore has a share of 59% in the decreasing of  $R_{\rm oc, ref}$ . The term  $R_{\rm s, Tref}$  decreases by about  $0.09\,\Omega$  cm<sup>2</sup> per week and therefore has a share of 41% in the decreasing of  $R_{\rm oc, ref}$ . Also for the long term degradation after week 6, the  $\beta$ -term dominates the degradation. However, the share of the  $\beta$ -term on  $R_{\rm oc, ref}$  decreases. The values of  $R_{\rm oc, ref}$  show a degradation of  $1.85\times10^{-3}\,\Omega$  cm<sup>2</sup> per week. Here, the  $\beta$ -term has, with a degradation of  $1.01\times10^{-3}\,\Omega$  cm<sup>2</sup> per week, a share of 55%. The rest (45%) of the  $R_{\rm oc, ref}$  degradation is due to  $R_{\rm s, Tref}$ .

## 5.2.4. Analysis of the fill factor

After the analysis of the  $V_{\rm oc}$ ,  $R_{\rm oc}$ , and  $G_{\rm sc}$ , the impact of these three parameters on the fill factor will be investigated in this subsection. In Figure 5.5, different calculations of the fill factor of the CdTe1 module in Tempe for ST conditions are shown. The black dots indicate the weekly STC values for the fill factor recalculated using the KH model and the measured data from the test site. The initial value of the FF is determined to be 64.92%. The first 6.5 weeks, the FF increases about 1.6% per week. At week 6.5 it achieves an end of the increasing with a value of around 74.03%. Afterwards, it degrades about  $1.81 \times 10^{-2}$ % per week.

As in the KH model the FF is computed from  $V_{\rm oc}$ ,  $J_{\rm sc}$ ,  $R_{\rm oc}$ , and  $G_{\rm sc}$ , the impact of the individual parameters on the FF can be determined. This was done for  $R_{\rm oc}$ ,  $G_{\rm sc}$ , and  $V_{\rm oc}$ . As shown in Figure 5.1a, at the beginning of this section, no degradation for  $J_{\rm sc}$  could be seen for the CdTe module. Therefore,  $J_{\rm sc}$  is not included in the investigation of the fill factor. The results for the other three parameters are shown in Figure 5.5 and will be explained in the following.

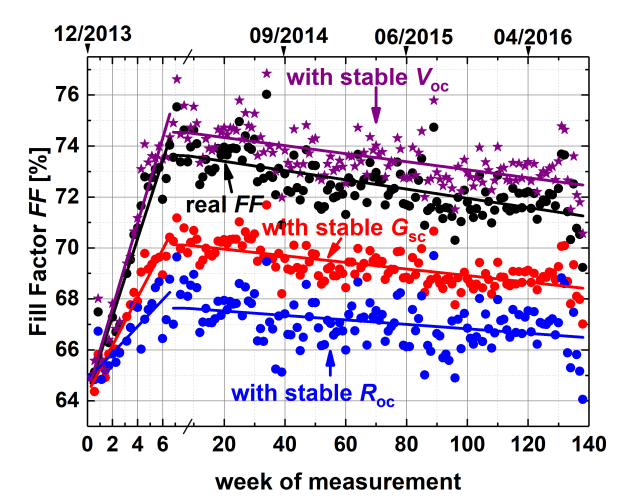


Figure 5.5. – Origin of fill factor behavior in Tempe for the CdTe1 module. Shown are the STC FF values on a weekly basis (black dots). For analysis, the weekly STC values for the FF were also calculated with stable  $R_{\rm oc}$  conditions (blue dots), stable  $G_{\rm sc}$  conditions (red dots) and stable  $V_{\rm oc}$  conditions (purple stars).

To analyze the influence of the  $V_{\rm oc}$  degradation on the FF behavior, the initial STC value of  $V_{\rm oc}$  was used for all weeks and the FF was re-calculated. The results are shown in Figure 5.5 as purple stars. The same was done for  $R_{\rm oc}$  (blue dots) and  $G_{\rm sc}$  (red dots). It can be seen that the degradation of  $V_{\rm oc}$  affects the FF less than  $G_{\rm sc}$  and  $R_{\rm oc}$ . The  $R_{\rm oc}$  influences the FF most, especially at the beginning. But also  $G_{\rm sc}$  has a big influence on how high the FF increases at the beginning of the outdoor exposure.

The time of the increasing of the FF in the first 6.5 weeks can also be described as a consolidation phase, which is then followed by a degradation phase. In Table 5.1, the key data of both phases are shown for the different FF types/calculations. Without the increase of  $R_{\rm oc}$  during the consolidation phase, the FF would only increase by about 0.52% per week in the first 6.5 weeks instead of 1.53%. Thus an increase of 1.01% ( $\approx 2/3$  of the entire increase), can be ascribed to the reduction of  $R_{\rm oc}$  during the consolidation phase. Similarly, for the degradation of FF after week 6.5, a rate of 0.94% per week can be ascribed to the increase of  $R_{\rm oc}$ . This makes  $R_{\rm oc}$  the most influential parameter for both the consolidation as well as the

**Table 5.1.** – Key data of the consolidation and degradation phase for the *FF* analysis of the CdTe1 module at the test site Tempe taking different stabilized parameters into account.

Type of FF	Average weekly linear increase from week 0-6.5	Value at week 6.5	Weekly degradation rate after week 6.5
real FF	1.53%	74.03%	$-1.81 \times 10^{-2} \%$
$FF$ with stable $V_{ m oc}$	1.66%	74.35%	$-1.58 \times 10^{-2} \%$
$FF$ with stable $R_{\rm oc}$	0.52%	68.77%	$-0.87 \times 10^{-2} \%$
$FF$ with stable $G_{\rm sc}$	0.94%	70.42%	$-1.3 \times 10^{-2} \%$

degradation of FF. Considering the data in Table 5.1, the  $G_{\rm sc}$  parameter turns out to be the second most important parameter for the consolidation and degradation phase of the FF.

For a more detailed analysis of the consolidation and degradation behavior of CdTe, finally an analysis of the ideality factor is necessary. This will be explained in the following subsection.

## 5.2.5. Ideality factor

The coefficient  $\beta_{Roc}$  is related to the ideality factor  $n_{\rm id}$  with  $\beta_{Roc} = \frac{n_{\rm id}k}{q}$  (see Section 4.3). In the following, the ideality factor determined from  $\beta_{Roc}$  will be defined as  $n_{\rm id,Roc}$ . The ideality factor  $n_{\rm id,Roc}$  is determined by the slope of  $R_{\rm oc,Tcorr}$  vs.  $1/J_{\rm sc,meas}$ . The value  $R_{\rm oc,Tcorr}$  indicates the temperature corrected data of the measured  $R_{\rm oc}$  values and is determined by

$$R_{\rm oc,Tcorr} = R_{\rm oc,meas} - \alpha_{\rm Roc} \left( T_{\rm sc,meas} - T_{\rm sc,ref} \right) - \beta_{\rm Roc} \left( T_{\rm meas} - T_{\rm ref} \right) / J_{\rm sc,meas}. \quad (5.3)$$

To determine  $n_{\rm id,Roc}$  from Equation 5.3, the linear fit of  $R_{\rm oc,Tcorr}$  vs.  $1/J_{\rm sc}$  is set equal to  $R_{\rm oc,meas}$  ( $J_{\rm sc,meas}$ ,  $T_{\rm ref}$ ) vs.  $1/J_{\rm sc}$  from the translation equation of  $R_{\rm oc}$  (see Equation 4.15). This way, the slope  $a_{\rm Roc}$  of the linear fit  $R_{\rm oc,Tcorr}$  vs.  $1/J_{\rm sc,meas}$  is equal to  $\beta_{\rm Roc}T_{\rm meas}$ . And from this,  $n_{\rm Roc}=a_{\rm Roc}\frac{q}{kT_{\rm ref}}$  is obtained with  $T_{\rm ref}$  =298.15 K. It has to be noted that only values are taken into account that were measured at

Degradation Analysis and Modeling of CdTe Outdoor Data

high irradiance and high temperature as defined in Section 4.3 ( $\phi > 800 \,\mathrm{W/m^2}$  and  $T > 25 \,^{\circ}\mathrm{C}$ ).

Ulbrich et al. [103] have shown that  $n_{id,Roc}$  can be described as

$$n_{\rm id,Roc} = \frac{J_{\rm sc}}{J_{\rm ph}\left(V_{\rm oc}\right)} n_{\rm id},\tag{5.4}$$

with  $J_{\rm ph}\left(V_{\rm oc}\right)$  the photo-generated current density at open circuit and  $n_{\rm id}$  the real ideality factor. The ratio  $\frac{J_{\rm sc}}{J_{\rm ph}(V_{\rm oc})}$  describes how much of the short-circuit current density is collected under open-circuit conditions. With increasing influence of voltage-dependent carrier collection, this ratio increases and therefore also the overestimation of  $n_{\rm id,Roc}$  compared to  $n_{\rm id}$ .

Another method to determine  $n_{\rm id}$  is over the slope of  $V_{\rm oc}$  vs.  $\log{(J_{\rm sc})}$ . This method uses the relation  $\varepsilon_{Voc} = n_{\rm id} k/q$  (see Section 4.3). Here, the same steps as before for  $R_{\rm oc}$  are done and the ideality factor is indicated as  $n_{\rm id,Voc}$ . First, the measured  $V_{\rm oc}$  values are translated to temperature corrected values with

$$V_{\text{oc,Tcorr}} = V_{\text{oc,meas}} - (\alpha_{\text{Voc}} - \varepsilon_{Voc} \log (J_{\text{sc,meas}})) (T_{\text{ref}} - T_{\text{meas}}).$$
 (5.5)

Afterwards, the linear fit of  $V_{\rm oc,Tcorr}$  vs.  $\log{(J_{\rm sc})}$  is set equal to  $V_{\rm oc,meas}$  ( $J_{\rm sc,meas}$ ,  $T_{\rm ref}$ ) vs.  $\log{(J_{\rm sc})}$ , taking the translation equation of  $V_{\rm oc}$  (see Equation 4.14) into account. The slope  $a_{\rm Voc}$  of this function can be set equal to  $\varepsilon_{\rm Voc}T_{\rm ref}$  and by this  $n_{\rm id,Voc}$  is obtained by  $n_{\rm id,Voc} = a_{\rm Voc} \frac{q}{kT_{\rm ref}}$ . Also here, only data measured at  $\phi > 800\,{\rm W/m^2}$  and  $T > 25\,{\rm ^{\circ}C}$  are taken into account to reduce the impact of the second diode with ideality factor 2.

Eron and Rothwarf have shown that in case of bias dependent current collection,  $n_{\rm id,Voc}$  underestimates the real ideality factor  $n_{\rm id}$  [132]. From [103], it can be derived

$$\frac{1}{n_{\rm id,Voc}} = \frac{1}{n_{\rm id}} - \frac{J_{\rm sc}}{J_{\rm ph}(V_{\rm oc})} \frac{kT}{q} \frac{\chi}{f_{\rm sc}},\tag{5.6}$$

with  $f_{\rm sc}$  the current-collection function at short circuit and  $\chi = df/dV_j$  the slope of the collection function at  $V_j = V_{\rm oc}$ . However, it should be noted here that the value of  $\chi$  is negative.

In Figure 5.6, the weekly data of  $n_{\rm id,Roc}$  and  $n_{\rm id,Voc}$  are obtained from the CdTe1 module in Tempe. The ideality factor  $n_{\rm id,Roc}$  is larger than the ideality factor  $n_{\rm id,Voc}$  as expected from Equation 5.5 and 5.6. The underestimation of  $n_{\rm id,Voc}$  compared to the real  $n_{\rm id}$  values explains why for  $n_{\rm id,Voc}$  values < 1 can be obtained. Both values decrease in the first six weeks, the consolidation phase. As the true ideality factor  $n_{\rm id}$  should lie inbetween  $n_{\rm id,Roc}$  and  $n_{\rm id,Voc}$ , it can be concluded that  $n_{\rm id}$  must decrease from a value around 2 to a value between 1 and 1.5. This may happen due to a decreasing of defects in the charge region, which leads to less voltage depended photo-current collection, which then leads to better  $G_{\rm sc}$  and  $R_{\rm oc}$  values and therefore to a better FF. The described relation of defects in the space charge region and voltage depended photo-current collection is in good agreement with models that assume that recombination in the depletion region is the dominant collection loss mechanism [115]. The ideality factor values of around 1 could in combination with the decreasing of  $V_{\rm oc}$  may be explained with higher recombination in the quasi-neutral regions due to the mentioned Cu diffusion.

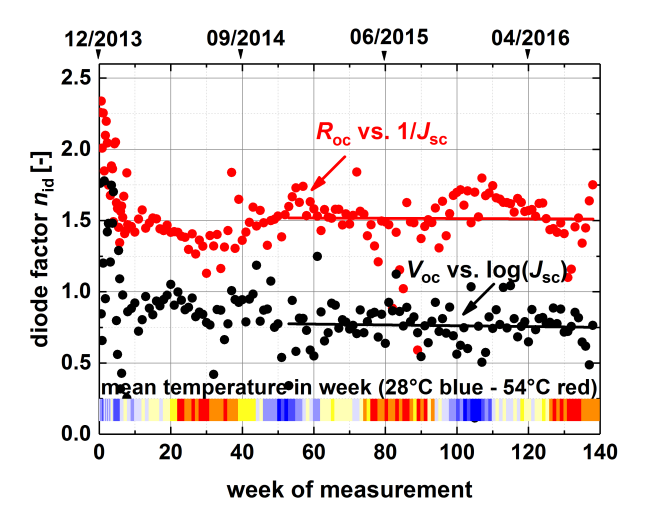


Figure 5.6. – Determination of the ideality factor  $n_{\rm id}$ . Shown are the ideality factors determined from the temperature-corrected data via the  $R_{\rm oc}$  vs.  $1/J_{\rm sc}$  method  $(n_{\rm id,Roc},$  red dots) and via the  $V_{\rm oc}$  vs.  $\log{(J_{\rm sc})}$  method  $(n_{\rm id,Voc},$  black dots). Data are taken from the CdTe1 module in Tempe.

After the first year, seasonal fluctuations in  $n_{\rm id,Roc}$  can be observed. The values

increase in the winter months with lower average temperatures and irradiance. This can explain that in seasons with lower irradiance and temperature, the metastable effects that were annealed at the beginning increase again and lead to higher recombination. The increasing of  $n_{\rm id,Roc}$  also leads to an increasing of  $R_{\rm oc}$ , which can be seen in Figure 5.4.

Despite the seasonal fluctuations, the values of  $n_{\rm id,Roc}$  and  $n_{\rm id,Voc}$  are fairly stable after the consolidation phase, which is indicated with a linear fit of these values from week 53 to week 138. This indicates that the long-term degradation of the parameters  $G_{\rm sc}$ ,  $R_{\rm oc}$ ,  $V_{\rm oc}$ , and by this also FF are not created due to a change of the ideality factor. They may be explained by other degradation effects of the material itself, for example a general increase of the  $R_{\rm oc}$  due to an increased resistance in the transparent front contact as it has been identified in [127]. However, this cannot be stated clearly from the data. Nevertheless, the analysis of the coefficients has shown that the consolidation and the degradation phase are driven by different reasons. The consolidation phase seems to be influenced by a decrease of the voltage-dependent photo-current, which also influences the seasonal variations. The long-term degradation is more influenced by a general material degradation which cannot be specified in detail based on the available data.

## 5.3. Analysis and modeling of different modules

In the previous section, a detailed analysis of the CdTe1 module in Tempe has been made. As can be seen from the data in Appendix C.2, also the other eleven CdTe modules (in total: three CdTe modules in four different regions) show a consolidation and degradation phase for  $P_{\rm mpp}$ , FF,  $R_{\rm oc}$ , and  $G_{\rm sc}$ . Analogously to the previous section, the analysis of  $V_{\rm oc}$ ,  $G_{\rm sc}$ ,  $R_{\rm oc}$ , and FF was made for all CdTe modules.

The changes during the two phases for all parameters by using the KH translation equations are summarized in the Appendix C.2.6. In addition, for  $V_{\rm oc}$  the degradation of the  $V_{\rm oc}$  itself and its coefficients of the respective translation equation over the entire outdoor exposure can also be found here for all twelve CdTe modules.

Despite their similarities, each CdTe module has its own degradation behavior

as no module has the exact physical characteristic than another module. For a detailed analysis of the degradation and metastable effects, two things have to been distinguished, namely the type of module and the location of the module. In this section, the influence of the module and the location will be investigated. For this, first the degradation behavior of the three CdTe modules at a same location and afterwards, the behavior of the CdTe1 module in the four climate zones is investigated considering  $V_{\rm oc}$ ,  $G_{\rm sc}$ , and  $R_{\rm oc}$ . Finally, also the  $P_{\rm mpp}$  and FF behavior are analyzed for all modules at each location.

#### 5.3.1. Analysis of different CdTe modules in Tempe

Considering all three modules at the same test site, for example Arizona, their different degradation behavior can be seen although they have seen the same environmental conditions. In Figure 5.7, the degradation for  $V_{\rm oc}$  and  $R_{\rm oc}$  for the three CdTe modules measured in Tempe are shown.

Figure 5.7a shows the results for  $V_{\rm oc}$ . It can be seen that for all CdTe modules the STC- $V_{\rm oc}$  values are decreasing. After 138 weeks, the modules lost 6 (CdTe2 and CdTe3) to 7 (CdTe1) % of their initial  $V_{\rm oc}$  value. The CdTe1 module has the highest initial value with 830 mV, followed by CdTe2 (803 mV) and CdTe3 (788 mV). The degradation behavior of the three CdTe modules differs by considering the degradation for the first ten weeks. For CdTe1, 75% of the total measured degradation happens in the first ten weeks. For CdTe2, it is even 83%. Only for CdTe3, it is only 50%. The CdTe1 and CdTe2 modules seem to reach a saturation value at the end of the measured weeks. However, the CdTe3 module seems to degrade further.

For the degradation of the STC- $R_{\rm oc}$  values, the similarity between the CdTe1 and CdTe2 modules gets even more clear. In Figure 5.7b, the results for the three CdTe modules are shown whereas the increasing and decreasing of  $R_{\rm oc}$  is described with respective linear fits. It can be seen that the initial  $R_{\rm oc}$  values are with  $4.25\,\Omega~{\rm cm}^2$  (CdTe1) and  $4.45\,\Omega~{\rm cm}^2$  (CdTe2) very close to each other. During the consolidation phase, which takes for both modules approximately six weeks, the  $R_{\rm oc}$  value decreases by about  $0.23\,\Omega~{\rm cm}^2$  per week for the CdTe1 module and by about  $0.24\,\Omega~{\rm cm}^2$  per week for the CdTe2 module. After that, a slow degradation takes

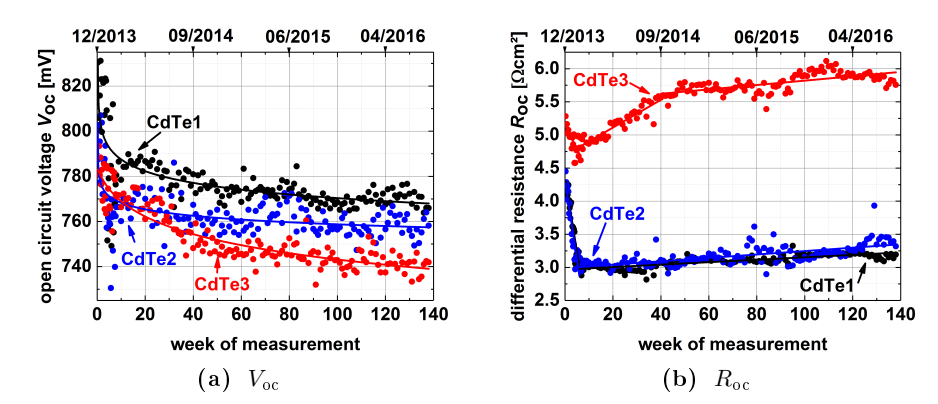


**Figure 5.7.** – Weekly parameter values for STC for different CdTe modules in Tempe. Shown are the values for a)  $V_{oc}$  and b)  $R_{oc}$ .

place. For the CdTe1 module, the  $R_{\rm oc}$  increases about  $2 \times 10^{-3} \,\Omega$  cm<sup>2</sup> per week and for the CdTe2 module it increases about  $3 \times 10^{-3} \,\Omega$  cm<sup>2</sup> per week.

The CdTe3 module shows a much worse behavior for the  $R_{\rm oc}$ . It has already a higher initial  $R_{\rm oc}$  value with 5.28  $\Omega$  cm<sup>2</sup>. Also in the consolidation phase, which also takes about six weeks, the  $R_{\rm oc}$  improves only about 0.03  $\Omega$  cm<sup>2</sup> per week. The degradation phase can then be divided into two phases. In the first phase, which takes place from week six to week 40, the  $R_{\rm oc}$  increases relatively strong with 0.02  $\Omega$  cm<sup>2</sup> per week. After week 40 the degradation rate gets lower with  $3 \times 10^{-3} \Omega$  cm<sup>2</sup> per week. However, at the end of the measurement, the  $R_{\rm oc}$  is with 5.8  $\Omega$  cm<sup>2</sup> even higher than at the beginning of the experiment.

In summary, it can be stated that the CdTe3 module suffers more under degradation than the CdTe1 and CdTe2 module. The CdTe1 and CdTe2 modules however show a very similar degradation behavior and similar initial parameters. Considering also  $G_{\rm sc}$ , both statements can be proof further (see for this Appendix C.1). Considering the values in the consolidation and degradation phase, it can be stated that the CdTe3 module improves less in the consolidation phase but degrades stronger in the degradation phase than the CdTe1 and CdTe2 modules. In the next subsection, the influence of the climate zone will be investigated.

#### 5.3.2. Analysis of CdTe in different climate zones

The second aspect, beside the different behavior of different modules, is the climate region that influences the degradation behavior. It should be noted that the four different climate zones of the test sites were described in Section 3.1. First of all, the influence on  $V_{\rm oc}$  considering different locations will be analyzed. Afterwards, the analysis of  $G_{\rm sc}$  and  $R_{\rm oc}$  follows.

It has been already discussed in the previous subsection that the  $V_{\rm oc}$  of the CdTe1 module measured in Tempe degrades much stronger at the beginning than after some weeks. This behavior can be also seen for the other locations (see Appendix C.1 for more details). It should be noted that for Tempe and Chennai, the first weeks have a higher impact than for Cologne and Ancona. However, in this subsection it will be concentrated on the long term degradation of the  $V_{\rm oc}$ . For the short term behavior of the  $V_{\rm oc}$  it will be forwarded to Appendix C.1.

In Table 5.2, the  $V_{\rm oc}$  degradation after 120 weeks for all test sites are shown. It can be seen that the highest degradation occurs in Chennai and the least one in Cologne. This fits very well with the temperatures that occur at both locations. Hot regions lead to higher degradation in the  $V_{\rm oc}$  than colder regions. This indicates a temperature activated degradation process. This also fits to the finding that the  $V_{\rm oc}$  degradation is due to Cu diffusion from the back contact (see Section 5.2) as the Cu diffusion is faster at higher temperatures [15]. The high degradation in Chennai compared to the other three locations also indicates a dependency on humidity as Chennai is located in a tropical region.

**Table 5.2.** – Degradation of  $V_{\text{oc}}$  of the CdTe1 module after 120 weeks at the test sites in Cologne, Ancona, Tempe, and Chennai.

Test site	Degradation	
Cologne	2%	
Ancona	4%	
Tempe	7%	
Chennai	15%	

Also the  $R_{\rm oc}$  and  $G_{\rm sc}$  values show different degradation behaviors in different climate zones. In Figure 5.8, the weekly STC values for  $R_{\rm oc}$  and  $G_{\rm sc}$  of the CdTe1 module are shown for the four different test sites. In Figure 5.8a, the  $R_{\rm oc}$  values for

#### Degradation Analysis and Modeling of CdTe Outdoor Data

Cologne and Tempe are shown. It can be seen that at the beginning the  $R_{\rm oc}$  values are similar. However, in Tempe the  $R_{\rm oc}$  value decreases faster and achieves lower values than the module in Cologne. After this consolidation phase, the degradation phase sets in. Here, the  $R_{\rm oc}$  value increases faster in Tempe than in Cologne. Although lower  $R_{\rm oc}$  values were obtained in Tempe during the consolidation phase, at the end of the exposure time, the  $R_{\rm oc}$  values at both countries are similar to each other due to the higher degradation rate in Tempe than in Cologne.

Comparing the  $R_{oc}$  behavior in Ancona and Chennai to each other, also here the consolidation phase and degradation phase show different behaviors (see Figure 5.8b). In Chennai, in only a few weeks the decreasing of the  $R_{\rm oc}$  value during the consolidation phase is over. After the consolidation phase, a relative high degradation rate sets in. In Ancona, however, the consolidation phase is much longer. At the beginning, the  $R_{\rm oc}$  values are similar for the modules in Ancona and Chennai. However, after the consolidation phase, the  $R_{oc}$  values in Ancona are much lower than in Chennai. The degradation in Ancona, however, is lower than in Chennai. The CdTe1 module shows in Ancona another interesting behavior. In the consolidation phase, a change of the slope is observed around week 17. After week 17, the  $R_{\rm oc}$  decreases stronger than before. This can be explained by considering the module temperature and in-plane solar irradiance. It has been measured that the maximum in-plane irradiance and module temperature both increase after week 17 (for a detailed view of the weekly measured module temperature and in-plane irradiance, it is referred to Appendix A). It appears that the rate of the change in  $R_{\rm oc}$ is at least in part governed by the irradiance and/or the temperature.

Table 5.3. – Key data of the consolidation and degradation phase for the  $R_{\rm oc}$  analysis of the CdTe1 module at the test sites in Cologne, Ancona, Tempe, and Chennai.

Test site	Duration of	Decreasing	Degradation rate
	Consolida-	during	after
	${f tion}$	Consolidation	Consolidation
Cologne	22 weeks	26%	$2 \times 10^{-4} \Omega \mathrm{cm}^2$
Ancona	30  weeks	30%	$9.6 \times 10^{-4} \Omega  {\rm cm}^2$
$\operatorname{Tempe}$	6  weeks	29%	$1.91 \times 10^{-3}  \Omega   \mathrm{cm}^2$
Chennai	5 weeks	27%	$2.56 \times 10^{-3} \Omega  \mathrm{cm}^2$

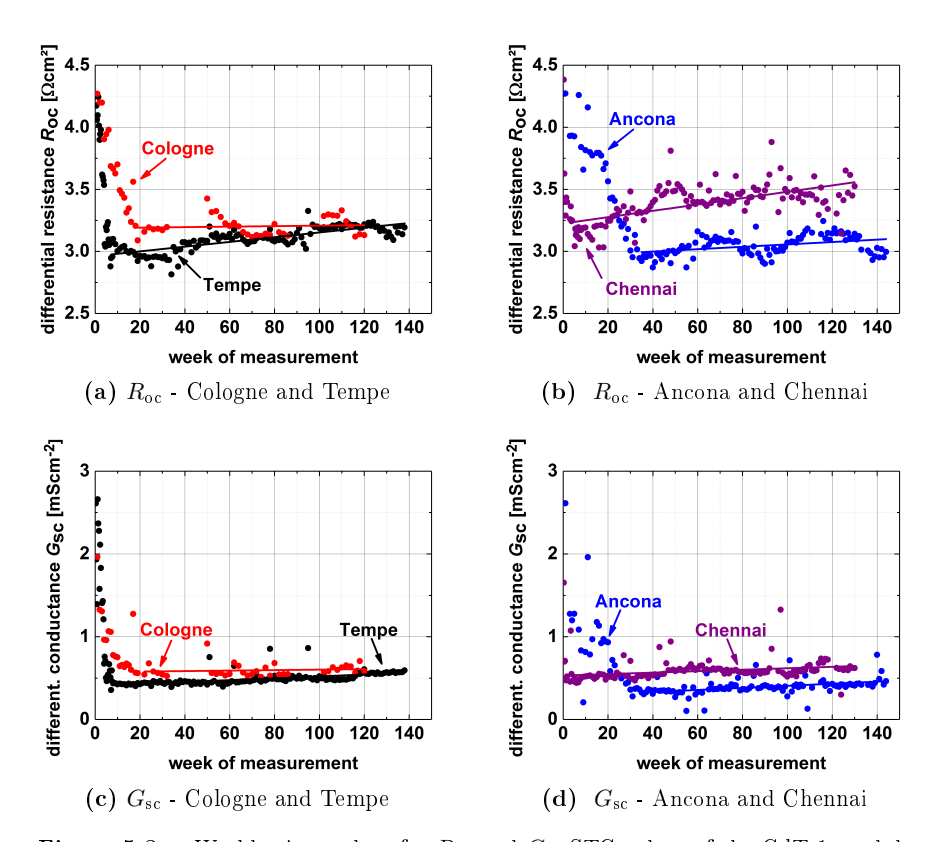


**Figure 5.8.** – Weekly time values for  $R_{\rm oc}$  and  $G_{\rm sc}$  STC values of the CdTe1 module for different climate zones. Shown are the values for a)  $R_{\rm oc}$  for Cologne and Tempe, b)  $R_{\rm oc}$  for Ancona and Chennai, c)  $G_{\rm sc}$  for Cologne and Tempe, and d)  $G_{\rm sc}$  for Ancona and Chennai.

In Table 5.3, the key data of the consolidation and degradation phases of the  $R_{\rm oc}$  values for the four test sites are summarized. It can be stated that similar to the  $V_{\rm oc}$  also for the  $R_{\rm oc}$  the degradation rate increases with increasing temperature. Also the duration of the consolidation time is linked to the temperature. In Chennai and Tempe higher temperatures and a shorter consolidation time are measured than in Ancona and Cologne. The decreasing of the  $R_{\rm oc}$  value during the consolidation phase seems to depend on the irradiance and gets lower with increasing temperature. The highest decreasing of  $R_{\rm oc}$  happens in Ancona and Tempe. Both locations show a

high irradiance. The lowest decreasing happens in Cologne and Chennai. In Chennai also a high irradiance occurs but also the highest temperature of all locations. The high temperature may damp the decreasing of  $R_{\rm oc}$ . In Cologne, the low decreasing of  $R_{\rm oc}$  can be explained with low irradiance that occurs here.

Considering the coefficient analysis of all modules, it can be stated that similar to the results of the CdTe1 module (see Section 5.2), the consolidation phase is due to a decreasing in voltage-dependent photo-current. The comparison of different locations indicates that this mechanism is stronger with high irradiance and low temperature. One explanation for this could be the annealing of trap defects in the material due to light soaking (see for example [13]).

Another point that needs to be considered is the seasonal variations of  $R_{\rm oc}$ . It can be seen for Cologne in Figure 5.8a and Ancona in Figure 5.8b that during the degradation phase  $R_{\rm oc}$  gets worse during the winter times (see for the temperature bars the Appendix C.1) and better during the summer times. For Chennai and Tempe, these seasonal effects are not so clear visible. Considering the irradiance and temperature variations for these test sites (see Figure 3.2 and Appendix A), it can be seen that in Cologne and Ancona the irradiance depends more on the seasons that in Chennai and Tempe. This shows again that the metastable effects in the CdTe modules have a lower influence at regions with high temperature and low irradiance fluctuations.

In Figure 5.8c and Figure 5.8d, the  $G_{\rm sc}$  behavior is shown for Cologne, Tempe, Ancona, and Chennai. It can be seen that in Cologne the  $G_{\rm sc}$  value decreases less in the consolidation phase than in Tempe. In Chennai the  $G_{\rm sc}$  value decreases less in the consolidation phase than in Ancona. In Tempe and Chennai the consolidation phases are much shorter than in Cologne and Ancona. Further, in Ancona the consolidation phase of  $G_{\rm sc}$  shows a change in the slope after week 17. It can be summarized that the statements that were made for  $R_{\rm oc}$  regarding the consolidation phase can be repeated for  $G_{\rm sc}$ . However, the  $G_{\rm sc}$  values decrease compared to their initial values much stronger than the  $R_{\rm oc}$ . In Cologne they decrease about 72%, in Ancona about 88%, in Tempe about 83%, and in Chennai about 72%.

Also a degradation phase can be observed for  $G_{\rm sc}$  for all four locations. However, compared to the decreasing during the consolidation phase, the increasing of  $G_{\rm sc}$  during the degradation phase has in all four locations only a small effect on the  $G_{\rm sc}$  value. Nevertheless, for a complete degradation analysis is has to be considered. It should also be mentioned that, compared to  $R_{\rm oc}$ , no seasonal variations can be observed in all four locations.

#### 5.3.3. Results for the maximum power density and fill factor

After the detailed coefficient analysis and the comparative analysis for different modules and different locations considering  $V_{\rm oc}$ ,  $G_{\rm sc}$ , and  $R_{\rm oc}$ , finally the previous obtained results are used for a general description of the fill factor and the maximum power density for all 12 modules.

In Figure 5.9, the changes of the fill factor for all 12 modules are shown. The abbreviation on the x scale defines the considered module. The modules are classified by their location and number. The abbreviations for the locations are: Ge - Germany, It - Italy, Az - Arizona, and In - India. The CdTe1 module in Germany is therefore as example classified as "Ge1".

The changes are divided in a) the consolidation and b) degradation phase. For the consolidation phase, the changes between the initial value and the value at the end of the consolidation phase is considered, according to

$$\Delta FF = FF(t_{\text{con}}) - FF(0) \quad , \tag{5.7}$$

with  $t_{\rm con}$  the time of the consolidation phase. For the degradation phase,  $\Delta FF$  is determined with a linear fit and then an average yearly change is determined. The results of  $\Delta FF$  are shown in Figure 5.9 with a black line.

In a next step, the influence of  $R_{\rm oc}$ ,  $G_{\rm sc}$ , and  $V_{\rm oc}$  on the fill factor has been determined. The method for this is based on the results of Section 5.2.4. For this, the fill factor is determined again with a stable  $R_{\rm oc}$  ( $FF_{\rm Roc}$ ), a stable  $G_{\rm sc}$  ( $FF_{\rm Gsc}$ ), and a stable  $V_{\rm oc}$  ( $FF_{\rm Voc}$ ). Afterwards, the difference to the real fill factor is determined by

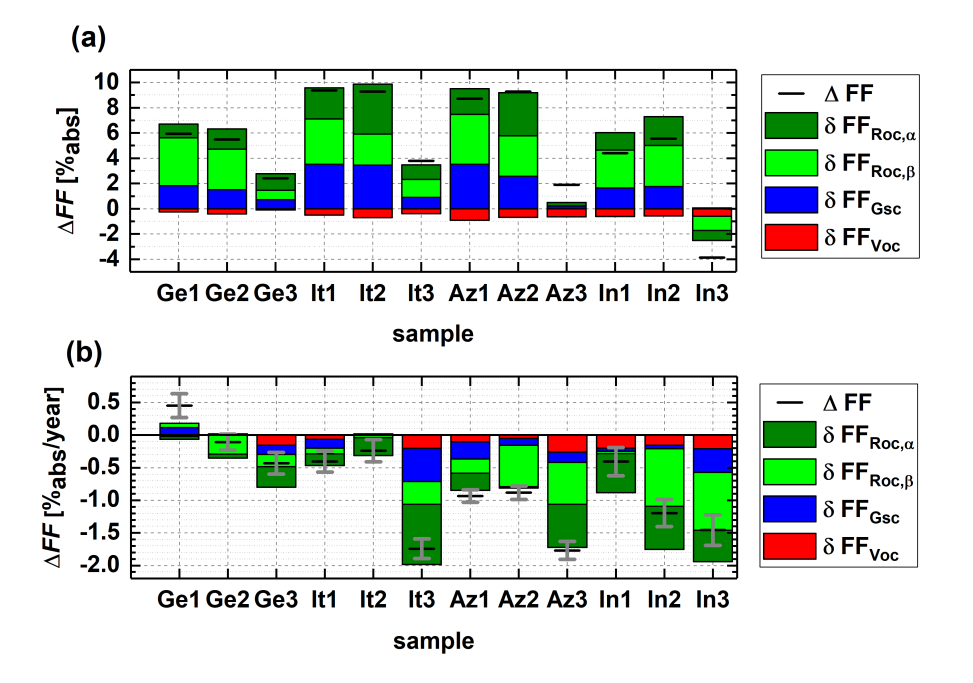


Figure 5.9. – Changes of fill factor for all 12 modules. Shown are the changes in a) the consolidation and b) the degradation phases. In addition, also  $\delta FF_{\rm Noc}$ ,  $\delta FF_{\rm Roc}$ ,  $\delta FF_{\rm Roc}$ , and  $\delta FF_{\rm Gsc}$  are shown.

$$\delta FF_{x} = \Delta FF - \Delta FF_{x}$$

$$= FF (t_{\text{con}}) - FF_{x} (t_{\text{con}}) , \qquad (5.8)$$

with  $x = \{\text{Voc}, \text{Roc}, \text{Gsc}\}$ . For the degradation phase, an annual average change is determined with a linear fit, which is indicated as  $\Delta FF_x$ . Afterwards,  $\delta FF_x = \Delta FF - \Delta FF_x$  is determined. It can be assumed that  $\Delta FF$  can then be calculated in a first order by

$$\Delta FF = \delta FF_{\text{Voc}} + \delta FF_{\text{Roc}} + \delta FF_{\text{Gsc}} \quad . \tag{5.9}$$

With this equation, the influence of  $R_{\rm oc}$ ,  $G_{\rm sc}$ , and  $V_{\rm oc}$  can be determined for the consolidation and degradation phase.

In the previous section, it has been shown that  $R_{\rm oc}$  can be considered as a sum of  $\beta_{\rm Roc}T_{\rm ref}/J_{\rm sc,ref}$  and  $R_{\rm s,\ Tref}$ . For a further insight into the influence of  $R_{\rm oc}$ ,  $\delta FF_{\rm Roc}$  has been divided into the influence of the  $R_{\rm s,\ Tref}$  term  $(\delta FF_{\rm Roc,\alpha})$  and into the influence of the  $\beta_{\rm Roc}T_{\rm ref}/J_{\rm sc,ref}$  term  $(\delta FF_{\rm Roc,\beta})$ . With this,  $\Delta FF$  can be described with

$$\Delta FF = \delta FF_{\text{Voc}} + \delta FF_{\text{Roc},\alpha} + \delta FF_{\text{Roc},\beta} + \delta FF_{\text{Gsc}} . \tag{5.10}$$

The results are shown in Figure 5.9. First of all, it can be observed that Equation 5.10 fits in general well to the data, especially for the consolidation phase. Considering the CdTe1 and CdTe2 modules in Germany, Italy, and Arizona, the difference between  $\Delta FF$  calculated with Equation 5.8 and Equation 5.10 is smaller than 9% (relative). The CdTe3 modules show higher fluctuation in the consolidation phase. Especially in Arizona, it has been difficult to determine the changes of the different parameters. This explains the higher deviation here between the direct calculated  $\Delta FF$  and the one with Equation 5.10. For India, it is in general difficult to determine the values of the consolidation phase as it is very short (<one week). For CdTe3, no clear consolidation phase could be observed in India as the consolidation phase is overlapped by a strong degradation phase, followed by a second smaller degradation. As no clear consolidation phase for the CdTe3 module could be determined, the entire changes due to the first degradation phase are taken into account for the consolidation phase. This should be considered when the results for

the CdTe3 module in India are considered.

For the degradation phase, the difference between the direct calculated  $\Delta FF$  and the one calculated with Equation 5.10 is small for the CdTe modules measured in Italy and Arizona (<20% - relative). For Cologne and India, the deviations are higher. The reason is that for Cologne in the winter times many data are missing which makes the linear fits more difficult to determine. The degradation time of India suffers under high fluctuations of the data which makes it also difficult to determine linear fits. Nevertheless, also here the main influences on FF can be determined.

The linear fits which are made for the degradation phase are influenced by fluctuation of the considered data. As a reference, the standard deviation for  $\Delta FF$  is given. It should be noted that also of course a standard deviation exists for  $\delta FF_{\rm Voc}$ ,  $\delta FF_{\rm Roc,\alpha}$ ,  $\delta FF_{\rm Roc,\beta}$ , and  $\delta FF_{\rm Gsc}$ . However, for better understanding of the plot only  $\Delta FF$  is given in Figure 5.9. Taking the standard deviation into account, it can be seen that the difference between the direct calculated  $\Delta FF$  and the one with Equation 5.10 is small.

Considering the data in the consolidation and degradation phase, it can be again stated that the CdTe1 and CdTe2 modules show similar behaviors, whereas CdTe3 suffers more under degradation. For all modules, the fill factor improves in the consolidation phase, except for the CdTe3 module in India. The CdTe1 and CdTe2 modules improve in each country more than the CdTe3 module. The best improvements of FF can be found in Italy and Arizona, with an FF improvement of almost 10% (abs) for the CdTe1 and CdTe2 modules. The improvements of FF is mainly due to  $G_{\rm sc}$  and  $R_{\rm oc}$ . The  $V_{\rm oc}$  degradation only plays a minor role for  $\Delta FF$ . In Section 5.2, it has been shown that the decreasing of  $R_{\rm oc}$  and  $G_{\rm sc}$  is linked to a decreasing of voltage-dependent photocurrent. However,  $R_{\rm oc}$  is the main driving force for the FF improvement. In general,  $\delta FF_{{\rm Roc},\beta}$  seems to be slightly bigger than  $\delta FF_{{\rm Roc},\alpha}$ . However, both terms have a big influence on the FF improvement.

The results of the previous sections in this chapter explain why the highest improvement can be found in Italy and Arizona as here the irradiance is high but the temperature not too much. This has a positive impact on the annealing of the metastable defects which then leads to a decreasing of  $R_{\rm oc}$  and  $G_{\rm sc}$  and therefore,

improves FF.

In the degradation phase,  $V_{\rm oc}$  decreases further for all modules. Also here,  $V_{\rm oc}$  does not show a high impact on FF. For the FF, it can be observed that it decreases for all modules. The highest degradation of the FF in each location can be observed for the CdTe3 module. For Italy, Arizona, and India it shows a degradation of more than 1.5% (abs) per year. The CdTe3 module in Italy degrades with 2% (abs) per year most of all modules. For the CdTe1 and CdTe2 modules, again a similar behavior is observed. These two modules degrade most in the two hottest locations: Arizona and India. All modules show in Germany the lowest degradation. This indicates again that the degradation process is influenced mostly by the temperature. Considering the influence of FF, it can be again stated that  $R_{\rm oc}$  plays the major role. The influence of  $G_{\rm sc}$  is not really important anymore in the degradation phase.

The question arises how the results can now be translated to the maximum power density, the most important parameter considering energy yield calculations. This will be done in the following.

The maximum power density is the product of FF,  $V_{\text{oc}}$ , and  $J_{\text{sc}}$ . The initial maximum power density  $P_{\text{mpp}}^0$  can therefore be calculated as

$$P_{\rm mpp}^0 = FF^0 \times V_{\rm oc}^0 \times J_{\rm sc}^0 \quad . \tag{5.11}$$

In Section 5.2, it has been shown that it is best to calculate  $P_{\rm mpp}$  with a constant  $J_{\rm sc}$  to reduce the influence of the high fluctuations of  $J_{\rm sc}$ . Therefore,  $P_{\rm mpp}$  will be calculated in the following only with  $J_{\rm sc}^0$ . This means that for  $P_{\rm mpp}$  it is only important to calculate the influence of FF and  $V_{\rm oc}$  on  $P_{\rm mpp}$ . The results of the behavior of  $P_{\rm mpp}$  for all modules during the outdoor exposure can be seen in detail in Appendix C.2.5.

The  $P_{\rm mpp}$  is again divided in a consolidation and a degradation phase. For the consolidation phase, the change of  $P_{\rm mpp}$  is calculated with

$$\Delta P_{\rm mpp} = P_{\rm mpp} \left( t_{\rm con} \right) - P_{\rm mpp}^{0} . \tag{5.12}$$

For the degradation phase,  $\Delta P_{\text{mpp}}$  is calculated by using a linear fit of the weekly

Degradation Analysis and Modeling of CdTe Outdoor Data

 $P_{\rm mpp}$  data and transform it to an average annual change.

Considering the change of  $P_{\rm mpp}$ , it can be stated with Equation 5.11 and Equation 5.12:

$$P_{\text{mpp}}^{0} + \Delta P_{\text{mpp}} = J_{\text{sc}}^{0} \times \left(V_{\text{oc}}^{0} + \Delta V_{\text{oc}}\right) \times \left(FF^{0} + \Delta FF\right)$$

$$= J_{\text{sc}}^{0} V_{\text{oc}}^{0} FF^{0} + J_{\text{sc}}^{0} V_{\text{oc}}^{0} \Delta FF +$$

$$J_{\text{sc}}^{0} FF^{0} \Delta V_{\text{oc}} + J_{\text{sc}}^{0} \Delta FF \Delta V_{\text{oc}} .$$

$$(5.13)$$

From Equation 5.13,  $\Delta P_{\text{mpp}}$  is obtained with:

$$\Delta P_{\text{mpp}} = J_{\text{sc}}^{0} V_{\text{oc}}^{0} \Delta FF + J_{\text{sc}}^{0} FF^{0} \Delta V_{\text{oc}} +$$

$$J_{\text{sc}}^{0} \Delta FF \Delta V_{\text{oc}}$$

$$= P_{\text{mpp}}^{0} \times \frac{\Delta FF}{FF^{0}} + P_{\text{mpp}}^{0} \times \frac{\Delta V_{\text{oc}}}{V_{\text{oc}}^{0}} +$$

$$P_{\text{mpp}}^{0} \times \frac{\Delta FF}{FF^{0}} \times \frac{\Delta V_{\text{oc}}}{V_{\text{oc}}^{0}} .$$

$$(5.14)$$

It should be noted that for the degradation phase, the values at the end of the consolidation phase are used instead of the initial values in Equation 5.14.

From Equation 5.14, it can be derived that the changes of  $P_{\rm mpp}$  can be divided in three terms. The first term  $(P_{\rm mpp}^{\rm FF}=P_{\rm mpp}^0\times\frac{\Delta FF}{FF^0})$  depends only on the change of the fill factor, the second term  $(P_{\rm mpp}^{\rm Voc}=P_{\rm mpp}^0\times\frac{\Delta V_{\rm oc}}{V_{\rm oc}^0})$  depends on the change of the  $V_{\rm oc}$ , and the third term  $(P_{\rm mpp}^{\rm mixed})$  is a mixed term.

In Figure 5.10, the results of the  $P_{\rm mpp}$  changes are shown. As a reference, the direct calculated  $\Delta P_{\rm mpp}$  is also shown including its standard deviation. The difference between the direct calculated  $\Delta P_{\rm mpp}$  and the one with Equation 5.14 is highest for the degradation phase for Cologne and India. The reasons for this are the same as for the previous calculated  $\Delta FF$  (lack of data and high fluctuations).

Considering all 12 modules in the consolidation phase, it can be stated that the increase of  $P_{\rm mpp}$  in the consolidation phase is only due to the fill factor. The increase is reduced a little bit by the degradation of  $V_{\rm oc}$ . This is also why the  $P_{\rm mpp}$  behavior is similar to the FF behavior: The CdTe1 and CdTe2 show similar improvements

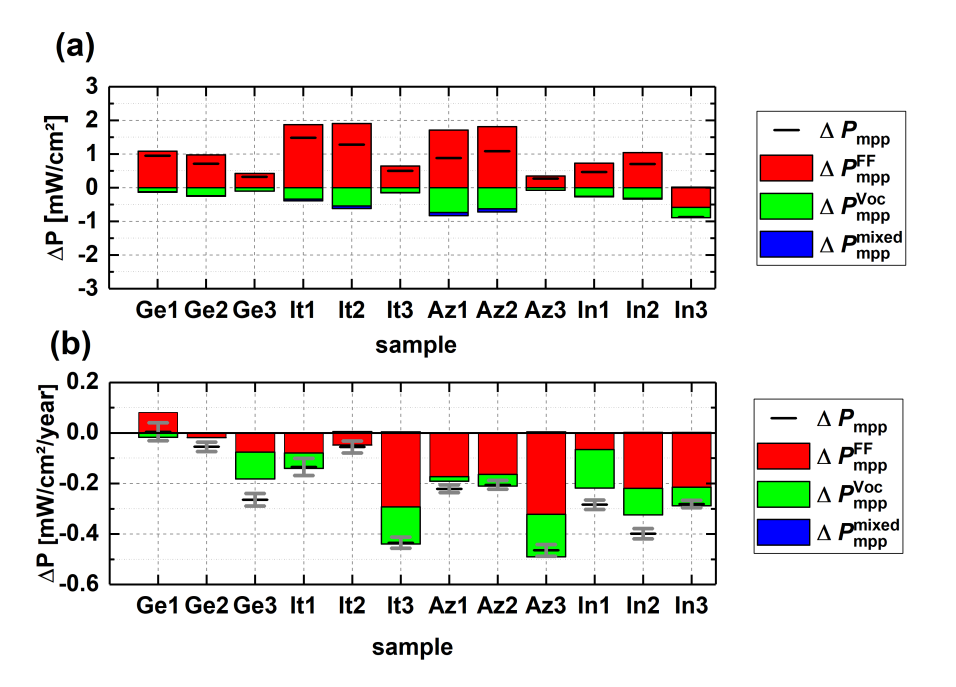


Figure 5.10. – Changes of maximum power density for all 12 modules. Shown are the changes in a) the consolidation and b) the degradation phases. In addition, also the three terms  $P_{\rm mpp}^{\rm FF}$ ,  $P_{\rm mpp}^{\rm Voc}$ , and  $P_{\rm mpp}^{\rm mixed}$  are shown.

and show higher improvements than the CdTe3 module. The highest improvements are obtained for the CdTe1 and CdTe2 modules in Italy and Arizona. The influence of the mixed term  $(P_{\text{mpp}}^0 \times \frac{\Delta FF}{FF^0} \times \frac{\Delta V_{\text{oc}}}{V_{\text{oc}}^0})$  does not have a big influence on  $\Delta P_{\text{mpp}}$ .

Considering the degradation behavior,  $P_{\rm mpp}$  decreases for all modules except for the CdTe1 module in Germany. The degradation of the other modules is again mainly influenced by the fill factor. Only for the CdTe3 module in Germany and the CdTe1 module in India, the degradation of  $V_{\rm oc}$  influences the degradation of  $P_{\rm mpp}$  stronger than the degradation of FF.

In summary, it can be stated that for the consideration of the energy yield of CdTe modules, it has to be distinguished between the consolidation and the degradation phase. The phases depend on the considered module and location whereas

Degradation Analysis and Modeling of CdTe Outdoor Data

high irradiance and low temperature lead to good improvements in the consolidation phase. For the degradation phase, it is more important to have low temperatures. For the understanding of the energy yield changes, it is most important to understand the behavior of  $R_{\rm oc}$  as  $R_{\rm oc}$  is the most important influence factor of FF, which is the most important influence factor of  $P_{\rm mpp}$ . The  $R_{\rm oc}$  value is driven by metastable effects and long term degradation. Therefore, it is essential to consider these effects in an energy yield performance model. In the following, a performance model which considers both effects is introduced.

#### 5.3.4. An empirical dynamic performance model

In the previous sections, the consolidation and degradation phases of CdTe modules have been investigated in detail. It was also shown that the  $R_{\rm oc}$  parameter is a very important parameter for the CdTe module performance.

In this section, an empirical dynamic performance model will be introduced to describe metastable and long term degradation effects. As an example, the model will be used to model the behavior of  $R_{\rm oc}$  for the CdTe1 module. The output of this model will be compared to the weekly average STC values of the  $R_{\rm oc}$  that are determined with the KH model. As described in Section 3.1, the back-of-module temperature and the in-plane irradiance were measured every 10 minutes. These data are used as the input for the empirical model. For the change of the  $R_{\rm oc}$  due to irradiance and temperature, a basic Arrhenius term is used according to

$$\frac{\delta R_{\rm oc}}{\delta t} = -a_1 \times G \times (R_{\rm oc} - R_0) \times \exp\left(\frac{-E_A}{kT}\right),\tag{5.15}$$

with t the time in weeks,  $a_1$  a fitting constant, G the in-plane-irradiance,  $R_0$  the limitation for  $R_{oc}$ ,  $E_A$  the activation energy, k the Boltzmann constant, and T the module temperature.

With the Arrhenius term, the decreasing of  $R_{\rm oc}$  at the beginning is described. The degradation and seasonal information are described with  $R_0$  according to

$$R_0 = a_2 + a_3 \times t + a_4 \times G, (5.16)$$

with the fitting constants  $a_2...a_4$ . The term  $a_3 \times t$  describes the long-term degradation and the term  $a_4 \times G$  the seasonal variation as well as the consolidation value. With  $a_1...a_4$  and  $E_A$  five constants need to be determined. The equations were fitted to the STC values obtained by the KH fit. The values of the fitting constants  $a_1...a_4$  as well as  $E_A$  are shown in Table 5.4. All constants were set to the same value for all four test sites. Only for the degradation term, the coefficient  $a_3$  is only valid for the hot regions Chennai and Tempe. For the colder regions, the coefficient was set to 0, i.e. the degradation term was neglected.

**Table 5.4.** – Values for the constants  $a_1...a_4$  and  $E_A$  of Equation 5.15 and Equation 5.16.

Constant	Value	
Activation Energy $E_A$	$1.2\mathrm{eV}$	
Prefactor $a_1$	$3.3069 \times 10^{10}  \mathrm{m^2 / W / s}$	
Reference value $a_2$	$4.84\Omega~\mathrm{cm}^2$	
Degradation rate $a_3$	$1.4550 \times 10^{-8}  \Omega   \mathrm{cm^2/s}$	
	(Chennai and Tempe);	
	0 (Cologne and Ancona)	
Irradiation factor $a_4$	$-2.64  imes 10^{-7}  \Omega   \mathrm{cm}^4   /\mathrm{W}$	

In Figure 5.11, the results of the simulation for  $R_{\rm oc}$  are shown for the four different test sites and are compared to the data from the KH fit that are calculated on a weekly basis. The simulation data are derived from solving Equation 5.15 with the measured T and G values on a 10 minute basis. As a start value of the simulation, the initial STC value of  $R_{\rm oc}$  from the KH fit was taken. It can be seen that all four simulations show a very good agreement with the STC values. The simulation data follows well the obtained trends of the STC values.

This work shows that a simple rate equation such as presented in Equation 5.15 and Equation 5.16 can adequately describe the dynamic behavior of metastable solar cells under various conditions.

### 5.4. Conclusion

In this chapter, the KH model has been used to analyze the CdTe metastable and degradation behavior. The fill factor is influenced mainly by the  $R_{\rm oc}$  and in second

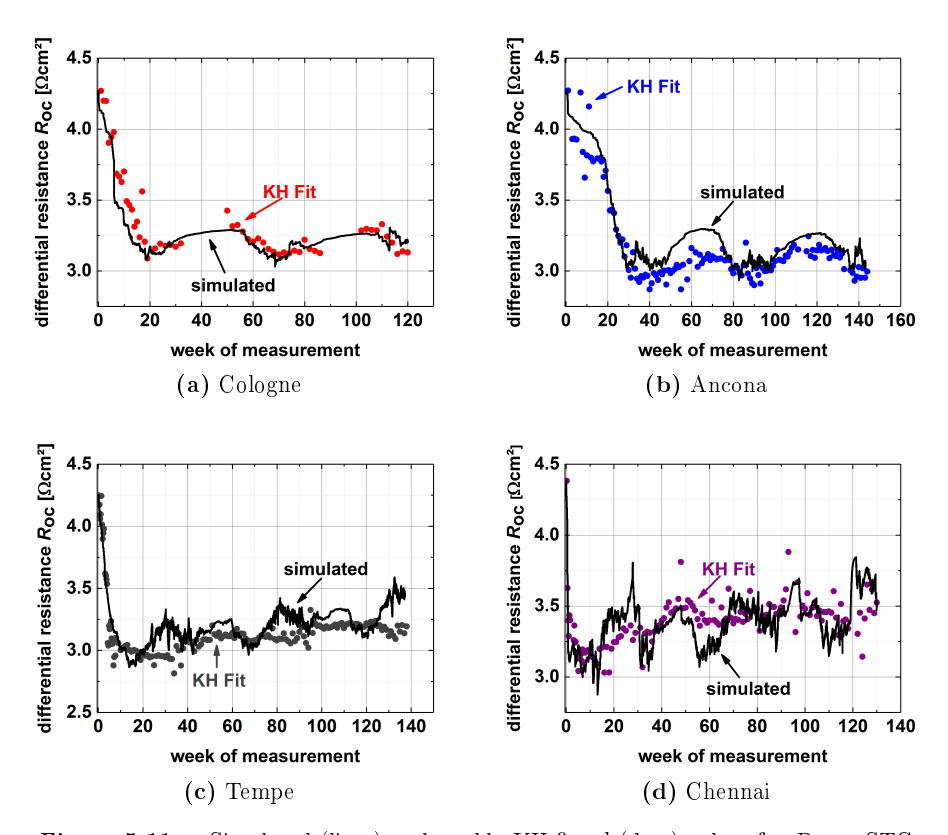


Figure 5.11. – Simulated (lines) and weekly KH fitted (dots) values for  $R_{\rm oc}$  at STC of the CdTe1 module. Shown are the data for a) Cologne, b) Ancona, c) Tempe, and d) Chennai.

order by the  $G_{\rm sc}$ . The fill factor first improves and then degrades slowly and so do the  $R_{\rm oc}$  and  $G_{\rm sc}$ . In total,  $R_{\rm oc}$ ,  $G_{\rm sc}$ ,  $P_{\rm mpp}$ , and FF can be divided in two parts, namely consolidation and degradation phase.

The translation equations of the KH model allow an in-depth analysis of the consolidation and degradation phases by investigating the coefficients of these equations. Doing so, it has been analyzed that the decreasing of  $G_{\rm sc}$  and  $R_{\rm oc}$  during the consolidation phase have to be separated from the increasing of both parameters in the degradation phase. The consolidation phase and seasonal variation are strongly influenced by metastable effects. During the consolidation phase and summer pe-

riods, the effect of voltage-dependent photo-current are reduced. Here, the driving force seems to be the irradiance. However, the degradation phase is more influenced by the temperature. With increasing temperature, the three parameters  $V_{\rm oc}$ ,  $R_{\rm oc}$ , and  $G_{\rm sc}$  degrade more and faster. One explanation for this may be the diffusion of Cu from the back-contact. However, for this a more detailed module investigation is necessary.

The degradation analysis can be done for all modules. All modules show a consolidation and a degradation phase. The detailed behavior of CdTe depends on the considered module and climate zone. However, it can be stated that the  $V_{\rm oc}$  degrades for all modules and climate zones. In warmer regions, the degradation is faster than in colder regions. For the short circuit current, no degradation could be observed. The  $R_{\rm oc}$  shows in some locations in addition to the degradation a seasonal variation, i.e. it is metastable. In winter times, it increases and in summer time  $R_{\rm oc}$  decreases. The characteristic of the consolidation and degradation phases depend on the climate zone and module.

The analysis of CdTe is then used to describe the general behavior and influence parameter of the FF and  $P_{\rm mpp}$  of all 12 CdTe modules. It can be stated that the metastable behavior of  $R_{\rm oc}$  is one of the most important parameters that influence the performance of the CdTe modules. Understanding the  $R_{\rm oc}$  behavior will have an important influence on the performance prediction.

Based on the parameter analyzing, an empirical dynamic performance model for  $R_{\rm oc}$  of the CdTe1 module was developed, which uses as input parameters just the initial  $R_{\rm oc}$  value, the time, the temperature and irradiance on a 10-minute interval. The developed rate equation describes the two phases of the  $R_{\rm oc}$  behavior and the seasonal variation with one equation and the same coefficients for all four climate regions. Only for the degradation term a division has been made between warm regions (Chennai and Tempe) and cold regions (Ancona and Cologne).

# 6. A new model for degradation and annealing of *a*-Si:H solar cells

In this chapter, finally the approach for a physical dynamic performance model will be investigated. The investigation is done for a-Si:H solar cells as already much is known about their metastable behavior. In Section 6.1, an overview is given about the degradation and annealing effects of a-Si:H. In Section 6.2, the results of the light-soaking experiment are shown. These results are used then in Section 6.3 to develop a dynamic performance model.

# 6.1. Annealing and degradation effects

It could be shown that the KH model is suitable to do analysis of outdoor thin film photovoltaic. This includes analysis of degradation effects (see Chapter 5) and short-term energy yield prediction (see Section 4.4). However, to improve the energy yield prediction, the degradation and annealing effects have to be included into the performance model. Until now no performance model exists that includes a suitable degradation model for outdoor modules. The most common approach for long-term prediction is to use degradation rates that were calculated before (see for example [12]). However, degradation rates are influenced by several factors.

In Chapter 5, a first empirical dynamic performance model for  $R_{\rm oc}$  for CdTe has been implemented. However, to obtain a physical consistent dynamic performance model, the causes of the metastable and degradation effects have to be investigated and modeled.

For a comprehensive performance model, metastable effects are very important to include. Only these factors can describe fast degradation and annealing effects at the beginning (see Chapter 5) and seasonal variations. Of course, the metastable effects depend on the investigated thin-film technology. This is why a model considering metastable effects of one technology cannot applied directly to another technology. In this chapter, a dynamic performance model will be developed for a-Si:H. Many investigations for the performance of a-Si:H modules taking metastable defects into account exist already (see [133, 17]). The effect that leads to the degradation effect of a-Si:H solar cells is called "Staebler-Wronski-effect" and was discovered almost 40 years ago [87]. In the following, the degradation and annealing effects of a-Si:H will be investigated further.

The Staebler-Wronski-effect describes the metastable change of a-Si:H material and solar cells upon exposure to light and application of a certain bias and temperature. The state of a light exposed solar cell is generally degraded with respect to the as-deposited state which is why it is often described as "light-induced degradation". However, the degradation effect is reversible. Hence, in response to changes in temperature, irradiation and bias conditions, the state of a solar cell changes for better or worse. This can be observed in seasonal variation of the energy output at same conditions for example at standard test conditions. Thus, describing the performance of those solar cells, it is necessary to include the Staebler-Wronski-effect into the calculation. Nevertheless, the detailed physics behind it has never been understood completely. Hence, multiple models exist for this effect [134, 135, 136], trying to explain the degradation effects on a microscopic level. Nevertheless, no consensus about the right model exists among the authors. Therefore, a brief overview of already existing models and main literature will be given in the following.

One of the widely used models is the "bond-breaking model" [137]. The bond-breaking model is based on the assumption that the recombination of photoexcited electron-hole pairs leads to a breaking of weak Si-Si bonds. This leads to so called dangling bonds which produce amphoteric electronic states near midgap [138]. Stutzmann  $et\ al.$  have experimentally found the dependence of the dangling bond concentration N on the time t and on the electron-hole pair generation rate G [139]:

$$N \propto G^{\frac{2}{3}} t^{\frac{1}{3}}$$
 (6.1)

This analysis depends on electron spin resonance (ESR) measurements of the neutral dangling bonds. Equation 6.1 shows that the degradation depends on the illumination time and intensity. However, the dependence  $N \propto t^{1/3}$  is only valid for specific time ranges [134]. At the beginning, the degradation is faster than after a few hours. For long times, the induced defects finally reach a saturation value  $N^{eq}$  which depends on the light intensity G as [139]

$$N^{eq} \propto G^{\frac{1}{3}} \quad . \tag{6.2}$$

However, this is only valid for intrinsic a-Si:H. Degradation rates change if the Fermi level is shifted by doping [137].

Also annealing effects have to be considered when describing the performance of a-Si:H solar cells. It should be noted that strictly speaking any defect annihilation process refers to a heat treatment. However, in literature on a-Si:H degradation the term is commonly used to refer to any defect annihilation process, which is also how the term will be used in the following. In case of defect recovery due to thermal treatment, the term 'thermal annaling' will be used.

Stutzmann  $et\ al.$  also consider thermal annealing by an ESR transient analysis as described in [140]. Based on this, Stutzman  $et\ al.$  show that the annealing kinetics are monomolecular, with a thermally activated decay rate R [141]:

$$\frac{dN}{dt} = -R \times N \quad . \tag{6.3}$$

Furthermore, it was shown that the activation energies for defect annealing in intrinsic a-Si:H vary in the range of 0.7 eV to 1.5 eV [141]. All annealing investigations in [141] were carried out under dark conditions. For the annealing rate of defects, often 'fast' and 'slow' defects are distinguished [142]. Note, however, that a range of activation energies already implies a continuous range of annealing rates, i.e. this distinction of fast and slow defects should be considered to be a simplification. The literature values of the activation energy differ from each other. For example,

A new model for degradation and annealing of a-Si:H solar cells

Jang et al. tend to higher activation energies around 1.5 eV [143]. Nevertheless, also for the high activation energies, Bennett et al. divided the thermal annealing in an initial period of a very fast annealing and a much longer, second period process [144]. In addition, they also observed that the activation energy is a function of the material and does not depend on the temperature at which the solar cells are light soaked nor on the duration of the light soaking [144].

It has been found out that the annealing rate not only increases with temperature but also with light intensity [145]. This light-induced annealing effect was postulated for the first time by Redfield in 1986 [146]. Caputo *et al.* carried out several studies on this effect [147, 148, 149]. They introduced a model which combines the defect-creation rate based on the bond-breaking model with a light-induced annealing term [148]:

$$\frac{\delta N(E,X)}{\delta t} = C_{\text{sw}} n(x) p(x) \times P(E) - \lambda [n(x) + p(x)] \times N(E) \quad . \tag{6.4}$$

They assumed that the defect-annealing rate is proportional to the sum of the electron (n) and hole (p) densities. In Equation 6.4,  $C_{\rm sw}$  and  $\lambda$  are thermally activated constants, E is the energy level, P(E) is the Gaussian distribution, and x is the local coordinate in the cell, varying from the surface to the back of the solar cells. In a further step, this equation can be combined with a device simulation tool, to obtain a degradation model for solar cells as demonstrated by Caputo  $et\ al.$  [147].

Stutzmann et al. [134] described an activation energy of 0.04 eV for the obtained ESR spin density of dangling bonds, when the illumination takes place at low temperature ( $T \leq 90^{\circ}$ C). They concluded from their measurement that  $C_{\rm sw}$  can be described as [134]

$$C_{\rm sw}(T) = C_{\rm sw}(0) \times \exp\left(\frac{-0.04 \text{eV}}{kT}\right)$$
 (6.5)

The previous described approaches are all spatial resolved models. They need to be applied to the whole solar cell to explain its degradation.

The critical part for the degradation of a solar cell is the intrinsic (i-) layer of the a-Si:H solar cells. Experimental investigations show that with increasing i-layer thickness the degradation rates of the solar cells are faster than for the ones with thinner i-layer [90]. Equation 6.1 does not show a direct relation to the i-layer thickness. The explanation can be found in the internal electric field of the solar cells. By increasing the i-layer thickness, the internal electrical field of the solar cell decreases. Hence, compared to thin cells, the defects have a larger impact on the performance in thick cells. This will be showed in detail later in this chapter.

In summary, the literature review shows that the following aspects have to be considered: light-induced degradation, thermal annealing, and light-induced annealing. In the following, a new degradation model will be developed and verified that includes all of these three aspects. Therefore, first of all the light soaking experiment and its results will be introduced that are then used to verify the degradation model. The experiment covers all main aspects for the annealing and degradation effects together. The main aspects that influence the degradation and annealing are time of light exposure, light intensity, thickness of the solar cell, and temperature.

## 6.2. Light soaking experiment

For the experiment,  $10 \times 5$  cm<sup>2</sup> size samples were investigated, where each sample consists of  $12~1 \times 1~\text{cm}^2$  size a-Si:H solar cells. The degradation setup consists of 12~sample holders with a size of  $10.8 \times 11.8~\text{cm}^2$ . On each sample holder, two samples were fixed by vacuum. The sample holders' temperature could be regulated independently from each other. The temperature for all holders was set at  $50^{\circ}\text{C}$ .

First, a light intensity measurement of the degradation setup was performed with a crystalline reference cell. The light intensity in the degradation setup was measured at  $11 \times 7$  points. Figure 6.1 shows the results for the spatial intensity distribution in the degradation setup. The measured intensity is the integral response of the silicon photodiode to the incident spectrum, where the silicon diode detects the light in the spectral range from approximately 365 nm up to 1100 nm. It can be seen that in this range of the photodiode response the light intensity varies up to 10%, where the intensity drops toward the edges. The highest intensity is reached

A new model for degradation and annealing of a-Si:H solar cells

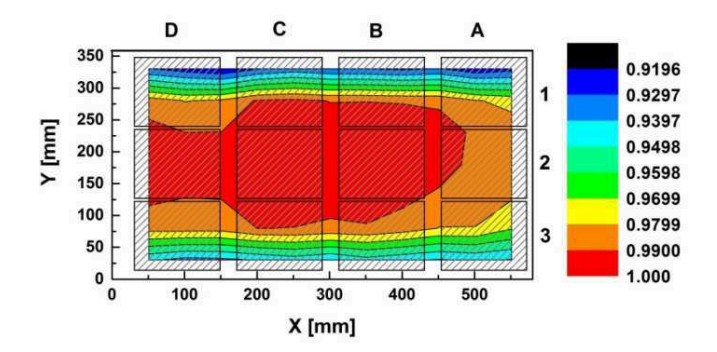


Figure 6.1. – Relative light intensity of the degradation set-up measured with a Si reference cell. The values are normalized to the highest measured value. The squares indicate the position of the sample holders. White space indicates not measured area.

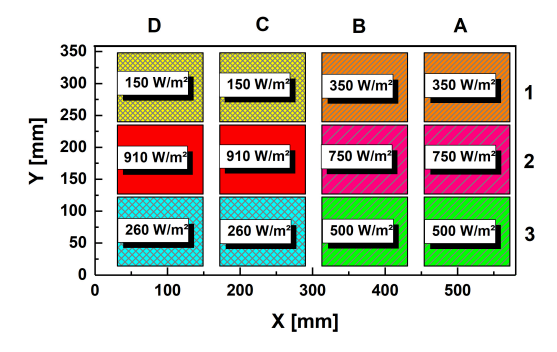


Figure 6.2. – Absolute light intensity of degradation set-up using grey filters. The squares indicate the position of the sample holders. The light intensity values are obtained by spectrum measurement in the middle of the sample holders. They are rounded to the nearest multiple of 10.

in the area D2 to B2. The intensity variation within the 1st row is stronger than the one in the 3rd row. In a second step, grey filters were used to achieve different intensities for the degradation experiment. The filters were positioned by taking the intensity distribution due to the lamps into account (see Figure 6.2). On the

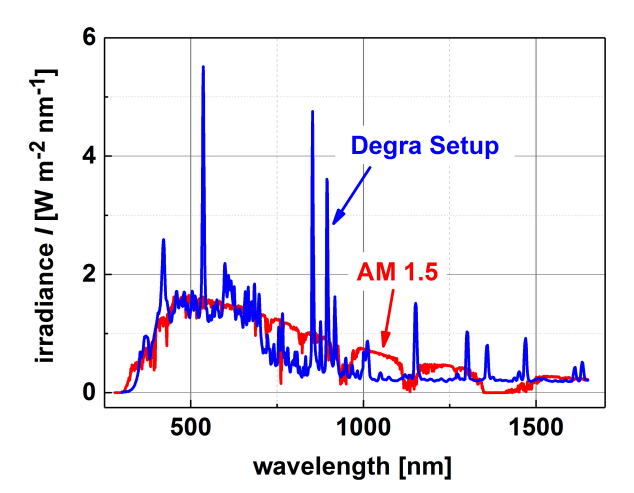


Figure 6.3. – Absolute irradiance of the degradation setup measured in the middle of position C2 without any grey filter (blue). In comparison, the AM 1.5 value is plotted as well (red line). Spectra are measured from 300 nm to 1650 nm.

positions C2 and D2 no grey filters were used. Furthermore, the light spectrum in the center of each sample holder were measured. In Figure 6.3, as an example, the spectrum for the degradation setup without grey filter is shown. The measurement was taken in the center of C2. The spectrum shows an intensity from around  $910\,\mathrm{W/m^2}$ . For comparison, also the AM 1.5 spectrum is plotted. In summary, 12 spectra were obtained (one for each sample holder position). The resulting intensities were then calculated from these measured spectra. Thereby, the following values were obtained:  $910\,\mathrm{W/m^2}$ ,  $750\,\mathrm{W/m^2}$ ,  $500\,\mathrm{W/m^2}$ ,  $350\,\mathrm{W/m^2}$ ,  $260\,\mathrm{W/m^2}$  and  $150\,\mathrm{W/m^2}$  (see also Figure 6.2).

## 6.2.1. Execution of the experiment

For the experiment, different a-Si:H cells were considered. All cells were fabricated after the same recipe but in different batches. Only the thickness of the i-layer was changed. The thickness of the p- and n-layer was kept constant at 10 nm and 20 nm, respectively. The total thickness of the investigated solar cell thicknesses

A new model for degradation and annealing of a-Si:H solar cells

were:  $150 \,\mathrm{nm}$ ,  $200 \,\mathrm{nm}$ ,  $300 \,\mathrm{nm}$ ,  $700 \,\mathrm{nm}$ . For every thickness six samples with  $12 \,\mathrm{1 \times 1 \, cm^2}$  solar cells were fabricated. So in total 288 solar cells were investigated.

First, all cells were measured under STC and in the dark at  $25\,^{\circ}$ C. Afterwards, the light soaking experiment was conducted. The experiment was divided in two parts. In part one of the experiment, one sample of every thickness was investigated under one of the six light intensities for 649 h. All samples were held at  $50\,^{\circ}$ C and degraded under open circuit. During the run, the cells were taken in regular time intervals from the degradation setup and were measured under STC and in the dark at  $25\,^{\circ}$ C.

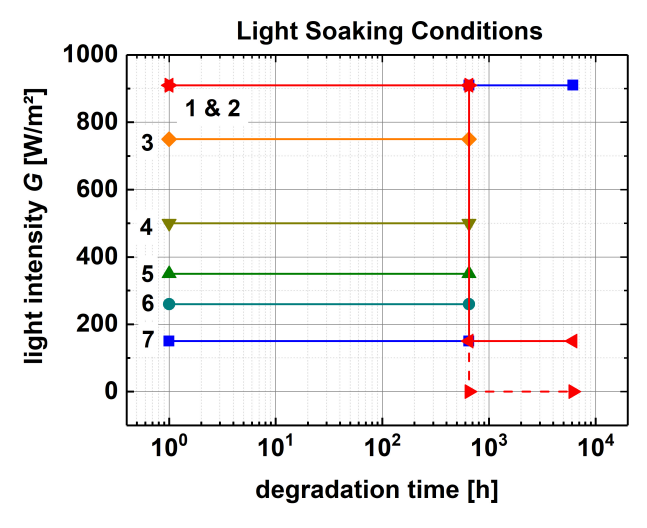


Figure 6.4. – Light soaking conditions for the experiment. The light changes are done for the high light intensity (1&2) and for the low light intensity (7). The light changes are done after 649 h. The other 4 light intensities are only considered in the first part of the light soaking experiment. Each of the seven runs was done for each solar cell thickness.

Then, in part two of the experiment, the degraded cells were divided in two groups. The first group contains all cells that were degraded under the following light intensities:  $750\,\mathrm{W/m^2}$ ,  $500\,\mathrm{W/m^2}$ ,  $350\,\mathrm{W/m^2}$ , and  $260\,\mathrm{W/m^2}$ . Those cells were annealed at  $160\,^\circ\mathrm{C}$  for 30 minutes. The second group consists of cells that were degraded under  $910\,\mathrm{W/m^2}$  and  $150\,\mathrm{W/m^2}$ . The cells that were degraded under  $150\,\mathrm{W/m^2}$  were then exposed to  $910\,\mathrm{W/m^2}$ . The cells degraded under  $910\,\mathrm{W/m^2}$ 

were split up in two groups. The first group was put under  $150 \, \mathrm{W/m^2}$  and the other group was placed in the dark. This was done for every thickness. The second run took an additional  $5470 \, \mathrm{h}$ . The overview of the light soaking experiment can be seen in Figure 6.4. Each run was carried out for each of the four solar cell thicknesses.

#### 6.2.2. Experimental results

As described in the previous subsection, seven different light soaking experiments for four different solar cell thicknesses were performed. In this section, the results of the experiment will be shown briefly.

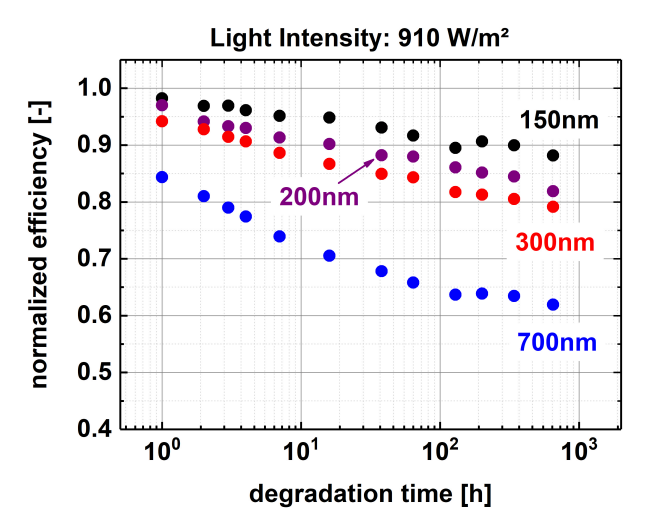


**Figure 6.5.** – Normalized efficiency for the four different solar cell thicknesses degraded under a light intensity of  $910 \text{ W/m}^2$  for 649 h.

Figure 6.5 shows the normalized efficiency of various solar cells during exposure with a light intensity of  $910 \, \mathrm{W/m^2}$ . The efficiencies are normalized to the initial efficiency of the respective cell. The investigated 700-nm thick solar cell has an initial efficiency of 10.97%, whereas the initial efficiencies of the 300-nm, 200-nm, and 150-nm thick solar cells are 10.23%, 9.76%, and 8.69%, respectively. After 100 hours the efficiencies of all solar cells begin to saturate. The strongest degradation is observed for the 700-nm thick solar cell. During the degradation time of  $649 \, \mathrm{h}$ ,

the solar cell lost almost 38% of its initial efficiency. On the other hand, the 150 nm one lost in the same time only 13% of its initial efficiency. The other two solar cell thicknesses are in between the values of the 150-nm and the 700-nm thick solar cells. It should be noted that to reduce the uncertainties due to fluctuations, the average value of the last four points were considered as saturation value of the respective solar cell.

Due to the high degradation rate of the 700-nm thick solar cell, this cell has with 6.79% the lowest absolute efficiency at the end of this light soaking experiment. The 150-nm thick solar cell still has an efficiency of 7.5%. The 200-nm and 300-nm thick solar cells have almost similar efficiencies with 8.07% and 8.1%, respectively.

Figure 6.6 shows a more detailed view on the solar cells degradation. Here, the degradation of the open voltage ( $V_{\rm oc}$ ) and the short circuit current ( $J_{\rm sc}$ ) for the 150-nm and 700-nm thick solar cell are considered. It can be seen that the open voltage degrades around 13% for both thickness. So the voltage's degradation is not very dependent on the solar cell thickness. The opposite is the case for the short circuit current. Here, strong dependencies on the solar cell thickness can be seen. In both cases, the short circuit reaches a saturation value after 100 h for the light intensity of 910 W/m². To reduce the uncertainties due to fluctuations, also here the average value of the last four points is considered as saturation value. By doing so, the short circuit current for the 150-nm thick solar cell lost only 2% of its initial value, whereas the short circuit current of the 700-nm thick solar cell degrades about 12%. So where in thin film solar cells the degradation in the open voltage is more critical than the one in the short circuit current, it is the opposite for thick a-Si:H solar cells.

From this part of the experiment two conclusions can be derived. First, due to the reached saturation value, the measured degradation range is suitable to determine the degradation rate under which the cells have suffered. Second, these results are consistent with the effect that a-Si:H solar cells with thicker i-layer degrade more than with thinner i-layer which is related to the internal electric field. Since the p- and n-layer were not changed, the 700-nm thick solar cells suffer from a smaller internal electric field than the thinner solar cells. Hence, compared to thin cells additional defects have a larger impact on the performance in thick cells.

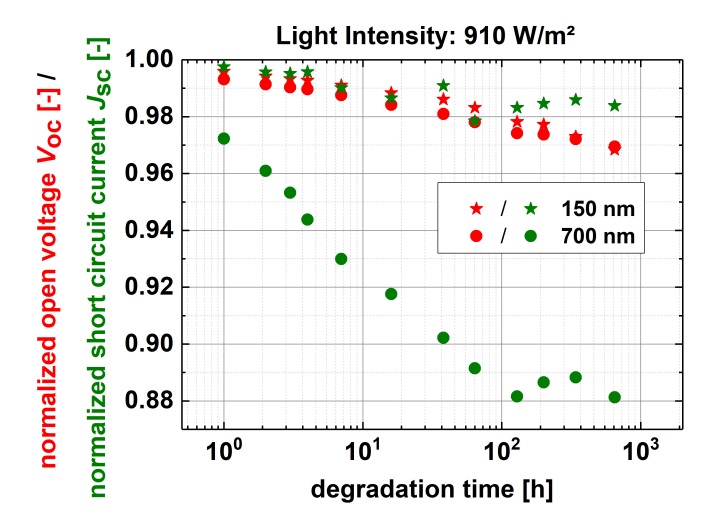


Figure 6.6. – Normalized open voltage (red) and short circuit current (green) for  $150 \,\mathrm{nm}$  (asterisk) and  $700 \,\mathrm{nm}$  (dots) solar cells. The cells were degraded for  $649 \,\mathrm{h}$  under  $910 \,\mathrm{W/m^2}$ .

Beside the different solar cell thicknesses, also the influence of different light intensities has been investigated. As an example, the results for this part of the experiment are shown in Figure 6.7 for the 700 nm thick solar cells. Before the light-sokaing experiment, the investigated cells were all in the same range of efficiency ( $\eta$ =10.5%...11%). From Figure 6.7, the light-induced degradation effect can be seen clearly. The cell under the lowest light intensity, i.e.  $150\,\mathrm{W/m^2}$ , degraded less. Here, the cell lost only 21% of its initial efficiency. Contrary, the cell degraded under the highest light intensity, i.e.  $910\,\mathrm{W/m^2}$ , degraded most. Here, the cell lost 38% of its initial efficiency. All other efficiency losses of the different light intensities are in between those two values.

Figure 6.8 shows finally results for the second part of the experiment, where the light intensities were changed for some of the cells. This change in the light intensity leads to new stabilized conditions. The 700-nm thick cells that were degraded under low light intensity (150  $\rm W/m^2)$  are subsequently exposed to a light intensity of 910  $\rm W/m^2$  (black squares). Upon this change, the efficiency decreased from 8.6% before the intensity change to 6.6% after 1800 h and so loses around 22%

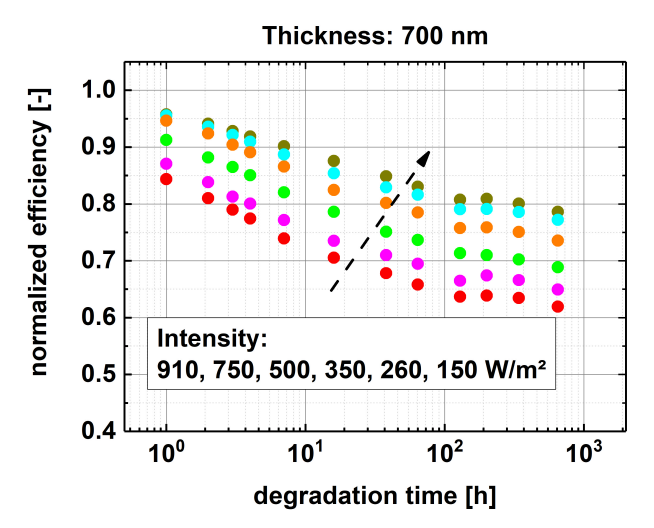


Figure 6.7. – Normalized efficiency for different light intensities for 700-nm thick solar cells. The degradation time was 649 h.

of its value before the light change. Comparing this to the first part of the experiment, this means that the cells under full light intensity degrade slower if they were degraded before under low light intensity. Without the pre-degradation the cell efficiency decreases with 38% in only 649 h. However, it can also be seen that the degraded state after a few 100 hours is comparable with the one from the first part of the experiment for the high light intensity, i.e. as if the first degradation step under low light intensity did not happen. After almost 3000 h the absolute efficiency was around 6.6% and so almost 40% lower than at the initial state.

After degradation under a light intensity of  $910\,\mathrm{W/m^2}$  some cells were kept in the dark at  $50\,^\circ\mathrm{C}$  (blue upwards triangles). For these cells, the cell efficiency increases from 6.6% to 8.5% in  $1840\,\mathrm{h}$ . This is an increase of 28%. After the thermal treatment, the cell efficiency was only 21% lower than at the initial state. This observed effect is the influence of thermal annealing.

Changing the light intensity from high to low intensity leads also to annealing effects (see red dots). Interestingly, the saturation efficiency of these cells is lower than the one of the cells that are degraded directly under the low light intensity. The inset in Figure 6.8 shows that until a degradation time of 1010 h, the cells under

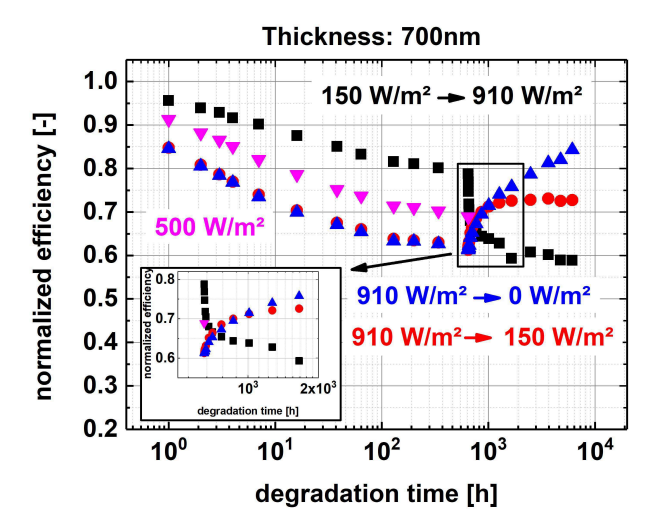


Figure 6.8. – Normalized efficiency for different light intensities and light changes for 700-nm thick solar cells.

low light intensity do anneal faster than those under dark conditions. This shows the existence of the light-induced annealing. After that time the efficiency reached a saturation efficiency of around 7.3%, i.e. 27% lower than the initial efficiency. Note, however, that in the dark the annealing progresses longer.

## 6.3. Simulation model

In Figure 6.9, the simulation procedure is illustrated. The model consists of a device simulation tool, for which here the Advanced Semiconductor Analysis (ASA) program [150] is used, and rate equations describing the evolution of metastable defects. In the device simulator, the information about the optical and electronic structure of the solar cell as well as the ambient condition are defined. From the device simulator, one obtains then the local defect distribution, the electron and the hole concentration at a time step t. These three parameters are then used in the degradation model. The degradation model itself consists of empirical rate equations. With these rate equations, the new defect concentration for the next time step  $t + \Delta t$  is calculated. With the new defect concentration and the device

simulator, one obtains the new device characteristics in time. This way, the rate equations can be integrated. In that procedure, the differential equations for defect creation and annealing are integrated for every position in the device. For this, the Octave solver "LSODE" (Livermore Solver for Ordinary Differential Equations) [151] was used. In addition, variable time steps were used. In the following two subsections, the parts of the simulation model (Device Simulator and Degradation Model) are explained in more detail.

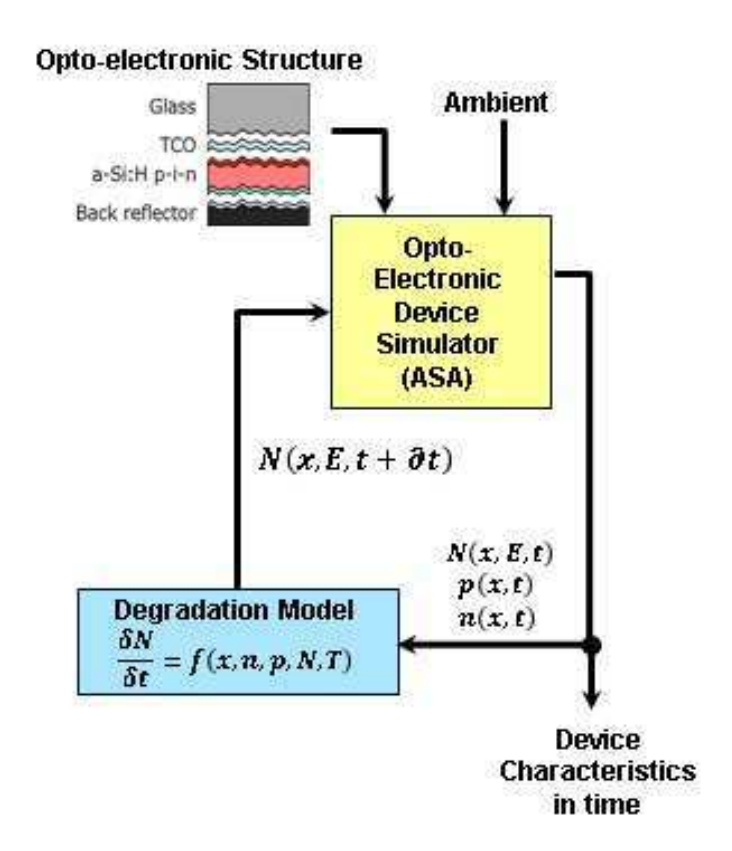


Figure 6.9. – Principle of the simulation model.

#### 6.3.1. Opto-electronic device simulator

The device simulator is one of the main parts for the simulation model. In this thesis, ASA has been chosen as the device simulator. ASA has been introduced in Section 2.2.1.

In a first step, the measured initial light and dark current-density (JV) curves of all solar cells are fitted with ASA to define the initial physical characteristic of the solar cells. For the fit, it was started with a basic parameter set derived from [20, 152, 153]. The shunt and series resistances were adapted via the dark JV curve. The fitting parameters were reduced to the electron and hole mobility, the density of states at the mobility valance and conduction band edge, the capture rate of holes and electrons in the tail states. Finally, a consistent parameter set were achieved with which a good fit were obtained for all dark and illumined JV characteristics for all thicknesses (i.e. using the same parameters for all devices apart from the thickness and a shunt resistance).

In Figure 6.10, an example for the fit for each thickness is shown. The fits show a good match with the measured JV curves. Considering the respective JV curve only in the fourth quadrant, the mean bias error between measurement and simulation for the thicknesses are: -6.15% (150 nm), 0.56% (200 nm), 1.09% (300 nm) and 5.9% (700 nm).

## 6.3.2. Degradation model

There are several rate equations describing defect creation and annealing. Considering literature and taking the light soaking experiment into account, it is justified to consider three influence terms, namely: light-induced degradation, light-induced annealing, and thermal annealing.

Hence, a first approach was using the rate equation from Caputo *et al.* [148] and combine it with a thermal annealing term from Stutzmann *et al.* [141]:

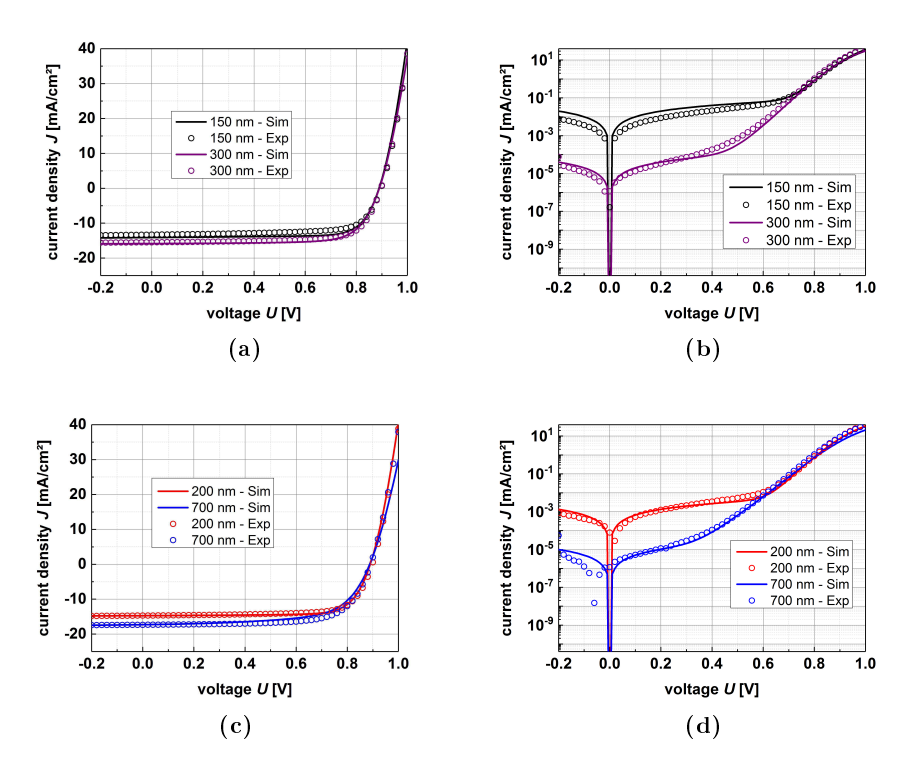


Figure 6.10. – Comparison between fit and measured dark and light JV curves for different thicknesses. Only one cell for each thickness is shown.

$$\frac{\delta N\left(E,x\right)}{\delta t} = C_{\text{sw}} n\left(x\right) p\left(x\right) \times P\left(E\right) - \lambda \left[n\left(x\right) + p\left(x\right)\right] \times f^{0} \times N\left(E,x\right) 
- v_{0} \times f^{0} \times N\left(E,x\right) \times \exp\left(-\frac{E_{A}\left(E\right)}{kT}\right) ,$$
(6.6)

where  $v_0$  is a constant,  $E_A$  the activation energy, k the Boltzman constant and T the temperature. With this equation, suitable results for the first part of the experiment could be achieved for all thicknesses for one light intensity [154]. In the model, a distribution of defects centered around 0.8 eV below the conduction band edge, i.e. around mid-gap, was assumed. With Equation 6.6, only the defect anhillation reactions for neutral dangling bonds by including the factor  $f^0(E)$ , the probability a defect at energy E is neutral, was calculated. The basis for this assumption is in thermodynamic considerations from which it is expected that the formation energy of a defect depends on the charged state of the defect [135, 155]. Following the work of, for example, Schumm *et al.* [156] and Winer [157], the factor  $f_0(E)$  was added.

For the activation energy, a linear dependence between E and  $E_A$  was assumed. The minimum  $E_A$  value was set to 1.3 eV and the highest to 1.5 eV. High activation energies close to the conduction band edge and low ones to the valence band edge are consistent with the model of Zhu et al. [91].

The experimental data were fitted to Equation 6.6. In general, the fit can be divided in three parts: The light-induced annealing term can be fitted to the first few hours of degradation time. The fit of the thermal induced annealing term can be made best at the saturation point and the fit of the light-induced annealing term can be done best in the middle, when the fast degradation of the beginning becomes slower.

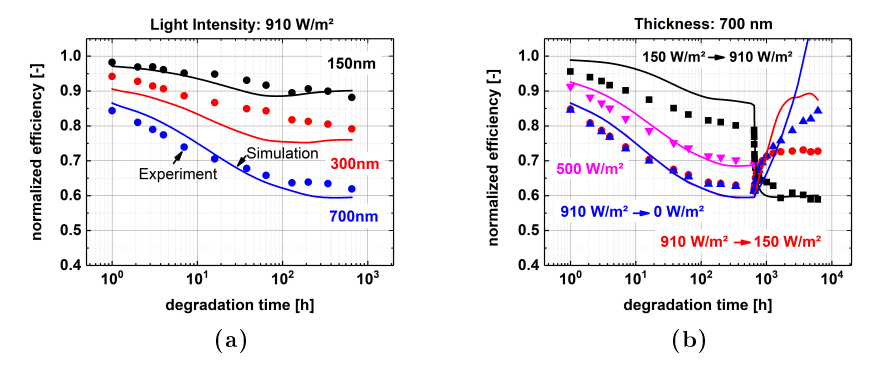


Figure 6.11. – Normalized efficiency for simulation and experimental results with Equation 6.6. a) shows the results for different solar cells thicknesses degraded under  $910\,\mathrm{W/m^2}$  for  $649\,\mathrm{h}$ . b) shows the results for the 700-nm thick solar cell degraded under different light intensities including light changes.

In Figure 6.11, the results for the simulation with Equation 6.6 are compared to the experimental results. Shown are the normalized efficiencies as explained in Section 6.2. Figure 6.11a shows the results for different solar cells thicknesses

degraded under 910 W/m<sup>2</sup> for 649 h and in Figure 6.11b the results for the 700-nm thick solar cell degraded under different light intensities including light changes are shown. It can be seen that using Equation 6.6, suitable results for the first part of the experiment could be achieved for all thicknesses for one light intensity (see Figure 6.11a). Problems with this fitting arise, when implementing this equation for low light intensities or changing of light intensities which can be seen in [154] and Figure 6.11b. In [154], it is observed that the impact of varying the light intensity is overestimated by the model, i.e. the model reproduces the high intensity behaviors fairly well but underestimates degradation under a low light intensity. One reason for the discrepancy between the model and the experiment could be the solar cell JV characterization during the degradation experiment, resulting in short periods of 1000 W/m<sup>2</sup>. For the low light experiments, these measurements may skew the results. Another explanation may be that the light-induced annealing term, introduced in the model by Caputo et al., underestimates the intensity dependency of light-induced annealing. A better result is obtained by considering in both annealing terms only the defects generated during the light soaking, i.e. assuming light induced defects are fundamentally different from the intrinsic defects. However, also with this assumption not a sufficient fit for the experiments could be achieved. For this reason, the light induced annealing term in Equation 6.6 was reconsidered, which will be explained in the following.

Caputo et al. also considered different approaches for the light-induced annealing term [149]. In this work, the authors came to the conclusion that the light-induced annealing term has the form for thermal annealing with a reduced annealing energy under illumination. They correlated this factor with the electron quasi-Fermi level. In the work of this thesis, better results were achieved with these approaches for different light intensities as well as light changes. Nevertheless, not a consistent parameter set for all thicknesses could be achieved.

Finally, the problem was solved by adding the hole concentration as a factor in the light induced annealing term. It should be noted that this is a purely empirical approach and cannot be explained physically. The final rate equation becomes:

$$\frac{\delta N\left(E,x\right)}{\delta t} = C_{\text{sw}} n\left(x\right) p\left(x\right) \times P\left(E\right) 
- \Lambda\left[n\left(x\right) + p\left(x\right)\right] \times p\left(x\right) \times f^{0} \times \left(N\left(E,x\right) - N_{0}\left(E,x\right)\right) \times \exp\left(-\frac{E_{A}\left(E\right)}{kT}\right) 
- v_{0} \times f^{0} \times N\left(E,x\right) \times \exp\left(-\frac{E_{A}\left(E\right)}{kT}\right) ,$$
(6.7)

with the thermally activated constant  $\Lambda$ . In the light-induced annealing term, only the light-induced defects are considered, whereas in the thermal annealing term all defects are considered.

Comparing to Equation 6.6, only the light-induced annealing term was changed. Here, only the newly generated defects are considered in the annealing process, i.e. photo-generated defects are treated differently from native defects.

With one degradation equation and two annealing equations, a simple approach to describe defect creation is obtained by Equation 6.7. The description in the annealing terms for the newly generated defects and all defects are in agreement with the approach that defect states of different characteristics are available in the a-Si:H material [142].

#### 6.3.3. Simulation results

With Equation 6.7, the device simulator ASA and the physical parameter set, the simulation was performed for all thicknesses and light intensities. In the following the results are shown as an example for some of the experiments.

A fit for the high light intensity and the 700 nm thick solar cells were made. Applying the fits to the other thicknesses, very good results for the different thicknesses were achieved. The parameters in Equation 6.7 were set to:  $C_{\rm sw} = 10^{-20} \, {\rm m}^3 \, / {\rm s}$ ,  $\Lambda = 9.6 \times 10^{-23} \, {\rm m}^6 \, / {\rm s}$ ,  $v_0 = 1.5 \times 10^{15} \, {\rm s}^{-1}$ . The  $C_{\rm sw}$  value is consistent with the one of Caputo *et al.* [148], who also measured at  $T = 50 \, {\rm ^{\circ}C}$ .

Figure 6.12 shows some of the results. Here, the first part of the light-soaking experiment for the four different cell thicknesses degraded for  $649\,\mathrm{h}$  under  $910\,\mathrm{W/m^2}$ 

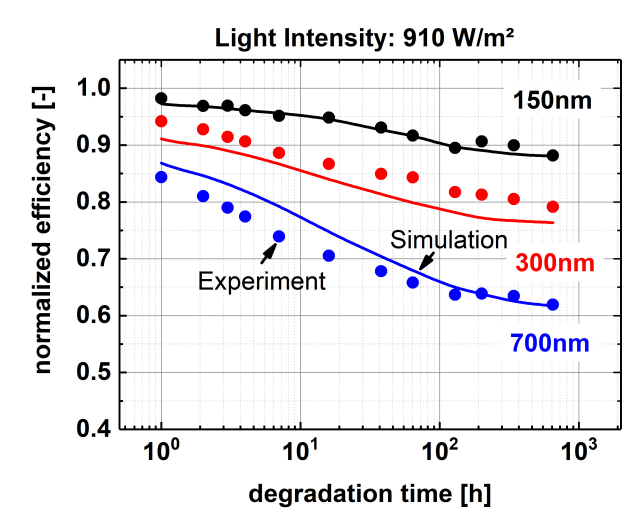


Figure 6.12. – Simulation results (lines) for the normalized efficiency compared to experimental values (dots). Shown are the cells with  $700\,\mathrm{nm}$  (blue),  $300\,\mathrm{nm}$  (red), and  $150\,\mathrm{nm}$  (black) cell thicknesses, degraded for  $649\,\mathrm{h}$  under  $910\,\mathrm{W/m^2}$ .

are shown for the simulation as well as for the experiment. The highest deviation between simulation and experiment can be found for the 300-nm thick solar cell thickness. At the degradation time of 64 h the difference between simulation and experiment is around 4.4% for the normalized efficiencies. The highest mean absolute error for the whole degradation experiment for the high light intensity can be found for the 300-nm thick solar cell and is 3.1%. The smallest mean absolute error can be found for the 150-nm thick solar cell and is 0.5%.

In Figure 6.13, some of the experimental and simulation results are shown for the 700-nm thick solar cell. Here, the degradation results under different light intensities and the change of light intensities are presented. It can be seen that good results are obtained for the different light intensities. The advantages of the adapted rate equation can be seen by applying the model to the changing light intensities. Here, the model obtains much better results than with Equation 6.6. With the adapted equation, especially the change from high to low light intensity is improved significantly. Now the light-induced annealing does not overestimate the impact of

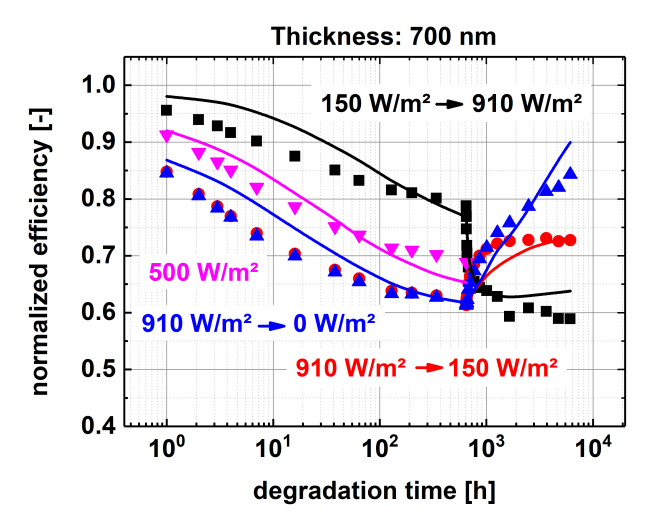


Figure 6.13. – Simulation results (lines) for the normalized efficiency compared to experimental values (dots). Shown are the cells with 700 nm cell thickness, degraded under different light intensities inclusive light changes.

the light intensity anymore. However, it can also be observed that the simulation model does not reproduce the light-induced annealing perfectly in the first hours after the light changes. In the experiment the cells that were first degrade under high light intensity anneal until a degradation time of 1010 h faster under low light intensity (red dots in Figure 6.8) than those under dark conditions (black dots in Figure 6.8). This behavior cannot be achieved with the simulation. Nevertheless, the general dynamic behavior during the experiment can be simulated very well with the simulation model.

Figure 6.14 shows JV characteristics at three time steps corresponding to one of the 700-nm thick solar cells that was first degraded under  $910\,\mathrm{W/m^2}$  for 649 h and afterwards put under  $150\,\mathrm{W/m^2}$  for additional 5470 h. The JV curves are shown for the simulation as well as for the experiment. It can be seen that the simulation results are here in very good agreement with the experiment. For a better analysis, the rms error for the JV curve is defined by

A new model for degradation and annealing of a-Si:H solar cells

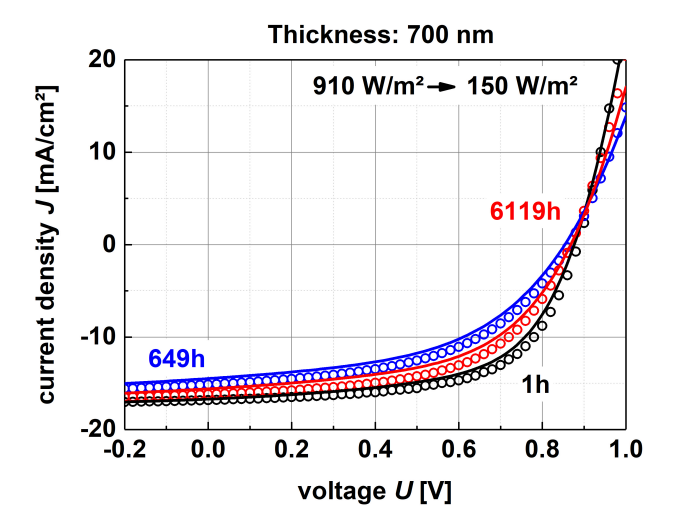


Figure 6.14. – Comparison between measured (dots) and simulated (lines) degraded JV curves. Investigated is the 700-nm thick solar cell that is first degraded for 649 h under a light intensity of  $910\,\mathrm{W/m^2}$ . Afterwards, the light intensity is changed to  $150\,\mathrm{W/m^2}$ .

rms error = 
$$\sqrt{\frac{1}{n} \sum_{i=1}^{n} \left(\frac{J_{\text{sim}}^{i} - J_{\text{meas}}^{i}}{J_{sc,\text{meas}}}\right)^{2}}$$
, (6.8)

where the index "sim" indicates the simulated values and "meas" the experimental measured values. The rms error for the JV curve after 1 h, 16 h, 649 h, and 6119 h are: 4.07%, 2.63%, 5.24%, and 5.2%, respectively. These values indicate that during the experiment the simulated JV curve does not vary significantly from the measured JV curve over the whole experiment. Beside the good fit of the simulation model to the experimental values, the simulation model also shows limitations in its application. These will be discussed in the following.

#### 6.3.4. Limitations of the simulation model

The limitations of the simulation model appear when considering the simulation results for long time intervals, going beyond the experimental time intervals. In

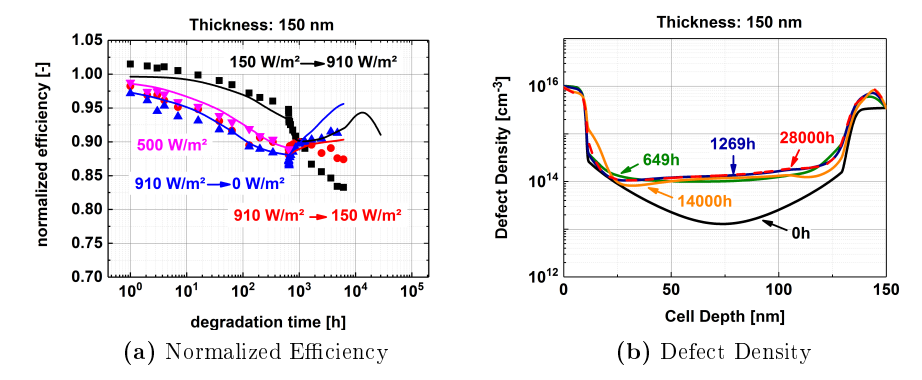


Figure 6.15. – Simulation results for the 150 nm-thick solar cell. In a) the simulation results (lines) for the normalized efficiency compared to experimental values (dots) are shown for cells that degraded under different light intensities inclusive light changes. In b) the simulated defect density is shown for a solar cell that is first degraded for 649 h under a light intensity of  $150\,\mathrm{W/m^2}.$  Afterwards, the light intensity is changed to  $910\,\mathrm{W/m^2}.$ 

Figure 6.15a, some of the experimental and simulation results are shown for the 150-nm thick solar cell. The degradation results under different light intensities and the change of light intensities are presented for the simulation and the experiment. In the first part of the experiment, the simulation and the experimental results match very well. In the second part of the experiment, most of the 150-nm thick solar cells did not survive the long experiment, which can be well seen for the cells that change from low to high irradiance (black dots) and from high to low irradiance (red dots). However, if the simulations are considered for the whole time of the light-soaking experiment, it can be seen for the simulation of the low to high irradiance (black line) that the simulated efficiency degrades from the light changes at 649 h to 1269 h. At this point, the saturation value would set in. However, the simulation leads beyond this point to an increase of the efficiency until a degradation time of  $14 \times 10^3$  h. After that, the efficiency starts to decrease again.

A more detailed view into this issue is shown in Figure 6.15b. Here, the simulated defect density over the cell depth is shown for the beginning (0 h), after 649 h, after  $1269\,\mathrm{h}$ , after  $14\times10^3\,\mathrm{h}$ , and after  $28\times10^3\,\mathrm{h}$ . The cell depth 0 nm indicates the

surface of the cell and 150 nm the back of the cell. The simulation shows that defects increase strongly in the bulk of the solar cell until 649 h. After the light change, the defects continues to increase in the cell depth between 35 nm and 117 nm. The defect profile does not change much compared to the time at  $28 \times 10^3$  h. However, in between those two time steps, the simulated defect profile at  $14 \times 10^3$  h indicates that high fluctuations occur at the p/i and i/n interfaces. This leads to the observed oscillations of the simulated efficiency.

For a further analysis of the spatial effects, the band profile and the charge carrier concentration are shown in Figure 6.16 and Figure 6.17, respectively. The band profile and the charge carrier concentration are shown for the five time steps 0 h, 649 h, 1269 h,  $14 \times 10^3$  h, and  $28 \times 10^3$  h. It should be noted that the plots are shown for the respective light intensity during the light-soaking experiment, i.e. at  $150\,\mathrm{W/m^2}$  for the time steps 0 h and 649 h and at a light intensity of  $910\,\mathrm{W/m^2}$  for the other three shown time steps.

The gradient of the conduction and valence band edges in Figure 6.16a indicates a strong electric field over the intrinsic layer which is necessary for a good charge carrier collection. As the Staebler-Wronski effect depends on the product of electron and hole concentration, the Staebler-Wronski effect is strongest where both concentrations are equal. Figure 6.17a indicates that at open voltage conditions both charge carrier concentrations are equal in the i-layer close to the p/i junction. For the simulation this means that at the beginning most defects are generated close to the p/i junction. A higher defect concentration affects the internal electric field. Figure 6.16b shows that the gradient of the simulated conduction and valence band edge are reduced at the end of the first part of the light-soaking experiment. Solving the Poisson equation (see Equation 2.6) this means that the transport of electrons and holes to the respective contacts are affected. Figure 6.17b shows that after 649 h the electron and hole concentration are equal over almost the whole i-layer. This indicates also a strong increasing of the SRH recombination in this part of the solar cell.

Changing the light intensity after 649 h to higher light intensity increases the charge carrier concentration and therefore also the defect generation in the i-layer due to the Staebler-Wronski effect. In Figure 6.15b, it can be seen that the defects

in the i-layer increases from 649 h to 1269 h. This additional increasing leads to an additional lowering of the gradient of the conduction and valence band edges which can be observed in Figure 6.16c. However, as the light induced-annealing term includes a quadratic hole dependence, the defects increases more towards the n/i junction. The lower internal electric field leads to an increasing of holes at the i/n junction which can be seen in Figure 6.17c. As the effect of the Staebler-Wronski effect in the i-layer gets lower, the impact of the two annealing terms of Equation 6.7 increases in the simulation model. A high defect concentration and an increasing hole concentration near the i/n junction leads to strong annealing effects in this region. Contrary, at the p/i junction the increasing of electrons near the p/i junction leads to an increasing effect of the Sraebler-Wronski effect in this region. However, the annealing effects towards the i/n junction have a higher influence than the degradation effects. This is why in the simulation an increasing efficiency is observed in the simulation between 1269 h and 14000 h. The annealing effects lead to an increasing gradient of the conduction and valence band edges which can be observed in Figure 6.16d. However, with decreasing defects the impact of the Staebler-Wronski term in the rate equation increases again and leads to a reversion of the effects and a return to the status of 1269 h.

The observed oscillations can therefore be traced back to a spatial effect of the rate equations as all three terms of Equation 6.7 affects the defects annealing and creating at different locations. The defects, the band diagram, and the spatial distribution of electrons and holes influences each other. The spatial changing distributions of electrons, holes, and defects influences the three terms of the rate equation differently. This explains why the observed efficiency oscillation is not avoidable in this dynamic simulation. Also the simulation with Equation 6.6 leads to oscillation effects. This can be observed in Figure 6.11 for the simulated normalized efficiency for the 700-nm thick solar cell degraded first under 910 W/m<sup>2</sup> and then under 150 W/m<sup>2</sup>. However, the strength of the oscillations can be, for example, regulated over the activation energy  $E_A$  for the defects. As this is one factor which determines when the impact of the annealing term increases compared to the degradation.

The simulated oscillation could not be compared to the experiment as the

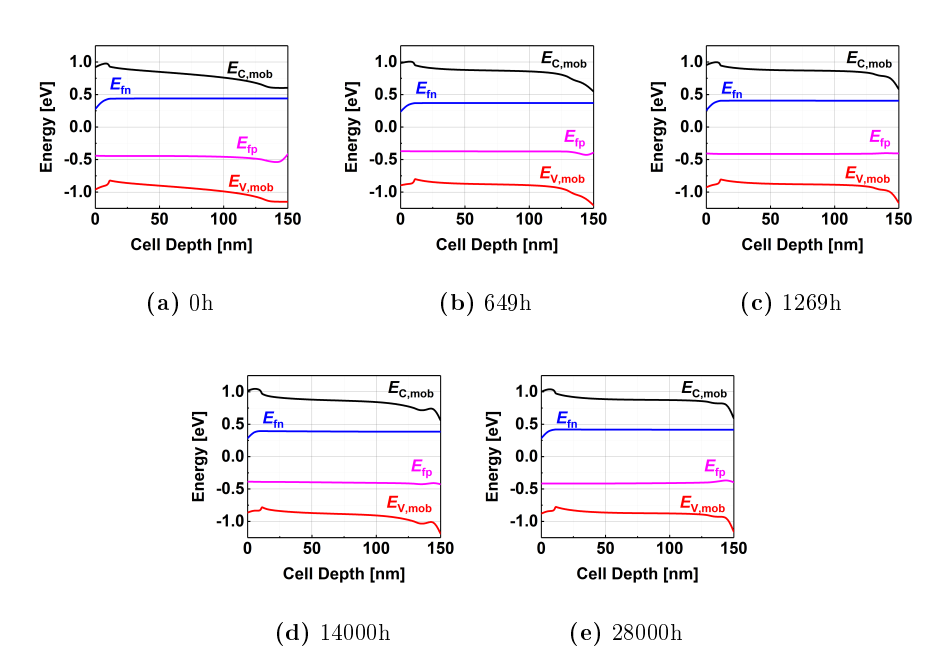
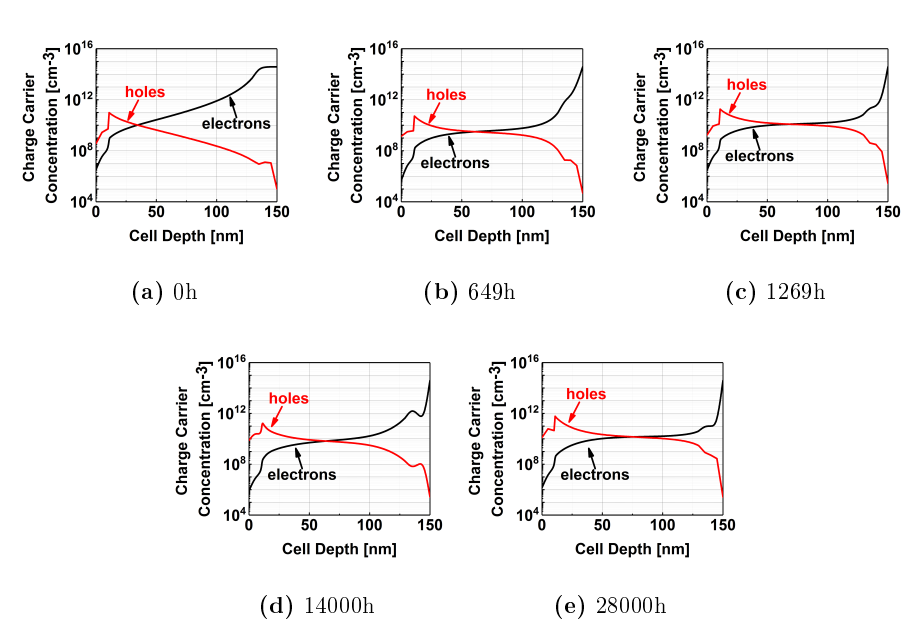


Figure 6.16. – Simulation results of the band diagrams for the 150 nm-thick solar cell. Shown are the mobility edge of the conduction band (black line), the electron quasi-Fermi level (blue line), the hole quasi-Fermi level (magenta line), and the mobility edge of the valence band (red line). The band diagrams are shown for open circuit condition and at different time and light intensities, namely a) at 0 h and 150 W/m², b) at 649 h and 150 W/m², c) at 1269 h and 910 W/m², d) at  $14\times10^3\,\mathrm{h}$  and  $910\,\mathrm{W/m²}$ , and e) at  $28\times10^3\,\mathrm{h}$  and  $910\,\mathrm{W/m²}$ .



**Figure 6.17.** – Simulation results of the electron (black) and hole (red) concentration for the 150 nm-thick solar cell. The charge carrier concentrations are shown for open circuit condition and at different time and light intensities, namely a) at 0 h and 150 W/m², b) at 649 h and 150 W/m², c) at 1269 h and 910 W/m², d) at  $14\times10^3\,\mathrm{h}$  and  $910\,\mathrm{W/m}^2$ , and e) at  $28\times10^3\,\mathrm{h}$  and  $910\,\mathrm{W/m}^2$ .

experiment is terminated before. Also in other experiments this oscillation could not be observed. Three possible explanations can be considered for the issue why the simulated oscillation is not observed in light-soaking experiments. First of all, the simulated oscillations are extremely slow. The onset of the oscillation sets in after more than 1269 h. During the oscillation the normalized efficiency increases from 90% to 96%. This efficiency increasing takes 12732 hours which are more than 530 days. Many experiments, as for example the one from D. Caputo et al. [148], finish already before this time. A second reason might be that while this simulated metastable effect is so slow, it is covered by overlying degradation effects during experiments such as contact degradation. The third reason, and probably the most likely one, is that the model does not describe the defect evolution completely. As the dynamic performance model also only considers all degradation effects as metastable effects, it can also be that the metastable effects are overestimated and therefore lead to this oscillation. All this reasons show that even if the metastable effects of a-Si:H have been investigated for a long time and much knowledge is already provided about it, still further investigations are necessary to simulate a proper defect evolution.

Another issue that should be discussed regarding the simulation model is the high amount of computational time for this kind of degradation model. As an example, for the simulation of the degradation and annealing of the 700-nm solar cell, that first degrades under high irradiance and was then put under low light intensity (black line in Figure 6.13), the simulation time took approximate eight hours. Considering the different performance models into account (see Chapter 2), a solution for this problem would be to substitute the device simulator with an equivalent circuit model. In the scope of this thesis, however, this has not been done.

## 6.4. Conclusion

In this chapter, a physical approach for the degradation of a-Si:H solar cells has been considered. For this, a-Si:H solar cells were degraded indoor under different and changing light intensities. Also different solar cell thicknesses have been consid-

ered. The model consists of a device simulator describing the optical and physical characteristics of the solar cell at a certain time and a rate equation describing the changing defects in time depending on temperature and irradiance. A first approach for the rate equation was made using the rate equation from Caputo et al. [148] and combine it with a thermal annealing term from Stutzmann et al. [141]. It could be shown that with this approach, the influence of the different light intensities as well as the light change could not be described properly with the same rate equation. This could be improved by adapting the light-induced annealing term of this equation with an additional hole term and an Arrhenius-term. Also only the light-induced generated defects after the exposure are considered in this annealing process, i.e. photo-generated defects are treated differently from native defects. With this approach, better results for the different light intensities and the light changes are obtained. However, problems arise in the stabilization phase and in first time of annealing, when changing from high to low light intensity. Also the calculation time is very high.

# 7. Conclusion

The increasing amount of photovoltaics for the energy supply, requires an improvement of the reliability and performance prediction of photovoltaics. As crystalline technologies have, with over 90%, the biggest market share, many performance models have been developed for this technology. However, thin film modules also have a promising potential to contribute to the future energy supply. Their main advantages are their low costs and their promising application for new markets, as for example for climate zones with a high amount of diffuse irradiance or their possibility to use them as building-integrated modules and deposit them on flexible substrate.

A big challenge for thin film technologies is the energy yield prediction as thin film solar cells exhibit metastabilities. Therefore, thin film technologies require dynamic performance models that describe the performance of the solar cell in dependence of the environmental conditions the cell were exposed to before. In this thesis, the performance of thin film solar cells and modules were investigated and modeled under outdoor and laboratory conditions, whereas two approaches of dynamic performance models were implemented to improve the performance prediction of thin film modules.

For analyzing and modeling of metastable effects, first a (stationary) performance model that only describes the current performance is necessary. In a later step, this performance model can be combined with rate equations to obtain a dynamic performance model. In Chapter 4, the KH model is investigated to find if it is a suitable performance model for thin film modules. The KH model needs only four parameters, namely  $J_{\rm sc}$ ,  $V_{\rm oc}$ ,  $G_{\rm sc}$ , and  $R_{\rm oc}$ , to describe the JV curve. For the investigation of the KH model, outdoor data from modules as CdTe, CIGS, a-Si:H/ $\mu$ c-Si:H, and a-Si:H are investigated. In addition, also data from poly-Si were taken into account. As a reference model, the well-known Loss-Factor Model is used.

#### Conclusion

For the analysis of the KH model and the comparison to the LFM, a four step procedure is used which is defined in Section 2.2.4. In the first step of the four step procedure, which is done in Section 4.1, the four fitting parameters of the KH model are compared with the parameters obtained from classical linear fits, i.e. one linear fit around V=0 to determine  $J_{\rm sc}$  and  $R_{\rm sc}$  and another linear fit around J=0 to determine  $V_{\rm oc}$  and  $R_{\rm oc}$ .

It was found that a fitting range of  $[V_{\min}, 1/2 \times V_{\text{mpp}}]$  is a suitable range for the linear fits to obtain a good compromise between the trade-off of a too high mean bias error and too high standard deviation. For  $R_{\text{oc}}$ , it is recommended to take small fitting ranges. In this thesis, a range of  $[J_{\min}, 1/7 \times J_{\text{mpp}}]$  is taken.

The highest discrepancy between the linear and KH fitting method can be found for the  $R_{\rm sc}$  vs.  $J_{\rm sc}$  behavior. This problem can be solved by a weighting factor of 30 in the range  $[V_{\rm min}, 1/2 \times V_{\rm mpp}]$ . With this weighting factor, it could be shown that the KH fitting method is a suitable method for determining the physical parameters  $R_{\rm sc}$ ,  $J_{\rm sc}$ ,  $V_{\rm oc}$ , and  $R_{\rm oc}$  from measured JV curves for thin film technologies as CIGS, CdTe, and a-Si:H. However, the results also show that for crystalline technologies, the  $R_{\rm sc}$  values are not fitted properly. The results of the KH parameter investigation allow to use the KH parameter also for other performance models as the LFM. This enables a better comparison between the KH model as a fitting model and the LFM as a factorization model.

In Section 4.2, the KH fit for the whole JV curve has been investigated and compared to the one-diode model. Considering the rms error for the fitted current density values, it could be found that the KH fit shows in average lower rms errors for the investigated thin-film JV curves than the one-diode model. However, also here it was found that the KH model cannot be recommended for crystalline Silicon modules. For the quality of the KH fit, a correlation to the irradiance was investigated. The JV curves of a-Si:H solar modules are fitted well under high irradiance, whereas the JV curves of CdTe modules are fitted with the KH model better under low irradiance. This correlation is also observed for the fit at the MPP. It could be shown that the  $P_{\rm mpp}$  fit of the KH model can be improved with a linear correction term.

For the parameter analysis of the KH fit, translation equations based on the

one-diode model, have been used. Those equations and the results have been compared to the LFM. It could be shown that for low irradiance, the translation equations are influenced by the second diode of the thin films. The translation equations of the LFM can compensate this effect by using additional  $\phi$  correlation terms compared to the translation equations of the KH model. However, there is no clear physical meaning of the additional coefficients, which does not allow to analyze the parameters further using their coefficients. Furthermore, it could be shown that the translation to STC is for the KH fit more stable regarding changing fitting ranges than for the LFM. However, to obtain translated reference values that are not influenced by non-linear effects at low irradiance and temperature, it is recommended to determine the coefficients of the KH translation equations at high irradiance ( $\phi$  > 800 W/m<sup>2</sup>) and temperature (T >25 °C).

Finally, in the last section of Chapter 4, the last step of the four-step procedure, namely the prediction, has been investigated for the KH model. Comparing the yield prediction of the LFM and the KH model, it could be shown that both models show similar results considering the mean and the standard value for the yield prediction. The results of Chapter 4 have shown for each step of the four-step procedure the disadvantages and advantages of the KH model. Regarding the available data set, the KH model is the most suitable model for analyzing the measured outdoor data.

Based on the results of Chapter 4, the KH model has been used in Chapter 5 to analyze the CdTe outdoor behavior. The translation equations of the KH model allow an in-depth analysis of the degradation and annealing effects by investigating the coefficients of these equations. Doing so, it has been analyzed for CdTe that the decreasing of  $G_{\rm sc}$  and  $R_{\rm oc}$  in the consolidation phase has to be separated from the increasing of the both parameters in the degradation phase. The consolidation phase and seasonal variation are more influenced by metastable effects. During the consolidation phase and summer periods, the effect of voltage-dependent photocurrent are reduced. Here, the driving force seems to be the irradiance. However, the degradation phase is more influenced by the temperature. With increasing temperature, the three parameters  $V_{\rm oc}$ ,  $R_{\rm oc}$ , and  $G_{\rm sc}$  degrade more and faster. One explanation for this may be the diffusion of Cu from the back-contact, however, for this, a more detailed module investigation is necessary. Also for the fill factor a

consolidation and degradation phase is observed that is mainly influenced by the  $R_{\rm oc}$  and in second order by the  $G_{\rm sc}$ .

Based on the parameter analysis, an empirical dynamic performance model for  $R_{\rm oc}$  of the CdTe1 module was developed which uses as input parameter just the initial  $R_{\rm oc}$  value, the time, the temperature and irradiance on a 10-minute interval. The developed rate equation describes the three characteristic parts, the consolidation and degradation phase as well as seasonal variation, with one equation and the same coefficients for all four climate regions. Only for the degradation term, a division has been made between warm regions (Chennai and Tempe) and cold regions (Ancona and Cologne). The results of the implemented performance model for  $R_{\rm oc}$  show that a simple rate equation can adequately describe the dynamic behavior of metastable solar cells under various conditions.

A more physical dynamic performance model approach is to model directly the causes of the metastable effects. This approach has been considered in Chapter 6 for a-Si:H. In Chapter 6, a dynamic performance model for a-Si:H based on the work of Caputo et al. [148] and Stutzmann et al. [141] was developed. To verify the model, an extensive set of degradation experiments that show the different influence parameters for a-Si:H degradation were performed. In particular, the measured data set shows the dynamic response to changes in light intensity. In total, 288 a-Si:H solar cells were investigated. For those cells, one physical parameter set were defined where the only variables are the solar cell thickness and the shunt resistance. These parameter set is used for the device simulator. The device simulator is then combined with the rate equation. With the rate equations by Caputo et al. and Stutzmann et al., not a good fit for the experimental data could be achieved. Based on these findings, a new rate equation for the degradation model was developed. For this, the light-induced annealing term was adapted empirically based on the experimental results. With this new term, the model is able to describe the degradation and annealing effects and the response to a change in light intensity in a suitable range. However, high fluctuations arise around the saturation point of the solar cells. It could be shown that these fluctuations are not avoidable in this dynamic simulation. A further improvement of the simulation, however, requires further investigation. For this, the developed dynamic performance model provides a very good template.

In summary, this thesis shows important results for the analysis and performance modeling of thin film solar cells and modules regarding their metastabilities, which can help to improve the reliability of this technology and so improve their future capacity. As CdTe is an important technology, the short-term outlook for this thesis is to extend the empirical dynamic performance model for  $R_{\rm oc}$  to  $G_{\rm sc}$ ,  $V_{\rm oc}$ , FF, and finally  $P_{\text{mpp}}$  in a first step. On a long-term outlook, a more physical dynamic performance model, comparable to the introduced one for a-Si:H, should be tried to develop for CdTe. The same procedure is also recommended for CIGS. The results of the physical dynamic performance model for a-Si:H have shown that also if the metastable effect is known very well there are still problems with the amount of detail in the model. The right parameterization is a nearly unsolvable problem as a detailed model input is required for this that is not obtained experimentally. Nevertheless, for developing dynamic performance models also for the other technologies, a further detailed investigation for the metastable behavior of the thin film solar cells technologies are required. The dynamic empirical performance model shows already promising results. In general, this thesis is a very good template for further investigations of dynamic performance models and metastable effects.

- S. Dröge, The Paris Agreement 2015 Turning Point for the International Climate Regime, Technical Report SWP Research Paper 2016/RP 04, Stiftung Wissenschaft und Politik, Berlin, 2016.
- [2] International Energy Agency, Key world energy statistics, Paris, 2016.
- [3] U.S. Energy Information Administration, *International Energy Outlook 2016*, EIA, Washington, DC, 2016.
- [4] P. Würfel, *Physics of Solar Cells From Basic Principles to Advanced Concepts*, WILEY-VCH Verlag GmbH & Co. KGaA, Weinheim, 2nd edition, 2009.
- [5] M. Rekinger and F. Thies, Global Market Outlook for Solar Power / 2015-2019, Technical report, SolarPower Europe, Brussels, 2015.
- [6] E. van Dyk, A. Audouard, E. Meyer, and C. Woolard, Solar Energy Materials and Solar Cells **91**, 167 (2007).
- [7] P. Mints, Photovoltaic crystalline and thin film capacity, production, shipments and inventory, 1982–2019; past and future trends, in 42nd IEEE Photovoltaic Specialists Conference, pages 1–3, New Orleans, Louisiana, 2015.
- [8] P. Mints and S. C. Siah, Thin film technology shipment and deployment, 1982 through 2012 and future prospects to 2016, in 39th IEEE Photovoltaic Specialists Conference, pages 2380–2382, Tampa Bay, Florida, 2013.
- [9] P. Mints, Thin film and crystalline technology competitiveness, past, present and future forecast, in 37th IEEE Photovoltaic Specialists Conference, pages 003260–003263, Seattle, Washington, 2011.
- [10] K. Masuko et al., IEEE Journal of Photovoltaics 4, 1433 (2014).
- [11] S. Kurtz, J. Granata, and M. Quintana, Photovoltaic-Reliability R&D toward

- a Solar-Powered World, in *SPIE Proceedings*, edited by N. G. Dhere, J. H. Wohlgemuth, and D. T. Ton, volume 7412, pages 74120Z-1-74120Z-12, 2009.
- [12] G. Makrides, B. Zinsser, G. E. Georghiou, M. Schubert, and J. H. Werner, Degradation of different photovoltaic technologies under field conditions, in 35th IEEE Photovoltaic Specialists Conference, pages 002332–002337, Honolulu, Hawaii, 2010.
- [13] R. Sasala and J. Sites, Time dependent voltage in CuInSe2 and CdTe solar cells, in 23rd Third IEEE Photovoltaic Specialists Conference, pages 543–548, Louisville, Kentucky, 1993.
- [14] U. Rau, M. Schmitt, J. Parisi, W. Riedl, and F. Karg, Applied Physics Letters 73, 223 (1998).
- [15] M. Gostein and L. Dunn, Light soaking effects on photovoltaic modules: Overview and literature review, in 37th IEEE Photovoltaic Specialists Conference, pages 003126–003131, Seattle, Washington, 2011.
- [16] V. Sharma and S. S. Chandel, Renewable and Sustainable Energy Reviews 27, 753 (2013).
- [17] R. Rüther and J. Livingstone, Solar Energy Materials and Solar Cells **36**, 29 (1995).
- [18] S. Sze and K. K. Ng, Physics of Semiconductor Devices, John Wiley & Sons, Inc., Hoboken, New Jersey, 3rd edition, 2007.
- [19] M. Stuckelberger, R. Biron, N. Wyrsch, F.-j. Haug, and C. Ballif, Renewable and Sustainable Energy Reviews (2016).
- [20] B. E. Pieters, Characterization of thin-film Silicon materials and solar cells through numerical modeling, Phd thesis, Technische Universiteit Delft, 2008.
- [21] M. Zeman, J. Willemen, L. Vosteen, G. Tao, and J. Metselaar, Solar Energy Materials and Solar Cells 46, 81 (1997).
- [22] P. Horodyský, R. Grill, and P. Hlídek, Physica Status Solidi (B) Basic Research 243, 2882 (2006).
- [23] P. T. Erslev, J. W. Lee, W. N. Shafarman, and J. D. Cohen, Thin Solid Films 517, 2277 (2009).

- [24] C. T. Sah and W. Shockley, Physical Review 109, 1103 (1958).
- [25] J. Melskens et al., IEEE Journal of Photovoltaics 3, 65 (2013).
- [26] W. Shockley and W. T. Read, Physical Review 87, 835 (1952).
- [27] R. N. Hall, Physical Review 87, 387 (1952).
- [28] D. Macdonald and A. Cuevas, Physical Review B 67, 075203 (2003).
- [29] P. P. Altermatt, Journal of Computational Electronics 10, 314 (2011).
- [30] H. K. Gummel, IEEE Transactions on Electron Devices 11, 455 (1964).
- [31] M. Burgelman, J. Verschraegen, S. Degrave, and P. Nollet, Progress in Photovoltaics: Research and Applications 12, 143 (2004).
- [32] X. Sun et al., A physics-based compact model for CIGS and CdTe solar cells: From voltage-dependent carrier collection to light-enhanced reverse breakdown, in 42nd IEEE Photovoltaic Specialist Conference, pages 8–13, New Orleans, Louisiana, 2015.
- [33] M. Gloeckler, A. Fahrenbruch, and J. Sites, Numerical modeling of CIGS and CdTe solar cells: setting the baseline, in 3rd World Conference on Photovoltaic Energy Conversion, volume 1, pages 491–494, 2003.
- [34] J. Merten et al., IEEE Transactions on Electron Devices 45, 423 (1998).
- [35] M. Gloeckler, C. R. Jenkins, and J. R. Sites, Materials Research Society Symposium Proceedings **763**, 1 (2003).
- [36] Y. Liu, Y. Sun, and A. Rockett, Solar Energy Materials and Solar Cells 98, 124 (2012).
- [37] A. Niemegeers and M. Burgelman, Numerical modelling of ac-characteristics of CdTe and CIS solar cells, in 25th IEEE Photovoltaics Specialists Conference, pages 901–904, Washington D.C., 1996.
- [38] M. Burgelman, P. Nollet, and S. Degrave, Thin Solid Films 361, 527 (2000).
- [39] B. E. Pieters, J. Krc, and M. Zeman, Advanced numerical simulation tool for solar cells - ASA5, in 2006 IEEE 4th World Conference on Photovoltaic Energy Conversion, WCPEC-4, volume 2, pages 1513–1516, Waikoloa, Hawaii, 2007.
- [40] W. Shockley, Bell System Technical Journal 28, 435 (1949).

- [41] M. B. Prince, Journal of Applied Physics 26, 534 (1955).
- [42] W. De Soto, S. Klein, and W. Beckman, Solar Energy 80, 78 (2006).
- [43] J. A. Duffie, W. A. Beckman, and W. M. Worek, Solar Engineering of Thermal Processes, 4nd ed., volume 116, WILEY-VCH Verlag GmbH & Co. KGaA, 2003.
- [44] J. Gray, The Physics of the Solar Cell, in *Handbook of photovoltaic science and engineering*, edited by S. S. Hegedus and A. Luque, John Wiley and Sons, 2011.
- [45] O. Breitenstein, The Physics of Industrial Crystalline Silicon Solar Cells, in Semiconductors and Semimetals - Advances in Photovoltaics: Part 2, edited by G. P. Willeke and E. R. Weber, volume 89, Newnes, 2013.
- [46] K. Nishioka, N. Sakitani, Y. Uraoka, and T. Fuyuki, Solar Energy Materials and Solar Cells **91**, 1222 (2007).
- [47] A. D. Rajapakse and D. Muthumuni, 2009 IEEE Electrical Power and Energy Conference (2009).
- [48] R. Miceli, A. Orioli, and A. Di Gangi, Applied Energy 155, 613 (2015).
- [49] H.-G. Wagemann and H. Eschrich, Grundlagen der photovoltaischen Energiewandlung: Solarstrahlung, Halbleitereigenschaften und Solarkonzepte, in *Teubner-Studienbücher: Angewandte Physik*, Teubner, Stuttgart, 1994.
- [50] S. S. Hegedus and W. N. Shafarman, Progress in Photovoltaics: Research and Applications **12**, 155 (2004).
- [51] V. Lo Brano, A. Orioli, G. Ciulla, and A. Di Gangi, Solar Energy Materials and Solar Cells **94**, 1358 (2010).
- [52] C. Hansen, A. Luketa-Hanlin, and J. Stein, Sensitivity of Single Diode Models for Photovoltaic Modules To Method Used for Parameter Estimation, in 28th European Photovoltaic Solar Energy Conference, pages 3258 – 3264, Paris, France, 2013.
- [53] C. W. Hansen, Parameter estimation for single diode models of photovoltaic modules, Technical Report SAND2015-2065, Albuquerque, New Mexico, 2015.
- [54] H. Tian, F. Mancilla-David, K. Ellis, E. Muljadi, and P. Jenkins, Solar Energy

- **86**, 2695 (2012).
- [55] G. Farivar and B. Asaei, Photovoltaic module single diode model parameters extraction based on manufacturer datasheet parameters, in 2010 IEEE International Conference on Power and Energy, pages 929–934, Kuala Lumpur, Malaysia, 2010.
- [56] K. Kennerud, IEEE Transactions on Aerospace and Electronic Systems AES-5, 912 (1969).
- [57] J. P. Charles, M. Abdelkrim, Y. H. Muoy, and P. Mialhe, Solar Cells 4, 169 (1981).
- [58] J. Phang, D. Chan, and J. Phillips, Electronics Letters 20, 406 (1984).
- [59] W. Kim and W. Choi, Solar Energy 84, 1008 (2010).
- [60] E. Dallago, D. Finarelli, and P. Merhej, Electronics Letters 46, 1022 (2010).
- [61] M. Villalva, J. Gazoli, and E. Filho, IEEE Transactions on Power Electronics 24, 1198 (2009).
- [62] K. I. Ishibashi, Y. Kimura, and M. Niwano, Journal of Applied Physics 103, 1 (2008).
- [63] X. Yuan, Y. Xiang, and Y. He, Solar Energy **108**, 238 (2014).
- [64] T. Ikegami, T. Maezono, F. Nakanishi, Y. Yamagata, and K. Ebihara, Solar Energy Materials and Solar Cells 67, 389 (2001).
- [65] M. Siddiqui and M. Abido, Applied Soft Computing 13, 4608 (2013).
- [66] N. Moldovan, R. Picos, and E. Garcia-Moreno, Parameter extraction of a solar cell compact model usign genetic algorithms, in 2009 Spanish Conference on Electron Devices, CDE'09, number C, pages 379–382, 2009.
- [67] H.-C. Kuo and C.-H. Lin, Applied Mathematics and Computation 219, 7348 (2013).
- [68] R. M. Corless, G. H. Gonnet, D. E. G. Hare, D. J. Jeffrey, and D. E. Knuth, Advances in Computational Mathematics 5, 329 (1996).
- [69] T. C. Banwell, IEEE Transactions on Circuits and Systems I: Fundamental Theory and Applications 47, 1621 (2000).

- [70] A. Jain, Solar Energy Materials and Solar Cells 81, 269 (2004).
- [71] J. C. Lagarias, J. A. Reeds, M. H. Wright, and P. E. Wright, SIAM Journal on Optimization 9, 112 (1998).
- [72] D. King, W. Boyson, and J. Kratochvill, Photovoltaic Array Performance Model, Technical Report SAND2004-3535, Albuquerque, New Mexico, 2004.
- [73] W. F. Holmgren, R. W. Andrews, A. T. Lorenzo, and J. S. Stein, PVLIB Python 2015, in 42nd IEEE Photovoltaic Specialist Conference, pages 1–5, New Orleans, Louisiana, 2015.
- [74] S. Sellner, J. Sutterlüti, L. Schreier, and S. Ransome, Advanced PV module performance characterization and validation using the novel Loss Factors Model, in 38th IEEE Photovoltaic Specialists Conference, pages 2938–2943, Austin, Texas, 2011.
- [75] D. King, J. Kratochvil, and W. Boyson, Temperature coefficients for PV modules and arrays: measurement methods, difficulties, and results, in 26th IEEE Photovoltaic Specialist Conference, pages 1183–1186, Anaheim, California, 1997.
- [76] International Electrotechnical Commission (IEC), IEC 60891 Ed.2: Photovoltaic devices - Procedures for temperature and irradiance corrections to measured I-V characteristics, Technical report, 2009.
- [77] D. E. G. Razo, Comparison and analysis of performance models for thin film modules under outdoor conditions with respect tomodule's degradation and energy yield prediction, Masters thesis, Technical University Berlin, 2016.
- [78] J. S. Stein, J. Sutterlueti, S. Ransome, C. W. Hansen, and B. H. King, Outdoor PV Performance Evaluation of Three Different Models: Single-Diode, SAPM and Loss Factor Model, in 28th European Photovoltaic Solar Energy Conference, pages 2865–2871, Paris, France, 2013.
- [79] S. Karmalkar and S. Haneefa, IEEE Electron Device Letters 29, 449 (2008).
- [80] A. K. Das, Solar Energy 85, 1906 (2011).
- [81] G. Friesen et al., Matrix method for energy rating calculations of PV modules in PV in Europe: From PV Technology to Energy Solutions, Rome, 2002.

- [82] A. G. D. Montgareuil et al., First Results of the Application of the MotherPV Method to CIS Modules, in 24th European Photovoltaic Solar Energy Conference, pages 3451–3455, Hamburg, Germany, 2009.
- [83] S. Williams, T. Betts, R. Gottschalg, and D. Infield, Site-Specific Condition (SSC): A Model for Real PV Modules Performance, in 2nd Photovoltaic Science, Applications and Technology Conference, pages 127–134, Loughborough, UK, 2005.
- [84] G. Friesen et al., Intercomparison Of Different Energy Prediction Methods Within The European Project "Performance" - Results Of The 1st Round Robin, in 22nd European Photovoltaic Solar Energy Conference, Milan, Italy, 2007.
- [85] S. Williams et al., Evaluating the State of the Art of Photovoltaic Performance Modelling in Europe, in 20th European Photovoltaic Solar Energy Conference, pages 1937–1941, Barcelona, Spain, 2005.
- [86] J. Merten et al., Fast and precise PV module performance prediction from simple indoor measurements, in 27th European Photovoltaic Solar Energy Conference, pages 3302–3305, Frankfurt, Germany, 2012.
- [87] D. L. Staebler and C. R. Wronski, Applied Physics Letters 31, 292 (1977).
- [88] Y. Wang, X. Geng, H. Stiebig, and F. Finger, Thin Solid Films **516**, 733 (2008).
- [89] T. Ishii, T. Takashima, and K. Otani, Progress in Photovoltaics: Research and Applications 19, 170 (2011).
- [90] A. Klaver and R. van Swaaij, Solar Energy Materials and Solar Cells **92**, 50 (2008).
- [91] J. Zhu, M. Bliss, T. R. Betts, and R. Gottschalg, Japanese Journal of Applied Physics **54** (2015).
- [92] M. Schweiger and W. Herrmann, Energy Rating Label for PV Modules for Improving Energy Yield Prediction in Different Climates, in 31st European Photovoltaic Solar Energy Conference, pages 1888–1892, Hamburg, Germany, 2015.

- [93] M. Schweiger and W. Herrmann, Comparison of energy yield data of fifteen PV module technologies operating in four different climates, in 42nd IEEE Photovoltaic Specialist Conference, New Orleans, Louisiana, 2015.
- [94] M. Schweiger and W. Herrmann, Electrical stability of PV modules in different climates, in 43rd IEEE Photovoltaic Specialist Conference, pages 3685–3687, Portland, Oregon, 2016.
- [95] M. Schweiger, W. Herrmann, A. Gerber, and U. Rau, IET Renewable Power Generation 11, 558 (2017).
- [96] M. Schweiger, J. Bonilla, W. Herrmann, A. Gerber, and U. Rau, Progress in Photovoltaics: Research and Applications (2017).
- [97] M. C. Peel, B. L. Finlayson, and T. A. McMahon, Hydrology and Earth System Sciences 11, 1633 (2007).
- [98] W. Herrmann, M. Schweiger, G. Tamizhmani, B. Shisler, and C. Kamalaksha, Soiling and self-cleaning of PV modules under the weather conditions of two locations in Arizona and South-East India, in 42nd IEEE Photovoltaic Specialist Conference, New Orleans, Louisiana, 2015.
- [99] S. xian Lun et al., Solar Energy **92**, 147 (2013).
- [100] H. Saleem and S. Karmalkar, Electron Device Letters, IEEE 30, 349 (2009).
- [101] S. Karmalkar and H. Saleem, Solar Energy Materials and Solar Cells 95, 1076 (2011).
- [102] E. I. Batzelis, G. E. Kampitsis, S. A. Papathanassiou, and S. N. Manias, IEEE Transactions on Energy Conversion **30**, 226 (2015).
- [103] C. Ulbrich, D. C. Jordan, S. R. Kurtz, A. Gerber, and U. Rau, Solar Energy 113, 88 (2015).
- [104] S. Ransome, J. Wohlgemuth, S. Poropat, and E. Aguilar, Advanced analysis of PV system performance using normalised measurement data, in 31st IEEE Photovoltaic Specialists Conference, pages 1698–1701, Lake Buena Vista, Florida, 2005.
- [105] J. Sutterlüti, S. Ransome, R. Kravets, and L. Schreier, Chracterising PV Modules under Outdoor Conditions: What's most important for energy yield,

- in 26th European Photovoltaic Solar Energy Conference, pages 3608 3614, Hamburg, Germany, 2011.
- [106] J. Sutterlueti, S. Ransome, J. Stein, and J. Scholz, Improved PV performance modelling by combining the PV\_LIB toolbox with the Loss Factors Model (LFM), in 42nd IEEE Photovoltaic Specialist Conference, New Orleans, Louisiana, 2015.
- [107] S. Ransome and J. Sutterlueti, Improving and Understanding kWh/kWp Simulations, in 26th European Photovoltaic Solar Energy Conference and Exhibition, pages 3255 3260, Hamburg, Germany, 2011.
- [108] S. Ransome and J. Sutterlueti, A Comparison of PV Performance Prediction Model Types for Different Technologies from Outdoor Measurements, in 31st European Photovoltaic Solar Energy Conference and Exhibition, pages 1893 – 1897, Hamburg, Germany, 2015.
- [109] S. Ransome and J. Sutterlueti, Degradation analysis of PV technologies using NREL and Gantner Instruments outdoor data, in 43rd IEEE Photovoltaic Specialists Conference, pages 3441–3446, Portland, Oregon, 2016.
- [110] S. Ransome and J. Sutterlueti, Using the Loss Factors Model to Improve PV Performance Modelling for Industrial Needs, in 29th European Photovoltaic Solar Energy Conference and Exhibition, pages 2870 – 2875, Amsterdam, The Netherlands, 2014.
- [111] S. Sellner, J. Sutterlueti, S. Ransome, L. Schreier, and N. Allet, Understanding PV Module Performance: Further Validation of the Novel Loss Factors Model and Its Extension to AC Arrays, in 27th European Photovoltaic Solar Energy Conference, pages 3199 – 3204, Frankfurt, Germany, 2012.
- [112] J. Sutterlüti, I. Sinicco, A. Hügli, T. Hälker, and S. Ransome, Outdoor Characterisation and Modelling of thin-film Modules and Technology Benchmarking, in 24th European Photovoltaic Solar Energy Conference, pages 3198–3205, Hamburg, Germany, 2009.
- [113] L. J. Gray et al., Reviews of Geophysics 48, RG4001 (2010).
- [114] D. B. Magare et al., International Journal of Energy and Environmental Engineering 7, 93 (2016).

- [115] S. Hegedus, D. Desai, and C. Thompson, Prog. Photovolt: Res. Appl. 15, 587 (2007).
- [116] J. E. Moore, S. Dongaonkar, R. V. K. Chavali, M. A. Alam, and M. S. Lundstrom, IEEE Journal of Photovoltaics 4, 1138 (2014).
- [117] J. Nelson, *The physics of solar cells*, Imperial College Press, London, 1 edition, 2003.
- [118] U. Rau and H. Schock, Applied Physics A: Materials Science & Processing 69, 131 (1999).
- [119] M. Wolf, G. Noel, and R. Stirn, IEEE Transactions on Electron Devices 24, 419 (1977).
- [120] J. H. Werner, Applied Physics A Solids and Surfaces 47, 291 (1988).
- [121] J. Roy, T. R. Betts, and R. Gottschalg, Japanese Journal of Applied Physics 51, 20 (2012).
- [122] E. Lorenz, T. Scheidsteger, J. Hurka, D. Heinemann, and C. Kurz, Progress in Photovoltaics: Research and Applications 19, 757 (2011).
- [123] Y. Su, L.-C. Chan, L. Shu, and K.-L. Tsui, Applied Energy 93, 319 (2012).
- [124] G. Makrides, B. Zinsser, M. Schubert, and G. E. Georghiou, Progress in Photovoltaics: Research and Applications 21, 500 (2013).
- [125] R. R. Wilcox, Fundamentals of Modern Statistical Methods, Springer New York, New York, NY, 2001.
- [126] P. Nollet, M. Burgelman, and S. Degrave, Thin Solid Films 361, 293 (2000).
- [127] T. Carlsson and A. Brinkman, Progress in Photovoltaics: Research and Applications 14, 213 (2006).
- [128] D. L. Bätzner, R. Wendt, A. Romeo, H. Zogg, and A. N. Tiwari, Thin Solid Films 361, 463 (2000).
- [129] T. D. Dzhafarov, S. S. Yesilkaya, N. Y. Canli, and M. Caliskan, Solar Energy Materials and Solar Cells 85, 371 (2005).
- [130] B. Späth, Rückkontaktbildung von CdTe-Solarzellen: Mechanismen und elektronische Eigenschaften, Phd thesis, Technischen Universität Darmstadt, 2007.

- [131] C. R. Corwine, A. O. Pudov, M. Gloeckler, S. H. Demtsu, and J. R. Sites, Solar Energy Materials and Solar Cells 82, 481 (2004).
- [132] M. Eron and A. Rothwarf, Applied Physics Letters 44, 131 (1984).
- [133] C. Radue and E. van Dyk, Solar Energy Materials and Solar Cells **94**, 617 (2010).
- [134] M. Stutzmann, W. B. Jackson, and C. C. Tsai, Physical Review B 32, 23 (1985).
- [135] M. J. Powell and S. C. Deane, Physical Review B 53, 10121 (1996).
- [136] H. M. Branz, Physical Review B 59, 5498 (1999).
- [137] M. Stutzmann, Philosophical Magazine B 56, 63 (1987).
- [138] H. Fritzsche, Annual Review of Materials Research 31, 47 (2001).
- [139] M. Stuckelberger et al., Progress in Photovoltaics: Research and Applications **24**, 446 (2016).
- [140] W. B. Jackson, M. Stutzmann, and C. C. Tsai, Physical Review B 34, 54 (1986).
- [141] M. Stutzmann, W. B. Jackson, and C. C. Tsai, Physical Review B 34, 63 (1986).
- [142] L. Yang and L. Chen, Applied Physics Letters **63**, 400 (1993).
- [143] J. Jang and C. Lee, Journal of Applied Physics 54, 3943 (1983).
- [144] M. S. Bennett, J. L. Newton, K. Rajan, and A. Rothwarf, Journal of Applied Physics 62, 3968 (1987).
- [145] R. Meaudre and M. Meaudre, Physical Review B 45, 12134 (1992).
- [146] D. Redfield, Applied Physics Letters **49**, 1517 (1986).
- [147] D. Caputo, Solar Energy Materials and Solar Cells 59, 289 (1999).
- [148] D. Caputo et al., Time Dependence of spatial Defect Profiles in a-Si:H Solar Cells with Light-Soaking, in *Materials Research Symposium Proceedings*, volume 377, pages 669–674, Materials Research Society, 1995.
- [149] D. Caputo, J. Bullock, H. Gleskova, and S. Wagner, Toward a Practical Model of a-Si:H Defects in Intensity-Time-Temperature Space, in *MRS Proceedings*,

- volume 336, page 165, 1994.
- [150] B. E. Pieters, H. Stiebig, M. Zeman, and R. A. C. M. M. van Swaaij, Journal of Applied Physics 105, 044502 (2009).
- [151] K. Radhakrishnan and A. C. Hindmarsh, Description and use of LSODE, the Livemore Solver for Ordinary Differential Equations, Technical report, Lawrence Livermore National Laboratory (LLNL), Livermore, CA, 1993.
- [152] T. C. M. Müller, Light absorption and radiative recombination in thin-film solar cells, Phd thesis, Aachen, Techn. Hochsch., Jülich, 2015.
- [153] J. Liang, E. A. Schiff, S. Guha, B. Yan, and J. Yang, Applied Physics Letters 88 (2006).
- [154] M. Görig and B. E. Pieters, Development and validation of a phenomenological model describing degradation and annealing of a-Si:H solar cells, in 31st European Photovoltaic Solar Energy Conference, Hamburg, Germany, 2015.
- [155] Y. Bar-Yam and J. Joannopoulos, Journal of Non-Crystalline Solids, 467 (1987).
- [156] G. Schumm, Journal of Non-Crystalline Solids, 317 (1993).
- [157] K. Winer, Physical review. B, Condensed matter 41, 150 (1990).

Appendices

A. Appendix for Chapter 3



**Figure A.1.** – Outdoor test sites in Ancona, Chennai, Cologne and Tempe. copyright: TÜV Rheinland

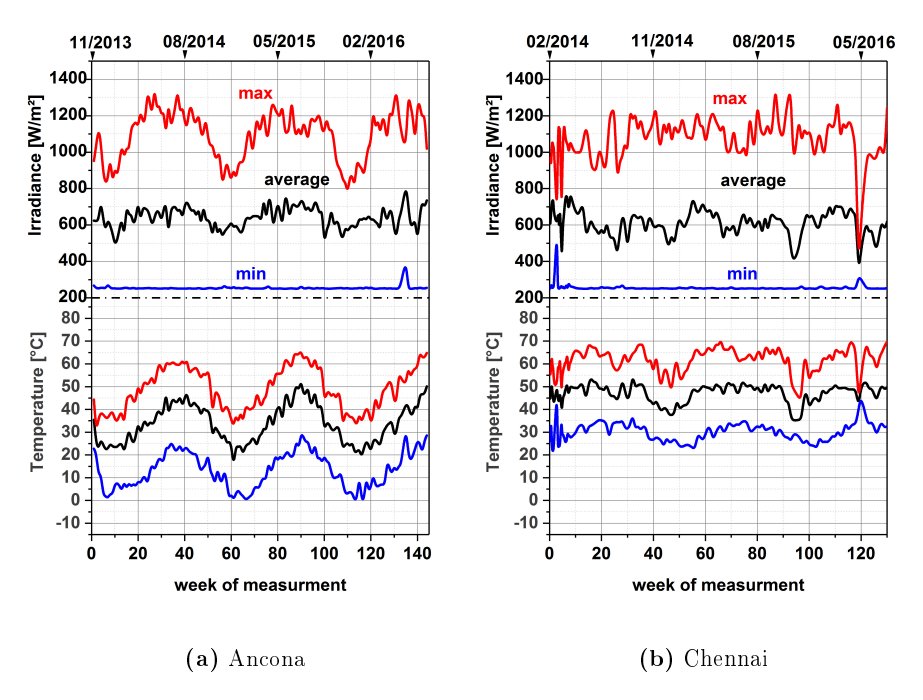


Figure A.2. – Weekly back-of-module temperature and in-plane solar irradiance measured for the CdTe1 module in a) Ancona and b) Chennai

B. Appendix for Chapter 4

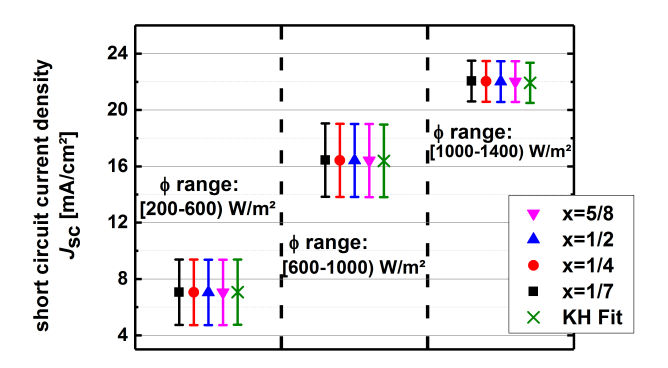


Figure B.1. – Mean and standard deviation for  $J_{\rm sc}$  for different irradiance ranges using different linear fitting ranges and the weighted KH fit. Each of the four following plots represents one of the following x values: 1/4 (black dots), 1/3 (red dots), 1/2 (blue dots), 5/8 (magenta dots). The green dots represent the values of the KH fit whereas the fit was weighted with a factor of 30 in the range  $[V_{\min}, 1/2 \cdot V_{\max}]$ .

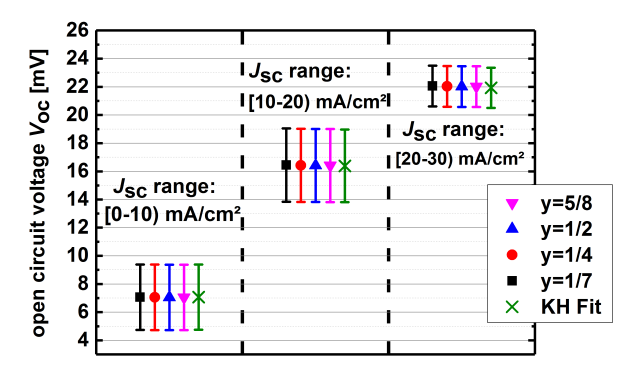


Figure B.2. – Mean and standard deviation for  $R_{\rm oc}$  for different  $J_{\rm sc}$  ranges using different linear fitting ranges and the KH fit. Each of the four following plots represents one of the following y values: 1/7 (black dots), 1/4 (red dots), 1/2 (blue dots), 5/8 (magenta dots). The green dots represent the values of the KH fit.

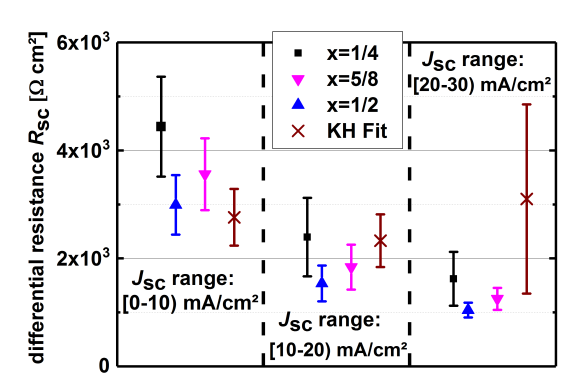


Figure B.3. – Mean and standard deviation for  $R_{\rm sc}$  for different  $J_{\rm sc}$  ranges using different linear fitting ranges and the KH fit. Each of the three following plots represents one of the following x values: 1/4 (black squares), 1/2 (blue up-pointing triangles), 5/8 (magenta down-pointing triangles). The dark red crosses represent the values of the KH with no weighting factor.

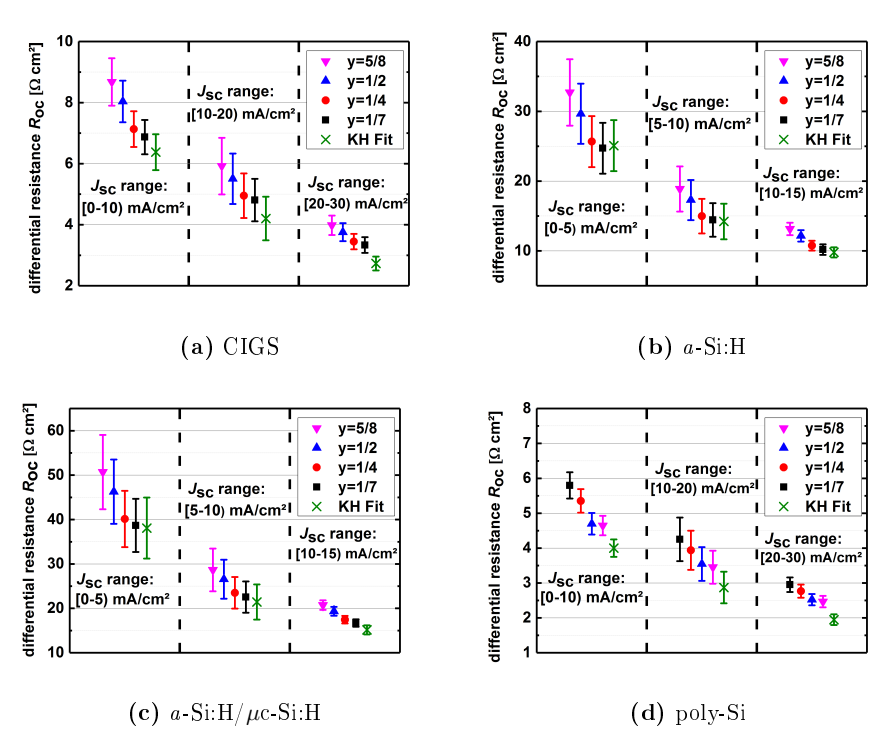
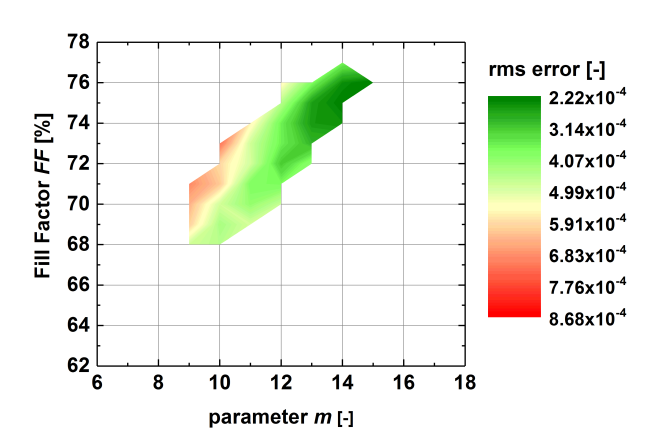


Figure B.4. – Mean and standard deviation for  $R_{\rm oc}$  for different  $J_{\rm sc}$  ranges using different linear fitting ranges and the weighted KH fit for a) CIGS, b) a-Si:H, c)  $a\text{-Si:H}/\mu\text{c-Si:H}$ , and d) poly-Si. Each of the three following plots represents one of the following y values: 1/7 (black squares), 1/4 (red dots), 1/2 (blue up-pointing triangles), 5/8 (magenta down-pointing triangles). The green crosses represent the values of the KH fit whereas the fit was weighted with a factor of 30 in the range  $[V_{\rm min}, 1/2\cdot V_{\rm mpp}]$ .



**Figure B.5.** – Correlation for m with FF and the rms error for the CdTe1 module in Cologne considering only data after the first 90 days. The rms error is calculated with Equation 4.5.

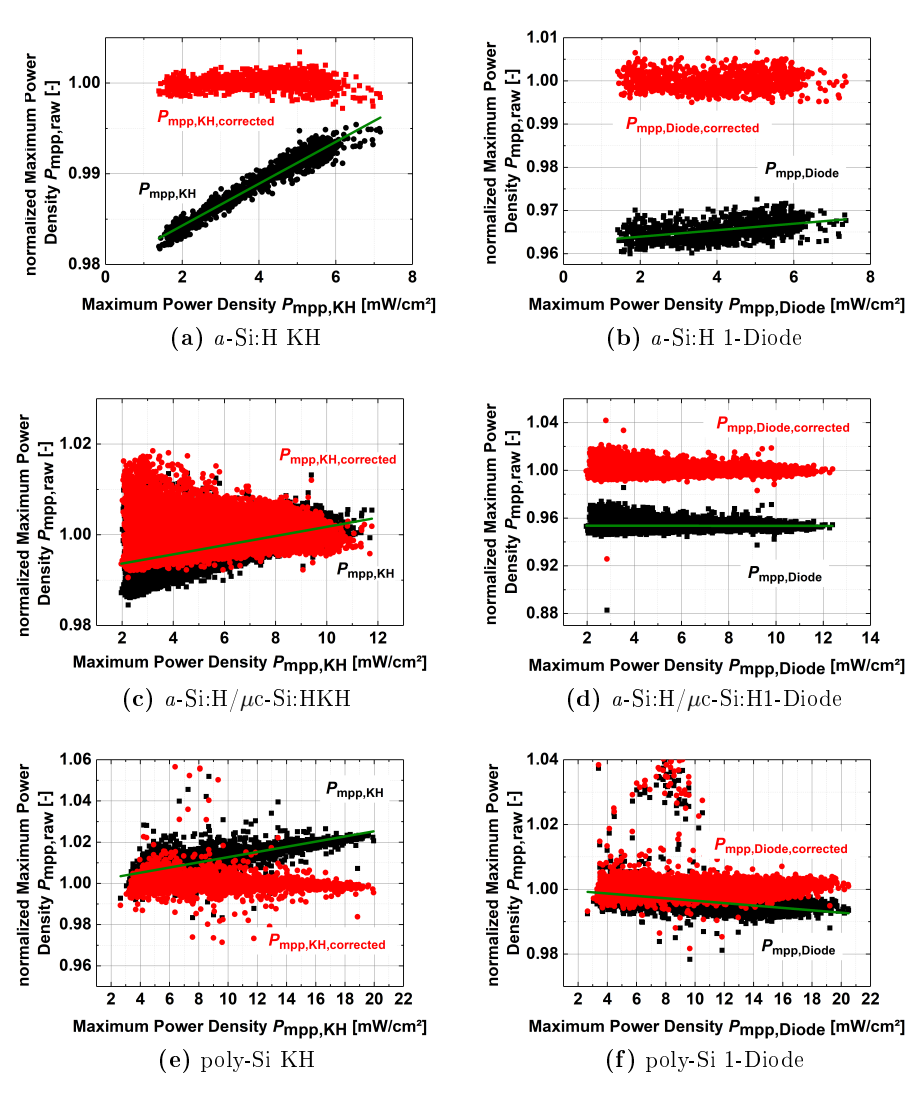


Figure B.6. – Uncorrected (black squares) and corrected (red dots)  $P_{\rm mpp}$  fits for different technologies measured in Cologne. The plots show the  $P_{\rm mpp,raw}/P_{\rm mpp,fit}$  ratio over  $P_{\rm mpp,fit}$ . The green line indicates the linear correction polynom. a) shows the results for the a-Si:H module fitted with the KH method, b) the a-Si:H module fitted with the one-diode model, c) the a-Si:H/ $\mu$ c-Si:H module fitted with the KH model, d) the a-Si:H/ $\mu$ c-Si:H module fitted with the one-diode model, e) the poly-Si module fitted with the KH model, and f) the poly-Si module fitted with the one-diode model.

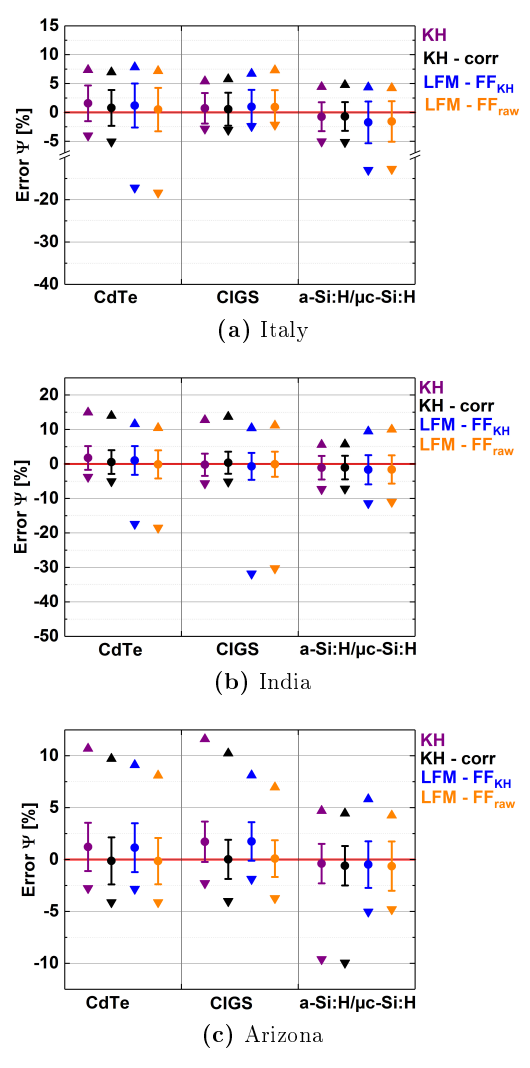
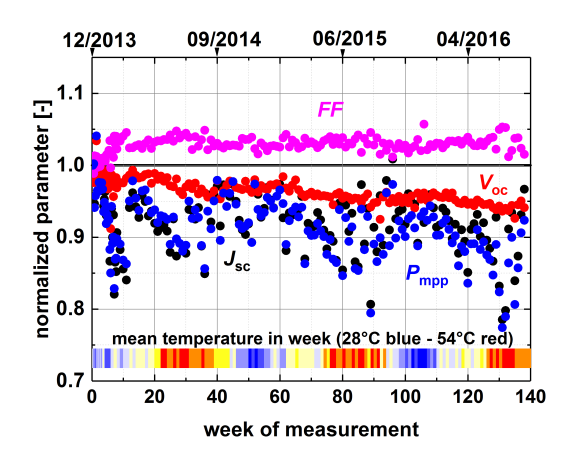


Figure B.7. – Comparison between the prediction error for  $P_{\rm mpp}$  calculated with the KH and the LF model. Investigated are the three technologies CdTe, CIGS, and  $a\text{-Si:H}/\mu\text{c-Si:H}$ . Shown are the mean error for one week (dot), the mean weakly standard deviation, the maximum mean weekly error (upwards triangle) and the minimum mean weekly error (downwards triangle). The colors indicate the investigated model: KH model without  $P_{\rm mpp}$  correction (purple), KH model with  $P_{\rm mpp}$  correction (black), LFM with FF taken from the KH fit (blue) and LFM with raw FF (orange). The location of the measured modules is for a) Italy, b) India, and c) Arizona.

# C. Appendix for Chapter 5

This chapter is divided in two sections. In Section C.2, the detailed analysis results for all 12 CdTe modules are shown and compared with each other. All more general additional information for Chapter C can be found in Section C.1.

# C.1. General results



(a) FF,  $P_{\mathrm{mpp}}$ ,  $J_{\mathrm{sc}}$ ,  $V_{\mathrm{oc}}$ 

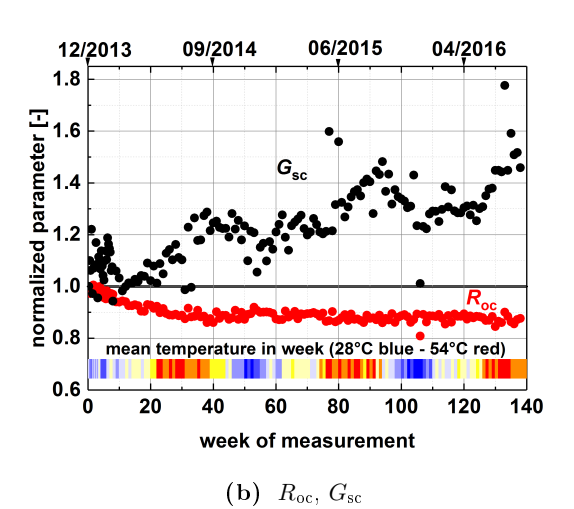
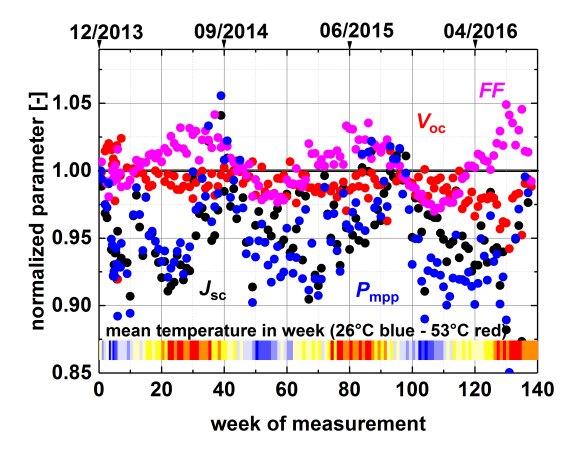
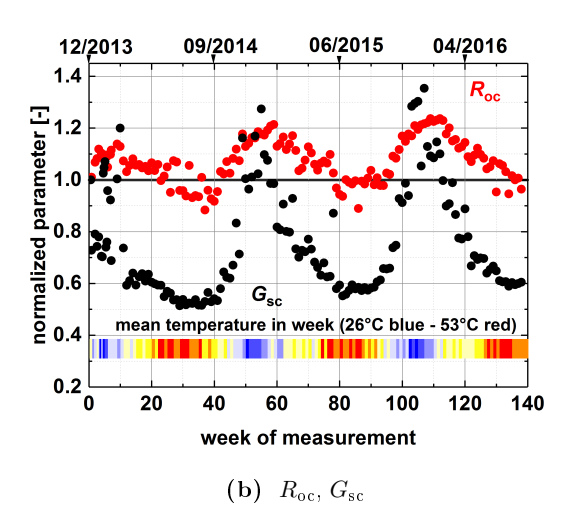


Figure C.1. – Weekly normalized parameters for the CIGS1 module in Tempe. Shown are the values for a) FF,  $P_{\rm mpp}$ ,  $J_{\rm sc}$ ,  $V_{\rm oc}$  and b)  $R_{\rm oc}$ ,  $G_{\rm sc}$ .



(a) FF,  $P_{\mathrm{mpp}}$ ,  $J_{\mathrm{sc}}$ ,  $V_{\mathrm{oc}}$ 



**Figure C.2.** – Weekly normalized parameters for the a-Si:H/ $\mu$ c-Si:H module in Tempe. Shown are the values for a) FF,  $P_{\rm mpp}$ ,  $J_{\rm sc}$ ,  $V_{\rm oc}$  and b)  $R_{\rm oc}$ ,  $G_{\rm sc}$ .

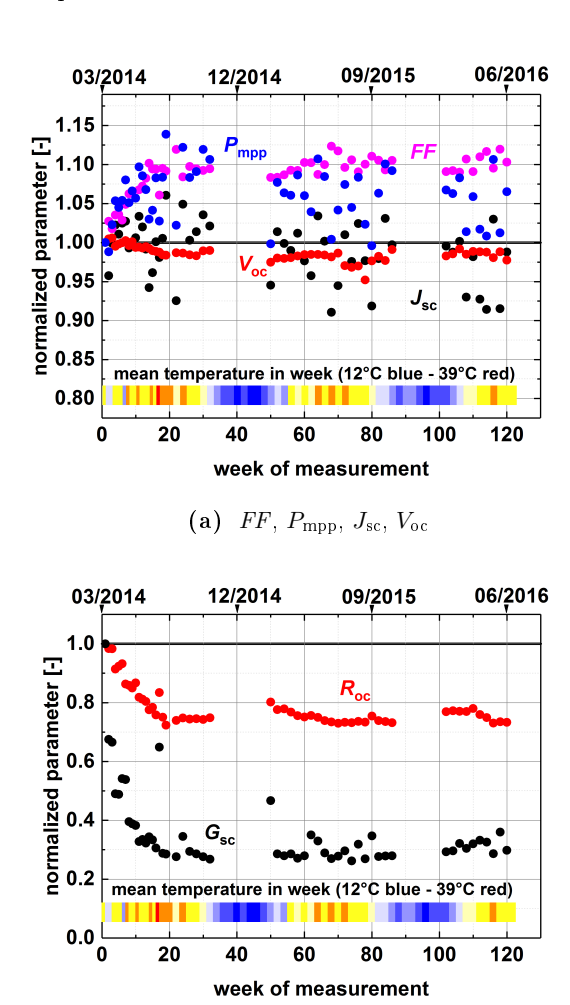
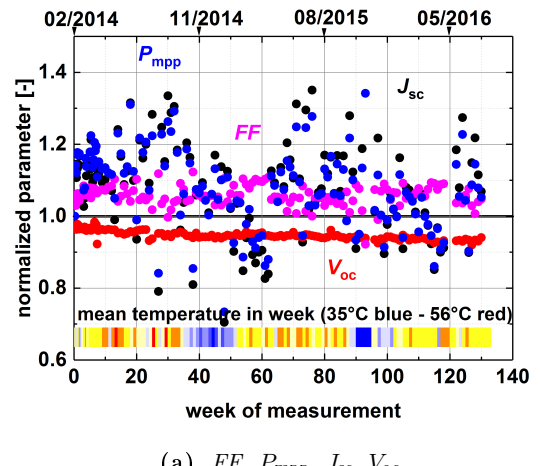


Figure C.3. – Weekly normalized parameters for the CdTe1 module in Cologne. Shown are the values for a) FF,  $P_{\rm mpp}$ ,  $J_{\rm sc}$ ,  $V_{\rm oc}$  and b)  $R_{\rm oc}$ ,  $G_{\rm sc}$ .

(b)  $R_{\rm oc},\,G_{\rm sc}$ 



(a) FF,  $P_{\rm mpp}$ ,  $J_{\rm sc}$ ,  $V_{\rm oc}$ 

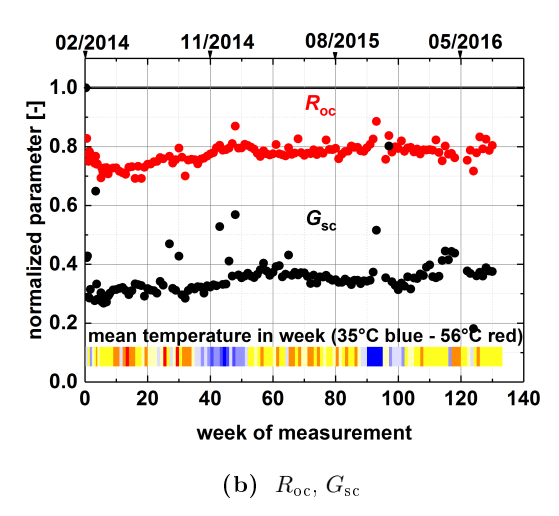


Figure C.4. – Weekly normalized parameters for the CdTe1 module in Chennai. Shown are the values for a) FF,  $P_{\rm mpp}$ ,  $J_{\rm sc}$ ,  $V_{\rm oc}$  and b)  $R_{\rm oc}$ ,  $G_{\rm sc}$ .

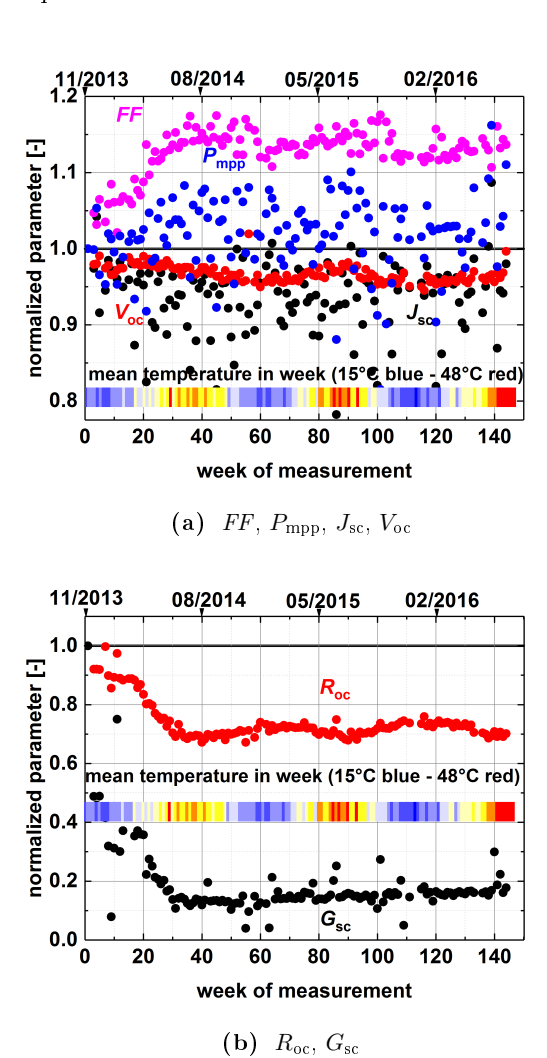
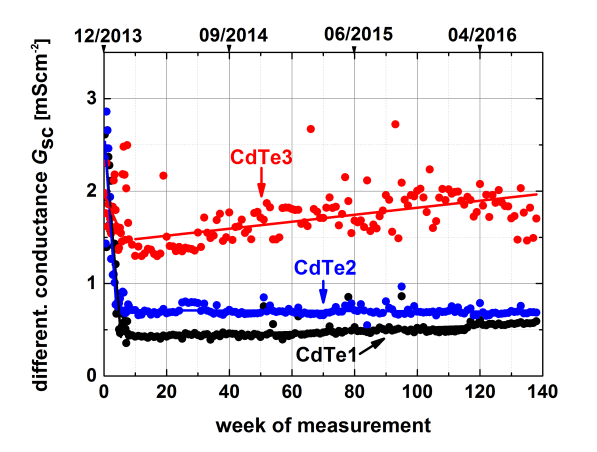
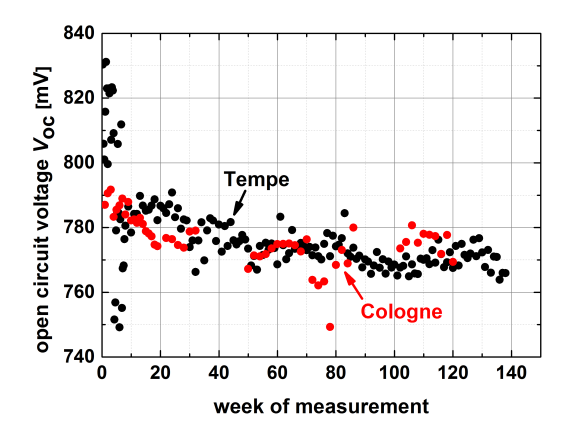


Figure C.5. – Weekly normalized parameters for the CdTe1 module in Ancona. Shown are the values for a) FF,  $P_{\rm mpp}$ ,  $J_{\rm sc}$ ,  $V_{\rm oc}$  and b)  $R_{\rm oc}$ ,  $G_{\rm sc}$ .



**Figure C.6.** – Weekly time values for  $G_{\rm sc}$  at STC for different CdTe modules in Tempe.



(a) Cologne and Tempe

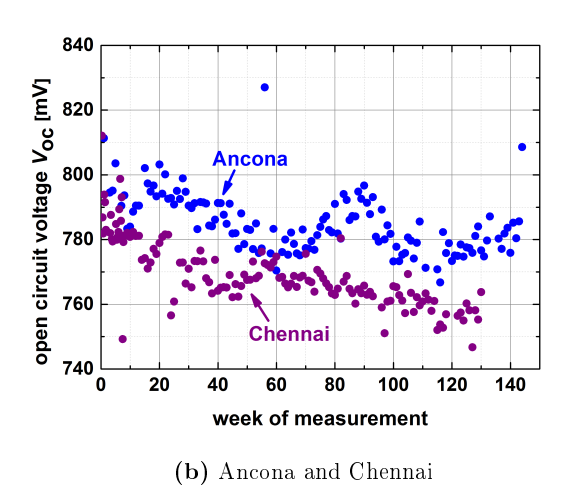


Figure C.7. – Weekly  $V_{\rm oc}$  values at STC for the CdTe1 modules. The modules were measured in a) Cologne and Tempe and b) Ancona and Chennai.

# C.2. Parameter and coefficient changes for all 12 CdTe modules

In the following, the analysis results of all 12 CdTe modules are shown. The results are ordered by module. For each module (CdTe1, CdTe2, CdTe3) the results are shown for all four locations (Germany, Italy, Arizona, India).

### C.2.1. Open circuit voltage

The Figures are based on Section 5.2.1.

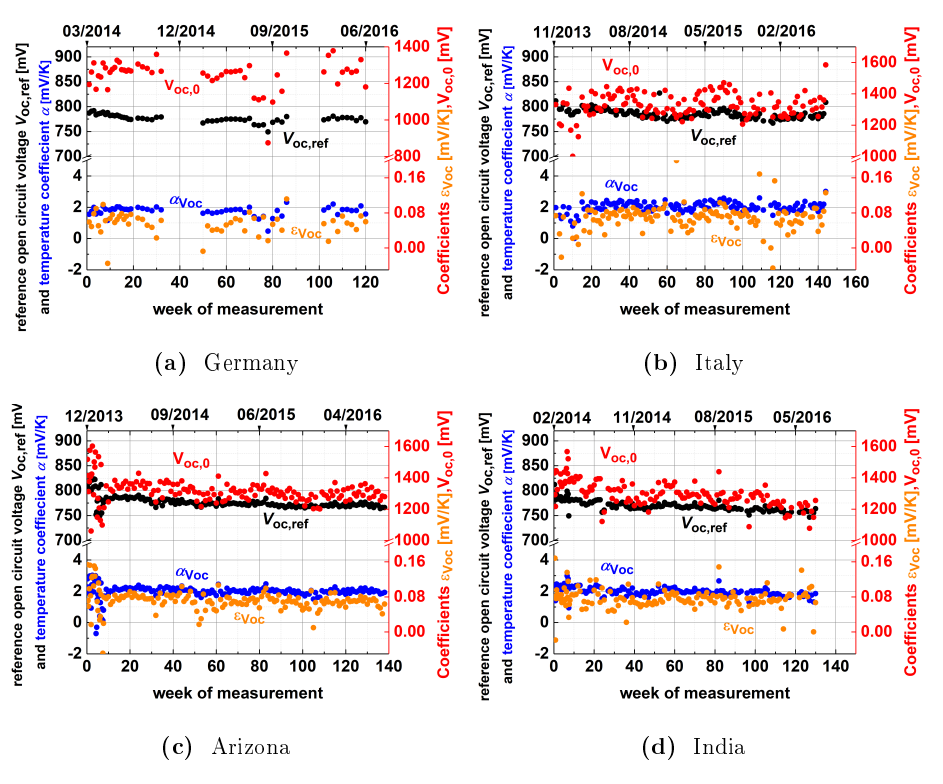


Figure C.8. – Weekly data of  $V_{\rm oc}$  (black points) at STC and the three coefficients  $V_{\rm oc}^0$  (red points),  $\alpha_{\rm Voc}$  (blue points), and  $\varepsilon_{\rm Voc}$  (orange points). The data are taken from the CdTe1 module measured in a) Cologne, Germany b) Ancona, Italy c) Tempe, Arizona, and d) Chennai, India.

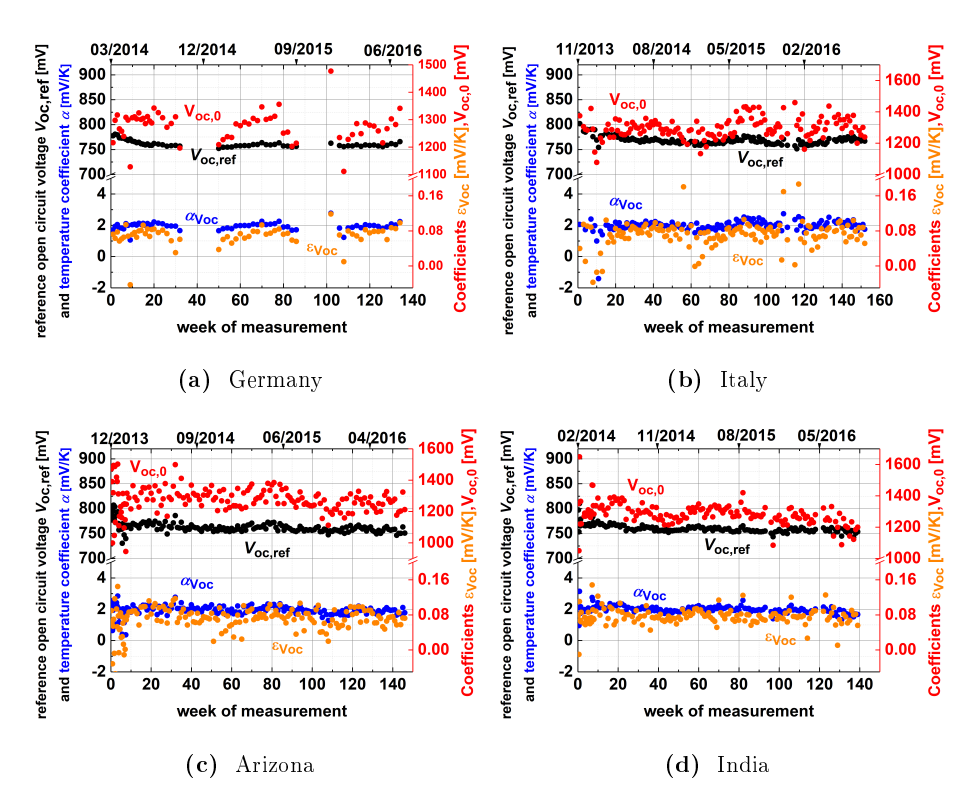
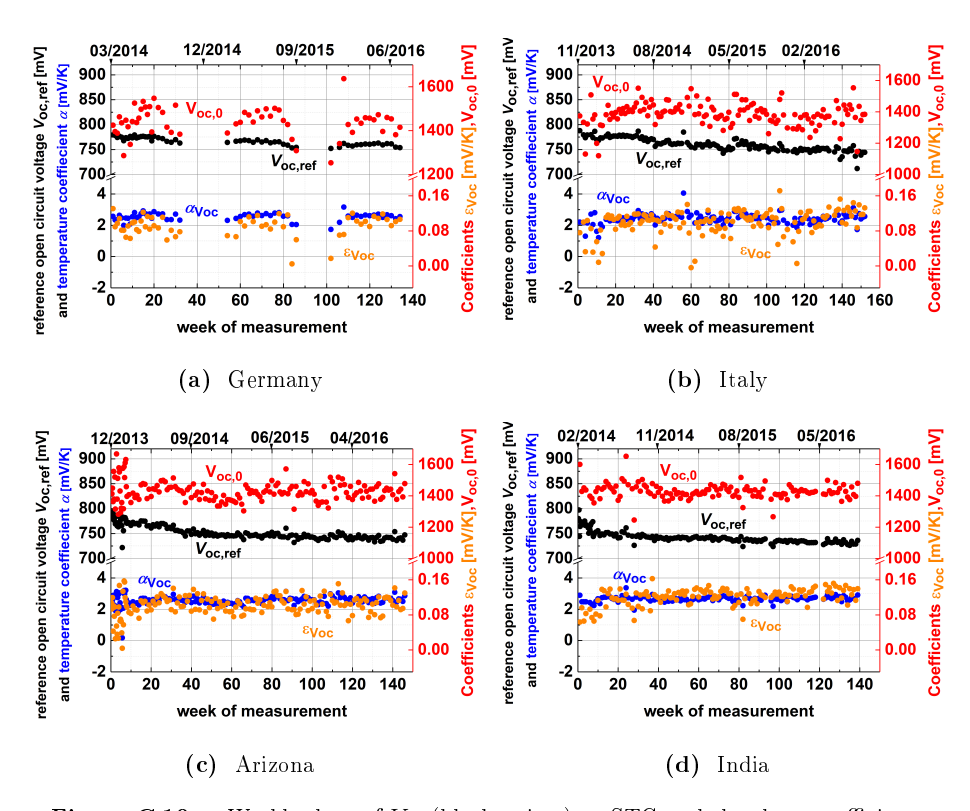


Figure C.9. – Weekly data of  $V_{\rm oc}$  (black points) at STC and the three coefficients  $V_{\rm oc}^0$  (red points),  $\alpha_{\rm Voc}$  (blue points), and  $\varepsilon_{\rm Voc}$  (orange points). The data are taken from the CdTe2 module measured in a) Cologne, Germany b) Ancona, Italy c) Tempe, Arizona, and d) Chennai, India.



**Figure C.10.** – Weekly data of  $V_{\rm oc}$  (black points) at STC and the three coefficients  $V_{\rm oc}^0$  (red points),  $\alpha_{\rm Voc}$  (blue points), and  $\varepsilon_{\rm Voc}$  (orange points). The data are taken from the CdTe3 module measured in a) Cologne, Germany b) Ancona, Italy c) Tempe, Arizona, and d) Chennai, India.

### C.2.2. Differential conductance at short circuit condition

The Figures are based on Section 5.2.2.

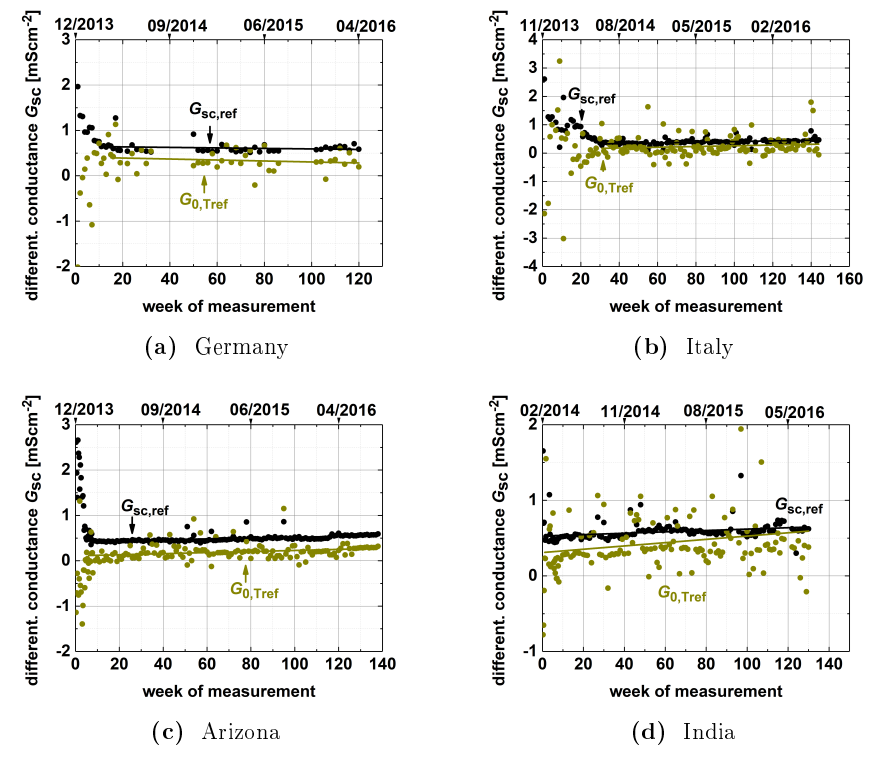


Figure C.11. – Weekly time values for STC for  $G_{\rm sc,ref}$  (black dots) and the term  $G_{\rm sc,0,Tref}$  (dark yellow dots). The data are taken from the CdTe1 module measured in a) Cologne, Germany b) Ancona, Italy c) Tempe, Arizona, and d) Chennai, India.

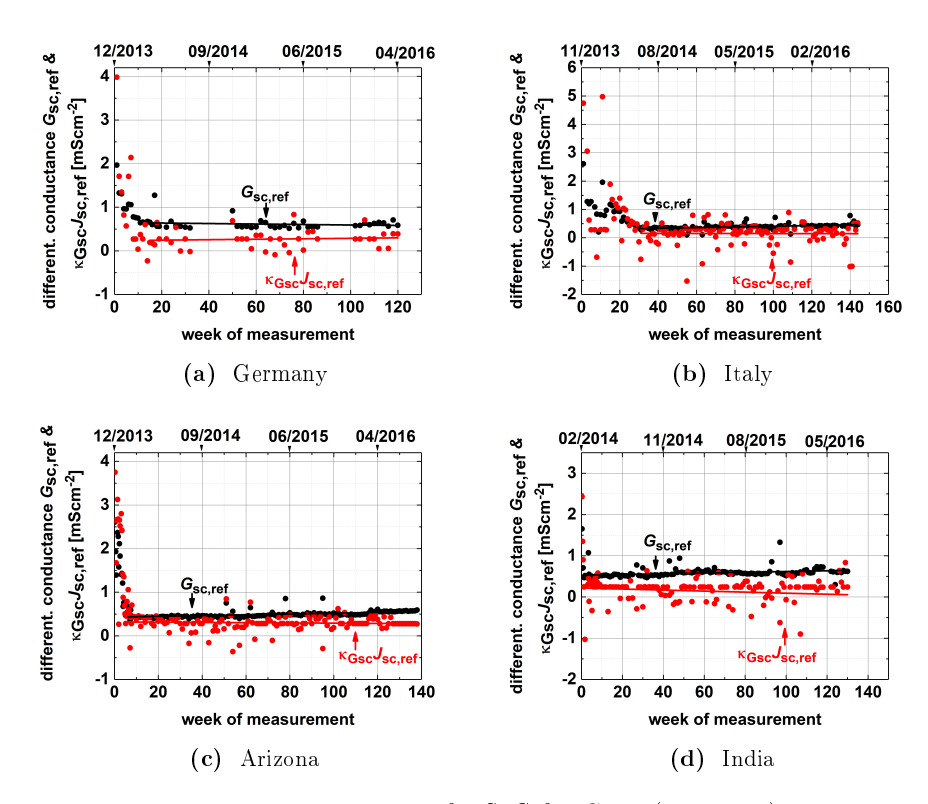
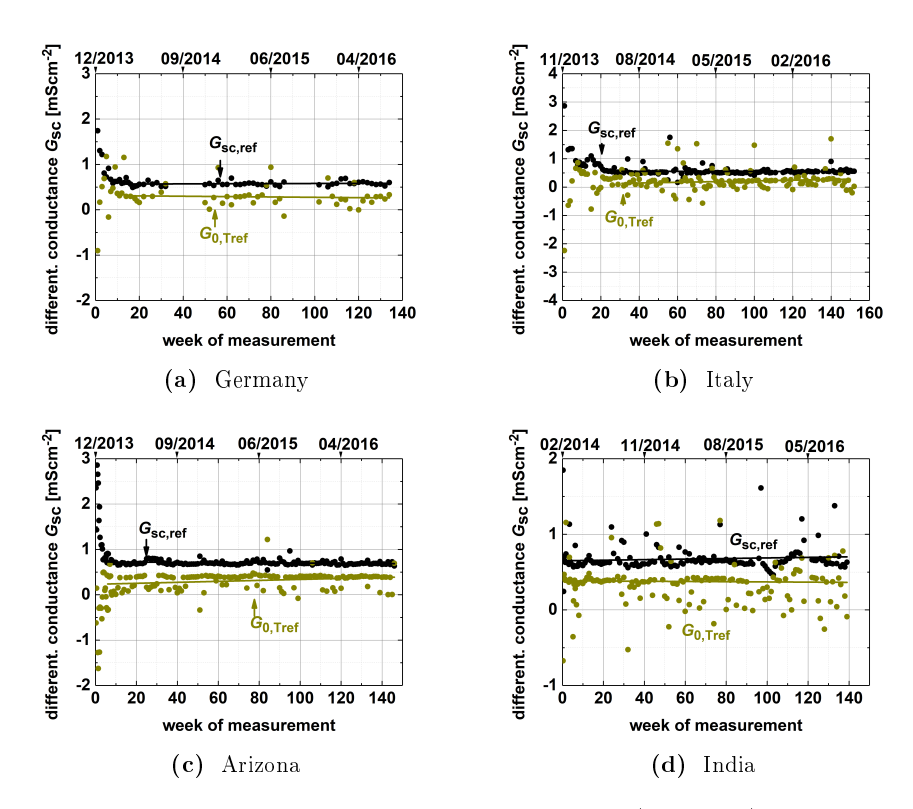


Figure C.12. – Weekly time values for STC for  $G_{\rm sc,ref}$  (black dots) and the term  $\kappa_{\rm Gsc}J_{\rm sc,ref}$  (red dots). The data are taken from the CdTe1 module measured in a) Cologne, Germany b) Ancona, Italy c) Tempe, Arizona, and d) Chennai, India.



**Figure C.13.** – Weekly time values for STC for  $G_{\rm sc,ref}$  (black dots) and the term  $G_{\rm sc,0,Tref}$  (dark yellow dots). The data are taken from the CdTe2 module measured in a) Cologne, Germany b) Ancona, Italy c) Tempe, Arizona, and d) Chennai, India.

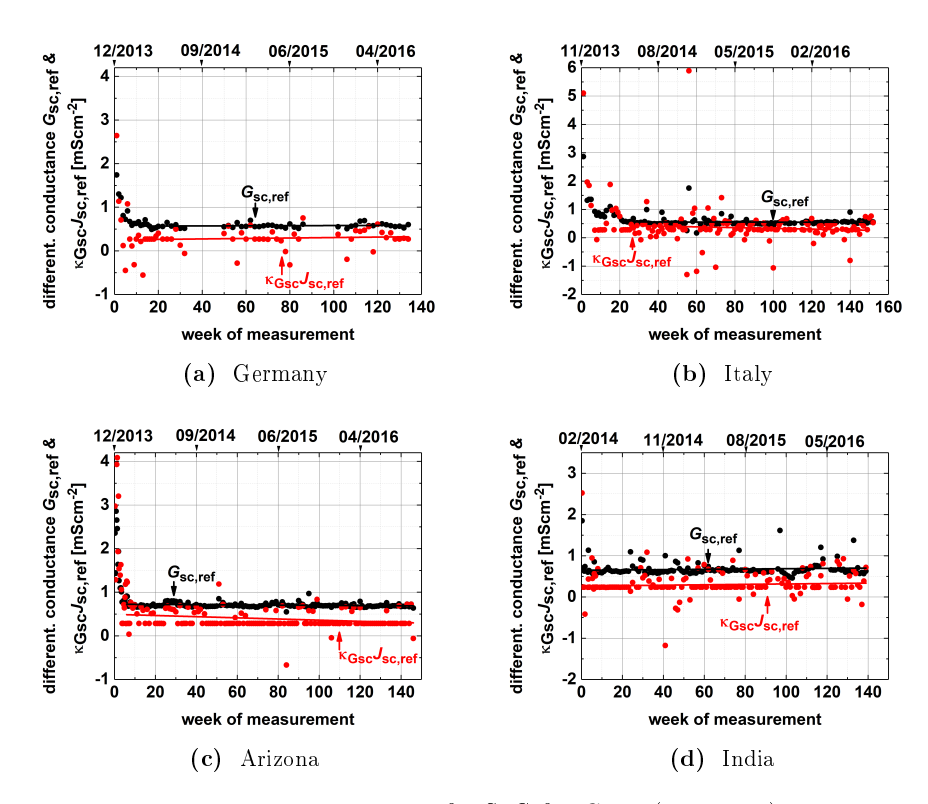
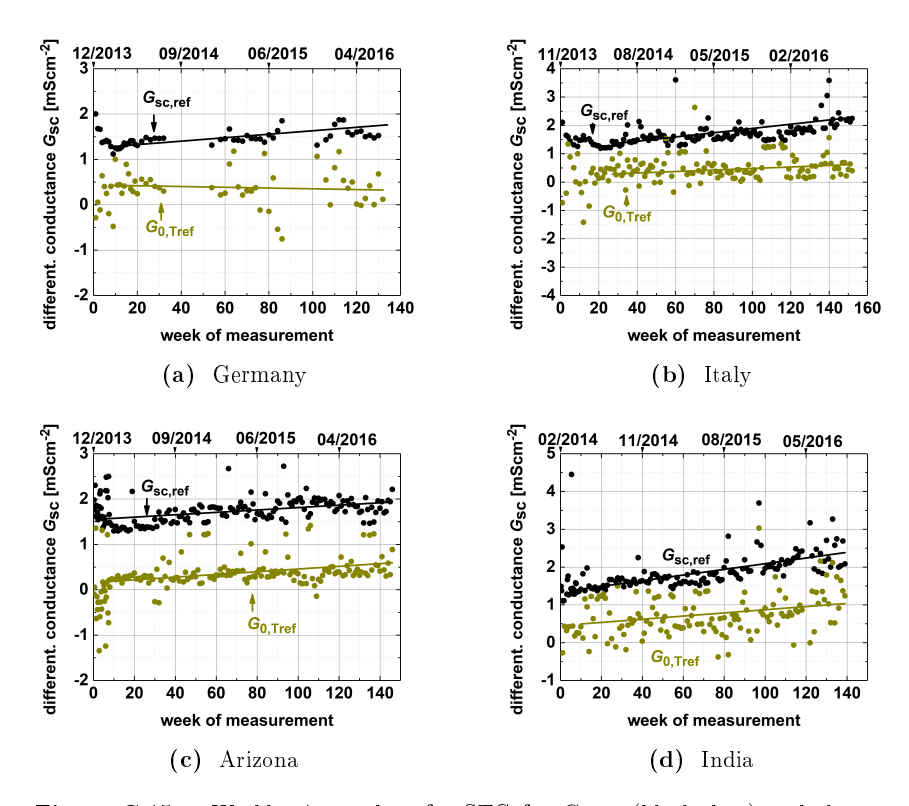


Figure C.14. – Weekly time values for STC for  $G_{\rm sc,ref}$  (black dots) and the term  $\kappa_{\rm Gsc}J_{\rm sc,ref}$  (red dots). The data are taken from the CdTe2 module measured in a) Cologne, Germany b) Ancona, Italy c) Tempe, Arizona, and d) Chennai, India.



**Figure C.15.** – Weekly time values for STC for  $G_{\rm sc,ref}$  (black dots) and the term  $G_{\rm sc,0,Tref}$  (dark yellow dots). The data are taken from the CdTe3 module measured in a) Cologne, Germany b) Ancona, Italy c) Tempe, Arizona, and d) Chennai, India.

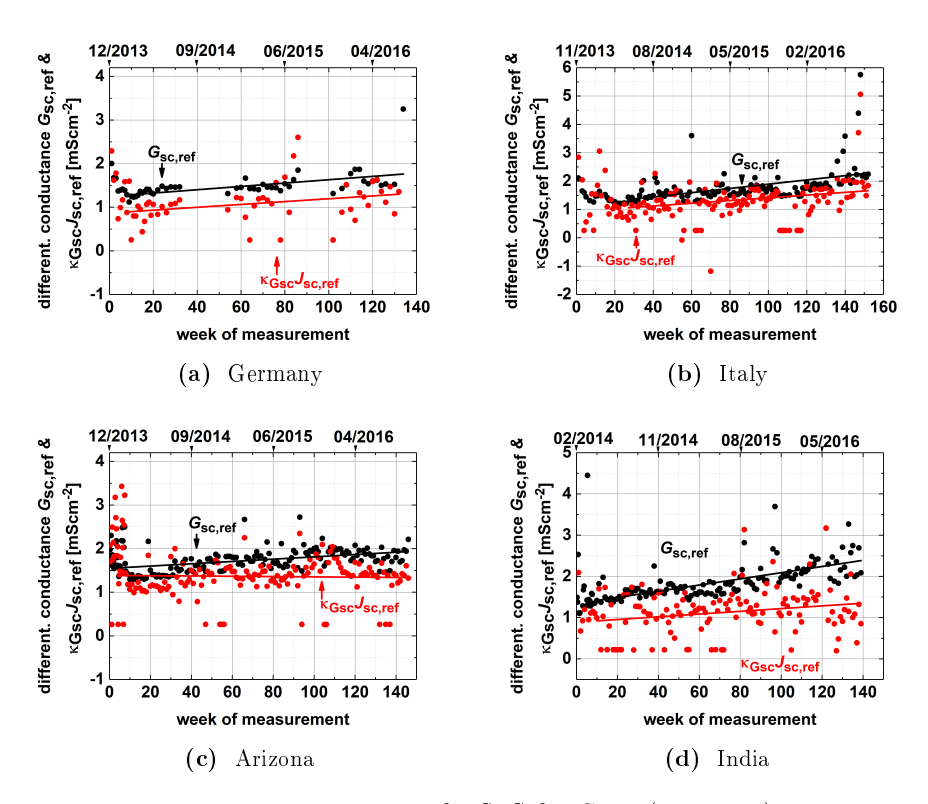


Figure C.16. – Weekly time values for STC for  $G_{\rm sc,ref}$  (black dots) and the term  $\kappa_{\rm Gsc}J_{\rm sc,ref}$  (red dots). The data are taken from the CdTe3 module measured in a) Cologne, Germany b) Ancona, Italy c) Tempe, Arizona, and d) Chennai, India.

### C.2.3. Differential resistance at open circuit condition

The Figures are based on Section 5.2.3.

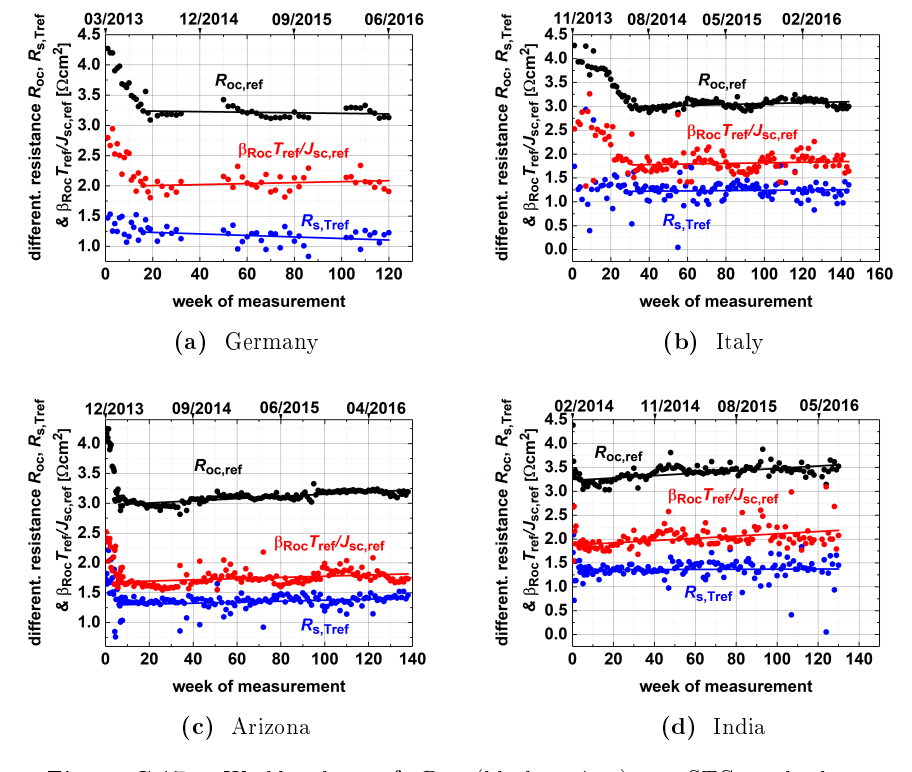


Figure C.17. – Weekly data of  $R_{\rm oc}$  (black points) at STC and the terms  $\beta_{\rm Roc}T_{\rm ref}/J_{\rm sc,ref}$  (red points) and  $R_{\rm s,\ Tref}$  (blue points). The data are taken from the CdTe1 module measured in a) Cologne, Germany b) Ancona, Italy c) Tempe, Arizona, and d) Chennai, India.

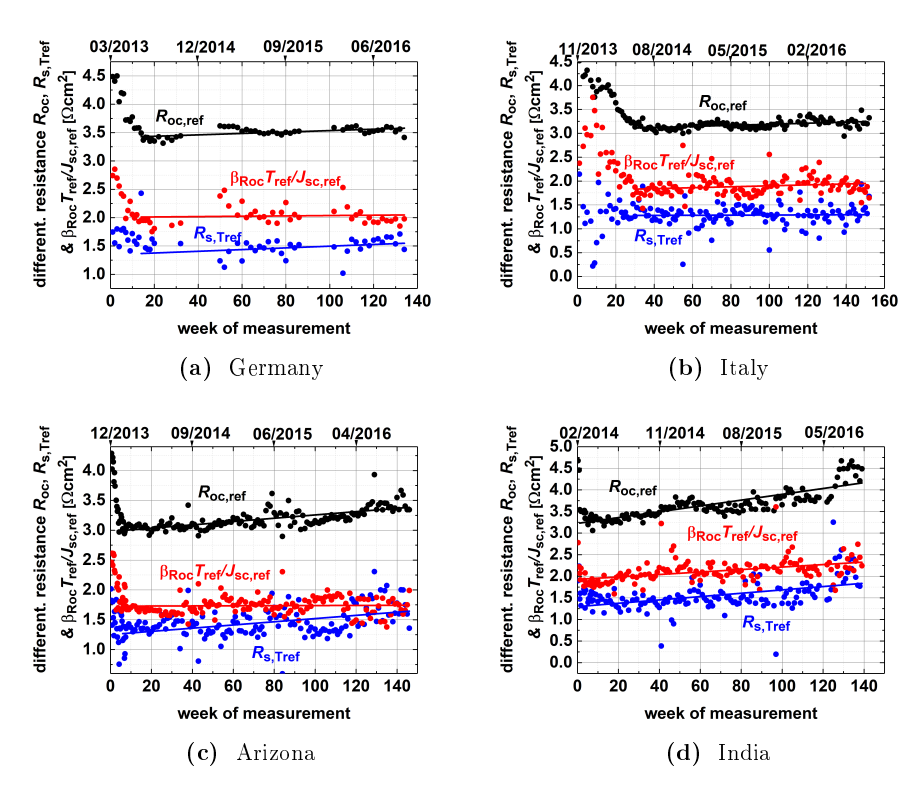


Figure C.18. – Weekly data of  $R_{\rm oc}$  (black points) at STC and the terms  $\beta_{\rm Roc}T_{\rm ref}/J_{\rm sc,ref}$  (red points) and  $R_{\rm s,\ Tref}$  (blue points). The data are taken from the CdTe2 module measured in a) Cologne, Germany b) Ancona, Italy c) Tempe, Arizona, and d) Chennai, India.

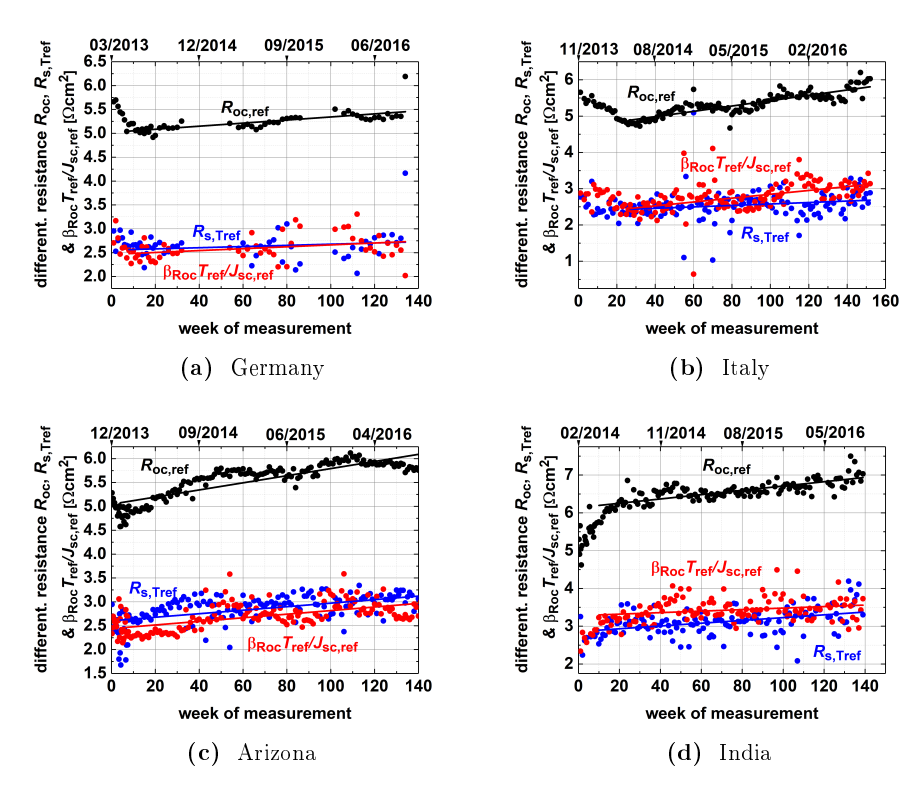
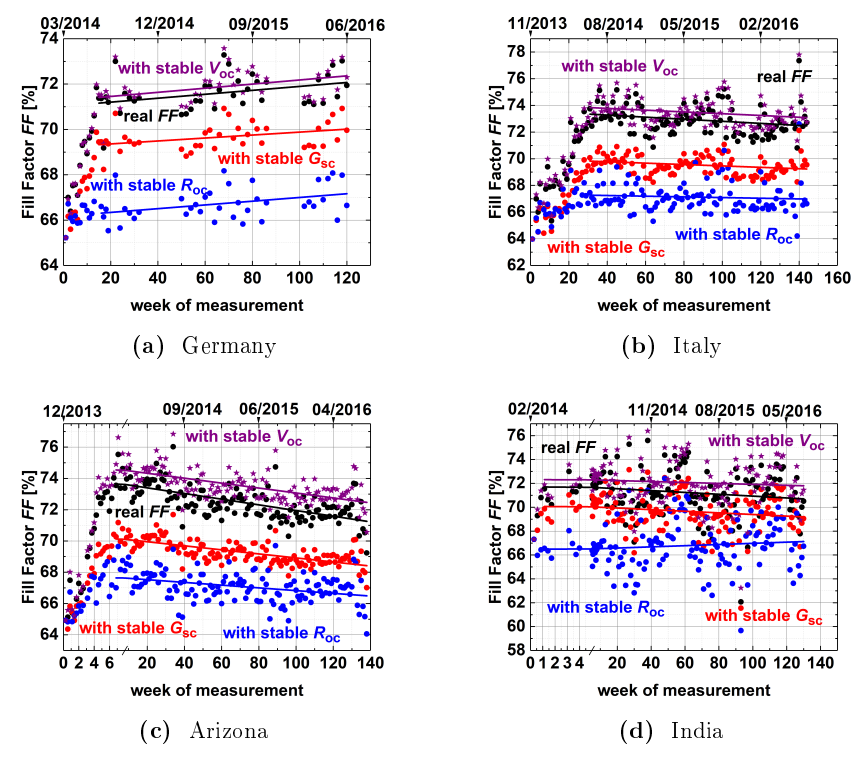


Figure C.19. – Weekly data of  $R_{\rm oc}$  (black points) at STC and the terms  $\beta_{\rm Roc}T_{\rm ref}/J_{\rm sc,ref}$  (red points) and  $R_{\rm s,\ Tref}$  (blue points). The data are taken from the CdTe3 module measured in a) Cologne, Germany b) Ancona, Italy c) Tempe, Arizona, and d) Chennai, India.

### C.2.4. Fill Factor

The Figures are based on Section 5.2.4.



 $\begin{array}{c} \textbf{Figure C.20.} - \text{Weekly data of the } FF \text{ (black points) at STC. For analysis, the weekly STC values for the } FF \text{ were also calculated with stable } R_{\text{oc}} \text{ conditions} \\ \text{(blue dots), stable } G_{\text{sc}} \text{ conditions (red dots) and stable } V_{\text{oc}} \text{ conditions} \\ \text{(purple stars). The data are taken from the CdTe1 module measured in a) Cologne, Germany b) Ancona, Italy c) Tempe, Arizona, and d) \\ \text{Chennai, India.} \end{array}$ 

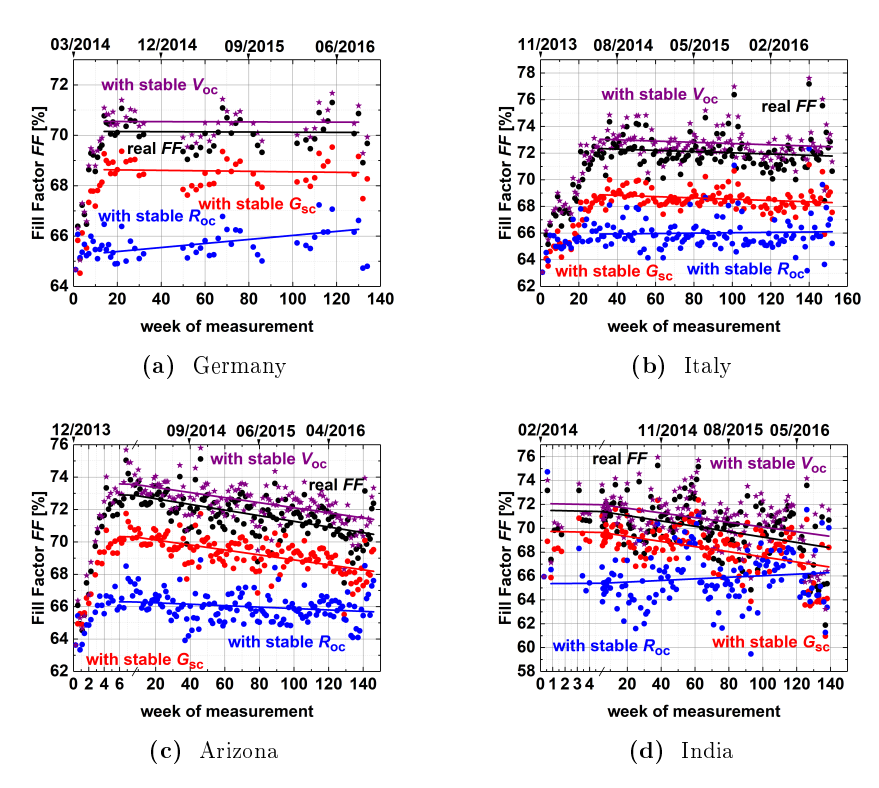
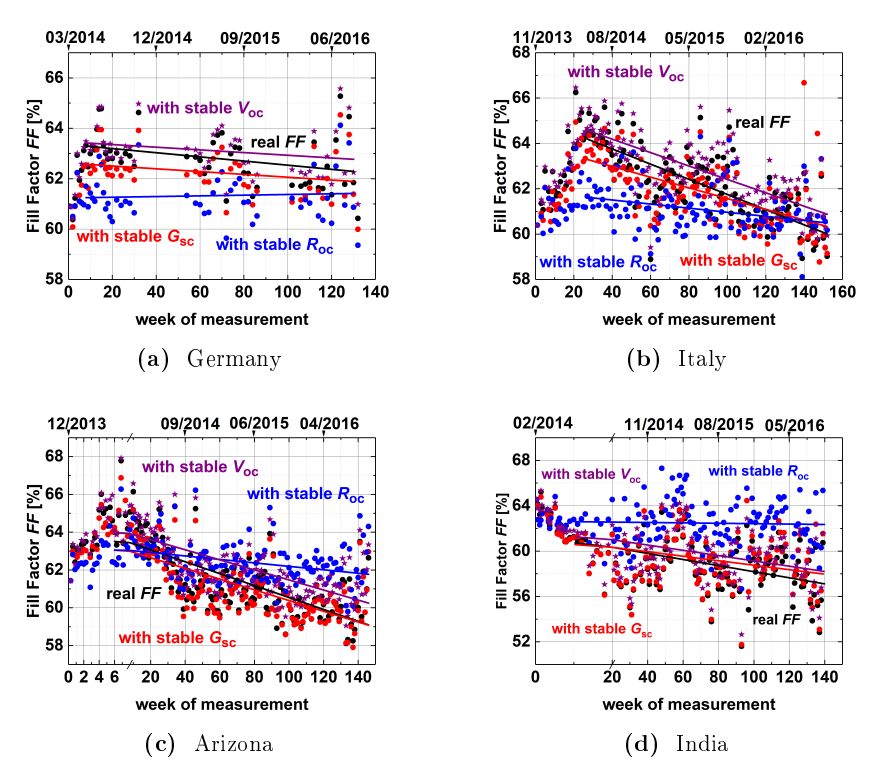
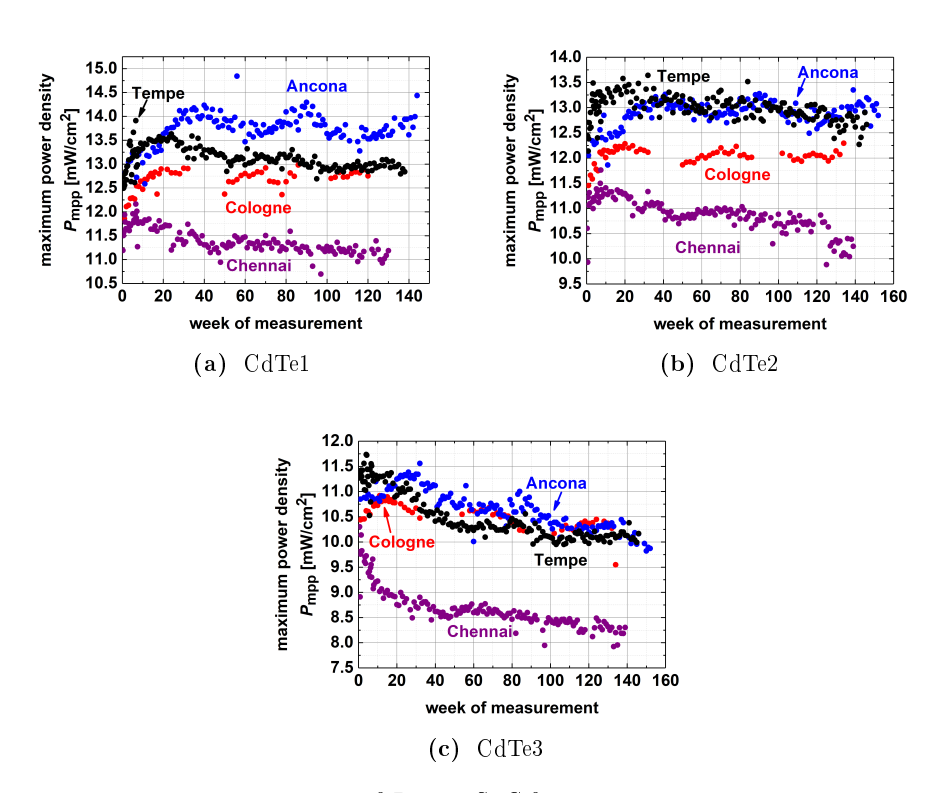


Figure C.21. – Weekly data of the FF (black points) at STC. For analysis, the weekly STC values for the FF were also calculated with stable  $R_{\rm oc}$  conditions (blue dots), stable  $G_{\rm sc}$  conditions (red dots) and stable  $V_{\rm oc}$  conditions (purple stars). The data are taken from the CdTe2 module measured in a) Cologne, Germany b) Ancona, Italy c) Tempe, Arizona, and d) Chennai, India.



### C.2.5. Maximum Power Density



 $\begin{tabular}{ll} \textbf{Figure C.23.} - Weekly data of $P_{\rm mpp}$ at STC for different modules. For each module the data are shown for Cologne, Germany (red dots), Ancona, Italy (blue dots), Tempe, Arizona (black dots), and Chennai, India (purple dots). The data are taken from the a) CdTe1 b) CdTe2 and c) CdTe3 module. The $P_{\rm mpp}$ value is calculated with the initial $J_{\rm sc}$ value for all weeks.$ 

### C.2.6. Tables with summarized analysis results

In the Table C.1 - C.5, the changes of the parameters and coefficients at STC are shown during the consolidation and degradation phases for all 12 measured CdTe modules. For convenient writing, some abbreviations have been used. These will be explained in the following.

The modules are classified by their location and number. The abbreviations for the locations are: Ge - Germany, It - Italy, Az - Arizona, and In - India. The CdTe1 module in Germany is therefore classified as "Ge1".

The abbreviations for the parameters and coefficients consideration are defined as followed:  $t_{\rm con}$  - time of consolidation phase;  $\Delta P_{\rm mpp}$  - change of  $P_{\rm mpp}$  with constant  $J_{\rm sc}$  value;  $FF_{\rm Voc}$  - fill factor with constant  $V_{\rm oc}$  value (see Section 5.2.4);  $FF_{\rm Gsc}$  - fill factor with constant  $R_{\rm oc}$  value;  $t_{\rm degr}$  - time of degradation phase.

The parameter  $P_{\rm mpp}$  FF,  $G_{\rm sc}$ , and  $R_{\rm oc}$  show a degradation phase and a consolidation phase. Table C.1 deals with the changes of  $P_{\rm mpp}$  and FF during the consolidation phase. However, as a reference also the changes of  $V_{\rm oc}$  are shown here. Table C.2 deals with the changes of  $G_{\rm sc}$  and  $R_{\rm oc}$  during the consolidation phase. The values in both tables show the changes from the initial value to the last value of the consolidation phase.

For the degradation phase of  $P_{\rm mpp}$ , FF,  $G_{\rm sc}$ , and  $R_{\rm oc}$ , the changes are shown in Table C.3 and C.4. Also here, the changes of  $V_{\rm oc}$  are shown as reference. A linear fit was applied to the values in this phase. From the linear fit an average change of one week could be determined. Assuming that a year contains 52 weeks, from the weekly average a yearly average could be determined.

For  $V_{\rm oc}$  and the respective coefficients from the translation equation, the absolute changes during the entire outdoor exposure are considered in Table C.5. The absolute changes are then transformed into a yearly change.

It should be noted that for India, the consolidation phase is very short. The determined consolidation phase was determined to be one week for the CdTe1 module and 0.8 weeks for the CdTe2 module. It can be assumed that the consolidation phase is even shorter than the value that could be determined from the data. This

leads to a small inaccuracy of these values which should be taken into account. For the CdTe3 module, the consolidation phase is overlapped by a strong degradation phase, followed by a second smaller degradation. As no clear consolidation phase for the CdTe3 module could be determined, the entire changes due to the first degradation phase are taken into account for the consolidation phase. This explains the higher amount of weeks for this phase in Table C.2.

It should be noted that for the CdTe2 and CdTe3 modules the outdoor exposure at each location is some weeks longer than the time given in Section 3.1. However, the starting time is for each location the same.

 $\begin{array}{lll} \textbf{Table C.1.} & - \text{Parameter and coefficient changes during the consolidation phase for all} \\ & 12 \text{ CdTe modules. Part 1 - shown are the values for } P_{\text{mpp}}, \textit{FF}, \text{ and } V_{\text{oc}} \\ & \text{at STC.} \end{array}$ 

	$t_{ m con}$	$\Delta P_{\mathbf{mpp}}$	$\Delta FF$	$\Delta FF_{ m Voc}$	$\Delta FF_{\mathbf{Gsc}}$	$\Delta FF_{\mathbf{Roc}}$	$\Delta V_{ m oc}$
$\mathbf{Module}$	[weeks]	$[\mathrm{mW/cm^2}]$	[%]	[%]	[%]	[%]	[mV]
			(abs)	(abs)	(abs)	(abs)	
Ge1	15	0.95	5.94	6.19	4.11	1.06	-8.14
${ m Ge2}$	14	0.72	5.48	5.88	3.96	0.67	-15.96
${ m Ge3}$	8	0.32	2.41	2.51	1.68	0.36	-7.26
It1	31	1.48	9.36	9.86	5.85	3.29	-21.59
It2	31	1.28	9.27	9.97	5.81	2.86	-33.5
It3	27	0.5	3.8	4.18	2.9	1.23	-10.94
Az1	7	0.88	8.72	9.62	5.21	2.72	-47.84
$\mathbf{A}\mathbf{z}2$	6	1.09	9.28	9.97	6.7	2.67	-40.79
Az3	4	0.27	1.89	2.53	1.66	1.62	-5.39
In1	1	0.46	4.39	5	2.75	0	-18.21
In2	0.8	0.71	5.55	6.11	3.8	0	-20.06
In3	10	-0.87	-3.87	-3.28	-3.94	-1.96	-24.27

Table C.2. – Parameter and coefficient changes during the consolidation phase for all 12 CdTe modules. Part 2 - shown are the values for  $G_{\rm sc}$  and  $R_{\rm oc}$  at STC

	$\Delta G_{ m sc,ref}$	$\Delta G_{\rm sc,0,Tref}$	$\Delta \kappa J_{\rm sc,ref}$	$\Delta R_{ m oc,ref}$	$\Delta R_{\mathrm{s,Tref}}$	$\Delta \beta_{\mathbf{Roc}} T_{\mathbf{ref}}$
						$/J_{ m sc,ref}$
Module	$[\mathrm{mScm}^{-2}]$	$[\mathrm{mScm}^{-2}]$	$[\mathrm{mScm}^{-2}]$	$[\Omega \ \mathrm{cm^2}]$	$[\Omega \ \mathrm{cm^2}]$	$[\Omega \ cm^2]$
$\overline{\mathrm{Ge1}}$	-1.32	2.42	-3.74	-1.03	-0.23	-0.8
${f Ge2}$	-1.17	1.21	-2.38	-1.06	-0.37	-0.73
${ m Ge}3$	-1.31	0.09	-1.4	-0.61	-0.39	-0.22
It1	-2.29	2.31	-4.6	-1.28	-0.52	-0.76
$\mathbf{It2}$	-2.3	2.37	-4.68	-1.41	-0.87	-0.54
It3	-0.77	1.02	-1.78	-0.76	-0.34	-0.42
Az1	0.15	1.26	-3.43	-1.27	-0.43	-0.84
Az2	-1.64	0.86	-2.49	-1.45	-0.75	-0.7
Az3	-0.42	0.26	-0.69	-0.2	-0.2	0
In1	-1.12	1.09	-2.21	-1.14	-0.36	-0.78
In2	-1.2	1.05	-2.25	-1.45	-0.6	-0.85
In3	-0.08	0.76	-1.17	0.9	0.66	0.96

Table C.3. – Parameter and coefficient changes during the degradation phase for all 12 CdTe modules. Part 1 - shown are the values for  $P_{\rm mpp}$ , FF, and  $V_{\rm oc}$  at STC.

	$t_{ m degr}$	$\Delta P_{\mathbf{mpp}}$	$\Delta FF$	$\Delta FF_{ m Voc}$	$\Delta FF_{\mathbf{Gsc}}$	$\Delta FF_{\mathbf{Roc}}$	$\Delta V_{\rm oc}$
Module	[weeks]		$[\%/\mathrm{year}]$	[%/year]	$[\%/\mathrm{year}]$	[%/year]	$[mV/cm^2]$
		/year]					/year]
		(rel)	(abs)	(abs)	(abs)	(abs)	
$\overline{\mathrm{Ge1}}$	105	0.0049016	84 0.45	0.47	0.34	0.43	-1.04
${ m Ge2}$	119	-0.05	-0.11	-0.11	-0.12	0.24	0.07
${ m Ge3}$	126	-0.26	-0.43	-0.28	-0.29	0.07	-7.44
$\mathbf{It1}$	113	-0.13	-0.41	-0.34	-0.27	-0.14	-3.38
$\mathbf{It2}$	121	-0.06	-0.24	-0.24	-0.25	0.07	0.31
It3	125	-0.43	-1.74	-1.54	-1.23	-0.47	-10.5
Az1	131	-0.22	-0.94	-0.83	-0.68	-0.45	-1.04
Az2	140	-0.21	-0.88	-0.83	-0.78	-0.23	-2.6
Az3	142	-0.46	-1.77	-1.51	-1.61	-0.46	-11.4
In1	129	-0.28	-0.41	-0.21	-0.35	0.23	-10.4
In2	138.2	-0.4	-1.20	-1.04	-1.14	0.35	-5.72
In3	129	-0.28	-1.46	-1.25	-1.09	-0.09	-6.24

**Table C.4.** – Parameter and coefficient changes during the degradation phase for all 12 CdTe modules. Part 2 - shown are the values for  $G_{\rm sc}$  and  $R_{\rm oc}$  at STC.

	$\Delta G_{\rm sc,ref}$	$\Delta G_{\rm sc,0,Tref}$	$\Delta \kappa J_{\rm sc,ref}$	$\Delta R_{\rm oc,ref}$	$\Delta R_{\rm s,Tref}$	$\Delta \beta_{\mathbf{Roc}} T_{\mathbf{ref}}$
						$/J_{ m sc,ref}$
Module	$ \mathrm{mScm}^{-2} $	$[\mathrm{mScm}^{-2}]$	$[\mathrm{mScm}^{-2}]$	$\Omega$ cm <sup>2</sup>	$[\Omega \mathrm{cm}^2]$	$\Omega$ cm <sup>2</sup>
	/year]	/year]	$/\mathrm{year}]$	/year]	/year]	/year]
Ge1	-0.03	-0.06	0.03	-0.02	-0.07	0.04
${ m Ge2}$	0.01	-0.02	0.03	0.07	0.08	0.02
${ m Ge3}$	0.13	-0.04	0.17	0.17	0.06	0.10
It1	0.06	0.07	-0.00009	0.05	0.02	0.03
$\mathbf{It2}$	-0.00009	0.06	-0.07	0.06	0.01	0.05
It3	0.39	0.14	0.25	0.38	0.10	0.28
Az1	0.05	0.06	-0.01	0.10	0.04	0.05
$\mathbf{Az2}$	-0.01	0.06	-0.07	0.15	0.14	0.01
Az3	0.14	0.15	-0.02	0.39	0.19	0.20
In1	0.05	0.11	-0.07	0.13	0.01	0.12
In2	0.02	-0.01	0.03	0.35	0.20	0.15
In3	0.39	0.22	0.17	0.30	0.19	0.10

**Table C.5.** – Parameter and coefficient changes for  $V_{\rm oc}$  during outdoor exposure for all 12 CdTe modules.

	0	<b></b>			
	$t_{ m total}$	$\Delta V_{\rm oc}$	$\Delta V_{\text{oc,0}}$	$\Delta \alpha_{ m Voc}$	$\Delta \epsilon_{\mathbf{Voc}}$
$\mathbf{Module}$	[weeks]	[mV/year]	[mV/year]	[mV/K/year]	$[\mathrm{mV/K/year}]$
$\overline{\mathrm{Ge1}}$	120	-6.60	31.46	0.10	-0.01
${ m Ge2}$	134	-6.94	26.04	0.13	0.01
${ m Ge}3$	134	-10.04	-3.76	-0.01	-0.01
$\mathbf{It1}$	144	-9.34	10.62	0.08	$7 \times 10^{-5}$
$\mathbf{It2}$	152	-11.99	-46.70	-0.10	$7 \times 10^{-5}$
It3	152	-14.85	3.42	0.12	0.02
Az1	138	-24.28	-80.44	-0.29	-0.03
$\mathbf{Az2}$	146	-18.44	-92.46	-0.27	-0.01
Az3	146	-16.96	-2.49	0.03	-0.01
$\mathbf{In1}$	130	-22.91	-114.16	-0.40	$-8.0 \times 10^{-5}$
$\mathbf{In2}$	139	-16.38	-19.30	-0.16	-0.01
$\mathbf{In3}$	139	-19.24	-77.06	0.02	-0.12

## D. List of Abbreviations and Symbols

### Common Abbreviations

Acronym	Meaning
AM	air mass
AMPS	Analysis of Microelectronic and Photonic
	Structures
ASA	Advanced Semiconductor Analysis
COP 21	21st United Nations Climate Change Confer-
	ence
DB	dangling bonds
DOS	density of states
ESR	electron spin resonance
GHG	greenhouse gas
IQR	interquartile range
JV curve	current-density voltage curve
KH	Karmalkar-Haneefa
LFM	Loss-Factor-Model
LSODE	Livermore Solver for Ordinary Differential
	Equations
meas	measured
MMF	miss-match-factor
MPP	maximum power point
O&M	operation and maintenance

List of Abbreviations and Symbols

Acronym	Meaning
OECD	Organisation for Economic Co-operation and $$
	Development
pr	Parameter
$\operatorname{pred}$	predicted
PV	Photovoltaics
poly-Si	poly-crystalline Silicion
Q1	first quantile
$Q_3$	third quantile
$\operatorname{ref}$	reference
${ m rms}$	root mean square
SAPM	Sandia Array Performance Model
SCAPS	Solar cell CAPacitance Simulator
SHJ	Silicon Hetero Junction
SRH	Schockley-Read-Hall
SSC	Site-Specific Condition
ST	standard test
STC	standard test condition
U.S.	United States

### Formula Abbreviations

$\mathbf{Symbol}$	Description	Typical Unit
$C_{ m sw}$	$thermally\ activated\ Staebler-Wronski\ con-$	$\mathrm{m^3}\ /\mathrm{s}$
	stant	
$D^0$	neutral state of dangling bond	-
$D^+$	positive state of dangling bond	-
$D^{-}$	negative state of dangling bond	-
E	energy level	V/m
$E_A$	activation energy	eV
$E_c$	conduction band edge	eV
$E_{c0}$	conduction band-tail slope energy	eV
$E_e$	effective irradiance	-
$E_F$	quasi-Fermi level	eV

Symbol	Description	Typical Unit
$E_g$	band gap	eV
$E_v$	valence band edge	eV
$E_{v0}$	valence band-tail slope energy	eV
$f^0$	probability for a neutral defect	=
$f_{ m sc}$	current-collection function at short circuit	=
FF	Fill Factor	%
G	irradiance	$ m W/m^2$
$G_i$	normalized plane of array irradiance	=
$G_{ m sc}$	differential conductance at short-circuit current	${ m mS\ /cm^2}$
$G_{ m sc,0}$	fitting constant for $G_{\rm sc}$ translation equation of the KH model	$\mathrm{mS}\ /\mathrm{cm}^2$
$G_{ m sc,0,Tref}$	$G_{ m sc}$ at reference temperature	$\mathrm{mS}/\mathrm{cm}^2$
J	current density	$\mathrm{mA}\ /\mathrm{cm}^{2}$
j	normalized current density	=
$J_0$	diode's ideal reverse-bias saturation current density	$mA\ /cm^2$
$J_{00}$	reference diode's ideal reverse-bias satura- tion current density	$mA\ /cm^2$
$J_L$	light generated current density	$\mathrm{mA}\ /\mathrm{cm}^2$
$J_{ m mpp}$	current density at the maximum power density	$mA\ /cm^2$
$J_{ m ph}$	photo-generated current density	$\mathrm{mA}/\mathrm{cm}^2$
$J_{ m sc}$	short-circuit current density	$\mathrm{mA}^{'}/\mathrm{cm}^{2}$
m	fitting parameter for the Karmalkar-	-
	Haneefa model	
N	dangling bond concentration	$1/\mathrm{m}^3$
$N_c$	effective density of states in the conduc-	$1/\mathrm{m}^3$
-	tion band edge	•
$N_{cbt}$	effective density of states in the conduc-	$1/\mathrm{m}^3$
	tion band-tail	,
$N_s$	number of cells in series	=

List of Abbreviations and Symbols

Symbol	Description	Typical Unit
$N_v$	effective density of states in the valence	$1/\mathrm{m}^3$
	band edge	
$N_{vbt}$	effective density of states in the valence	$1/\mathrm{m}^3$
	band-tail	
n	concentrations for electrons	$1/\mathrm{m}^3$
$n_{ m id}$	ideality factor	-
$n_i$	intrinsic carrier concentration	$1/\mathrm{m}^3$
$n_{ m Roc}$	ideality factor determined via the $R_{\rm oc}$ vs.	-
	$1/J_{ m sc}$ method	
$n_{ m Voc}$	ideality factor determined via the $V_{\rm oc}$ vs.	-
	$\log{(J_{ m sc})}$ method	
P	power density	$\mathrm{mW}/\mathrm{cm}^2$
$P\left( E\right)$	Gaussian distribution	-
p	concentrations for holes	$1/\mathrm{m}^3$
$p^+$	a high $p-$ type doping concentration	
$P_{ m mpp}$	maximum power density	$\mathrm{mW}/\mathrm{cm}^2$
R	recombination rate	$1~/\mathrm{m}^3~/\mathrm{s}$
$R_{ m oc}$	differential resistance at open-circuit volt-	${ m m}\Omega\ /{ m cm}^2$
	age	
$R_{ m s}$	fitting constant for the $R_{\rm oc}$ translation	${ m m}\Omega\ /{ m cm}^2$
	equation of the KH model	
$R_{ m s, \ Tref}$	$R_{ m oc}$ at reference temperature	${ m m}\Omega\ /{ m cm}^2$
$R_{sh}$	parallel resistances	$\Omega~{\rm cm}^2$
$R_{ m sc}$	differential resistance at short-circuit cur-	$\Omega~{\rm cm^2}$
	rent	
T	(back-of-module) temperature	$^{\circ}\mathrm{C}$
$T_c$	cell temperature inside the module	$^{\circ}\mathrm{C}$
t	time	S
v	normalized voltage	-
$v_0$	constant	1/s
$V_{ m mpp}$	voltage at the maximum power density	mV
$V_{ m oc}$	open circuit voltage	mV

Symbol	Description	Typical Unit
$V_{ m oc}^0$	fitting constant for $V_{\rm oc}$ translation equa-	mV
	tion of the KH model	
$\alpha$	temperature coefficient	1 / K
β	coefficient describing the dependence on	$\mathrm{mV/K}$
	$T/J_{ m sc}$	
$\gamma$	fitting parameter for the Karmalkar-	-
	Haneefa model	
$\epsilon_r$	relative dielectric constant	=
$\varepsilon$	coefficient describing the dependence on	$\mathrm{mV/K}$
	$\log(J_{\rm sc})$ and $T$	
$\kappa$	irradiance coefficient	1 /V
Λ	thermally activated constant	$\mathrm{m}^6/\mathrm{s}$
$\lambda$	thermally activated constant	$\mathrm{m^3}\ /\mathrm{s}$
$\mu$	band drift mobility	$\mathrm{cm^2}\ /\mathrm{V}\ /\mathrm{s}$
ho	space charge density	$\rm C/m^3$
au	lifetime	S
$\phi$	plane of array irradiance	$\mathrm{W}/\mathrm{m}^2$
$\varphi$	vacuum level related electrostatic poten-	V
	tial	
χ	slope of the collection function at $V_{ m oc}$	1 / mV
$\psi$	error	=

### Superscripts for the Loss-Factor-Model

m measured
n normalized
r reference

### **Chemical Symbols**

a-Si:HHydrogenated amorphous siliconc-Sicrystalline SiliconCdSCadmium sulfide

### List of Abbreviations and Symbols

CdTe Cadmium telluride

CIGS Copper indium gallium

(di)selenide

Cu Copper

CuInSe2 Copper indium diselenide

Te Tellur

 $\mu$ c-Si:H hydrogenated microcrystalline

Silicon

### Constants

k Boltzmann constant  $8.6173303 \times 10^{-5} \,\mathrm{eV}$  /K

q elementary charge  $1.602\,176\,620\,8\times10^{-19}\,\mathrm{C}$ 

 $\epsilon$  — dielectric constant of  $8.854\,187\,817\,62\times 10^{-12}\,\mathrm{F}\ /\mathrm{m}$ 

vacuum

### E. List of publications

#### Publications related to this work

- 1. C. Ulbrich, S. Kurtz, D. Jordan, M. Görig, A. Gerber, U. Rau, *Direct analysis of the current-voltage curves of outdoor-degrading modules*, IEEE 40th Photovoltaic Specialist Conference (PVSC), 2856 2861 (2014)
- 2. M. Görig, B. Pieters, Development and validation of a phenomenological Model describing degradation and annealing of a-Si:H solar cells, 31st European Photovoltaic Solar Energy Conference and Exhibition (2015)
- M. Görig, C. Ulbrich, B. Pieters, A. Gerber, U. Rau, Determination of PV Outdoor Parameters for Thin Film Modules, IEEE 43rd Photovoltaic Specialists Conference (PVSC), 2666 – 2670 (2016)

### Oral presentations related to this work

- M. Görig, C. Ulbrich, A. Gerber, E. Barykina, U. Rau, Comparison of performance models in respect to degradation studies and yield prediction, EMN Meeting on Photovoltaics, (2015) Orlando, Florida, invited talk
- 2. M. Görig, C. Ulbrich, A. Gerber, E. Barykina, U. Rau, Karmalkar-Haneefa Modell zur Analyse von Energieerträgen und Degradationseffekten, 1. Industrieworkshop BMWi Forschungsvorhaben "Energieertrag von Dünnschicht-PV-Modulen unter verschiedenen klimatischen Bedingungen (PV-KLIMA)" (2015), Cologne, Germany
- 3. M. Görig, B. Pieters, Development and validation of a novel phenomenological approach for modelling degradation and annealing of a-Si:Hsolar cells and their dynamic response, 32nd European Photovoltaic Solar Energy Conference

### List of publications

and Exhibition (2016), Munich, Germany

### Poster presentations related to this work

- M. Görig, B. Pieters, Development and validation of a phenomenological Model describing degradation and annealing of a-Si:Hsolar cells, 31st European Photovoltaic Solar Energy Conference and Exhibition (2015)
- 2. M. Görig, C. Ulbrich, B. Pieters, A. Gerber, U. Rau, *Parameterization of Thin Film Modules*, NREL PV Module Reliability Workshop 2016 (2016), Denver, Colorado, **Poster Award**
- 3. M. Görig, C. Ulbrich, B. Pieters, A. Gerber, U. Rau, *Determination of PV Outdoor Parameters for Thin Film Modules*, IEEE 43rd Photovoltaic Specialists Conference (PVSC), 2666 2670 (2016)

### F. Curriculum Vitae

#### Personal details

Name Marzella Görig

Date of birth August 1st, 1988

Place of birth Herdecke, Germany

Citizenship German

#### Education

1995-1999 Grundschule Im Dorf, Herdecke

1999-2008 Friedrich-Harkort-Gymnasium, Herdecke

2008-2011 Bachelor of Engineering in Solar Technology (dual study)

at Anhalt University of Applied Science, Köthen

Focus: Technology

Bachelor thesis at Q-Cells SE, Bitterfeld

Title: Solare Brüter - unter besonderer Berücksichtigung

der Erntefaktoren von PV und Windkraft

2011-2013 Master of Science in Physical Technologies at Clausthal

University of Technology

Focus: Energy science and energy systems

Master thesis at Hanwha Q-Cells GmbH, Bitterfeld

Title: Optische Simulation von monokristallinen Industriesolarzellen für die Berechnung des Einkapselungseffek-

tes bei Glas-EVA Modulen

### Curriculum Vitae

2014-2017 PhD thesis at the Forschungszentrum Jülich GmbH, IEK5-

Photovoltaics

### Professional Experience

2000 2012	
2008-2013	Student Trainee at Hanwha Q Cells GmbH, Bitterfeld
	Topic: Research work in the field of crystalline Silicon solar
	cells
2012	Student Research Trainee at Clausthal University of Tech-
	nology
	Working group: High-temperature sensors
	Topic: Thin film calorimetry – on the example with Al and
	$MoS_2$ coated Langasite resonators
2012-2013	Student Research Trainee at Clausthal University of Tech-
	nology
	Working group: Energy conversion
	Topic: Bandoffsets simulations of GaN detectors for space
	applications
2013	Visiting Researcher at the University of Texas at Austin,
	USA
	Working group: Solid-state electronics
	Topic: Optical simulation of III-V quantum-well hetero-
	structures
2014-2017	PhD student /scientist at Forschungszentrum Jülich GmbH
	Working group: IEK5-Photovoltaics
	Topic: Numerical simulation and analysis in the field of
	degradation of thin film solar cells and modules
2017	Scientist at Lappeenranta University of Technology, Fin-
	land
	Working group: Solar economy
	Topic: Energy-Return-On-Investment calculations of en-
	ergy systems
	0191 01200110

### Acknowledgments

I would like to express my deep gratitude to all those who made this work possible and supported me in different ways during the last three years. Especially I would like to thank:

- Professor Dr. Uwe Rau first of all for giving me the opportunity to work as a PhD student in his institute. I appreciated also his great supervision, his constant confidence in me, and his interest in my work. The regular discussions with him made an important impact for this work. And finally, I would like to thank him for the examination of this thesis.
- Professor Dr. Ralph Gottschalg for the external mentoring and examination of this thesis. In addition, I acknowledged the wonderful and interesting time in Loughborough.
- Dr. Bart E. Pieters for being a good supervisor and who taught me much about scientific writing as well as about amorphous silicon solar cells. He also gave me the chance to supervise students by my own.
- Dr. Carolin Ulbrich for her great scientific input of my work considering the Karmalkar-Haneefa Model.
- Sabine Kasper and Christoph Zahren who helped me much with the degradation experiment, especially Sabine Kasper who was willing to wake up very early to calibrate the sun simulator for me.
- Markus Schweiger from TÜV Rheinland for the providing of the outdoor data and answering all my questions about their measurement setup. And all the other project partners from "PVKlima" and the regular discussion of the work.

Joachim Kirchhoff for preparing the a-Si:H samples.

Dirk Erdwig and Dorian Guzman for supporting me with the data base for the

#### Acknowledgments

outdoor measurement.

- Dr. Andreas Lambertz for providing me with a lot of a-Si:H papers.
- Dr. Yael Augarten for her willingness to correct my posters and the great USA trip.
- Vito Huhn for the great company during most of the conferences and workshops I visited, and the helpful discussions.
- Jan Mock for the awesome support during the writing time of this thesis, the discussion of pictures and LATEX details and his care about my lunch and tea breaks.
- Claudia Maurer and Samia Ahmed Nadi for being great colleagues and the amazing time inside as well as outside the office.

Manuela Meyer for the regular nice meeting in the morning at the coffee machine.

Petra Lorbach for the great administrative support.

- All colleagues at the Forschungszentrum Jülich who helped me in different ways during my PhD.
- And last, but not least, my family, who gave me an amazing support during my whole academic education, and Mathias Diefenthal, who gave me the best emotional support during my PhD time. Especially in trouble times, they always listened to my problems and motivated me.

Band / Volume 418

The Dynamics of Electrons in Linear Plasma Devices and its Impact on Plasma Surface Interaction

M. Hubeny (2018), 141 pp ISBN: 978-3-95806-316-7

Band / Volume 419

Tomographic reconstruction of gravity wave parameters from satellite-borne airglow observations

R. Song (2018), 136 pp ISBN: 978-3-95806-317-4

Band / Volume 420

Reduktion von Edelmetallen in der Wasserstoffelektrode bei der Polymerelektrolyt-Wasserelektrolyse

P. Paciok (2018), VII, 187 pp ISBN: 978-3-95806-320-4

Band / Volume 421

Mechanismen des Hochtemperaturrisswachstums in einem ferritischen Stahl an Luft und in Wasserdampf

T. Fischer (2018), VIII, 216 pp ISBN: 978-3-95806-326-6

Band / Volume 422

Selbstheilende plasmagespritzte  $Mn_{1,0}Co_{1,9}Fe_{0,1}O_4\text{-Schutzschichten}$  in Festoxidbrennstoffzellen

N. Grünwald (2018), x, 140 pp ISBN: 978-3-95806-327-3

Band / Volume 423

Sonochemical Synthesis of Silicon Hydride Polymers and Silicon Nanoparticles from Liquid Silanes

A. P. Cádiz Bedini (2018), viii, 132, XVIII pp

ISBN: 978-3-95806-329-7

Band / Volume 424

Synthesis and Stability Assessment of Uranium Microparticles: Providing Reference Materials for Nuclear Verification Purposes

R. Middendorp (2018), X, 145 pp ISBN: 978-3-95806-330-3

Band / Volume 425

Herstellung und Charakterisierung von Lithiumlanthanzirkonat-Funktionsschichten für Lithium-Festkörperbatterien

T. Reppert (2018), vii, 187 pp ISBN: 978-3-95806-331-0

### Schriften des Forschungszentrums Jülich Reihe Energie & Umwelt / Energy & Environment

Band / Volume 426

Proton Conduction and Gas Permeation through Polymer Electrolyte Membranes during Water Electrolysis

M. Schalenbach (2018), VI, 212 pp ISBN: 978-3-95806-333-4

Band / Volume 427

Improved characterization of root zone soil moisture by assimilating groundwater level and surface soil moisture data in an integrated terrestrial system model

H. Zhang (2018), x, 125 pp ISBN: 978-3-95806-335-8

Band / Volume 428

Manipulation of magnetism in iron oxide nanoparticle / BaTiO<sub>3</sub> composites and low-dimensional iron oxide nanoparticle arrays L. Wang (2018), VI, 151 pp ISBN: 978-3-95806-338-9

Band / Volume 429

Characterization of spatial-temporal varying riverbed hydraulic conductivity and its role on the estimation of river-aquifer exchange fluxes with data assimilation

Q. Tang (2018), xv, 117 pp ISBN: 978-3-95806-339-6

Band / Volume 430

Der Einfluss von Wasserdampf auf den Sauerstofftransport in keramischen Hochtemperaturmembranen F. Thaler (2018), ii, 93, XXXI pp

ISBN: 978-3-95806-340-2

Band / Volume 431

Analysis & modeling of metastable photovoltaic technologies: towards dynamic photovoltaic performance models

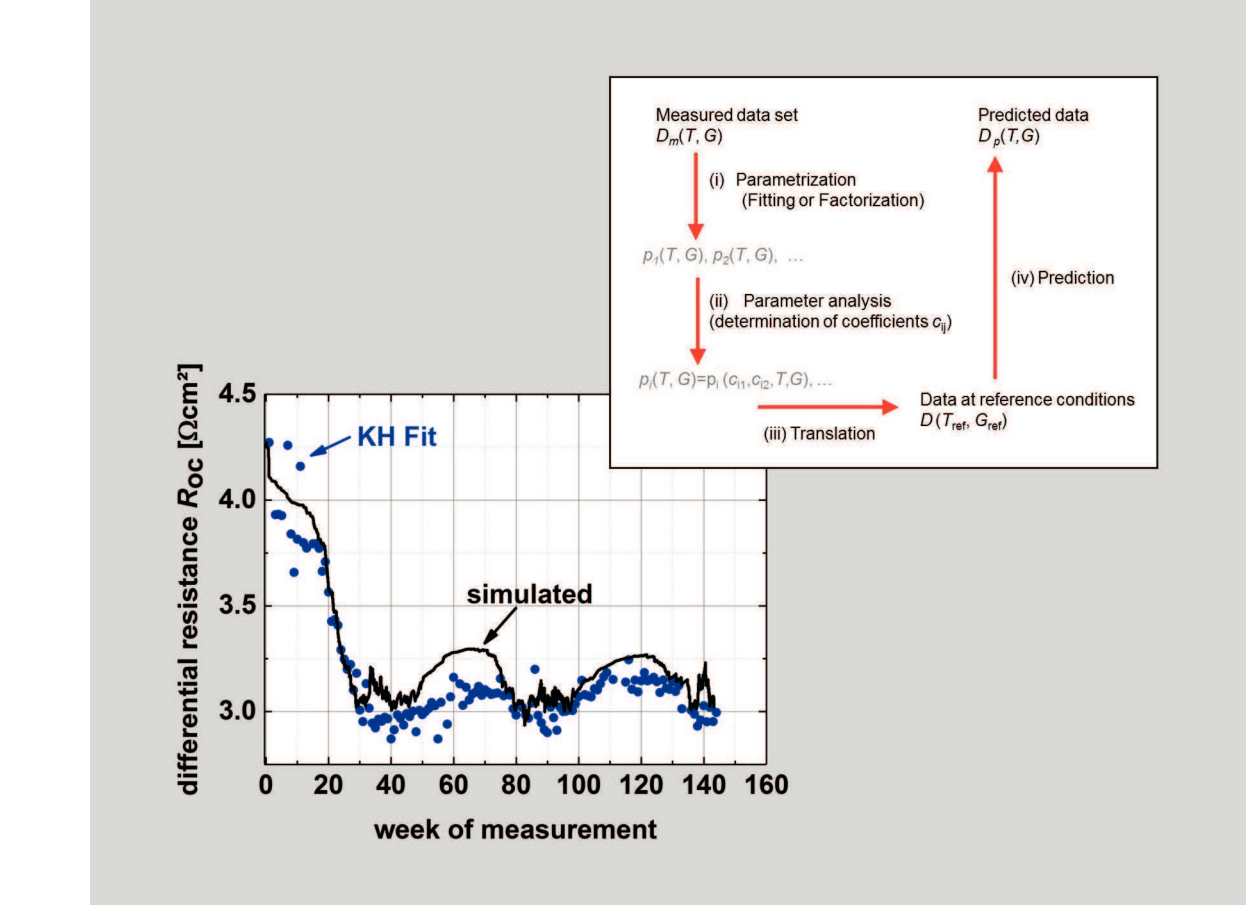
M. Görig (2018), 246 pp ISBN: 978-3-95806-342-6

Weitere Schriften des Verlags im Forschungszentrum Jülich unter

http://wwwzb1.fz-juelich.de/verlagextern1/index.asp

Energie & Umwelt Energy & Environment

Analysis & modeling of metastable photovoltaics



431

Analysis & modeling of metastable photovoltaic technologies: towards dynamic photovoltaic performance models

Marzella Amata Görig

Marzella Amata Görig

Energie & Umwelt / Energy & Environment Band / Volume 431 ISBN 978-3-95806-342-6

Energie & Umwelt / Energy & Environment Band / Volume 431 ISBN 978-3-95806-342-6





